FÍSICA
REVISTA CUBANA DE FÍSICA
Sociedad Cubana de Física
y Facultad de Física,
Universidad de La Habana
VOL.37 NO.2
DICIEMBRE, 2020

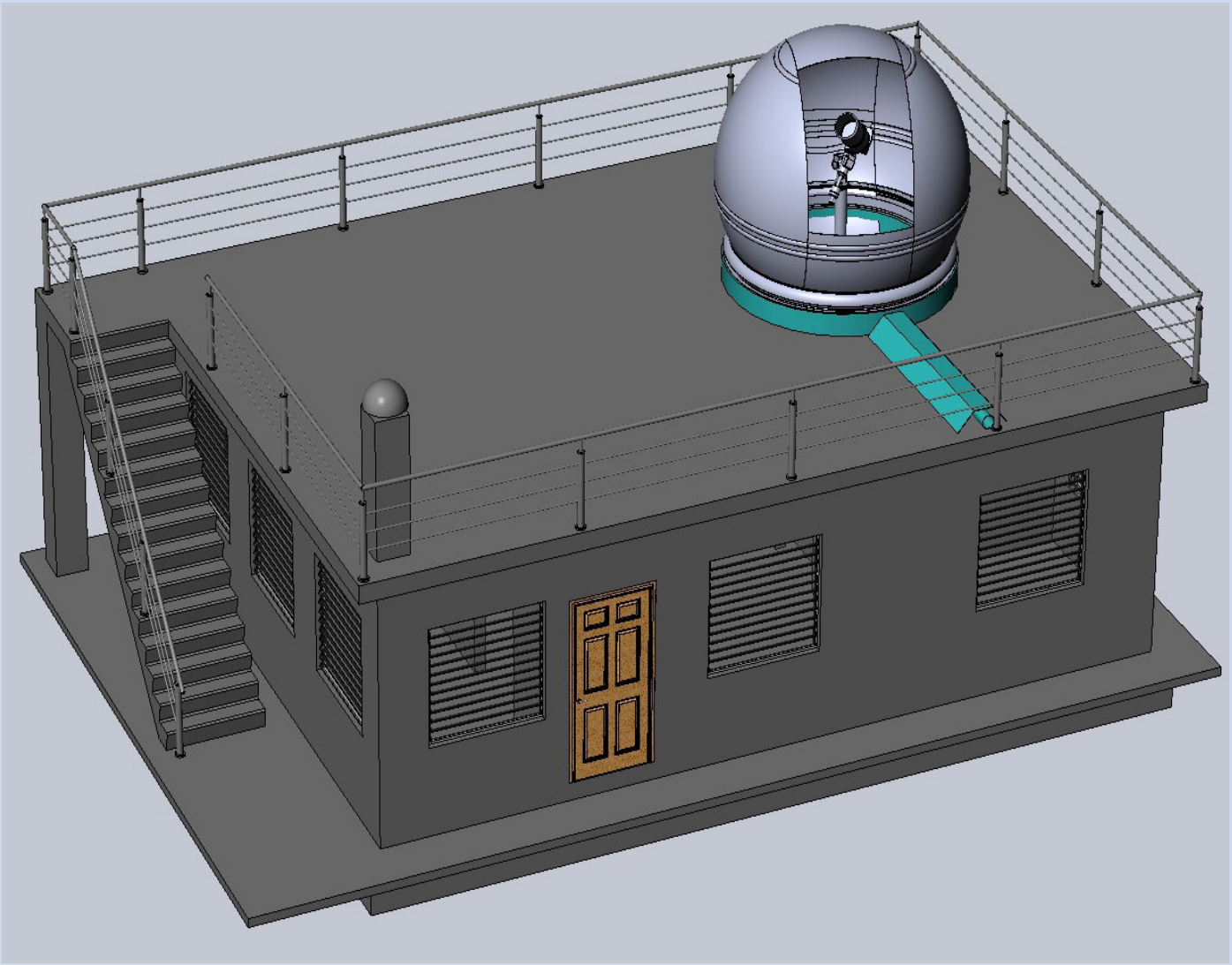

HACIA LA RENOVACIÓN DE LAS OBSERVACIONES ASTRONÓMICAS EN CUBA

Revista Cubana de Física
ISSN 0253-9268
Online ISSN 2224-7939

REVISTA CUBANA DE FÍSICA
Vol. 37, No. 2 (15 Diciembre 2020)
ISSN 0253 9268 Online 2224 7939

Portada: sketch of a new optical telescope to be installed at IGA thanks to Russia-Cuba collaboration. See article in page 162.

Todos los artículos en formato -e:
www.revistacubanadefisica.org

La Revista Cubana de Física es una publicación semestral de la Sociedad Cubana de Física

COORDENADAS

ARTÍCULOS ORIGINALES

COMUNICACIONES ORIGINALES

PARA FÍSICOS Y NO FÍSICOS

MOMENTOS DE LA FÍSICA EN CUBA

CORONAVIRUS AND COVID-19 OUTBREAK: WHEN PHYSICS AND ENGINEERING GO VIRAL

BROTE DE CORONAVIRUS Y COVID-19: CUANDO LA FÍSICA Y LA INGENIERÍA SE VUELVEN VIRALES

E. E. Ramírez-Miquet

Associate Editor of Revista Cubana de Física

The recent outbreak produced by SARS-CoV-2 virus has overwhelmed the world in an unprecedented way. After nearly a year of lockdowns, rampant death tolls and declining economies, the disease derived from this virus, COVID-19, has shown that the challenges to address have become more and more complex. While the scenario may look unmanageable, it poses an opportunity for revisiting ways of conducting and implementing practical research around engineering and physics aimed at virus assessment.

Despite the fact that some recent reviews and views see this crisis as a lost opportunity for micro and nanotechnology, especially for M/NEMS [1], I think that it is actually fertile ground for raising scientific arguments. In fact, I believe that the time is ripe to examine the progress made in physics and biomedical engineering with a broad perspective, following the lead of a recent review on the subject [2].

I will refer to two existing technologies that are available for virus detection and/or identification, which rely on novel engineering solutions based on physical phenomena involving material sciences, optics and acoustics and their interplay. I believe the Cuban scientists will find these approaches motivating and eventually connected to physics fields they currently work on at home and abroad.

The first approach I will focus on is related to the gold standard used to detect the SARS-CoV-2 in saliva or mucus samples: polymerase chain reaction (PCR), in this case enabled by acousto-fluidics. Combining the properties of surface acoustic waves propagating over a piezoelectric material with an engineered array of materials acting as phononic crystals, it is possible to shape the field of the waves and enable them to propagate into a liquid sample [3]. This workflow is excellently explained and detailed in some of the papers from the group of Prof. Cooper from the James Watt School of Engineering at University of Glasgow. I fully recommend the readers watching the plenary talk he tenured at SPIE Photonics West 2012 entitled "Developing Diagnostics for the Developing World". While this talk is mainly focused on bacteria and parasite detection in liquid samples with accessible instrumentation, it establishes the foundations for extending the involved techniques beyond the scope of "large" microorganisms identification and exploring their suitability in detecting nanometric sized viruses.

Now I briefly explain the working mechanism of the device, where Physics and Engineering are intimately interwoven. The system contains a piezoelectric substrate with micro-sized electrodes patterned on top of it. When the electrodes are excited electrically they generate a vibration on the surface that produces a mechanical wave. This mechanical energy travels through the piezo material as a surface acoustic wave depending on the crystal features such as orientation and processing finishing. Given the complexity associated to processing and manufacturing of some piezoelectric substrates, in particular Lithium Niobate ($LiNbO_3$), Prof. Cooper's group members chose to place a superstate on top of it to produce a selective actuation. This actuation is enabled by shaping the field of the acoustic forces via the superstrate, which is designed and fabricated with custom made arrays of structures and materials that act as acoustic waveguides [3]. Taking full advantage of the phononic crystal principles, and using modeling software tools, it is possible to customize the frequency bands that are enabled for the surface acoustic wave to travel from the substrate to the superstrate by convenient shaping, thus creating a path for producing a selective actuation over targets. The liquid medium containing the bacteria, parasites or potentially viruses is placed as a small droplet over the substrate, so it is submitted to acoustic actuation [4, 5]. If the right shape of the field is achieved, then the liquid sample can be subject to streaming and heated up to certain temperature producing the breakdown of the biological material within it. Not only this heating process is possible, but also allows multiple droplets to merge and produce biochemical reactions that are necessary in the series of procedures leading to PCR. This PCR process allows DNA amplification, which ultimately leads to a clear identification of the molecular information within the droplet sample, thus accessing to the fingerprint of the pathogen (bacteria, parasite or virus).

The above technology is compatible with other techniques including, for example, micro-sized object manipulation by optical tweezers. Some work on this area was developed in Cuba in partnership with French institutions around 2008-2009 [6–8]. Using these tweezers, and with careful adaptation of the setup, it is also possible to merge solid particles with the sample droplet in order to enable other focused studies.

The second technology that I want to refer to is optomechanical sensing of mass and stiffness using microresonators. Optomechanics is currently a very active

branch of research: many groups in the developed world focus on the interaction of electromagnetic fields in the optical domain with mechanical resonators. For some texts spanning the basics and applications, I refer the readers to [9–11].

Currently, a European consortium of labs in Spain, France, The Netherlands, Greece and Germany are collaborating on the ViruScan project, which searches implementing micro and nano optomechanical resonators to identify viruses. This is a very promising approach whereas there is no need to presuppose what is the virus that is attempted to be identified.

Optomechanics is at the interception of three areas that physicists and engineers have developed for decades: microelectronics, photonics and materials science. Miniaturized objects, typically micro and nanoresonators, are excited with light which drives the mechanical movement and at the same time, the optical field is varied as light goes through the resonators. As a consequence, the interplay of optics and mechanics converges to inspect the spectroscopic features of the resonators together with the mechanical features (vibration frequency and amplitude) of their motion. Now, ViruScan seeks to explore the unique features of this motion when a virus is placed on top of the resonator. The modes of the "loaded" resonator are expected to shift and differ from the natural modes of the resonator alone, thus providing information on the new frequencies related to the vibration modes of the virus, providing information on the its mass and stiffness. In this way, and given the fact that viruses are simple nanometric structures, it is expected that they can be identified. As of today, it was recently reported on the vibration modes of a single bacterium via these optomechanical resonators [12, 13]. It is the first proof of concept of how extremely small biological objects can be sensed and how their physical features can be identified.

In comprehensive recent reviews, other techniques around nanophotonics applied to biological media characterization are explained in the context of virus detection [2,14]. I strongly encourage our readers to consult these publications, which bring together many subjects plenty of contemporary and exciting physical ideas.

In the era of COVID-19 one thing is clear: the scientific advancements, physics and engineering included, are enabling us to address a complex challenge in ways that were unthinkable only twenty years ago. For the world's physics and engineering communities, standing where we currently are is actually a privilege and a reason to feel proud of being part of the knowledge generation.

REFERENCES

[1] T. Leïchlé, L. Nicu and T. Alava, ACS Sens. **5**, 3297 (2020).
[2] M. Soler, M.C. Estevez, M. Cardenosa-Rubio, A. Astua, and L.M. Lechuga, ACS Sens. **5**, 2663 (2020).
[3] Y. Bourquin, R. Wilson, Y. Zhang, J. Reboud and J. M. Cooper, Adv. Mater. **23**, 1458 (2011).
[4] R. Wilson, J. Reboud, Y. Bourquin, S. L. Neale, Y. Zhang, and J. M. Cooper, Lab Chip **11**, 323 (2011).
[5] Y. Bourquin, J. Reboud, R. Wilson, Y. Zhang, and J. M. Cooper, Lab Chip **11**, 2725 (2011).
[6] M. Rodriguez-Otazo, A. Augier-Calderin, J-P. Galaup, J-F. Lamère, and S. Fery-Forgues, Appl. Opt. **48**, 2720 (2009).
[7] M. Rodriguez-Otazo, A. Augier-Calderin, and J-P. Galaup, Opt. Commun. **282**, 2921 (2009).
[8] J.-P. Galaup, M. Rodríguez-Otazo, A. G. Augier-Calderín, J-F. Lamère, S. Fery-Forgues, Rev. Cubana Fis. **28**, 45 (2011).
[9] M. Aspelmeyer, T. J. Kippenberg, and F. Marquard, Rev. Mod. Phys. **86**, 1391 (2014).
[10] L. Ding, C. Baker, P. Senellart, A. Lemaitre, S. Ducci, G. Leo, and I. Favero, Phys. Rev. Lett. **105**, 263903 (2010).
[11] E. Gil-Santos, M. Labousse, C. Baker, A. Goetschy, W. Hease, C. Gomez, A. Lemaître, G. Leo, C. Ciuti, and I. Favero, Phys. Rev. Lett. **118**, 063605 (2017).
[12] E. Gil-Santos, J. J. Ruz, O. Malvar, I. Favero, A. Lemaître, P. M. Kosaka, S. García-López, M. Calleja, and J. Tamayo, Nat. Nanotech. **15**, 469 (2020).
[13] D. Xu and Y-F. Xiao, Nat. Nanotech. **15**, 420 (2020).
[14] X. Jiang, A. J. Qavi, S. H. Huang, and L. Yang, Matter **3**, 371 (2020).

THE PARAXIAL APPROXIMATION, REVISITED

LA APROXIMACIÓN PARAXIAL, REVISITADA

V. Ivchenko

Department of Natural Sciences Training, Kherson State Maritime Academy, Kherson 73000, Ukraine; reterty@gmail.com
† corresponding author

Recibido 23/7/2020; Aceptado 07/8/2020

We define the paraxial ray as the ray making infinitesimal angles with a central axis and normal to a reflecting or refracting surface. We show that for some physical situations these conditions can be relaxed, while for others non-compliance with one of them can lead to catastrophic deviations in the behavior of the output light beam. We first derive and analyze the generalized spherical mirror formula. Next, we consider the case of refracting ball and show that there can occur the situation, where the parallel input light beam is split into converging and diverging output beams in it. The issues outlined in this article will be useful for students, when learning the basics of geometrical optics.

Definimos el rayo paraxial como el rayo que forma ángulos infinitesimales con un eje central y normal a una superficie reflectante o refractante. Mostramos que para algunas situaciones físicas estas condiciones se pueden relajar, mientras que para otras el incumplimiento de una de ellas puede conducir a desviaciones catastróficas en el comportamiento del haz de luz de salida. Primero derivamos y analizamos la fórmula del espejo esférico generalizado. A continuación, consideramos el caso de la bola refractora y mostramos que puede ocurrir la situación en la que el haz de luz de entrada paralelo se divide en haces de salida convergentes y divergentes en él. Los temas descritos en este artículo serán útiles para los estudiantes que estudian los conceptos básicos de la óptica geométrica.

PACS: General physics (physics education) (física general, enseñanza de la física), 01.55.+b; geometrical optics (óptica geométrica), 42.15.-l; lenses in optical systems (lentes en sistemas ópticos), 42.79.Bh.

I. INTRODUCTION

The paraxial rays approximation is the basic concept of Gaussian (paraxial) optics by means of which the simple equations for spherical mirror and thin lens can be derived. The discussion of the paraxial approximation is presented in Refs. [1] and [2]. Serway and Jewett [3] talk about the paraxial rays as the rays making small angles with the principal axis. Halliday, Resnick and Walker [4] define the paraxial rays as the rays close to the central axis. In Ref. [5] the rays almost parallel with the central axis and close to it are called paraxial. Thus, the textbook definitions of these rays are rather unclear and imply that one or two conditions should be met. In our opinion, the most precise definition of this concept should be as follows: the paraxial ray is the ray making infinitesimal angles with a central axis and normal to a reflecting or refracting surface. In this paper we show that for some physical situations these conditions can be relaxed, while for others non-compliance with one of them can lead to catastrophic deviations in the behavior of the output light beam. The issues outlined in this article will be useful for students, who study the basics of geometrical optics.

II. THE GENERALIZED SPHERICAL MIRROR FORMULA

Let us consider a spherical mirror with radius of curvature R. In Fig. 1 we set the position of the incident light ray using two parameters: object distance s, measured from vertex V to the point of ray intersection with optic axis and angle φ between this axis and the ray (instead of s we could choose, as a parameter, angle θ between the incident ray and normal to a reflecting surface).

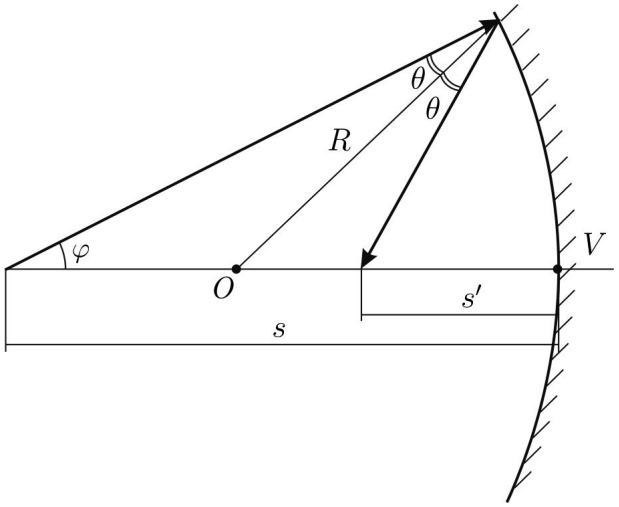

Figure 1. Reflection of an arbitrary ray from a concave mirror.

The image distance s' is measured from vertex V to the point of reflected ray intersection with the optic axis.

According to Cartesian sign convention [6]:

1. Light initially propagates from left to right.
2. Distances measured normal to the optic axis are positive above and negative below.
3. Distances measured in the direction opposite to the direction of incident light are taken as negative. Distances measured in the same direction as the incident light are considered positive.

4. Angles are positive when produced by clockwise rotation from the optic axis or the surface normal, and negative when produced by counter-clockwise rotation.

5. If the vertex lies to the left of the center of curvature, the radius of curvature is positive. If the vertex lies to the right of the center of curvature, the radius of curvature is negative.

Applying the sign convention for the case shown in Fig. 1, we have: $s < 0$, $s' < 0$, $R < 0$, $\varphi < 0$ $(-\pi/2 < \varphi < 0)$, $\theta > 0$. Then, using the law of sines, we get:

$$\frac{R}{\sin\varphi} = \frac{R-s}{\sin\theta}, \tag{1}$$

$$\frac{R}{\sin(2\theta-\varphi)} = \frac{R-s'}{\sin\theta}. \tag{2}$$

Solving this system with respect to s', we find:

$$s' = R\left[1 + \frac{x-1}{2(x-1)^2\sin^2\varphi - 1 - 2(x-1)\cos\varphi\sqrt{1-(x-1)^2\sin^2\varphi}}\right], \tag{3}$$

where $x = s/R$. Therefore, in reality, the value of distance s' depends not only on R and s, but also on angle φ, that is, the spherical mirror always present spherical aberration [1], [7]. Equation (3) is invariant under transformation $\varphi \to -\varphi$, which is consistent with the symmetry of the problem. Despite the fact that this equation is obtained for the case shown in Fig. 1, it is valid for the whole range of object distance values $(-\infty < x < \infty)$.

In the paraxial approximation angles φ and θ are small. Then $\sin\varphi \approx \varphi$, $\sin\theta \approx \theta$, $\sin(2\theta - \varphi) \approx 2\theta - \varphi$ and from equations (1), (2) we derive the well known approximate object-image relationship for spherical mirror:

$$\frac{1}{s} + \frac{1}{s'} \approx \frac{2}{R}. \tag{4}$$

Using equation (4) we obtain the value for the image distance s'_0 in the paraxial approximation:

$$s'_0 = \frac{x}{2x-1}R. \tag{5}$$

Equations (3), (5) allow one to highlight the domain on plane (x, φ), for which equation (5) gives approximately correct value for image distance. In Fig. 2 we present the results of numerical calculation of contour line, along which the relative error $\delta_{s'} = |(s' - s'_0)/s'|$ in the determination of image distance is equal to 5 %.

The domain corresponding to a large value of this quantity is shaded gray.

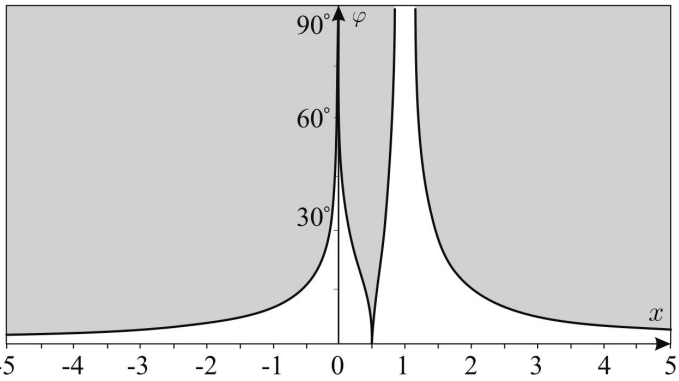

Figure 2. Domains of credibility (white) and incredibility (gray) of the paraxial approximation for a spherical mirror at $\delta_{s'} = 5\,\%$.

It is seen that for large relative object distance ($|x| \gg 1$) both paraxial conditions should be satisfied, that is both φ and θ should be small. For object lying near the mirror's center of curvature the angles of incidence θ are always very small, whereas φ can take arbitrary values. Due to this fact $s \approx s' \approx R$ and equations (4), (5) are well performed (the relative error $\delta_{s'}$ is small). For object lying near the principal focus of mirror ($x = 1/2$) both φ and θ should be again very small, since only within these conditions the reflected ray is almost parallel to the principal axis. At last, for object position close to vertex V ($s \to 0$), both φ and θ can take arbitrary equal values (we remind that in general case these values are related through Eq. (1)). This fact can be explained in the following way. Since $s \to 0$, then from equation (1) we have approximately: $\varphi \approx \theta$. At this rate using equation (2) we get: $s' \to 0$ so that $s \approx -s'$. This equality agrees well with approximate equation (5).

III. THE REFRACTING BALL

It is known that the violation of the second paraxial condition (the ray makes large angles with a normal to a reflecting or refracting surface) leads to the spherical aberration effect [1], [7]. Let us consider the parallel light beam, which is incident on the transparent ball of radius R and relative refractive index $n > 1$. We find distance d_{cr} from the central axis to the incident ray, which, after refraction, falls to the point of intersection of this axis with the ball (Fig. 3).

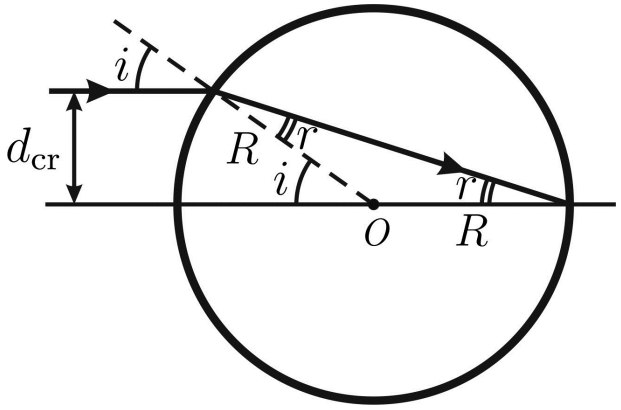

Figure 3. Geometry used to derive equation (9).

Considering Fig. 3 and applying the Snell's law, we get:

$$\sin r = (\sin i)/n. \tag{6}$$

Furthermore

$$r = \frac{i}{2}, \tag{7}$$

$$\sin i = d_{\text{cr}}/R. \tag{8}$$

Solving system of equations (6)-(8) with respect to d_{cr}, we obtain:

$$d_{\text{cr}} = \frac{n\sqrt{4-n^2}}{2}R. \tag{9}$$

In Fig. 4 we plot d_{cr} as the function of n using equation (9).

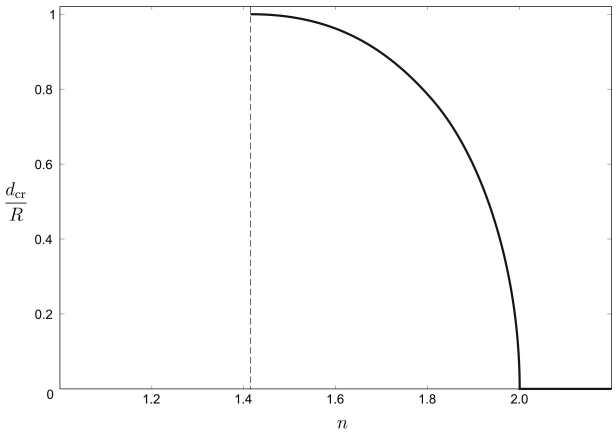

Figure 4. d_{cr} as the function of n according to equation (9).

For $1 < n < \sqrt{2}$ all incident rays converge at various focal points behind the ball (Fig. 5), that is, this ball is a classical converging lens. Another words, the value of $d_{\text{cr}} > R$, so it is impossible to find a ray that, after refraction, falls to the point of intersection of the axis with the refracting sphere.

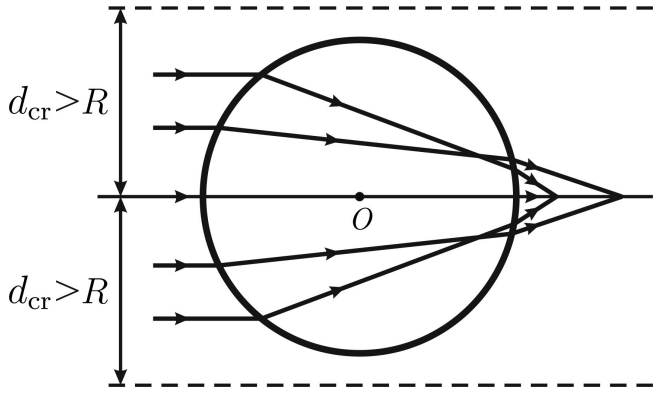

Figure 5. The ray tracing in a refracting ball for $1 < n < \sqrt{2}$.

If n increases, then the refractive power of the ball increases too and for $\sqrt{2} < n < 2$ incident rays lying inside a cylinder of radius $d_{\text{cr}} < R$ are also collected at various focal points behind the ball, whereas peripheral rays with $d_{\text{cr}} < d < R$ intersect at different points lying inside the ball (Fig. 6).

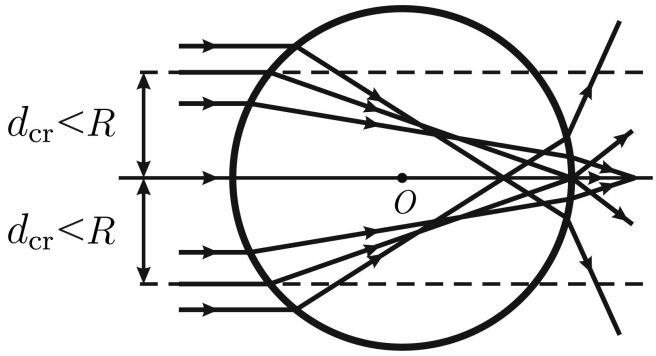

Figure 6. The ray tracing in a refracting ball for $\sqrt{2} < n < 2$.

Therefore, the parallel input light beam is split into converging and diverging output beams. The considered effect is a consequence of the simultaneous violation of the second paraxial condition and the finite thickness of the lens [8] (the refracting ball). Finally, for $n > 2$ this ball is a diverging lens even for the paraxial rays (Fig. 7).

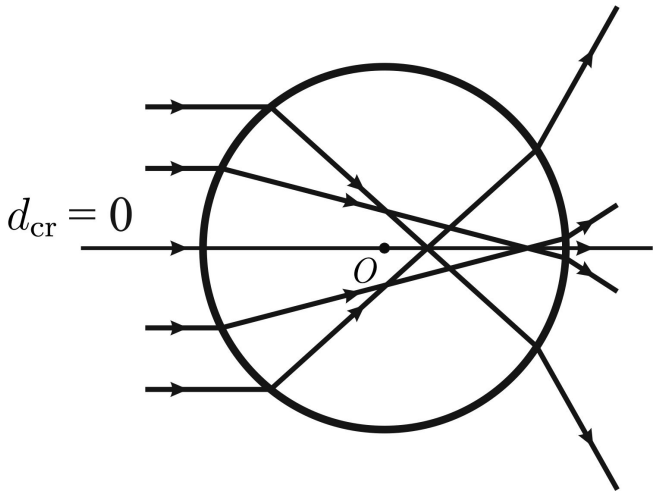

Figure 7. The ray tracing in a refracting ball for $n > 2$.

We should note that at present time there are several ways of creation of the paraxial singlet lenses free of spherical aberrations. For example [9], the selection of the shape of the input surface is carried out so, that the rays inside the lens do not cross each other as well.

IV. CONCLUSION

In this paper we present two useful in geometrical optics teaching examples that facilitate the students grasping such an important concept as paraxial ray. First, we show that for object lying near the mirror's center of curvature or its vertex the angles between optic axis and the incident light rays can take arbitrary values, that is, the usual paraxial condition can be relaxed in these cases. Next, we consider the refracting ball and show that there can occur the situations, where the paraxial model is unable to describe the behavior of the

refracted rays even qualitatively (the biconvex lens with $n > 1$ is a diverging lens for all or some rays).

V. REFERENCES

[1] C. Medina, S. Velazco, Rev. Bras. Ensino. Fis. **40**, e2314 (2018).

[2] R. J. Beck, Am. J. Phys. **12**, 231 (1944).

[3] R. A. Serway and J. W. Jewett, Physics for Scientists and Engineers with Modern Physics, 9th Ed. (Boston: Cengage learning, 2013), ch 36.2.

[4] D. Halliday, R. Resnick and J. Walker, Fundamentals of Physics, 9th Ed. (New York: Wiley, 2011), ch 34.9.

[5] P. Mouroulis and J. Macdonald, Geometrical Optics and Optical Design (New York/Oxford: Oxford University Press, 1997), ch 3.2.

[6] P. Mouroulis and J. Macdonald, Geometrical Optics and Optical Design (New York/Oxford: Oxford University Press, 1997), ch 3.1.

[7] P. Carpena and A. V. Coronado, Eur. J. Phys. **27**, 231 (2006).

[8] V. V. Ivchenko, Eur. J. Phys. Educ. **2**, 33 (2011).

[9] R. G. González-Acuña and H. A. Chaparro-Romo, Appl. Opt. **57**, 9341 (2018).

EVALUACIÓN DE CALIDAD DE IMAGEN EN TOMOGRAFÍA COMPUTARIZADA CON CONTRASTE DE FASE USANDO HACES DE SINCROTRÓN Y RECONSTRUIDA POR MÉTODOS ITERATIVOS

IMAGE QUALITY EVALUATION IN PHASE CONTRAST COMPUTED TOMOGRAPHY FROM SYNCHROTRON–BEAMS RECONSTRUCTED BY ITERATIVE METHODS

J. Marquez-Díaz[a†], R. Orozco-Morales[b], J.V. Lorenzo-Ginori[c], M. Pérez-Díaz [b]

a) Departamento de Física, Universidad Central "Marta Abreu" de las Villas (UCLV); jomarquez@uclv.cu[†]
b) Departamento de Automática y Sistemas Computacionales, Universidad Central "Marta Abreu" de las Villas (UCLV)
c) Centro de Investigaciones de la Informática, Universidad Central "Marta Abreu" de las Villas (UCLV)
† autor para la correspondencia

Recibido 23/3/2020; Aceptado 03/9/2020

En este trabajo se hizo un estudio sobre la base de un conjunto de datos de imágenes de tomografía con contraste de fase (PC-CT) adquiridas con un maniquí físico, utilizando rayos X producidos en un sincrotrón. Se implementaron cuatro protocolos de adquisición de los sinogramas. Estos sinogramas fueron reconstruidos implementando sobre Matlab, cinco algoritmos de reconstrucción; el tradicional FBP y cuatro iterativos. La calidad de imagen obtenida fue comparada utilizando diversos parámetros físicos. Se obtuvo que los métodos SIRT y SART fueron mejores para obtener bajos niveles de ruido, mientras que CGLS y SART produjeron mejores valores de contraste imagen. La resolución espacial no fue sensiblemente afectada por los algoritmos de reconstrucción iterativos respecto a la lograda con FBP. La disminución del número de proyecciones o de la energía del haz condujo a la disminución del contraste imagen y de la relación contraste–ruido.

In this work a study was made based on a set of phase contrast computed tomography imaging data (PC-CT) acquired with a physical phantom, using X-rays produced in a synchrotron. Four protocols were implemented for the acquisition of sinograms. These were reconstructed by implementing five reconstruction algorithms on Matlab; the traditional FBP and four iterative ones. The image quality was compared using various physical parameters. It was observed that the lowest noise levels were obtained by the SIRT and SART methods, while the best image contrast was obtained with CGLS and SART. Spatial resolution was not significantly affected by the iterative reconstruction algorithms with respect to that achieved with FBP. The decrease in the number of projections or beam energy led to the decrease of image contrast and noise contrast ratio.

PACS: Medical Imaging (Imaginería médica) 87.59.-e; X-ray imaging (Imagniería por rayos X) 87.59.-g; Computed tomography in medical imaging (Tomografía computarizada en la imagniería médica) 87.57.Q-.

I. INTRODUCCIÓN

La mama es uno de los principales sitios de cáncer en términos de tasas de mortalidad entre las mujeres a nivel mundial. La mamografía es la prueba de detección primaria utilizada para reducir la mortalidad. Sin embargo, a pesar de que este examen es importante en la detección temprana del cáncer de seno, presenta varias limitaciones como son: su sensibilidad se encuentra entre el 75 % y el 85 % [1], mientras que su especificidad está entre un 80 % y un 95 % [2]. Estos valores se afectan aún más para las mamas densas (características en mujeres jóvenes), ya que los tejidos malignos tienen un coeficiente de atenuación lineal muy similar al de los tejidos glandulares sanos, lo cual produce bajo nivel de contraste imagen, afectando la detección temprana de las lesiones o el correcto diagnóstico. Además, la mamografía requiere de una alta resolución espacial para detectar microcalcificaciones, pero la resolución espacial está limitada por restricciones de dosis.

Como resultado, se han desarrollado otras técnicas imagenológicas para solucionar el problema anterior, entre las cuales la más reciente es la tomografía con contraste de fase usando haces de sincrotrón [3]. La calidad de una imagen radiográfica se puede mejorar significativamente, si aprovechamos las propiedades de la radiación x de un sincrotrón y su dualidad onda-patícula. Con esta técnica es posible seleccionar con un monocromador la energía más adecuada, optimizando la dosis administrada a la paciente. Además, la alta colimación natural permite rechazar la dispersión de los fotones. Finalmente, la alta coherencia espacial, producida por el pequeño tamaño de la fuente, combinado con una gran distancia entre la fuente y la muestra, permite tener sensibilidad al cambio de fase que experimentan las ondas electromagnéticas durante su interferencia, mejorando el contraste entre los tejidos blandos.

Hay un segundo aspecto que ha contribuido a mejorar la calidad de imagen tomográfica, que es el método de reconstrucción de las imágenes. La retroproyección filtrada (FBP) es el algoritmo de reconstrucción más utilizado por su precisión y rapidez. Sin embargo, las imágenes 2D y 3D que proporciona son ruidosas, no tienen la resolución espacial deseada y presentan artefactos. Por tal motivo, se

han desarrollado algoritmos que resuelven estos problemas, denominados iterativos.

Los métodos de reconstrucción iterativa (IR) se introdujeron en la década de 1970 durante los primeros estudios en CT de transmisión, pero se abandonaron temprano debido a la alta capacidad computacional requerida por la resolución de imagen [4]. Sin embargo, la creciente capacidad computacional en CPU y GPU ha permitido desde el año 2008, la introducción de estos métodos en la rutina clínica. Presentan como ventaja sobre la FBP, que no requieren teóricamente que los datos de adquisición sean continuos, y por lo tanto, tienen mejores resultados con pocas proyecciones, permitiendo la reducción de la dosis.

En este trabajo se compara la calidad de imagen tomográfica con contraste de fase, usando haces x de sincrotrón, que se obtiene tras reconstruir las imágenes por los siguientes métodos: SART (Técnica de reconstrucción algebraica simultanea), SIRT (Técnica de reconstrucción iterativa simultánea), CGLS (gradiente conjugado de mínimos cuadrados), ART (Técnica algebraica de reconstrucción)y FBP (retroproyección filtrada).

II. MATERIALES Y MÉTODOS

En este trabajo se hizo un estudio sobre la base de una data de imágenes de PC-CT adquirida con un maniquí físico, utilizando rayos x producidos en un sincrotrón. Se implementaron cuatro protocolos de adquisición de los sinogramas (funciones a partir de las cuales se obtienen las imágenes 3D) variando la cantidad de proyecciones a adquirir en 800 y 1000 y la energía del haz en 32, 35 y 38 KeV. Dichos sinogramas fueron reconstruidos implementando en Matlab varios algoritmos, el tradicional FBP y 4 iterativos: ART, SIRT, SART y CGLS. La calidad de imagen obtenida fue comparada utilizando los parámetros físicos: Relación señal-ruido, relación contraste-ruido, el contraste imagen, error cuadrático medio y la función de transferencia de la modulación como indicador de la resolución espacial.

II.1. La tomografía con y sin contraste de fase

La tomografía de rayos x (CT) y la tomografía de rayos x con contraste de fase (CP-CT) son dos métodos por el cual se obtienen imágenes 3D del objeto, al obtener proyecciones del mismo (sinogramas) cuando tanto el emisor de rayos x como el detector se rotan en 360 grados alrededor de este y luego mediante un procesamiento matemático esas proyecciones se reconstruyen en la imagen 3D. En la CT la distancia objeto-detector es aproximadamente cero, por lo que el contraste es debido solamente a la atenuación de los rayos x en el tejido (Ver Figura 1 *a*)).

En CP-CT en cambio, se cumple la relación de distancia objeto-detector$0 < Z_1 < a^2/\lambda$, donde a es el tamaño del detalle esperado o resolución espacia y λ la longitud de onda de los rayos x. El detector capta en este caso tanto la atenuación de los rayos en el objeto como la interferencia de las ondas salientes (Ver figura 1 *b*)).

El cambio de fase en b) ocurre por la variación de la velocidad de la onda al pasar de un de medio a otro. El índice de refracción, se expresa por la ecuación 1.

$$n = 1 - \delta + i\beta. \tag{1}$$

Donde δ es es el cambio de fase y β la absorción de los fotones.

Este trabajo se circunscribe al caso b).

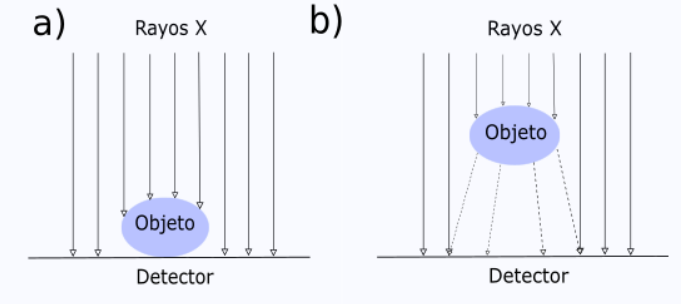

Figura 1. Adquisición de una proyección en a) CT, b) PC-CT.

II.2. Descripción del maniquí utilizado y obtención de los datos

El maniquí utilizado es un maniquí físico que se emplea para calibrar un tomógrafo que utiliza PC-CT usando haces de sincrotrón (ver Fig. (2)).

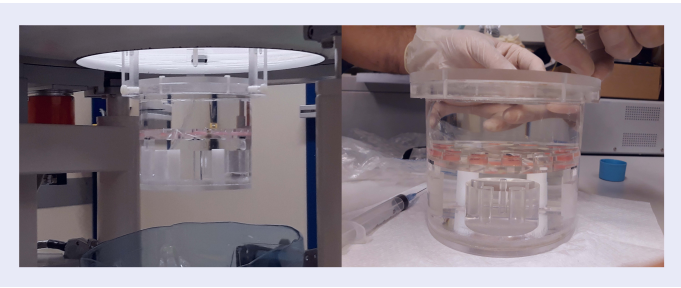

Figura 2. Maniquí físico usado.

La estructura exterior del phantom es un cilindro de metacrilato (PMMA) de 10*cm* de altura y 12*cm* de diámetro llenado en su interior con agua desmineralizada. Un centímetro de disco grueso de PMMA es suspendido en la región central del maniquí. Diez platos de ceras están incrustados en la media altura, cinco contienen agregados de cuarzo de diferentes diámetros (150, 170, 200, 250 y 300μm) y los otros cinco, alambres de nailon de diferentes espesor (380, 450, 500, 600 y 700μm). Cuatro conductos se insertan a través del cilindro, cada uno con una inclinación de 23^o respecto a la dirección horizontal. Estos insertos se utilizan para medir la respuesta del sistema a los pequeños detalles de alto nivel de contraste como podrían ser las masas y microcalcificaciones en las mamas y los conductos galactóforos.

II.3. Mamógrafo digital usado.

El detector usado en este experimento fue el *FUJIFILM Medical Systems* y de uso general en radiografía.

- Detector: Selenio (dimensiones: 24x18cm)
- Distancia detector-muestra:2m
- Filtración adicional: no necesaria
- Matriz resultante: 2350 × 2350 píxel
- Dimensión del píxel: 50μm
- Rango dinámico: 16 *bits*
- Radiación monocromática (0.2 % de ancho de banda)
- Energía variable entre (32, 35 y 38) keV
- Flujo de fotones de 10^8 $fotones/(mm^2 sec)$

II.4. Obtención de los datos a procesar.

En este trabajo se utilizó un conjunto de 65 sinogramas del maniquí descrito. Fueron adquiridos en el sincrotrón Elettra de la ciudad de Trieste, Italia, para parámetros de adquisición que varían respecto a la energía del haz de rayos x (32 keV, 35 keV y 38 keV) y el número de proyecciones con las que fueron obtenidos (800 proyecciones y 1000 proyecciones, ver Tabla 1).

Tabla 1. Diferentes protocolos de adquisición usados.

	Energia (keV)	Número de proyecciones
1	32	800
2	32	1000
3	35	1000
4	38	1000

II.5. Métodos de reconstrucción utilizados.

Para este trabajo se utilizó para el procesamiento de los sinogramas (reconstrucción de las imágenes) un método analítico,el de retro-proyección filtrada (FBP) y cuatro iterativos: ART, SIRT, SART, CGLS para posteriormente comparar la calidad de imagen de todos ellos. Se obtuvieron por cada protocolo de adquisición una tomografía (3D) consistente en 65 cortes reconstruidos por cada uno de los 5 algoritmos de reconstrucción. En total se comparó la calidad de imagen de 20 PC-CT del maniquí físico utilizado. En la Figura 3 se muestra un mismo corte de las 20 PC-CT para los 4 protocolos de adquisición, procesados con los 5 algoritmos de reconstrucción.

II.6. Herramienta computacional usada.

La herramienta usada con este propósito es ASTRA, una herramienta que agrupa varias técnicas de reconstrucción de imágenes. Esta herramienta se encuentra implementada en MATLAB.

II.7. Determinación de la calidad de imagen obtenida

Las medidas de calidad de imagen utilizadas en este trabajo miden los parámetros físicos de calidad de imagen siguientes: ruido, resolución, contraste imagen y distorsión. Seguidamente describiremos dichas métricas.

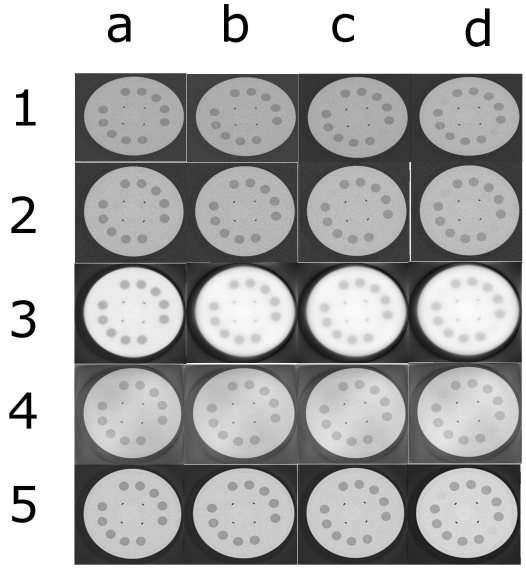

Figura 3. Recostrucciones obtenidas (1- FBP, 2- ART, 3- SIRT, 4- SART, 5- CGLS) para el corte número 46 de cada protocolo de adquisición (a- 32keV y 800 proyecciones, b- 32keV y 1000 proyecciones, c- 35keV y 1000 proyecciones, d- 38keV y 1000 proyecciones).

Relación señal-ruido: Como indicador del nivel de ruido sobre la imagen utilizamos la relación señal a ruido univariada (SNR_u). La misma utiliza la definición, a partir de la estadística de Poisson que caracteriza a estas imágenes, donde la desviación típica de la señal es igual a la raiz cuadrada de la media de la señal, que en este caso es el valor de intensidad de píxel en una región de interés seleccionada de 24 x 26 píxeles.

$$SNR_u = \sqrt{N}, \tag{2}$$

donde N es el número de fotones útiles en la imagen (región de interés ROI).

Relación contraste-ruido: La relación contraste a ruido es una medida que expresa la habilidad de un sistema de imagen para detectar detalles, o lo que es lo mismo [5]:

$$CNR = \frac{x_i - x_f}{\sigma_f}, \tag{3}$$

donde x_i y x_f son la media de los valores de intensidad de la región de interés objeto y la de fondo; σ_f es la desviación típica de la región de fondo.

Contraste imagen: Por definición es la diferencia de intensidad de píxel entre dos regiones (tejidos o estructuras) sobre la imagen y expresan la diferencia entre el grado de atenuación entre los distintos tejidos o estructuras del cuerpo.

$$c = \frac{D_1 - D_2}{D_1}, \tag{4}$$

donde D_1 y D_2 son la intensidad media de dos ROIs diferentes donde la primera, es decir, D_1 es medida en la región central del corte y la otra en las regiones donde se pueden observar las diversas estructuras.

MTF: La MTF (*Modulation Tranfer Function*) es una herramienta matemática que brinda información sobre la resolución espacial y el contraste imagen de un sistema de adquisición de imágenes. Matemáticamente, se corresponde con la magnitud de la transformada de Fourier de la función de dispersión de línea (LSF: del inglés *Line Spread Function*) de un sistema. Está dada por la ecuación (5), donde la LSF representa la distribución de intensidades a ambos lados de las líneas representativas de una resolución espacial específica. La LSF se obtiene a partir de la función de dispersión de borde o (ESF: del inglés *Edge Spread Function*) (ver ecuación 6) y en la distribución de intensidades de la imagen la línea referencial se verá como un escalón unitario.

$$MTF(u) = |F[LSF(x)]| = |\int_{\infty}^{-\infty}[LSF(x)e^{-2\pi jxu}udx]|, \tag{5}$$

$$LSF(x) = \frac{d[ESF(x)]}{dx}. \tag{6}$$

MSE: Como medida de la distorsión que a nivel de píxel introducen los algoritmos de reconstrucción iterativa, se utilizó el error medio cuadrático (MSE). El mismo se implementa a partir de ROI tomadas sobre la imagen FBP utilizada como referencia y sobre la reconstrucción por un método iterativo [5]:

$$MSE = \frac{1}{MN}\sum_{x=0}^{M-1}\sum_{y=0}^{N-1}[r(x,y) - t(x,y)]^2, \tag{7}$$

donde $r(x, y)$ es la imagen reconstruida por el método FBP y $t(x, y)$ es la imagen reconstruida por cualquiera de los métodos iterativos.

II.8. Determinación de las ROI

Teniendo en cuenta que el tiempo de reconstrucción por corte fue de alrededor de veintisiete minutos, con un procesador Mobile DualCore Intel Core i5-4200U, a 1600 MHz y 8 Gb de RAM, se reconstruyeron solo completamente los algoritmos FBP y SIRT, mientras que para ART, SART y CGLS se escogieron los siete cortes más interesantes (cortes 0000, 0013, 0022, 0038, 0046, 0060, 0065). Estos cortes son los que recogen los detalles estructurales del maniquí con mayor intensidad. Luego, la comparación de la calidad de imagen entre los cuatro protocolos de adquisición y los cinco algoritmos de reconstrucción se hizo para los mismos siete cortes de todo el estudio. Para estos cortes se definieron 8 regiones de interés de 18×19 píxeles. El tamaño de la región de interés garantiza que solo incluya las estructuras de interés como son las simulaciones de masas, microcalcidicaciones y fibras.

De las estructuras presentes en las imágenes reconstruidas se seleccionaron 8 ROIs [ver figura 4] donde se calcularon las métricas de calidad de imagen para los cuatro protocolos de adquisición y las cinco métodos de reconstrucción.

Para calcular *CNR* se tomaron dos de las tres regiones que simulan masas, la ROI # 2 y la ROI # 3. Para la desviación típica en región de fondo se usó una ROI tomada en la región central (ROI # 6) así como para determinar el valor de x_f.

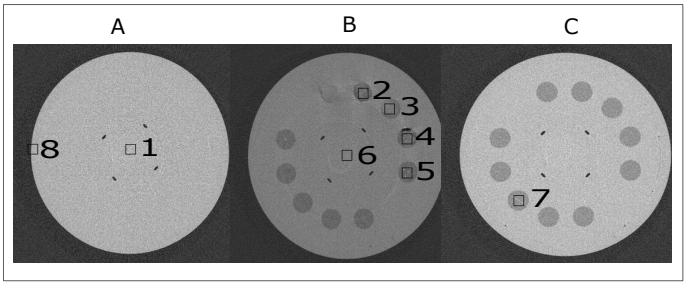

Figura 4. Forma en que se enumeraron las ROIs seleccionadas. Cortes 0000, 0013, 0038 (A, B y C respectivamente) de la imagen obtenida con 800 proyecciones y 32keV.

En el caso del contraste imagen se mide igual que la anterior, pero en la ROI # 6 en lugar de calcular su σ se toma la media de la señal y para x_i se sustituye por el valor en la ROI # 2 en un caso y por el valor de la ROI # 3 en el otro.

Para la determinación de la MTF se seleccionó la región de interés en el borde, entre el fondo negro y la imagen (ROI # 8).

Para MSE se usó una de las ROIs donde se puede apreciar fibras (ROI # 7) y una donde se puede apreciar microcalcificaciones (ROI # 5).

III. ANÁLISIS DE LOS RESULTADOS

III.1. Análisis de la SNR-univariada

En la tabla II se muestran los diferentes valores de SNR_u para cada algoritmo de reconstrucción y para cada protocolo de adquisición. Este valor, como anteriormente se menciona, fue medido en la ROI # 1 que se encuentra en el corte 0000.

Tabla 2. Valor de relación señal-ruido-univariada(%).(32keV y 800 proyecciones, 32keV y 1000 proyecciones, 35keV y 1000 proyecciones, 38keV y 1000 proyecciones)

	Protocolo de adquisición			
Algoritmo	32/800	32/1000	35/1000	38/1000
FBP	12,69	12,89	13,26	13,19
ART	13,30	13,56	13,72	13,59
SIRT	15,35	15,70	15,75	15,78
SART	14,25	14,28	14,52	14,55
CGLS	13,94	14,10	14,25	14,38

En dicha tabla, se puede apreciar que la relación señal a ruido mejora de FBP a SIRT, siendo SIRT el mejor algoritmo de reconstrucción en todos los casos. También se aprecia que al aumentar el número de proyecciones los valores de SNR mejoran, igual ocurre en la mayoría de los casos si aumentamos la energía de adquisición de los sinogramas, aunque las diferencias entre las energías de 35 y 38 keV son no significativas ($p = 0.597$), considerando una distribución aproximadamente normal, para un 95 % de confianza.

En la Fig. (5) se muestra la ROI # 1 para cada uno de los cortes y los protocolos de adquisición. La reconstrucción SIRT proporciona valores de intensidad de píxel visiblemente mayores que las otras reconstrucciones, de ahí la mayor SNRu.

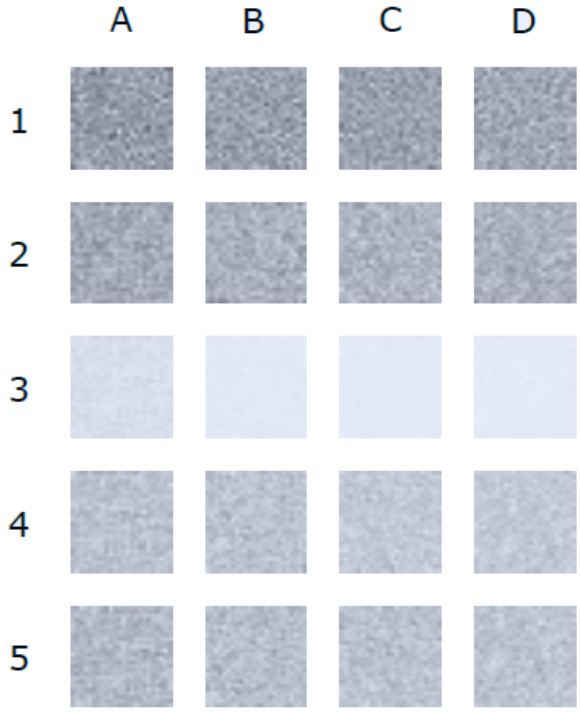

Figura 5. ROI # 1 (1- FBP, 2- ART, 3- SIRT, 4- SART, 5- CGLS) para el corte número 00 de cada protocolo de adquisición (a- 32keV y 800 proyecciones, b- 32keV y 1000 proyecciones, c- 35keV y 1000 proyecciones, d- 38keV y 1000 proyecciones).

III.2. Relación contraste-ruido

En la Tabla (3) se aprecian los valores de CNR para cada protocolo de adquisición y para los cinco métodos de reconstrucción. Dichos valores se obtuvieron para las ROIs #2 y # 3, que son regiones donde se pueden observar las simulaciones de masas tumorales del maniquí físico.

Tabla 3. Valor de la relación contraste-ruido para cada protocolo de adquisición reconstrucción. (32keV y 800 proyecciones, 32keV y 1000 proyecciones, 35keV y 1000 proyecciones, 38keV y 1000 proyecciones)

		Protocolo de adquisición			
Algoritmo	ROI	32/800	32/1000	35/1000	38/1000
FBP	2	1,59	1,54	1,56	2,48
	3	0,91	0,87	0,72	2,21
ART	2	2,31	2,41	2,40	3,23
	3	1,29	1,40	1,12	2,83
SIRT	2	13,65	23,93	21,82	33,23
	3	8,09	14,33	12,22	31,13
SART	2	3,11	3,56	3,53	5,40
	3	1,09	1,12	0,67	3,63
CGLS	2	3,75	3,95	3,64	5,83
	3	2,18	2,26	1,60	5,23

En la tabla anterior se puede apreciar que los valores más bajos de CNR se encuentran para el protocolo FBP y los mas altos para el SIRT, aumentando con el aumento de la energía y con el aumento de las proyecciones, aunque en 35 keV se aprecia una pequeña fluctuación experimental que hasta el momento no ha sido explicada. El mejor valor de CNR se encuentra para el algoritmo SIRT con 38keV y 1000 proyecciones.

III.3. Contraste imagen

La Tabla (4) muestra el valor de contraste imagen, en porciento, presente en las imágenes reconstruidas por los diferentes algoritmos utilizados. Al igual que el epígrafe anterior, dichas medidas se realizaron en las ROIs donde se pueden observar las simulaciones de las masas tumorales, es decir, ROI #2 y ROI #3.

Todos los valores de contraste se pueden considerar buenos, por encima del 4 % [6], que es el valor que distingue el ojo humano. Los valores de mayor contraste se obtienen con CGLS, seguido por ART, SIRT, FBP y SART. Se debe resaltar que el método SIRT, en este caso no tiene el mejor contraste ya que se saturan los valores con alta intensidad de píxel.

Tabla 4. Valor de contraste imagen para cada protocolo de adquisición reconstrucción. (32keV y 800 proyecciones, 32keV y 1000 proyecciones, 35keV y 1000 proyecciones, 38keV y 1000 proyecciones)

Algoritmo	ROI	Protocolo de adquisición			
		32/800	32/1000	35/1000	38/1000
FBP	2	13,49	14,98	12,94	20,87
	3	7,74	8,71	5,98	18,60
ART	2	15,74	15,91	14,50	21,75
	3	8,78	9,51	6,78	19,02
SIRT	2	20,15	16,29	13,68	18,88
	3	11,95	9,91	7,66	17,69
SART	2	13,71	15,73	14,60	18,39
	3	4,79	5,18	2,79	12,34
CGLS	2	16,68	16,92	15,91	25,21
	3	9,68	9,99	7,01	22,61

La Fig. (6) muestra las dos ROIs consideradas en el análisis para el corte 0013, en los cinco algoritmos de reconstrucción con los cuatro protocolos de adquisición.

III.4. Valores de MTF

La Fig. (7) muestra el comportamiento de la MTF para cada uno de los cuatro protocolos de adquisición y de los cinco métodos de reconstrucción como medida robusta para evaluar la relación entre el contraste imagen y la resolución espacial. Para la determinación de dicha MTF de utilizó la ROI # 8 para todos los casos.

Comparando todos los protocolos de adquisición y los 5 algoritmos de reconstrucción, se aprecia que las diferencias introducidas en el área bajo la curva son extremadamente pequeñas. Esto significa que ninguno de los procedimientos iterativos afectó sensiblemente la resolución espacial con respecto al estándar FBP. Podría decirse, a partir de los resultados previos, que el método que más ruido elimina fue SIRT para el protocolo a 38 keV y 1000 proyecciones.

Consecuentemente, este es el protocolo que menor resolución espacial presenta, pero las diferencias introducidas respecto al resto no son sensibles visualmente. Esto puede ser apreciado en la Fig. (8), para las ROIs que muestran detalles que simulan microcalcificaciones y fibras, que son los primeros que deben afectarse ante pérdidas sensibles de resolución espacial.

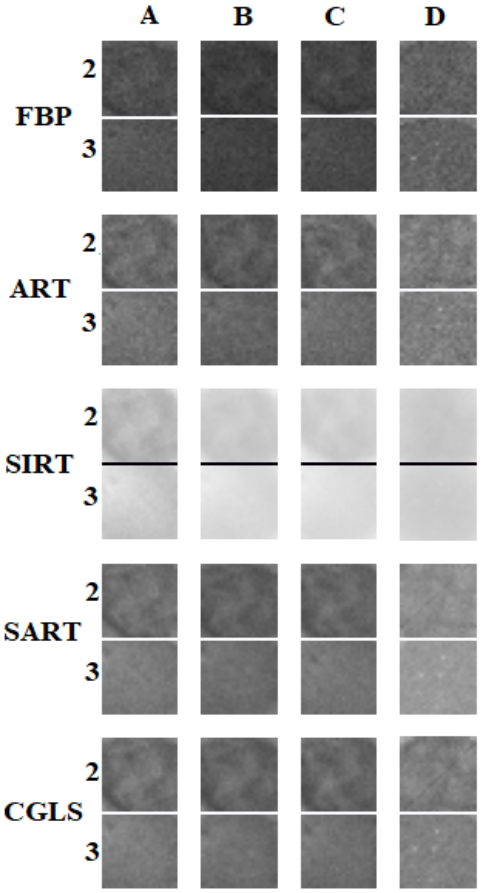

Figura 6. ROI # 2 y # 3, donde se pueden apreciar simulaciones de masas tumorales, para cada protocolo de adquisición (A- 32keV y 800 proyecciones, B- 32keV y 1000 proyecciones, C- 35keV y 1000 proyecciones, D- 38keV y 1000 proyecciones).

Se puede observar que todos los algoritmos permiten apreciar la totalidad de las fibras y microcalcificaciones, sin degradar sensiblemente la resolución espacial respecto al estándar FBP.

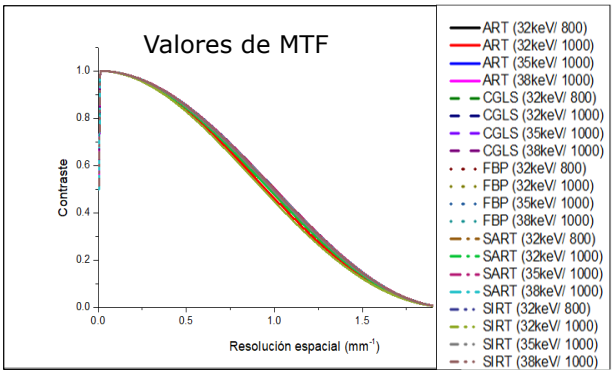

Figura 7. Valores de las MTF para los cuatro protocolos de adquisición y los cinco métodos de reconstrucción.

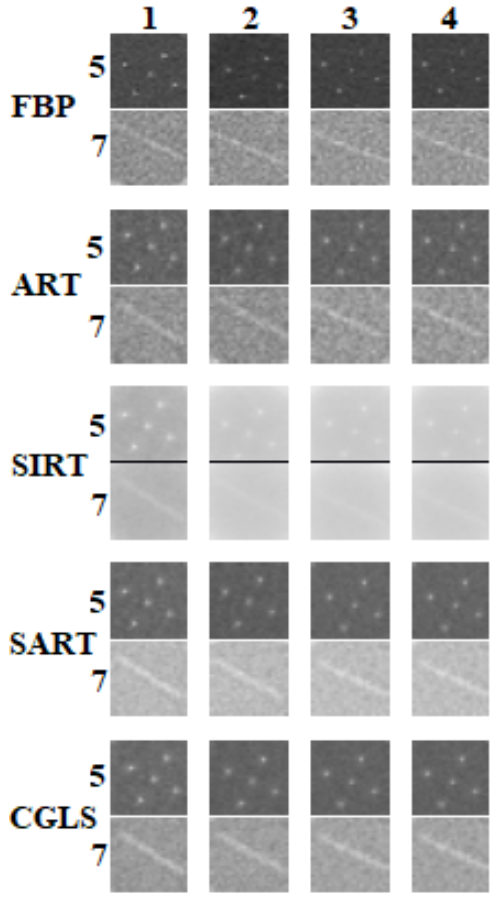

Figura 8. ROI #5 y #7, donde se puede apreciar simulaciones de microcalcificaciones y fibras, para cada protocolo de adquisición (A- 32keV y 800 proyecciones, B- 32keV y 1000 proyecciones, C- 35keV y 1000 proyecciones, D- 38keV y 1000 proyecciones).

Tabla 5. Valor de error cuadrático medio (32keV y 800 proyecciones, 32keV y 1000 proyecciones, 35keV y 1000 proyecciones, 38keV y 1000 proyecciones)

		Protocolo de adquisición			
Algoritmo	ROI	32/800	32/1000	35/1000	38/1000
ART	4	600,97	820,34	997,94	799,76
	7	139,28	155,30	161,00	574,91
SIRT	4	9167,14	17867,66	17144,71	11095,42
	7	1481,83	3394,36	2871,29	14809,29
SART	4	1218,64	1392,64	1340,46	2770,32
	7	1349,05	1665,40	1455,34	3428,08
CGLS	4	821,57	1431,86	1004.90	932.86
	7	148,52	210,42	192.,52	872,39

III.5. Error cuadrático medio

La Tabla (5) muestra los valores de MSE de los métodos de reconstrucción iterativos si se toma como referencia el método FBP. Dichos valores se midieron en las ROIs #4 y #7 que simulan microcalcificaciones y fibras respectivamente, como estimación de las diferencias (distorsiones) introducidas a nivel píxel por cada algoritmo de reconstrucción iterativa.

El valor mayor representa al método que más difiere con respecto a la FBP. Según la tabla anterior este se corresponde con el algoritmo SIRT. Se aprecia además, que debido a la

saturación de intensidad a nivel de píxel con este algoritmo, los resultados para la más alta energía (38keV) son menores que para 35keV.

III.6. Comparación de resultados con autores previos en el tema

Como esta tecnología es tan nueva, hay muy pocos trabajos publicados en el tema que nos compete. No obstante, en [7] se presenta un trabajo que tiene como objetivo la comparación entre los rendimientos de los algoritmos de reconstrucción estándar e iterativos en diferentes condiciones experimentales, evaluando cuantitativamente la calidad de la imagen en términos de relación de contraste a ruido y nitidez de bordes. Para este propósito, las PC-CT de un tejido de mastectomía se adquirieron a una dosis glandular fija de 5 mGy, con diferentes energías de rayos x (32, 35 y 38 keV) y series de proyecciones (600, 900 y 1200 proyecciones en 180 grados). Los algoritmos de reconstrucción usados fueron: FBP, SIRT SART, ART, además, también se varió la relación δ/β obteniendo las siguientes conclusiones:

- Al aumentar δ/β la relación contraste-ruido disminuía a energía fija. El mejor resultado lo obtuvo SIRT y el peor FBP.
- Al aumentar el número de proyecciones la relación contraste-ruido aumentaba a energía y δ/β fija. El mejor resultado lo obtuvo SIRT 1200 proyecciones y 38 keV.
- La resolución espacial la midieron a través de PSF (*Point Spread Function*) en un borde entre dos tejidos. El mejor resultado se obtuvo con 1200 proyecciones y 38 keV con $\delta/\beta = 1083$. Fue mejor en FBP y peor en SIRT.
- Los resultados apuntan a que es posible bajar el número de proyecciones a 900 pero nunca hasta 600 ya que se deteriora mucho la resolución espacial.
- Los algoritmos de reconstrucción iterativa utilizados en ese trabajo, muestran resultados muy prometedores, en comparación con el estándar *Filtered Back Projection*, con un número limitado de proyecciones, lo que permite obtener imágenes con alto contraste y poca pérdida de resolución.

Aunque esos resultados fueron obtenidos con condiciones experimentales algo diferentes, los resultados del presente trabajo concuerdan plenamente con las conclusiones a que llagaron los anteriores autores.

III.7. Análisis de optimización de los resultados

El tiempo de cómputo de reconstrucción por corte en SIRT fue de 27 minutos y en SART 25 minutos para el procesador utilizado. En el resto es semejante a SART con excepción de FBP que es de 6 minutos. En general el algoritmo de reconstrucción que obtiene buenos indicadores en todos los parámetros de calidad de imagen fue SART a 38keV con 1000 proyecciones.

IV. CONCLUSIONES

A partir de los resultados obtenidos en esta investigación podemos concluir que:

- La relación contraste-ruido fue mejor en el método SIRT y aumentó con el número de proyecciones y con la energía del haz. Sin embargo, el contraste imagen se satura en el método SIRT para la más alta energía (38 keV).
- Los algoritmos SIRT y SART a 38 keV y 1000 proyecciones fueron los mejores para reducir ruido en las imágenes, mientras que CGLS y SART fueron mejores para obtener buen contraste imagen a (38 keV-1000 proyecciones).
- La mejor resolución espacial se obtiene en FBP (38 keV-1000 proyecciones) pero sin diferencias significativas respecto a los algoritmos iterativos.
- El método que más difiere a nivel de píxel del estándar FBP es SIRT, según el valor del error cuadrático medio.
- Teniendo en cuenta todo lo anterior, en la PC-CT la combinación óptima para calidad de imagen en protocolo de adquisición/reconstrucción se obtuvo con SART a 38 keV-1000 proyecciones para una dosis de 5 mGy y una relación δ/β de 2321.
- Todos los algoritmos iterativos estudiados proveen mejor calidad de imagen que FBP para la PC-CT pero son muy costosos computacionalmente, por lo que su implementación en condiciones de rutina clínica requiere de avances tecnológicos en las prestaciones de los procesadores.

REFERENCIAS

[1] J. M. Boone, K. K. Lindfors, and S. J.A., Med. Decis. Making **22**, 228 (2002).

[2] H. Vainio and F. Bianchini, IARC Handbooks of Cancer Prevention, (IARC Press, 2002).

[3] F. Arfelli, V. Bonvicini, A. Bravin, *et. al.*, Radiology **215**, 286 (2000).

[4] M Beister, D. Kolditz, and W. A. Kalender, Physica Medica **28**, 94 (2012).

[5] L. Fardin, https://doi.org/10.1016/j.ejmp.2016.07.729 (2015).

[6] M. Pérez, *et. al.*, Rev. Cubana. Fis. **28**, 1E7 (2011).

[7] L. Lhotska, *et. al.*, IUPESM World Congress on Medical Physics and Bio-Medical Engineering. Prague 2018. IFMBE Proceedings, 68/1. (Springer, Singapore, 2018).

THE IMPACT OF TORSIONAL ANGLES TO TUNE THE NONLINEAR OPTICAL RESPONSE OF CHALCONE MOLECULE: QUANTUM COMPUTATIONAL STUDY

IMPACTO DE LOS ÁNGULOS TORSIONALES EN LA RESPUESTA ÓPTICA NOLINEAL DE LA MOLÉCULA DE CALCONA: ESTUDIO CUÁNTICO COMPUTACIONAL

S. Resan[a], R. Hameed[a], A. Al-Hilo[a], M. Al-anber[a†]

Molecular Engineering and Computational Modeling Lab, Department of Physics, University of Basrah, Basrah, Iraq; mohanned.mohammed@uobasrah.edu.iq†
† corresponding author

Recibido 14/4/2020; Aceptado 3/8/2020

The study of linear and nonlinear optical properties of molecules is essential for the design and construction of new optical devices that might be useful in electronic communication and photonic treatments. Hence, we have determined related nonlinear properties such as HOMO-LUMO, dipole moments, static polarizabilities, the anisotropy of polarizability, and first hyperpolarizabilities with the dihedral angles. Some dihedral angles can make switching behaviours in the two components of dipole moment and hyperpolarizability. The molecules with multi- torsional angles have nonlinear properties different than those who has a single torsional angle. The behaviours and results were compared with available theoretical data determined from different computational methods.

En el diseño y construcción de nuevos dispositivos ópticos potencialmente útiles en las comunicaciones ópticas son esenciales los estudios de las propiedades ópticas lineales y no lineales de las moléculas. Por ello, determinamos propiedades no lineales como el HOMO-LUMO, momentos dipolares, polarizabilidades estáticas, la anisotropía de la polarizabilidad y las primeras hiperporalizabilidades en función de los ángulos dihedros. Las moléculas que presentan varios ángulos torsionales manifiestan propiedades no lineales diferentes a las que tienen solo un ángulo torsional. Los resultados y comportamientos obtenidos son comparados con la data teórica disponible a partir de diferentes métodos computacionales.

PACS: Nonlinear optical materials (materiales ópticos no-lineales), 42.70.Mp, = 42.70.Nq; ab initio calculations (cálculos ab initio), 31.15.A-; polarizability of molecules (polarizabilidad de las moléculas), 33.15.Kr

I. INTRODUCTION

As nonlinear optical (NLO) substances have amazing features, they play a real role in future technology demands, such as the using of photons as information carriers [1]. They have a high potential for designing photonic devices such as active wavelength filters, modulators, optical switches and for THz wave generation [2–4]. During the last decades, different theoretical techniques have been used to study and design a wide variety of NLO materials, which can be are organic, inorganic, and also organic-inorganic hybrids [5–9]. They are efficient in the fields of optoelectronics (EO), optical rectification (OR), and optical parametric oscillation (OPO) [10]. Also, they have good prospects for fabrication and integration into devices. Besides, they have low dielectric constants [11–14]. Furthermore, the transition metal (organometallic and coordination) complexes show a nonlinear response [15, 16]. Due to the extensive structural diversity of organic materials and their remarkable NLO coefficients, they will be at the frontline in nonlinear applications [17–19]. Therefore, many works have been devoted to find materials with a massive second-order NLO response [20]. Strategies are used to modify the response of NLO organic donor-π-conjugated-acceptor (D-π-A) configuration [21–23] and many similar others, such as twisted-π-conjugated structures [24,25]. Another technique is to use chiral molecules or chiral complexes [26,27]. Based on their non-centrosymmetric structures, they achieve the NLO response to be recognised. Also, it is well understood that the use of heavy metal atoms inside the chiral ligand shows the progression in the second-order NLO response (β) value due to the robust charge transfer (CT) of the NLO chromophores [20]. Due to the scope of NLO applications of chalcone and its derivatives, it has been researched during recent years [28,29]. It has also excellent transparency through blue-yellow transmittance [30, 31]. Likewise, yellow colour crystals of chalcone derivatives (with methoxy phenyl terminal groups) have been grown, and they showed second harmonic generation (SHG) with efficiency 15 times larger than the urea molecule [32]. Moreover, the single crystals of pyridine-based chalcone derivatives showed efficient NLO in the visible and infrared ranges [33]. Many researchers focused on the side group(s) substitution strategy to enhance the nonlinear optical properties [34–37]. Also, on the inverse relationship between the energy gap and first static hyperpolarizabilities [35–37], while very few publications have been focused on determining how large is the influence of the rotation around the central axis of the nonlinear optical molecules [38–41]. Nevertheless, more computational data of nonlinear optical behaviour for different materials are required. In particular, it would seem desirable to evaluate the nonlinear optical responses of nanotubes according to their dimensions [42, 43] and fullerenes [44, 45]. In addition, the nonlinear optical

behaviour of nanotubes has been used in anti-cancer drugs [46, 47]. However, investigators have shown an increased interest in the nonlinear optical responses of the nitrogen bases of DNA and its mutations [48,49], because these have not been considered in computational studies. The identification of the structure-property relationship and the NLO response origin of the aromatic molecules is an essential issue for achieving further understanding of their performance improvement. For this purpose, three issues of torsional angles were adopted. In principle, theoretical computations can provide a detailed description of the whole torsional potential, electronic and nonlinear optical properties. For conformational analysis of chalcone, a comprehensive review of literature can be found in a paper by Muhammad [49]. Our aim is, firstly, to perform *ab initio* computations for the most significant chalcone, in order to analyse the interplay of conjugative, steric and electrostatic interactions in determining torsional barriers of this molecule. Up to now, calculations on the torsional behaviour of chalcone has not been made. So, our aim is to cast light on the photophysical characteristics of chalcone molecules and the assessment of their configurations to find their nonlinear optical origin according to their microscopic structure.

II. COMPUTATIONAL DETAILS

The electric dipole moment μ of molecules is a quantity of fundamental interest in a structural molecule. While a molecule is subject to an external electric field ϵ, the molecular charge density may reset and so the dipole moment may change. This change can be described as the first derivative of the energy E to a component of the electric field (ϵ_i) that gives a component of the electric dipole moment: $\mu_i = (\partial E/\partial\epsilon_i)(\epsilon = 0)$. The polarizability can be understood as the gradient of the induced dipole: $\alpha_{ij} = (\partial^2 E/\partial\epsilon_i\partial\epsilon_j)(\epsilon = 0)$. The average static polarizability $\langle\alpha\rangle$ tensor is defined as $\langle\alpha\rangle = (\alpha_{xx} + \alpha_{yy} + \alpha_{zz})/3$, where α_{xx}, α_{yy}, and α_{zz} are the diagonal elements of the polarizability tensor matrix [50]. The anisotropic polarizability ($\Delta\alpha$) amplitudes are usually defined as $\Delta\alpha = [(\alpha_{xx} - \alpha_{yy})^2 + (\alpha_{yy} - \alpha_{zz})^2 + (\alpha_{zz} - \alpha_{xx})^2 + 6(\alpha_{xy}^2 + \alpha_{xz}^2 + \alpha_{yz}^2)]^{1/2}/2$. The equations for the calculation of molecular hyperpolarizability are given as follows: $\beta_{ijk} = (\partial^3 E/\partial\epsilon_i\partial\epsilon_j\partial\epsilon_k)(\epsilon = 0)$. The complete equation for calculating the magnitudes of β from Gaussian 09 output provides ten components of this matrix as β_{xxx}; β_{xxy}; β_{xyy}; β_{yyy}; β_{xxz}; β_{xyz}; β_{yyz}; β_{xzz}; β_{yzz}; β_{zzz}, reported in atomic units (AU) [51]. So that, $\beta_{tot} = [\beta_x^2 + \beta_y^2 + \beta_z^2]^{1/2}$, where $\beta_x = (\beta_{xxx} + \beta_{xyy} + \beta_{xzz})$, $\beta_y = (\beta_{yyy} + \beta_{yzz} + \beta_{yxx})$, $\beta_z = (\beta_{zzz} + \beta_{zxx} + \beta_{zyy})$. The component of the first hyperpolarizability β_{tot} along the direction of the dipole moment is represented by β_μ which is usually defined as $\beta_\mu = (\mu_x\beta_x + \mu_y\beta_y + \mu_z\beta_z)/\mu$. The XY-plane hyperpolarizability (β_{xy}-plane) is given as β_{xy}-plane = $\beta_{xxx} + \beta_{xxy} + \beta_{xyy} + \beta_{yyy}$, which reflects the amount of β_{tot} in XY-plane of the molecule. Full geometry optimization of chalcone, (E)-1- (2,5-dimethylthiophen-3-yl) -3-phenylprop-2-en-1-one with methoxy group para-position, was performed (Fig. 1). Individual torsion potentials were obtained for the molecule as a function of inter-atom $C_2 - C_8$, $C_8 - C_9$, $C_{10} - C_{11}$ dihedral angles, named as θ_1, θ_2, θ_3 respectively. During the scan process, the whole geometrical parameters were simultaneously relaxed, so that they were varied between 0 and 180° in 10° steps (Fig. 1). Accurate calculation of dipole polarizabilities requires the use of extended basis sets. Here, 6-311G (d,p) is a split-valence triple-zeta basis (Pople-type basis), which adds one set of d functions to heavy atoms plus p polarization functions for hydrogen [52–54]. The dipole moment, static polarizability and first static hyperpolarizability calculations are performed using density functional theory through the B3LYP functional using 6-311G (d,p) basis set [55–58]. The B3LYP functional is a combination of Becke's three-parameter hybrid exchange functional (B3) and the Lee-Yang-Parr correlation functional (LYP) [55, 56]. All computations were done using the Gaussian 09 package program [51].

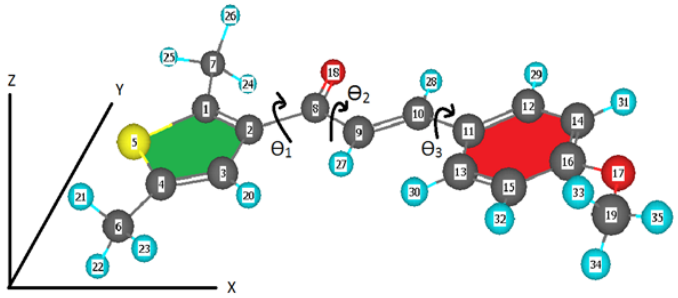

Figure 1. Optimised molecular geometry of the chalcone molecule at the B3LYP/6-311G(d,p) level of theory. θ_1, θ_2, θ_3 are the three torsional angles that were adopted.

III. RESULTS AND DISCUSSION

The variation of relative stability ΔE with the dihedral angles for chalcone is shown in Fig. 2. We checked the geometrical effect of these torsional angles, to add robustness to the NLO response of chalcone during its design [32]. The symmetry of the molecule imposes strictly equivalent minima for θ_3 only. At the same time, θ_2 showed the instability of the structure for the higher torsional angles, if they are compared with the results by Yoruk et al. [39]. So, any results for the torsional angle θ_1 and θ_2 beyond 150° will not be considered. In this work, we will focus on NLO properties because the torsional angles calculations of chalcone previously had not been studied. We reported the calculations of dipole moment, average polarizability, the anisotropy of polarizability and first static hyperpolarizability by changing the dihedral angle (θ_1, θ_2, θ_3) for chalcone. The variation of dipole moment, static polarizability and anisotropy of polarizability with the dihedral angles for chalcone is graphically shown in Figs. 3, 5, 7. The dipole moment (μ), which is given as $\mu = (\mu_x^2 + \mu_y^2 + \mu_z^2)^{1/2}$, illustrates the amount of intermolecular interactions, as shown in Fig. 3. The intermolecular interactions include the non-bonded type of dipole-dipole interactions. Furthermore, the higher dipole moments give stronger intermolecular interactions. The calculations show that θ_1 increases the total

dipole moment, unlike to the other angles θ_2 and θ_3.

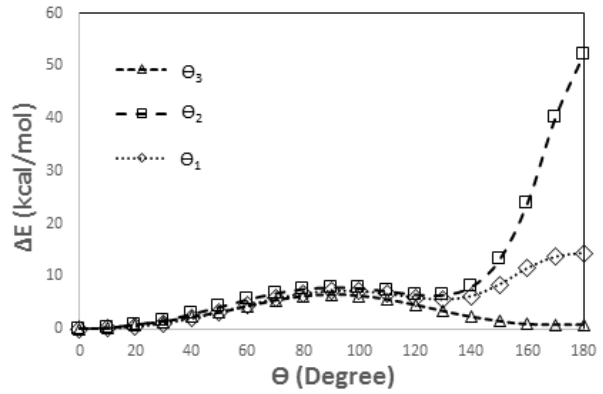

Figure 2. Dependence of ΔE with the angle, for the three dihedral angles (θ_1, θ_2, θ_3) corresponding to the chalcone molecule.

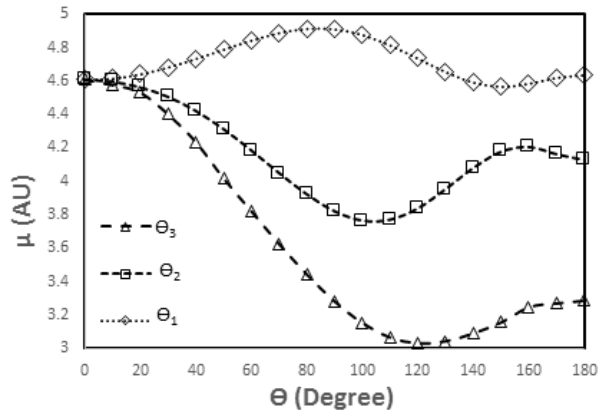

Figure 3. Dependencs of the total dipole moments (μ) with the angle, for the three dihedral angles (θ_1, θ_2, θ_3), corresponding to the chalcone molecule.

Furthermore, the role of θ_1 is evident in the two dipole components (μ_x and μ_y) during the operation of switching between the angles $80^\circ \sim 90^\circ$, as shown in Fig. 4. Another significant molecular characteristic in the electronic properties is its average polarizability $\langle\alpha\rangle$, where it is enhanced with the increase of the torsional angles θ_2 and θ_1, as illustrated in Fig. 5. Likewise, this will increase the molecule's refractive index too. The θ_2 and θ_3 were in good agreement with Ayar et al. [41] up to dihedral angles of 90° approximately, while θ_1 was dissimilar. The behaviour of the torsional algles is reported in Fig. 6.

The other NLO properties for this molecule is the anisotropic polarizability $\Delta\alpha$ which depends on the direction of the electric field. It was found to be significantly smaller than the average polarizability $\langle\alpha\rangle$, as indicated in Fig. 7. There, it can be seen that the torsional angles (θ_2 and θ_3) enhanced the polarizability parallel to the symmetry axes of the molecule, as compared to the perpendicular polarizability. Only θ_1 compares well with the results in [39].

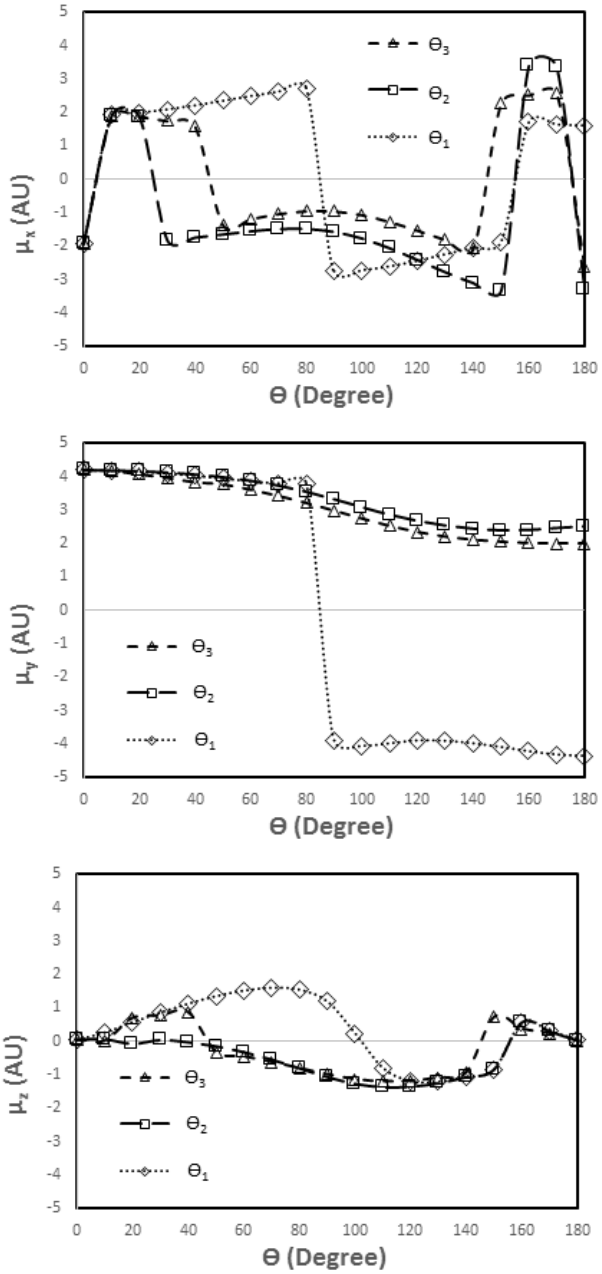

Figure 4. Dependence of the μ_x, μ_y and μ_z components of the dipole moment with the angle, for the three dihedral angles (θ_1, θ_2, θ_3), corresponding to the chalcone.

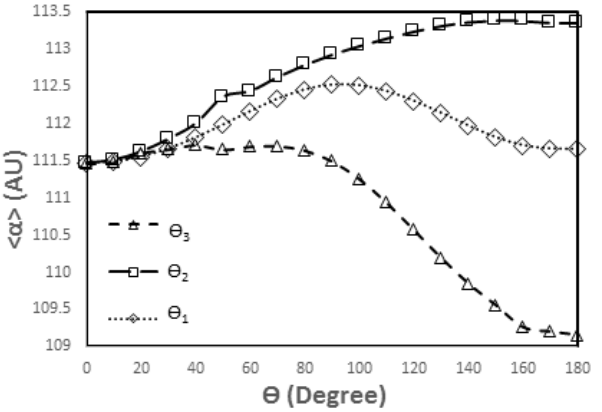

Figure 5. The variation of polarizability $\langle\alpha\rangle$ with the dihedral angles (θ_1, θ_2, θ_3) for chalcone molecule.

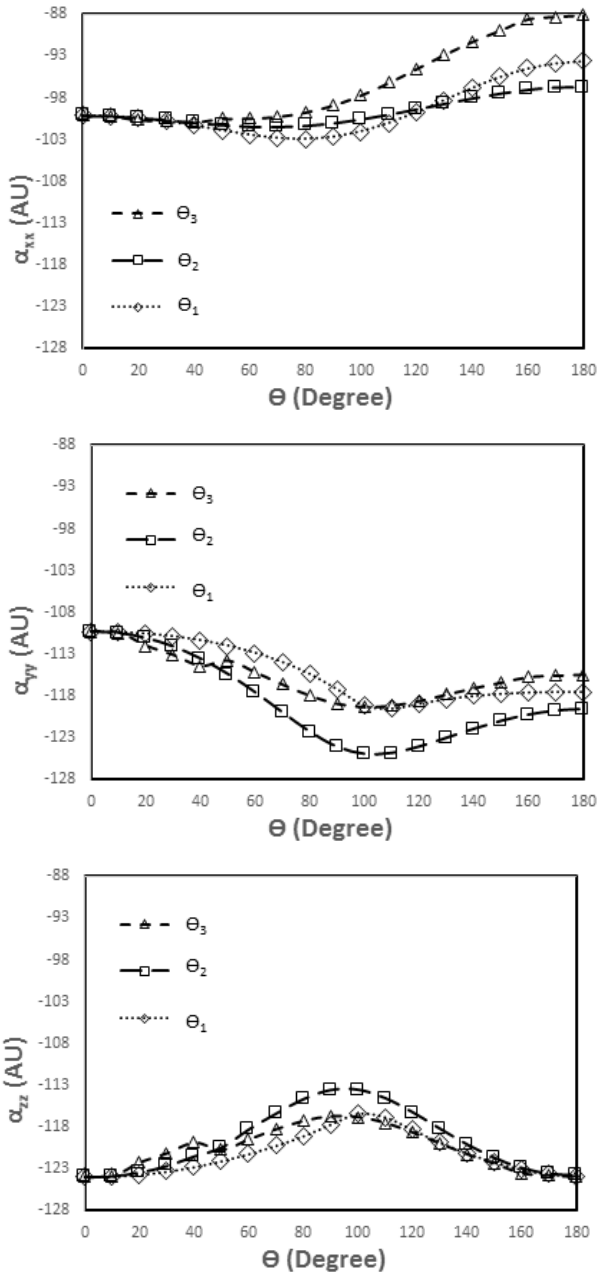

Figure 6. Dependence on the angle, of the static polarizability components (α_{xx}, α_{yy} and α_{zz}) corresponding to the three dihedral angles (θ_1, θ_2, θ_3), for the chalcone molecule.

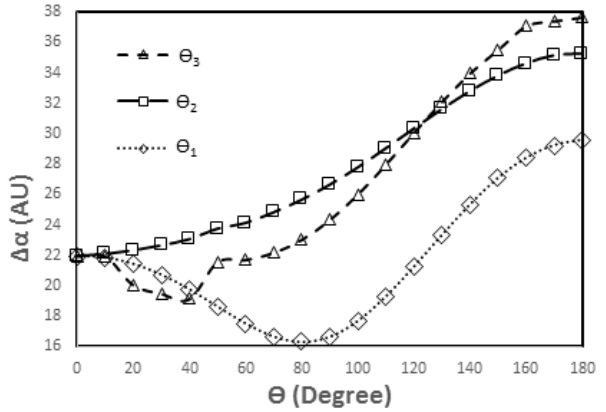

Figure 7. The variation of anisotropy of polarizability $\Delta\alpha$ with the angle, studied for the three dihedral angles (θ_1, θ_2, θ_3) for chalcone molecule.

The theoretical resolution of molecular hyperpolarizability (β_{tot}) is considered useful in explaining the relationship between molecular fabrication and non-linear optical properties. There is a maximum in the total hyperpolarizability β_{tot} for chalcone for dihedral angle θ_1, as evident from the Fig. 8. If we examine variations of β_μ, which is the hyperpolarizability along the direction of the dipole moment, with the dihedral angles we can infer there is high synchronisation between them, see Fig. 9.

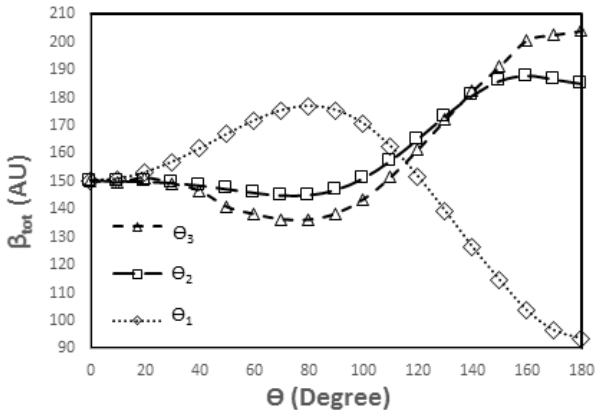

Figure 8. Angular variation of first static hyperpolarizability β_{tot} for the three dihedral angles (θ_1, θ_2, θ_3) for the chalcone molecule.

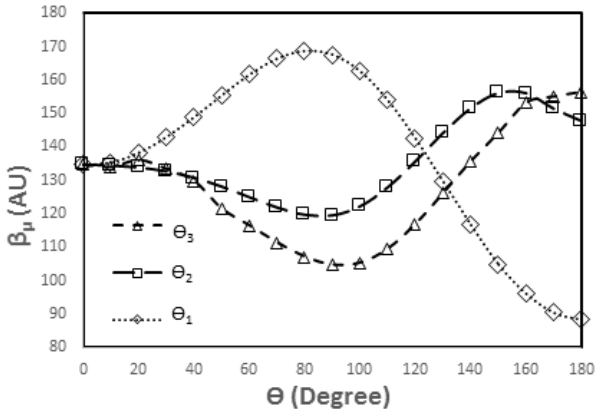

Figure 9. Angular variation of β_μ with the dihedral angles (θ_1, θ_2, θ_3) for the chalcone molecule.

The variation of the XY-plane hyperpolarizability (β_{xy}-plane), which is given as β_{xy}-plane = $\beta_{xxx} + \beta_{xxy} + \beta_{xyy} + \beta_{yyy}$, illustrates the amount of β_{tot} in the XY-plane of a molecule, as shown in Fig. 10. Only the torsion angle θ_1 peaked as β_{tot} in the XY-plane. So, is expected that θ_1 will improve the charge transfer along the plane of the central molecule axis.

The variation of HOMO–LUMO energy gap with the dihedral angles (θ_1, θ_2, θ_3) for chalcone is given in Fig. 11. Hyperpolarizability is associated with molecular electronic distribution under the influence of the electrical field depending on loosely or tightly bound electrons. Therefore, there is an approximate inverse relationship between the hyperpolarizability and HOMO–LUMO energy gaps, as we can see in Figs. 8 and 11, respectively. Generically, the inverse relationship between the energy gaps and the hyperpolarizabilities may be more depending on the substitution effects and position of some side groups [34–37]. The change in energy gap with the dihedral angles was within 50 % of the value which reported by Alyar et al. [41].

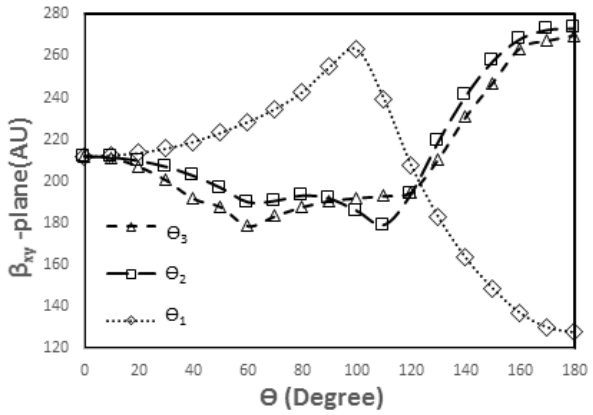

Figure 10. XY-plane of hyperpolarizability (β_{xy}-plane) due to the dihedral angles (θ_1, θ_2, θ_3) for the chalcone molecule.

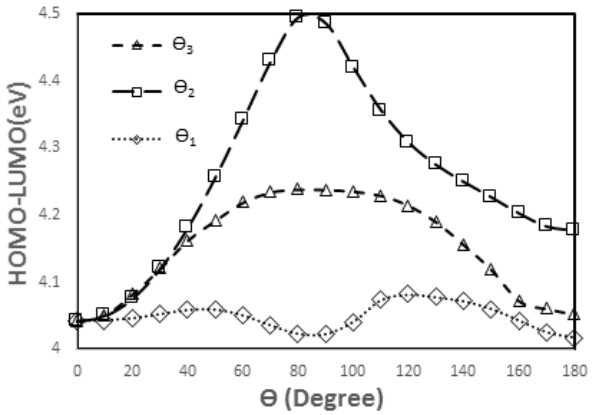

Figure 11. The angular variation of the HOMO-LUMO energy gap for the three dihedral angles (θ_1, θ_2, θ_3) for the chalcone molecule.

We examined the variations of hyperpolarizability components (β_x, β_y and β_z) with the dihedral angles for the chalcone molecule, so only β_x and β_y are sensitive to the variation of the dihedral angle θ_1 compared with θ_2 and θ_3, as illustrated in Fig. 12. Furthermore, β_x and β_y showed the same behaviour of μ_x and μ_y, as shown in Fig. 3.

IV. CONCLUSIONS

We have performed a theoretical study of torsional angles, electronic and nonlinear optical properties such as dipole moment, HOMO–LUMO energy gap, average static polarizability, the anisotropy of polarizability and static hyperpolarizability values for chalcone molecule, which were computed at the B3LYP/6-311G(d,p). Some of our results do not agree completely with previous results, where molecules with one dihedral angle only are studied. Additionally, we have observed that the energy gap, average polarizability and anisotropy of polarizability depend lightly on the dihedral angle. Some dihedral angles displayed switching behaviours in the two components of the dipole moment and hyperpolarizability, which are in the molecular plane. Furthermore, the dipole moment and hyperpolarizability had an equivalent dependence on the dihedral angles. However, the hyperpolarizability is massively dependent on the dihedral angle. These results are potentially useful for the design of chalcone-in-molecule-based technologies.

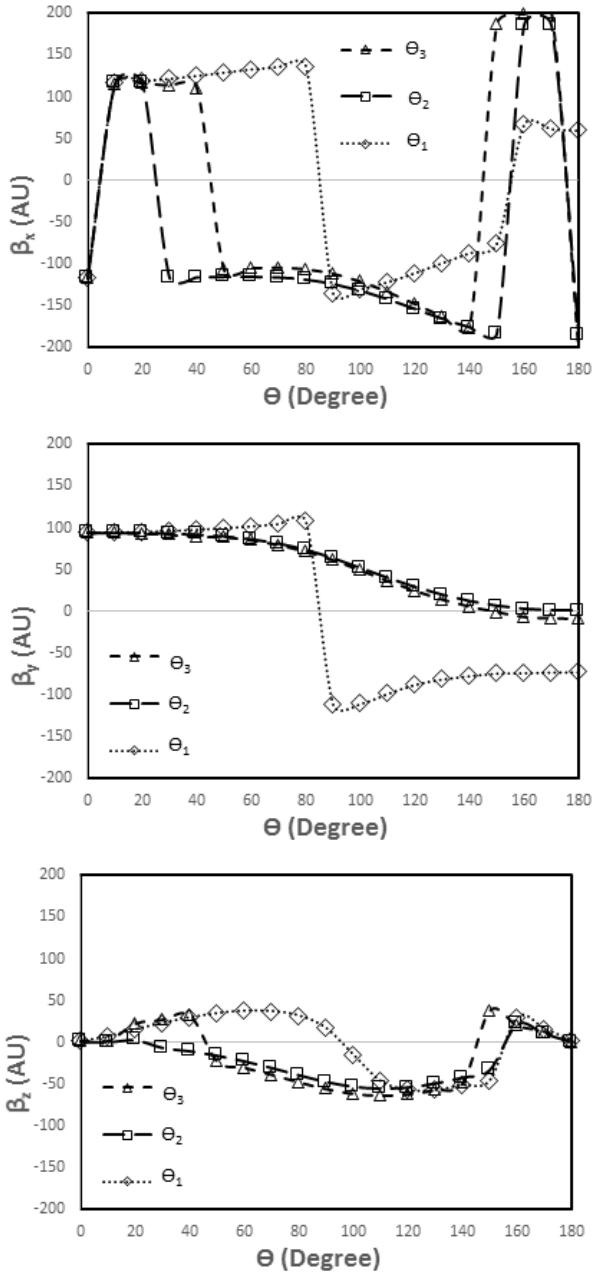

Figure 12. The angular variation of β_x, β_y, and β_z as a function of the dihedral angles (θ_1, θ_2, θ_3) for the chalcone molecule.

V. REFERENCES

[1] R. Hadfield, Nat. Photonics **3**, 696 (2009).

[2] P. Gunter, Nonlinear Optical Effects and Materials, Springer, (Berlin, Heidelberg, New York, 2000).

[3] H.S. Nalwa, Handbook of Advanced Electronic and Photonic Materials and Devices, Nonlinear Optical Materials, (Academic Press, New York, 2001).

[4] H.S. Nalwa, Organic Electronics and Photonics, (American Scientific Publishers, USA, 2008).

[5] M. Papadopoulos, A. Sadlej, J. Leszczynski, Non-linear optical properties of matter, (Springer, Heidelberg, 2006).

[6] H. Kurtz, J. Stewart, K. Dieter, J. Comput. Chem. **11**, 82 (1990).
[7] M. Shkir, Spectrochim. Acta. A Mol. Biomol. Spectrosc. **143**, 128 (2015).
[8] S. Muhammad, A. Irfan, M Shkir, A. Chaudhry, A. Kalam , S. AlFaify, A. Al-Sehemi, A. Al-Salami, I. Yahia, and H. Xu, J. Comput. Chem. **36**, 118 (2015).
[9] S. Muhamma, M. Nakano, Nanoscience and Computational Chemistry, (Apple Academic Press, New York, 2013).
[10] H. Ma, A.K.-Y. Jen, L.R. Dalton, Adv. Mater. **14**, 1339 (2002)
[11] L. Xu, Z. Li, Z. Su, S. Muhammad, F. Gu, and K. Harigaya, J. Phys. Chem. C **113**, 15380 (2009).
[12] S. Muhammad, H. Xu, R. Zhong R, Z. Su, A. Al-Sehemi, and A. Irfan, J. Mater. Chem. C **1**, 5439 (2013).
[13] D. Escudero, W. Thiel, B. Champagne, Phys. Chem. Chem. Phys. **17**, 18908 (2015).
[14] C. Manzur, M. Fuentealba, J. Hamon, D. Carrillo, Coord. Chem. Rev. **254**, 765 (2010).
[15] S. Wang, Y. Wang, C. Cai, J. Phys. Chem. C **119**, 16256 (2015).
[16] S. Di Bella, Chem. Soc. Rev. **30**, 355 (2001).
[17] Ch. Bosshard, J. Hulliger, M. Florsheimer, P. Gunter, Organic nonlinear optical materials, (CRC Press, Boca Raton, 2001).
[18] M. Shkir, S.AlFaify,H. Abbas, S. Muhammad, Spectrochem. Acta. A Mol. Biomol. Spectrosc. **147**, 84 (2015).
[19] R. Zhong, J. Zhang, S. Muhammad, Y. Hu, H. Xu, Z. Su, Chem. Eur. J. **17**, 11773 (2011).
[20] L. Chunyu, S. Yanling, S. Shaoqing, Y. Guochun, and P. Xiumei, Dalton Trans. **45**, 7285 (2016).
[21] C. Zhang, C. Lu, J. Zhu, G. Lu, X. Wang, Z. Shi, F. Liu, and Y. Cui, Chem. Mater. **18**, 6091 (2006).
[22] J. Hansen, J. Becher, J. Jeppesen, E. Levillain, M. Nielsen, B. Petersen, J. Petersen, and Y. Şahin, J Mater. Chem. **14**, 179 (2004).
[23] S. Muhammad, J Mol. Graph. Model. **59**, 14 (2015).
[24] G. He, J. Zhu, A. Baev, M. Samoć, D. Frattarelli, N. Watanabe, A. Facchetti, H. Ågren, T. Marks, and P. Prasad, J Am. Chem. Soc. **133**, 6675 (2011).
[25] I. Albert, T. Marks, M. Ratner, J. Am. Chem. Soc. **120**, 11174 (1998).
[26] T. Verbiest, *et. al.*, Science **282**, 913 (1998).
[27] D. Cornelis, *et. al.*, J. Am. Chem. Soc. **133**, 1317 (2011).
[28] J. Indira, P. Karat, B. Sarojini, J. Cryst. Growth. **242**, 209 (2002).
[29] S. Shettigar, K. Chandrasekharan, G. Umesh, B. Sarojini, and B. Narayana, Polymer **47**, 3565 (2006).
[30] B. Zhao, W. Lu, Z. Zhou, Y. Wu, J. Mater. Chem. **10**, 1513 (2000).
[31] D. Fichou, *et. al.*, Jpn. J. Appl. Phys. **27**, L429 (1988).
[32] V. Shettigar, *et. al.*, J. Cryst. Growth **295**, 44 (2006).
[33] A. Menezes, A. Jayarama, J. Mol. Struct. **1075**, 246 (2014).
[34] N.S. Labidi, A. Djebaili, and I. Rouina, J. Saudi Chem. Soci. **15**, 29 (2011).
[35] N. Labidi, Arab. J. Chem. **9**, S1252 (2016).
[36] G. Park, W. Jung, and C. Ra, Bull. Korean Chem. Soc. **25**, 9 (2004).
[37] K. Thanthiriwatte, K. Silva, J. Mol. Struc. (Theochem) **617**, 169 (2002).
[38] N. Abeyasinghe, R. de Silva, K. Silva, Int. Res. J. Pure & App. Chem. **13**, 2 (2016).
[39] M. Bahat, E. Yörük, A Computational Study on Structural, Electronic and Nonlinear Optical Properties of Furylpyridine Molecules, Proceedings of the 9th WSEAS international conference on Applied computer science, Genova, Italy, 2009.
[40] S. Siddiqui, T. Rasheed, M. Faisal, A. Pandey, and S. Khan, Spectroscopy **27**, 185 (2012).
[41] H. Alyar, M. Bahat, E. Kasap, Z. Kantarcı, Czech. J. Phy. **56**, 349 (2006).
[42] M. Alanber, Rev. Cubana Fis. **30**, 72 (2013) .
[43] M. Alanber , Z. Abdullah, S. Resan, A. Ali, J. Mater. Environ. Sci. **3**, 636 (2012).
[44] M. Alanber, A. Al-Mowali, A Ali, Act. Phy. Polo. A **126**, 845 (2013).
[45] M. Alanber, Orb. Elec. J. Chem. **6**, 156 (2014).
[46] M. Alanber, N. Al-Masoudi, Rev. Colomb. Quim. **41**, 299 (2012).
[47] M. Al-Anber, A. Ali, S. Resan, A. Al-Mouali, Int. J. Green Nanotech. **3**, 238 (2011).
[48] M. Alanber, Z. Abdalla, A. Salih, Fizi. A (Zagreb) **17**, 151 (2008).
[49] S. Muhammad,A. G. Al-Sehemi, A. Irfan, A.. Chaudhry, H. Gharni, S. AlFaify, M. Shkir, and A. Asiri, J. Mol. Model. **22**, 73 (2016).
[50] N. Labidi, Z. Kabier, Acad. J. Envi. Sci. **5**, 022 (2017).
[51] M. J. Frisch, G. W. Trucks, H. B. Schlegel, *et. al*, Gaussian 09, Revision C.01, Gaussian, Inc., Wallingford, CT, 2010.
[52] P. C. Hariharan, J. A. Pople, J. Chem. Phys. **27**, 209 (1974).
[53] R. Ditchfield, W.J. Hehre, J. A. Pople, J. Chem. Phys. **54**, 724 (1971).
[54] W. J. Hehre, R. Ditchfield, J. A. Pople, J. Chem. Phys. **56**, 2257 (1972).
[55] A. D. Becke, J. Chem. Phys. **98**, 5648 (1993).
[56] C. Lee, W. Yang, R. G. Parr, Phys. Rev. B. **37**, 785 (1988).
[57] B. Miehlich, A. Savin, H. Stoll, H. Preuss, Chem. Phys. Lett. **157**, 2000 (1989) .
[58] M. J. Frish, J. A. Pople, and J. S. Binkley, J. Chem. Phys. **80**, 3625 (1984).

ISO-DOSE MAP GENERATION AND DOSE-AREA PRODUCT CALCULATION THROUGH DIGITAL IMAGE PROCESSING OF SCANNED IRRADIATED RADIOCHROMIC FILMS

GENERACIÓN DE MAPAS DE ISO-DOSIS Y CÁLCULO DEL PRODUCTO DOSIS-ÁREA USANDO PROCESAMIENTO DIGITAL DE IMÁGENES EN PELÍCULAS RADIOCRÓMICAS IRRADIADAS Y ESCANEADAS

Y. Ruiz-Gonzalez[a†], S. Rodríguez-Ledesma[b], J.E. Paz Viera[c], J.V. Lorenzo Ginori[a]

a) Centro de Investigaciones de la Informática, Universidad Central "Marta Abreu" de Las Villas, Santa Clara, Cuba; yuselyr@uclv.edu.cu†
b) Centro de Ingeniería Clínica y Electromedicina, Santa Clara, Cuba.
c) Zimmer Biomet, Toronto, Canada.
† corresponding author

Recibido 08/7/2020; Aceptado 15/9/2020

Iso-dose maps creation and kerma-area products calculation are important procedures in radiotherapy and medical imaging. In this work, a method is presented to obtain iso-dose maps through digital processing of the images obtained from radiochromic films, which are employed to estimate the dose absorbed by the patient. The kerma-area product in selected regions of interest (ROIs) in the iso-dose map was then evaluated. The images were obtained by scanning the irradiated films using a commercial flatbed scanner. The iso-dose areas were extracted by means of an image segmentation algorithm, while calibration for a particular film to obtain a sensitometric curve relating dose to film darkening, was also made. A software interface allowed introducing the scanned image for the estimation of kerma-area products by defining the ROI interactively. The methods developed in this work allowed to implement a software application to obtain the iso-dose maps and kerma-area product in selected ROIs.

La creación de mapas de isodosis y el cálculo subsiguiente del producto kerma-área son procedimientos importantes en radioterapia e imagenología médica. En este trabajo se presenta un método para obtener mapas de isodosis a través del procesamiento digital de imágenes de las películas radiocrómicas utilizadas para estimar las dosis absorbidas por los pacientes en estos procedimientos. También se evalúa el producto kerma-área en regiones de interés (ROI) seleccionadas en los mapas de isodosis. Las imágenes se obtuvieron escaneando las películas irradiadas utilizando un escáner plano comercial. Las áreas de isodosis se extrajeron mediante un algoritmo de segmentación, además se realizó la calibración utilizando una película en particular, para obtener una curva sensitométrica que relaciona la dosis con el oscurecimiento de la película. Una interfaz de software unifica los métodos desarrollados y permite procesar imágenes escaneadas para la estimación de productos dosis–área definiendo las ROI de forma interactiva.

PACS: Dosimetry/exposure assessment of X-rays (evaluación de dosimetría / exposición a rayos X), 87.53.Bn; digital radiography (radiografía digital), 87.59.bf; digital imaging image processing algorithms (algoritmos de procesamiento de imagenes digitales), 07.05.Pj

I. INTRODUCTION

The measurement of ionizing radiation has evolved progressively over the last decades with the introduction of new methods as well as new detectors. Among the latest, radiochromic films have gained attention due to their suitable properties for the task of measuring the absorbed dose. Some of these properties are: accuracy, precision, operational dose range, good response to dose in terms of changes in film darkness, spatial resolution, near tissue-equivalence absorption properties, and ease of handling. Such properties make these materials closer to the ideal dosimeters and ahead of other methods and materials [1, 2]. Additionally radiochromic films do not require any special developmental procedure so they can give a permanent absolute value of the absolute dose at any time when they are preserved correctly. Radiochromic media for dosimetry can be found also in various forms including liquid solutions, gels, waveguides and films. Recent examples of current applications of radiochromic films which include applications outside the medical field can be found in [2–5]. A radiochromic film has the special feature of altering its coloration according to the radiation dose absorbed, which is - related to its internal composition. A typical film contains an active layer in its interior made of an opacifying agent. This layer is protected by other external layers such as two polyester protecting layers in the most external positions which enclose an adhesive surface and the active layer [6,7].

Upon irradiation, a polymerization process is initiated in the polyacetylenic compound resulting in the immediate change in the color of the coating. The color darkens in proportion to the radiation exposure [1, 6]. The reduction in light passing through the film is a measure of its 'blackness' or optical density (OD). This metric can be calculated as follows:

$$\mathrm{OD} = \frac{1}{4}\log_{10}\left(\frac{I_0}{I}\right), \tag{1}$$

where I_0 is the light intensity with no film present and I is the light intensity after passing through the film. Note

that since $\left(\frac{I_0}{I}\right)$ has an exponential relationship to the dose, the OD is appropriately linear with dose. The acceptance of this relationship has led to the wide use of the film as a dosimeter [1].

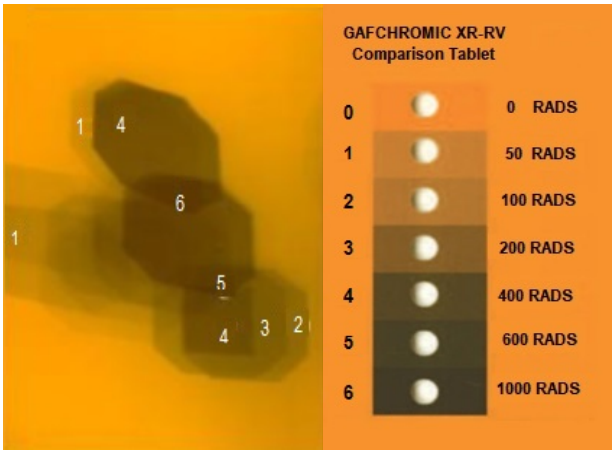

Figure 1. Scanned image of an irradiated film showing the labels of the differently irradiated zones.

Fig. 1 shows the scanned image of an irradiated film and a comparison strip which usually accompanies the film pack when it is purchased. It is used to have an estimate of radiation dose by visually comparing the opacity of the film with the strip specific values. This way, the precision of estimated values is affected by quantization as well as by the subjective evaluation of the observer.

Usually the film is placed between the radiation source and the object to be irradiated. Then, the degree of darkening can be measured by employing apparatus such as reflection or transmission densitometers, spectrophotometers, scanners and opto-electronic instrumentation [8, 9].

It is a regular practice to neglect small uncertainties such as the overall uncertainty of the dose measurement in the reference field, the uncertainty due to the non-uniform thickness of the film sensitive layer, and uncertainties associated with the equipment used to measure OD. Then, if the films are correctly calibrated, they can operate as absolute dosimeters yielding information directly about absorbed dose in absorbed radiation measurement units (Gy) [1, 2, 10].

Radiochromic films have been used in therapy [3, 11] as well as in diagnostic or treatment [12], to have an estimate of the absorbed dose by the patient subjected to any of these procedures. In this case, the film is placed between the radiation source and the patient, covering the area to be irradiated and remaining in that position until the procedure is done. No further procedure is required with the film (such as development or other chemical treatment) to estimate the degree of opacity caused by the absorbed radiation.

Previous dosimeters such as semiconductors or TLDs, usually mounted in ensembles, while offering precise measurements in certain locations, also offered a lower spatial resolution. With the introduction of radiochromic films, an accurate value of absorbed dose can be estimated at any point within the area covered by the film. Since the film darkens in proportion to radiation exposure, it is possible to measure the darkening and use it as a means for determining the amount of radiation exposure. In this way, the film may be employed not only as a radiation dosimeter but also to map radiation fields [1].

Previous works have measured film opacity employing the calibration strip to perform statistical analysis of irradiation procedures [6]. However, in the last years there has been an increase of methods for estimating absorbed dose from the films by employing apparatus such as densitometers, or more advanced methods such as automatically estimating absorbed dose from processing digital images of the scanned irradiated films [11–14].

Making use of appropriate Digital Image Processing algorithms, this work aims at the automatic segmentation of iso–dose areas in digital images from scanned irradiated films. In order to accomplish this, the way to obtain a two-dimensional (2D) OD fluence map is to be developed, which in turn can be converted to a 2D dose map. Segmenting the 2D map in areas whose dose is constrained to some interval in order to allow differentiating areas in the film that were irradiated in a similar amount, was the previous step in order to build the corresponding iso-dose map. This map has the purpose of facilitating the task (for the specialist) of easily locating these areas in order to measure the received patient radiation dose. This could be accomplished by simply pointing at them using computer software with an adequate visualization system. Another objective is the calculation from the iso-dose map of the kerma-area product for polygonal areas defined interactively.

II. MATERIALS AND METHODS

II.1. General aspects of the calibrating procedure

Film calibration is a process that yields a relationship between absorbed dose and film opacity. It is the first step before any other procedure is realized with the film in order to obtain any value of absorbed dose within the film's operation range from its opacity degree. Film opacity can be measured either by employing transmission or reflection densitometers, spectrophotometers, and/or flatbed scanners. In the case of scanners the acquired images should be stored in lossless compression file formats such as TIFF or BMP in order to maintain the highest quality of image representation avoiding the effects of lossy compression [15]. The curve obtained is called the sensitometric curve and is a characteristic of the film employed(in these experiments (GAFCHROMIC XR-RV2 film [16, 17]). This film usually comes in a landscape format of 14 (height) $\times$ 17 (wide) inches. In order to characterize the film, a group of small pieces of size 3×4 cm were sectioned from it maintaining the same landscape direction.The manufacturer specifies that GAFCHROMIC XR-RV2 could be used within the range 0.02 Gy to 50 Gy, with an energetic dependence less than 8 %, and between 30 keV and 30 MeV. In this case to the effect of selecting an appropriate method for interpolation, the range of radiation doses used in the samples was extended up to 100 Gy. It is known that the manufacturer recommends the use of the film in the range 0.02-50 Gy, however it is also

known that the human visual system is capable to discern only up to 30 intensity levels in an image. This means that in the comparisons table of Fig. 1, the darkest samples look very similar and the naked human eye could not discern clearly darker regions. This is not the case with digital images having intensities represented by 8 bit pixels: the computer could discern 256 intensity levels and it is possible to consider the hypothesis that with the method used in this work the useful irradiation dose range could be extended beyond 50 Gy. With the purpose of obtaining a preliminary clue about the ability of the method used here to discern high irradiation levels beyond the recommended range for the radiochromic film used in this application, as well as selecting an appropriate interpolation method capable of working properly in these conditions, here the range was extended up to 100 Gy as can be appreciated in the samples shown in Fig. 2, samples 14-16.

The protocol designed for the manipulation of the films (and the film pieces during calibration) pre- during-, and post-irradiation was established according to previous reviews [1, 18]. In the conducted experiments the OD estimation of irradiated film (and/or of the film segments) was carried out employing the conventional flatbed scanner HP ScanJet 3500c. All calculations were done employing MatLab [19].

II.2. Film calibration

As a first step, a group of 16 film pieces of size 3×4 cm were cut off out of the radiochromic film in order to irradiate them at different doses, and then, to measure film opacity at this values to obtain the curve relating OD with the absorbed dose. The dose values were: 125, 250, 375, 500, 750, 1000, 1500, 2000, 2500, 3000, 3500, 4000, 5000, 6500, 8000 and 10000 mGy. Irradiation took place at Departamento de Energía Nuclear (DEN), UFPE, Brasil, using a Pantak industrial X-Ray equipment, bipolar model, series 2HF420, with energies RQR6 (V = 80 kV, I = 10 mA, and beam quality of 3.01 mmAl of CSR) and RQR8 (V = 100 kV, I = 10 mA, and beam quality of 3.97 mmAl of CSR) [14]. An envelope was built in order to hold the pieces together within an irradiation area of 15 cm diameter at 100 cm distance to the source.

Twenty four hours after all pieces were irradiated, the OD was measured employing scanner HP Scanjet 3500c and digital image processing algorithms. Fig. 2 shows the scanned images of a set of irradiated film pieces.

The analysis of film opacity could be done using separately the intensity corresponding to any of the three RGB color components (Red, Green and Blue) or their combination in the Visual channel instead, obtained by means of the relation:

$$\begin{aligned} V &= 0.299 I_R + 0.587 I_G + 0.114 I_B, \\ V &= 0.299 R + 0.587 G + 0.114 B, \end{aligned} \tag{2}$$

where I_R, I_G, and I_B are the pixel intensities in the Red, Green and Blue channels respectively [16]. However, it has been demonstrated in previous works [16, 20] that the intensity of the red component is more sensitive to radiation in radiochromic films. Having this in mind, the OD was calculated from the red channel pixel intensities in the scanned images according to the relation:

$$\mathrm{OD}_{net} = \mathrm{OD}_i - \mathrm{OD}_n = \log\left(\frac{I_n - I_b}{I_i - I_b}\right), \tag{3}$$

where OD_i and OD_n are the ODs of irradiated and non-irradiated films respectively, I_b is the background pixel value obtained while scanning a black surface and I_i and I_n are the pixel values in irradiated and non-irradiated images respectively using the red component. This process does not depend upon the file format used to save the images.

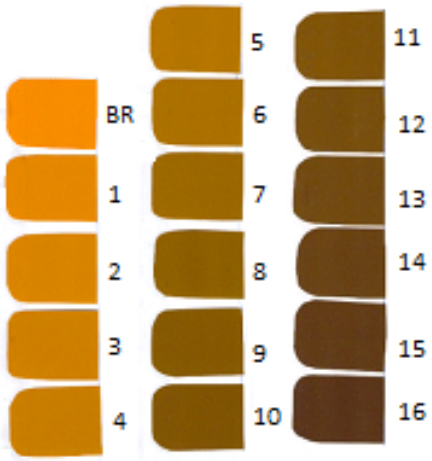

Figure 2. The sixteen irradiated pieces (1 to 16) of GAFCHROMIC XR-RV2 film, plus the non-irradiated piece (BR) at energy RQR6. The film sections and their respective doses are as follow: 1-125, 2-250, 3-375, 4-500, 5-750, 6-1000, 7-1500, 8-2000, 9-2500, 10-3000, 11-3500, 12-4000, 13-5000, 14-6500, 15-8000 and 16-10000 mGy.

To the effects of image processing, calibration curves were calculated to allow determining the dose corresponding to the specific irradiation in a film point, expressed in terms of the intensity's complement in the digital image. Here, if the intensities of the digital images from the pieces are represented in a scale such that $0 \leq I \leq 1$, the intensity's complement $C_i = 1 - I$ is an indicator of the film darkness that holds a bi-univocal relationship with the image intensity and with OD_{net} in equation (3) thus allowing determining a direct relationship between dose and intensity. The values of irradiation corresponding to every value of intensity can be obtained by interpolating the ordered intensity-irradiation pairs corresponding to the above-mentioned sixteen irradiated film pieces.

II.3. Determining the Ci-dose curves through interpolation

In order to determine the dose corresponding to any point in the image of the scanned radiochromic film, the curves C_i-dose are to be determined from the experimental values calculated for the sixteen irradiated pieces previously mentioned, using interpolation techniques.

Conventional polynomial and cubic splines were the interpolation methods implemented and tested in order

to select the one that provides the best results. For polynomial interpolation, a continuous polynomial function Φ determined from the 16 experimental points should be capable of predicting the dose value from C_i for all the other values inside and near to the interval extended from lowest to highest dose. Here is an example for a given polynomial of order n,

$$C_i = \Phi(x; a_0, \ldots, a_n) = a_0 + a_1 x + a_2 x^2 + \ldots + a_n x^n, \quad (4)$$

where C_i is the intensity's complement and x is the dose (D). Polynomials of degrees 3, 4 and 5 were used to obtain the curves and compare their effectiveness.

Cubic splines use third order polynomials for a piecewise interpolation between the experimental points, with the constraint that the first and second derivatives of the curves must have the same value at both sides of the initial points. Notice that with this method the interpolated curve is forced to pass across the experimental data points.

Decimation was used to compare the interpolation methods. In this case, one out of two and one out of three were chosen to determine the polynomial coefficients or the coefficients for the cubic splines. Then, the ordinate values at the remaining points were compared to the value predicted by the interpolated curve at the respective abscissas and the root mean squared (rms) errors were compared statistically by means of the Wilcoxon signed rank test [21]. In this case the null hypothesis was that the mean rms error was the same for the given pair of methods ($\mu_1 = \mu_2$, against the alternative hypothesis that one of the methods is better than the other $\mu_1 \neq \mu_2$, with $p = 0.05$. Once the interpolation method to be used was determined, it was actually used to obtain interpolated values of D from the C_i values of the pixels in the film, using the corresponding function characterized by their sets of coefficients.

II.4. Obtaining the iso-dose map

Once the C_i-dose curves were obtained, a continuous dose map was created in which the intensity of each pixel in the scanned radiochromic film was substituted by its corresponding dose value. Then, the map was median filtered to eliminate possible outliers and afterwards segmented in areas for which the dose values pertain to a prescribed interval. The intervals used for this segmentation are shown in Table 1.

Binary images were obtained by thresholding the intensity image at the pre-defined levels and assigning the value 1 to the region with a dose higher than the threshold. Then, a binary image associated to the corresponding iso-dose region was obtained by the set intersection $A \cap B^C$, where A and B are regions that correspond to contiguous threshold levels (where threshold in A is lower than that in B), as shown in Fig. 3 together with the general intensity histogram.

Each connected component (region) associated to the corresponding dose interval in the image was then labeled with a capital letter, as indicated in Table 1. In the image to be shown in the graphical interface, positioning the letters for this labeling was not a trivial task, as these letters should appear as centered as possible in each region. In order to accomplish this, the maximum of the distance transform in a binary image in which the logical value 0 was assigned to the region of interest and a logical 1 to the background, was used to determine the most centered points. The distance transform [22] of a binary image is defined as follows: for every pixel x in set A, $DT(A)$ is its distance from x to the complement of A,

$$DT(A)(x) = min\left\{d(x, y),\ y \in A^C\right\}. \quad (5)$$

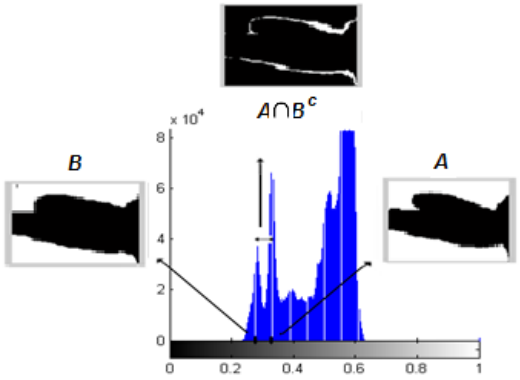

Figure 3. Binary images A and B obtained by thresholding the intensity image at the levels indicated in the histogram, and the difference image obtained through $A \cap B^C$.

Table 1. Iso-dose intervals and identifying characters.

Label	Lower dose	Higher dose
A	0	150
B	150	250
C	250	500
D	500	750
E	750	1000
F	1000	1500
G	1500	1750
H	1750	2000
I	2000	2250
J	2250	2500
K	2500	3000
L	3000	3500
M	3500	4000
N	4000	4500
O	4500	5000
P	5000	Inf

From the definition of the distance transform it is clear that $DT(A)$ will exhibit at least one maxima at the farthest point from the region borders. In case that more than one maximum exist, one of them is selected for placement of the character that will identify the corresponding iso-dose region. Then, a binary image is created with a 'one' in each of the $DT(A)$ maximum points and zero level in the rest of the image. These characters were built by morphological dilation of the binary

points with a binary image of the character that identifies the region (see Table 1). Fig. 4 shows the various steps in labeling one iso-dose region from the distance map calculation, where each labeled iso-dose region is to be distinguished by its color according to an appropriate color map.

II.5. Calculation of the kerma-area products.

Calculation of the kerma-area product in a user-defined region can be easily accomplished once the continuous dose map was obtained. In order to perform this calculation, it is necessary to know the area covered by one pixel in the image. Let R be the selected region, d_i the dose associated to the i-th pixel p_i within this region and A_p the radiochromic film area associated to an individual pixel in the image. Then, the kerma-area product can be obtained as:

$$DAP = A_p \sum \lim_{p_i \in R} d_i. \tag{6}$$

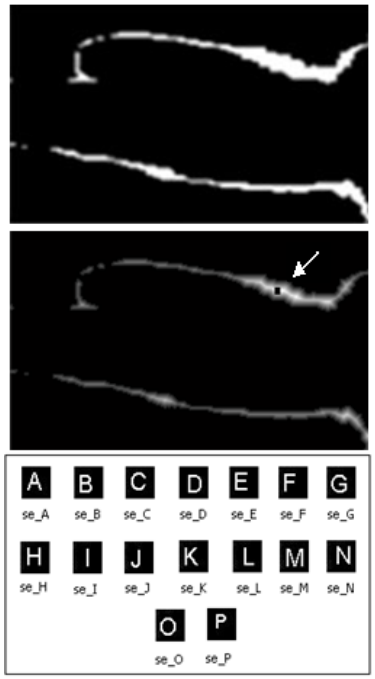

Figure 4. Labeling an iso-dose region, from top to bottom: binary map of the iso-dose region, distance map showing a maximum (most centered) pixel, small black square pointed by an arrow, and binary letters used as structuring elements for morphological dilation.

II.6. The software for film image analysis

The software algorithm created to obtain the iso-dose maps and kerma-area calculations was structured in two operation modes: calibration and measurement. In the calibration mode, the dose values corresponding to the irradiated radiochromic film pieces and the scanned images of the pieces are introduced as data. Then, the C_i-dose curve is obtained by interpolation and shown graphically.

In the measurement mode, the image of a radiochromic film to be evaluated is loaded, and the pixel area is also introduced. Here the pixel area depends upon both the scanner resolution employed and the actual film size. Segmentation by thresholding is performed to obtain the iso-dose areas. These are labeled by means of morphological operations as was explained before. Finally, a polygonal region where the iso-dose area is to be evaluated is defined interactively by the user and the corresponding kerma-area product is calculated.

III. RESULTS AND DISCUSSION

In this work, the complementary intensity versus irradiation dose curves were used and two interpolation methods were tested: polynomial and splines. In the case of polynomial interpolation it was found experimentally that order 4 provided the best results and it was used in the comparison to splines, which is shown in Table 2 for an experiment with an irradiation dose interval from 0 to 5000 mGy. Fig. 5 shows the interpolated curves corresponding to these two methods. It is apparent that for the data used to obtain these curves, the fact that splines force the interpolated curve to pass across the experimental points determined the presence of a larger rms error using this method. It was found also that when the experimental points are measured carefully this difference was not statistically significant when subjected to the Wilcoxon signed rank test.

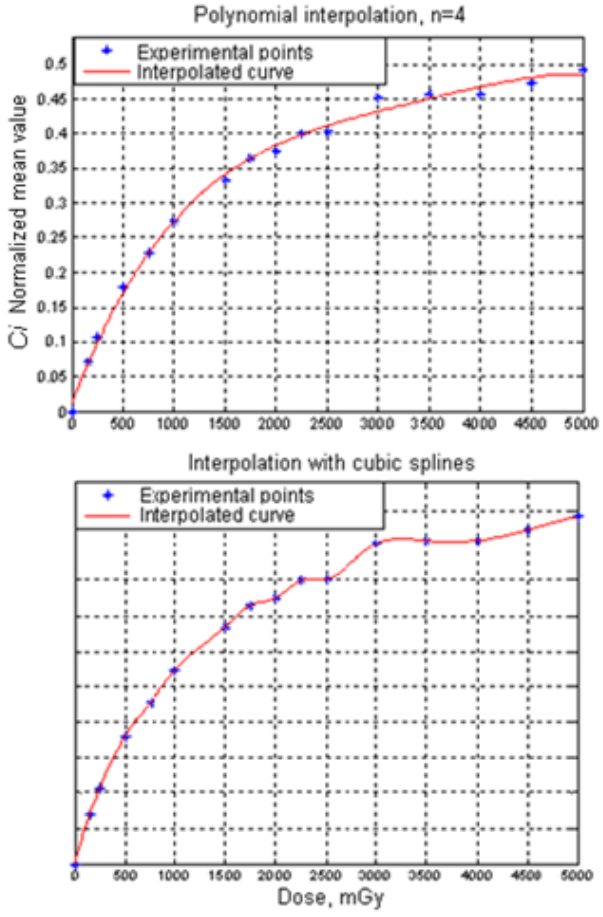

Figure 5. Comparison of interpolation by polynomial fitting and cubic splines.

Table 2. Errors in the interpolation methods. A: Predicting 8 samples from the remaining 8 (decimating by 2), B Predicting 10 samples from the remaining 6 (decimating by 3).

	Polynomial 4th order	Cubic splines
A	0.0715	0.2077
B	0.1056	0.1314

However, when using a wider irradiation range up to 10000 mGy, this situation changes because the polynomial fitting tends to exhibit some degree of oscillation in the range of high values. This determined that in a statistical evaluation using again the Wilcoxon signed rank test for this entire interval, the spline interpolation exhibited a better result than the polynomial one. This determined the use of splines as the method of choice (see Fig. 6). Notice also that the points obtained for the highest irradiation values suggest that the radiochromic film might discern and estimate radiation doses beyond 5000 mGy when using digital image processing techniques, a result that should be confirmed with more formal experiments.

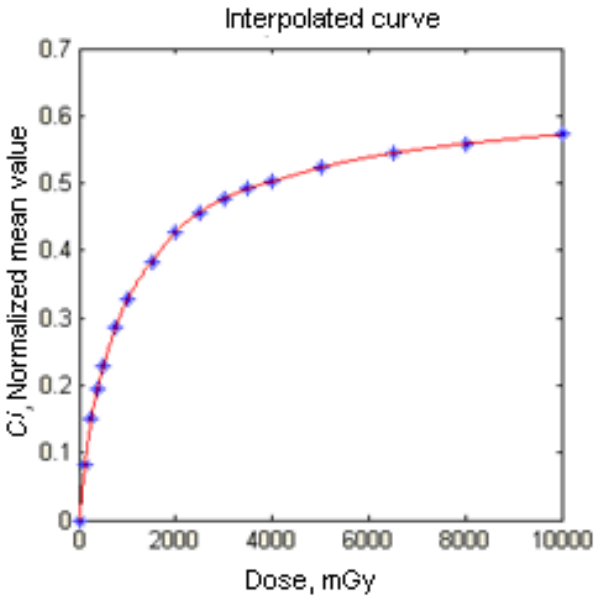

Figure 6. Interpolation with splines for the entire range up to 10000 mGy.

Iso-dose maps can be obtained in low computation time, even considering that the morphological procedures used for labeling tend to increase the computational load. Fig. 7 shows a typical iso-dose map and Table 3 shows the computation time for the processing of a specific radiochromic film, including that corresponding to the interpolation phase. For these measurements, an implementation in Matlab 7.0 was executed in a computer with an Intel Quad-Core processor at 2.33 MHz and with 2 GB RAM.

Table 3. Computer time for some of the main processes.

Program function	Time (seconds)
Polynomial Interpolation	0.93
Spline interpolation	0.92
Iso-dose map	21.32
kerma-area product	0.033

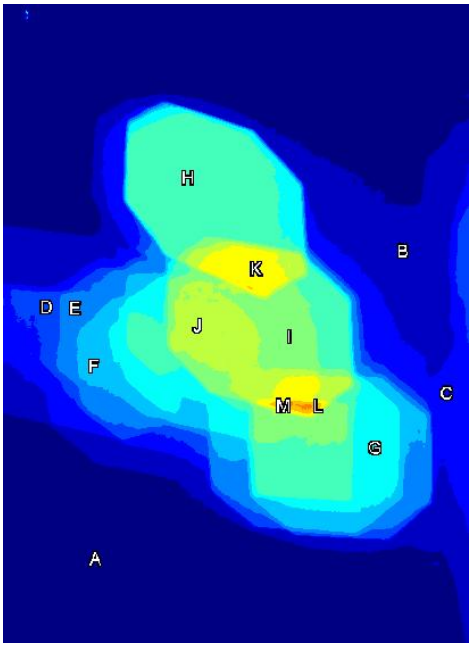

Figure 7. An example of labeled iso-dose map.

IV. CONCLUSION

A complete software system devoted to the creation of iso-dose maps from images of irradiated radiochromic films scanned in a conventional flatbed scanner has been presented in this paper. Special attention was devoted to find the best interpolation method to construct a complementary intensity-dose curve that allowed calculating the dose corresponding to a pixel with some value of intensity in the digital image produced by the scanner. It was found that there was not a statistically significant difference between polynomial and spline interpolation up to 5000 mGy while splines showed a better performance in the range up to 10000 mGy, which can be attributed to the effects of oscillation in the polynomials.

To conclude, a method to segment the film image into iso-dose regions using thresholds, and labeling these regions by means of morphological image processing, was introduced and demonstrated. This would allow differentiating areas in the film that were irradiated in a similar amount. The system would facilitate the specialists to easily locate these areas in order to measure the radiation dose received by the patient. Kerma-area products for an interactively defined polygonal area can also be calculated easily from the iso-dose map obtained. The computer time consumption of the developed software is low, allowing an efficient application of the system.

ACKNOWLEDGMENTS

This research was partially funded by the Canadian International Development Agency Project Tier II-394-TT02-00 and by the Flemish VLIR-UOS Programme for Institutional University Co-operation (IUC). The authors also thank Dra. Maria do Socorro Rocha da

Silva from Departamento de Energia Nuclear (DEN), GDOIN-Universidade Federal de Pernambuco (UFPE), Brasil, as well as to that institution.

V. REFERENCES

[1] S. Devic, N. Tomic, and D. Lewis, Physica Medica **32**, 4, (2016).

[2] Y. Tiantan, L.H. Luthjens, A. Gasparini and J.M. Warman, Rad. Phys. Chem. **133**, 37 (2017).

[3] S. Devic, L. LiHeng, N. Tomic, H. Bekerat, M. Morcos, M. Popovic, P. Watson, S. Aldelaijan and J. Seuntjens, Physica Medica **64**, 40 (2019).

[4] R. Holla et al., J. Med Phys. **44**(3), 145 (2019).

[5] R. Yan, J. Yun, J. Gurtler, and X. Fan, Postharvest Biol. and Technol. **127**, 14 (2017).

[6] S. Devic, Physica Medica **27**, 3 (2011).

[7] H.-Y. Shih, D. Lewis, and J. Anyumba, EP1430310A4, (2014).

[8] J. M. Lárraga-Gutiérrez, O. A. García-Garduño, C. Treviño-Palacios, and J. A. Herrera-González, Phys. Medica Eur. J. Med. Phys. **47**, (2018).

[9] P. Casolaro, et al. Scientific Reports Open **9**(5307), 1 (2019).

[10] S. Devic, et al., Med. Phys. **32**, 7 (2005).

[11] M. C. Battaglia, "Dosimetry studies for radiation therapy with photons and radiobiology using low-energy protons", PhD Thesis, Universidad de Sevilla, España, 2017.

[12] A. Neocleous, E. Yakoumakis, G. Gialousis, A. Dimitriadis, N. Yakoumakis, and E. Georgiou, Radiat. Prot. Dosimetry **147**, 1 (2011).

[13] W. V. Segura, Tecnol. **33**, 1 (2020).

[14] M.E. Howard, M.G. Herman, M.P. Grams, PLoS ONE **15**(5), e0233562 (2020).

[15] R. C. Gonzalez and R. E. Wood, Digital Image Processing Using Matlab, (GP, New Delhi, 2009).

[16] A. I. Mendoza-Moctezuma et al., AIP Conference Proceedings **1310**, 1 (2010).

[17] R. Sánchez, E. Vano, J. M. Fernández, A. Machado, and N. Roas, Radiat. Prot. Dosimetry **147**, 1 (2011).

[18] A. Niroomand-Rad, *et al.*, Med. Phys. **25**, 11 (1998).

[19] "MATLAB Documentation" (https://www.mathworks.com/help/matlab/).

[20] N. Lunelli, M. S. Rochas, J. E. Paz-Viera, and H. J. Khoury, in V Latin American Congress on Biomedical Engineering CLAIB 2011 edited by J. F. Folgueras et al.(Springer, IFMBE proceedings, 2013).

[21] F. Wilcoxon, Biom. Bull. **1**, 6 (1945).

[22] P. Soille, Morphological Image Analysis - Principles and Applications, (Germany, Springer Verlag, 2003).

NUMERICAL SIMULATION OF RADIAL AND AXIAL EVOLUTION OF REDUCED ELECTRIC FIELD ON THE CONVERSION OF NITROGEN OXIDES

SIMULACIÓN NUMÉRICA DE LA EVOLUCIÓN RADIAL Y AXIAL DEL CAMPO ELÉCTRICO REDUCIDO EN LA CONVERSIÓN DE ÓXIDOS DE NITRÓGENO

A. K. Ferouani[a,b†], M. Lemerni[b], S. Belhour[c], S. Askri[d]

a) Ecole Supérieure en Sciences Appliquées, Tlemcen, 13000, Algeria; ferouani_karim@yahoo.fr†
b) L.P.T Laboratory, University A. Belkaid of Tlemcen, 13000, Algeria.
c) L.P.M.P.S, Department of Physics, Faculty of Exact Sciences, University of Freres Mentouri, Constantine 1, 25000 , Algeria.
d) L.E.V.R.E.S Laboratory, University of El Oued, 39000, Algeria.
† corresponding author

Recibido 01/9/2020; Aceptado 05/10/2020

In this paper, we propose to numerically simulate the spatial-temporal (axial and radial) evolution of the density of certain nitrogen oxides present in the gaseous mixture: 74 % N_2, 10 % O_2, 8 % H_2O and 8 % CO_2 which is subject to a negative corona discharge at room temperature and atmospheric pressure. We study the influence of the reduced electric field E/n (E electric field, n the density) on the chemical kinetics of this mixture. The gas chemistry takes into account 18 species such as: the radicals N, O, H, OH, the ground state molecules N_2, O_2, H_2O, CO_2, O_3, H_2, HNO_3, the nitrogen oxides NO, N_2O, NO_2, NO_3, N_2O_5, metastable species $N(^2D)$ and the electrons e^-, reacting with one another 80 selected chemical reactions. The purpose of this simulation is to complete these studies by analyzing different plasma species under three selected values of reduced electric fields: 100, 200 and 300 Td. The results obtained show an evolution closely related to the reduced electric field.

En este trabajo, proponemos simular numéricamente la evolución temporal (axial y radial) de la densidad de determinados óxidos de nitrógeno presentes en la mezcla gaseosa: 74 % N_2, 10 % O_2, 8 % H_2O y 8 % CO_2 sujeta a una descarga corona negativa a temperatura ambiente y presión atmosférica. Estudiamos la influencia del campo eléctrico reducido E/n (E campo eléctrico, n la densidad) sobre la cinética química de esta mezcla. En la química del gas se tienen en cuenta 18 especies como: los radicales N, O, H, OH, las moléculas del estado fundamental N_2, O_2, H_2O, CO_2, O_3, H_2, HNO_3, el óxido de nitrógeno NO, N_2O, NO_2, NO_3, N_2O_5, especies metastable $N(^2D)$ y los electrones e^-, que reaccionan entre sí mediante 80 reacciones químicas seleccionadas. El propósito de esta simulación es completar estos estudios analizando diferentes especies plasmáticas con tres valores seleccionados de campos eléctricos reducidos: 100, 200 y 300 Td. Los resultados obtenidos muestran una evolución estrechamente relacionada con el campo eléctrico reducido.

PACS: Corona discharges (descargas de corona), 52.80.Hc; plasma kinetic equations (ecuaciones cinéticas de plasma), 52.25.Dg; plasma simulation (simulación de plasma), 52.65.-y.

I. INTRODUCTION

Nowadays, gas discharge plasmas and their applications in physics, chemistry, biology, and environmental programs are being widely studied. They can be used for reforming the poisonous pollutants, such as NO_x, SO_x, CO_x. These studies are based on the numerical equations for the reduction of NO_x gases in reactors [1,2].

Plasmas are able to initiate chemical reactions in normally inert gas mixtures [3]. The common thermal and catalytic techniques used for many years to eliminate NO_x and SO_x present in industrial or vehicle-generated fumes will not make it possible to respect the new emission limits which become more and more severe to protect the environment [4–6]. These effects can also have a direct impact on targeted applications such as electron beams particularly studied for the treatment of gaseous effluents polluted by nitrogen oxides, production of sulfur and/or ozone, medical applications and treament of surface [7,8]. The development of industrial and automotive activities in recent years has led to an increase in energy consumption, which has become increasingly important over the years [9,10]. This rapid growth in industrial and technological development has had a major impact on air quality, and has led to increased pollution most important As a result, the implementation of environmental standards on emissions compounds organic volatile as well as various oxides (NO_x, SO_x,...) has motivated the search for new ways of depollution [10]. Among the polluting species emitted in the atmosphere, it can be said that nitrogen monoxide NO and nitrogen dioxide NO_2 which are emissions mainly from combustion plants (i.e thermal power stations, solar heating...) and vehicles are the main pollutants in the atmosphere. The discharge of these effluents is now regulated and the standards are increasingly binding on industry and the automotive sector. These standards require the improvement of existing processing techniques or the development of new cleaner processes if they have reached their economic or technological limits [11–13].

The so-called conventional abatement techniques have successfully reduced harmful emissions. However, a new

technology based on non-thermal plasmas [14, 15] is used in many areas such as the control of gas pollution, production ozone, or surface treatment. Cold plasmas at atmospheric pressure exist in different forms. In this work, only plasmas generated by discharges point-to-plane crowns are modelled. This type of landfill is a very efficient active species. Pollution control by crown discharge requires two successive steps: the first, discharge phase which allows to generate by collisions between energetic electrons and gas molecules, active radicals such as O, N, OH, O_3...,the second, the post-discharge phase is where the formed radicals diffuse and react with the pollutants to destroy or transform them into new, less harmful species.

The numerical simulation that we will discuss in this paper concerns the spatial-temporal evolution of the density (radial and axial) of the species present in the gas mixture composed of 74 % N_2, 10 % O_2, 8 % H_2O and 8 % CO_2 (The choice of these species is related to their relative importance in polluted gases, especially oxides of azotes). The mixture is subjected to a point-to-plane of negative corona discharge with an inter-electrode distance equal to 20 mm (Fig. 1). These different species react to each other according to 80 chemical reactions. We consider the whole at room temperature and atmospheric pressure. The transfer of energy between the system electric and the gas mixture is modeled by the reduced electric field E/n. We have chosen the following three values 100, 200 and 300 Td (remember that 1Td=10^{-21} V.m^2)

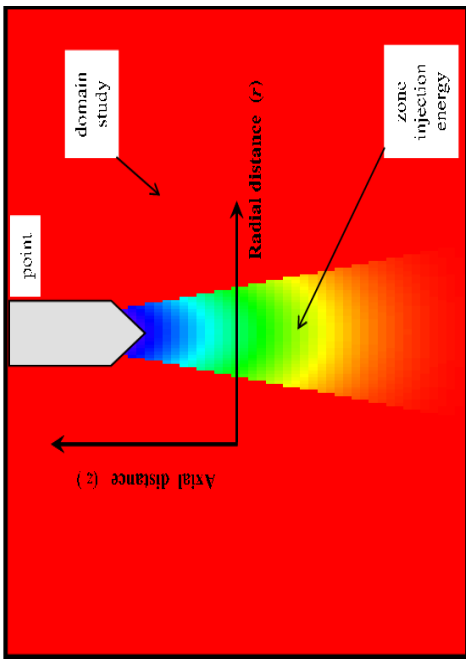

Figure 1. Schematic of a typical corona reactor geometry (pointed electrode and plane electrode).

II. BASIC FORMULAE

The mathematical model used in the present work consists of a system of equations that takes into account the variation of the density and the chemical kinetics of the environment, we adopt a developed order numerical code to resolve the transport equations. The algorithm is based on the time integration of the system of equations under consideration.

II.1. Rate equation model

In a volume-averaged approach, the state of the system is completely specified by the mass fractions of each species in the system, the temperature and the pressure. These properties change due to chemical reactions and the release of heat. Thus, we obtain the following conservation equations [16, 17].

Conservation of the overall mass m of the mixture, can be written as:

$$\frac{\partial(\rho\, V)}{\partial t} = \frac{\partial m}{\partial t} = 0 \tag{1}$$

where ρ is volume density (in kg m^{-3}), m denotes mass (in kg) and V is volume (in m^3).

Conservation of the species mass fraction ξ_i of species i, is defined by:

$$\frac{\partial \xi_i}{\partial t} - \frac{M_i\, \dot{\xi}_i}{\rho} = 0 \tag{2}$$

where ξ_i is mass fraction of the species i, $\dot{\xi}_i$ is rate of formation of the species i (in mol m^{-3} s^{-1}) and M_i is molar mass of the species i (in kg mol^{-1}).

Conservation of energy, can be written as:

$$\frac{\partial T}{\partial t} - \frac{1}{\rho\, C_p}\frac{\partial p}{\partial t} + \frac{1}{\rho\, C_p}\sum_i H_i\, M_i\, \dot{\xi}_i = 0 \tag{3}$$

where T is temperature, C_p molar heat capacity at the constant pressure (in J K^{-1} mol^{-1}), p is pressure and H_i is specific enthalpy of the species i (in J kg^{-1}).

To close this system of ordinary differential equations the ideal gas law:

$$p = \rho\, R\, T \sum_i \frac{\xi_i}{M_i} \tag{4}$$

where R is gas constant (in J K^{-1} mol^{-1}).

II.2. Chemical kinetics

The basic chemical kinetics used in the present paper, consist of a mathematical system of equations that takes into account the variation of the density and the chemical kinetics of the environment. The chemical kinetics equation systems can be described by an ordinary differential equation system obeying the following form [18].

$$\frac{d\, n_i}{d\, t} = \sum_{j=1}^{j_{\max}} F_{ij}, \qquad j \in [1, ..., j_{\max}] \tag{5}$$

where

$$F_{ij} = \varphi_{ij} - \chi_{ij} \tag{6}$$

n_i means the species densities vector, and F_{ij} mean the source term vector depending on the rate coefficient and

corresponding to the contributions from different processes. φ_{ij} and χ_{ij} represent respectively the gain and loss of species i due to the chemical reactions. The solution of such a system requires the knowledge of the initial concentrations.

However, the reactivity of the gas were taken into account to the source term F_{ij} (density conservation) Eq (5).

$$\varphi_{ij} = \sum_{\gamma} K_{\gamma}(T)(n_i\, n_j)_{\gamma} \tag{7}$$

and

$$\chi_{ij} = \sum_{\eta} K_{\eta}(T)(n_i\, n_j)_{\eta} \tag{8}$$

$K_{\gamma}(T)$ and $K_{\eta}(T)$ are the coefficients of the chemical reaction number γ or η, $(n_i\, n_j)$ means the product of densities of species i and j.

These coefficients satisfy Arrhenius formula [19]:

$$K_{\gamma}(T) = \kappa_1 \exp\left(\frac{\theta_{\gamma}}{T}\right) \tag{9}$$

and

$$K_{\eta}(T) = \kappa_2 \exp\left(\frac{\theta_{\eta}}{T}\right) \tag{10}$$

where κ_1 and κ_2 are the constant factors and θ_{γ} and θ_{η} are the activation energy of the chemical reaction.

The system of conservation equations are discretized by using a finite control volume with the approximation of a centred difference at the frontiers and solved by the F.C.T (Flux Corrected Transport) algorithm fully described by Refs. [20–22].

All the species considered in this simulation react with each other according to 80 chemical reactions which have been chosen in the literature and more precisely in the work on the chemical kinetics of industrial effluents [23–25]. It should be mentioned that all reactions taken into account and their reaction coefficients are shown in the Table 1.

III. RESULTS AND DISCUSSIONS

The results we will present in this section are shown below:

- Axial evolution of the density of nitrogen oxides NO, NO_2 and radicals N, O.
- Radial evolution of the density of nitrogen oxides NO and NO_2.

The spatial distribution of the density of two species that we have chosen NO and NO_2 for their contributions in this mixture, we present this distribution for different time in the ranges of 50-500 ns.

III.1. Evolution of nitrogen monoxide density NO

We present an axial and radial analysis of the evolution of the density of the NO molecule to better understand the reactivity of this species.

To analyse the axial evolution of the nitrogen monoxide density, we have shown in *at left* Fig. 2, changes in this species for three field values reduced electricity: (a): 100 Td, (b): 200 Td and (c): 300 Td. If we examine these graphs visually, we immediately notice a difference in the density of nitrogen monoxide for the three reduced electric fields. Indeed, Fig. 2(a), there is a variation in density between 10^6–10^8 m^{-3}, while for Fig. 2(b), the values records 10^7–10^9 m^{-3}, and for Fig. 2(c) we get asignificant variation between $10^{15} - 10^{17}$ m^{-3}. We can clearly see the influence of the transfer of energy ionised gas/neutral particle on the evolution of the density of nitrogen monoxide. It can also be noted in these Figs. (*at left* Fig. 2) that the more the intensity of the reduced electric field increases, the more the evolution of nitrogen monoxide in the inter-electrode space becomes significant. For example, in Fig. 2(a), we can see a significant increase in density between 50-250 ns along the axis of the discharge. Then, between ~ 300-500 ns the density begins to decrease with level of the point, while for the plane to the middle of the axis, it continues to increase. If we pass to Fig. 2(b), we notice the same phenomenon as before, except that in the cathode region the density becomes roughly equal to that of the point. For Fig. 2(c), the evolution of density is completely different from the previous two. In effect, from the beginning we notice a decrease in density throughout the axis of the with the appearance of three distinct zones: the plane zone, the central zone where the density is the lowest, and the point area with the highest density. We can therefore conclude that the energy injected into the gas mixture has a significant influence on the evolution of the nitrogen monoxide density over time.

To complete the previous analysis, we propose to see the behaviour of the molecule NO in the radial direction. For this we presented on the *at right* Fig. 2 density evolution for the same reduced electric field values. We notice on all the curves given on the two Fig. 2(a-b):

The convective movements that cause a slight depopulation of the axial area which varies over time.

The radial expansion towards the walls which decreases as one moves away from the discharge axis.

Regarding the Fig. 2(c) shows a very clear depopulation on the axis gradually over time and becomes very important from $t \simeq 400$ ns. Indeed, this decrease from $\sim 8 \times 10^{16}$ m^{-3} at $t = 50$ ns to $\sim 2 \times 10^{15}$ m^{-3} at $t = 450$ ns. This variation in density causes a blast wave to form at ~3 mm from the axis and reach its maximum at 15 mm from the axis. This depopulation on our axis the reduction of nitrogen monoxide, whereas for 100 and 200 Td we had a production of this species.

III.2. Evolution of the density of NO_2

Fig. 3 shows the time evolution of nitrogen monoxide density axial and radial for three values of the reduced electric field.

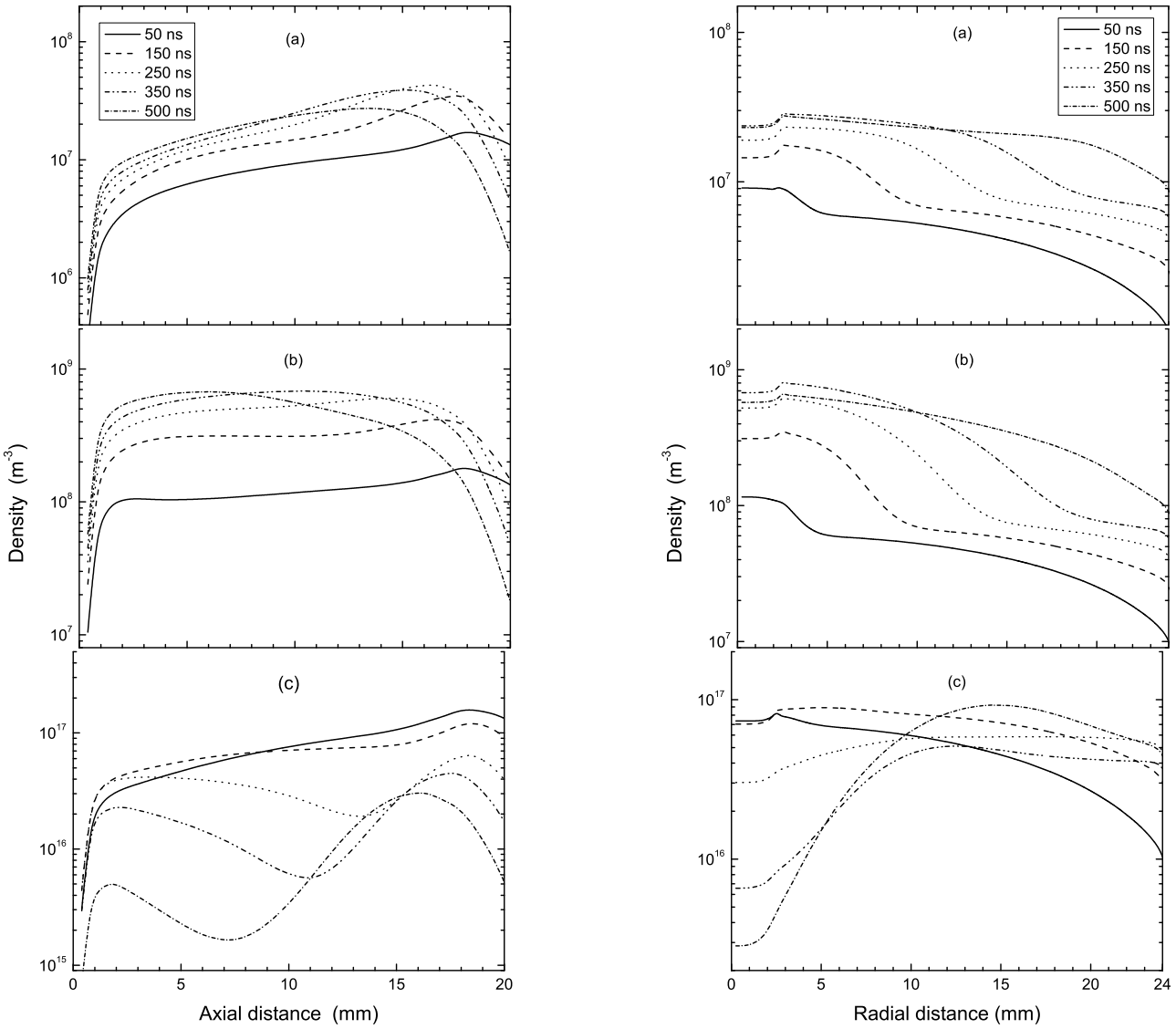

Figure 2. Evolution of the density of NO for a negative point discharge for three values of the reduced electric field, such as (a): 100 Td, (b): 200 Td and (c): 300 Td and for different times between 50 and 500 ns. At left axial evolution of NO; At right radial evolution of NO.

It is clearly seen that in *at left* Fig. 3(a,b) that there is a significant increase with the increase in time, this follows from the fact that there is a density more important depopulation in the inter-electrode space, whereas for Fig. 3(c) we have a decrease in density. For example, for 100 Td, there is a variation in density between $10^6 - 10^8$ m^{-3}, while for 200 Td, the values $10^7 - 10^9$ m^{-3}, and for 300 Td we get a variation between $10^{15} - 10^{16}$ m^{-3}. This is completely natural since nitrogen dioxide is created from nitric oxide by the following reaction:

$$O_3 + NO \rightarrow NO_2 + O_2$$

We also note on these curves (*at left* Fig. 3), that the more the intensity of the reduced electric field increases, the more the evolution of the density of nitrogen dioxide varies unevenly in the inter electrode space.

In Fig. 3(a) the density growth is seen along the discharge.

In Fig. 3(b), the density which was initially significant at the plane and minimal at the point becomes homogeneous in almost all space.

In Fig. 3(c), the density is completely different from the previous two since we have the appearance of three distinct zones: the plan, the center and the point, we also observe in Fig. 3(c) a density almost equal to the plane and point a density almost equal to the plane and at the point.

We can therefore conclude that part of the *at left* Fig. 3 is that the energy transfer between the plasma modeled by the reduced electric field and the NO_2 molecule which is created in the gas mixture, plays an important role in the evolution of density.

We now proceed to examine the behavior of the NO_2 molecule in the radial direction. In *at right* Fig. 3, we show the, the radial evolution of NO_2 for several times. We notice on all the curves that are given on the two Fig. 3(a-b):

The convective movements that cause a slight depopulation of the axial area which varies over time.

The radial expansion towards the walls that decreases as you move away the axis of the discharge.

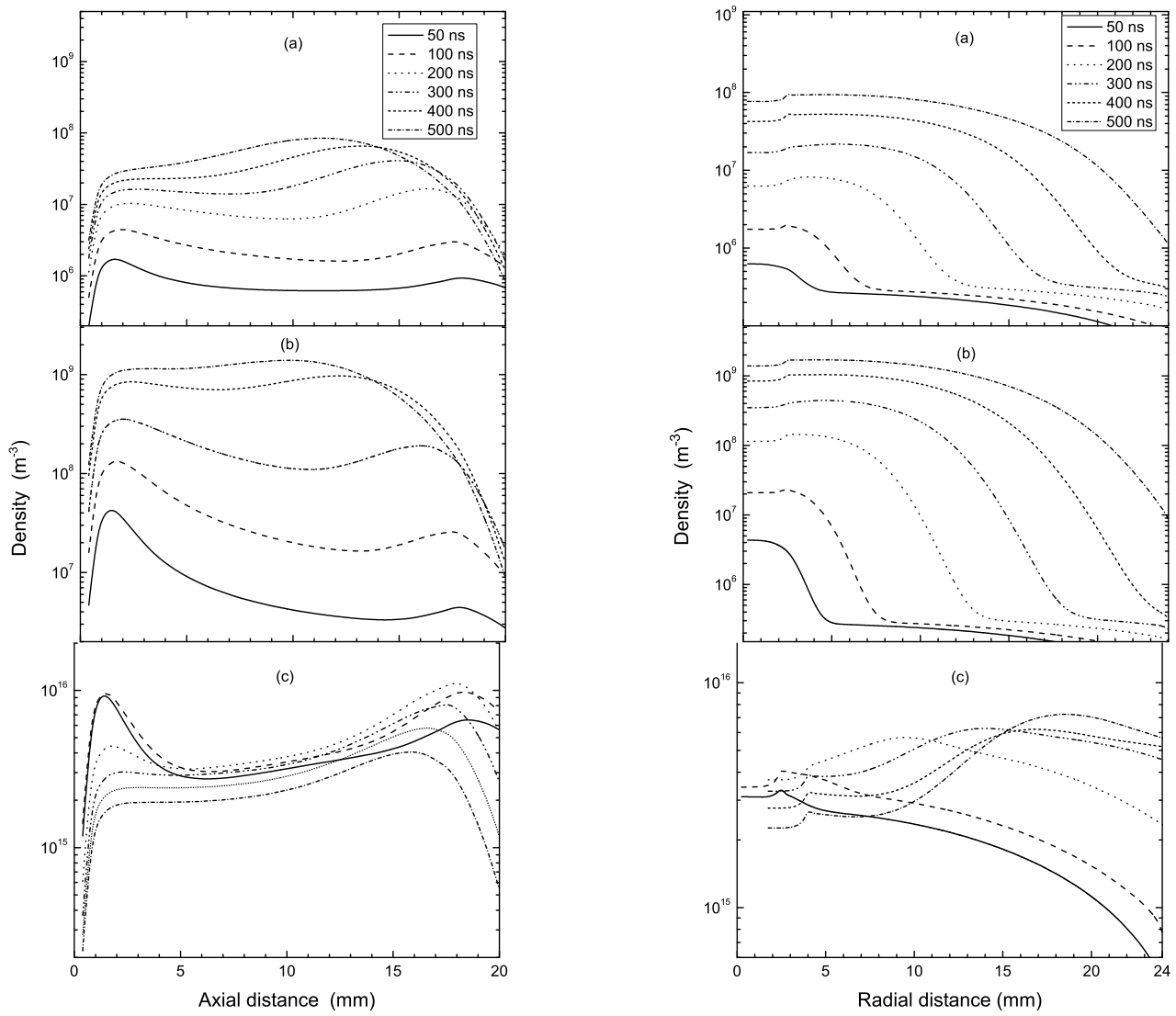

Figure 3. Evolution of the density of NO_2 for a negative point discharge for three values of the reduced electric field, such as (a): 100 Td, (b): 200 Td and (c): 300 Td and for different times between 50 and 500 ns. At left axial evolution of NO_2; At right radial evolution of NO_2.

In Fig. 3(c) shows a very clear depopulation on the axis gradually over time and becomes very important from $t \simeq 300$ ns. Indeed, this decay passes from $\sim 4\times10^{19}$ m^{-3} at $t = 50$ ns at the value $\sim 7\times10^{19}$ m^{-3} at $t = 500$ ns. This variation in density causes a blast wave to form at 3 mm from the axis and reach its maximum at 16 mm from the axis. This depopulation on our axis information on the reduction of nitrogen dioxide, whereas for 100 and 200 Td we had a production of this species.

III.3. Evolution of the density of N

In all the results presented previously in Figs. 2-3, we have presented as a function of evolution of the axial and radial density as a function of the inter-electrode space. In Figs. 4-5 we have represented the evolution of the density of nitrogen N for the three reduced electric fields as a function of the time, calculated for three different positions in inter-electrode space 6 mm, 12 mm and 18 mm. To better understand the evolution of nitrogen monoxide NO, because this last one is bound to nitrogen by reactions:

$$N + 2O \rightarrow NO + O$$

$$N + O + O_2 \rightarrow NO + O_2$$

$$N + O + N_2 \rightarrow NO + N_2$$

We observe, in the beginning from 50 ns to ~ 310 ns, a little rise of the density followed by a significant reduction especially for three values of the reduced electric fild. We note also that the N generation decreases with the increase of thereduced electric field. It is clear that the most significant differences the three position between in the vicinity of the point the heating starts to increase significantly.

III.4. Evolution of the density of O

We have shown in Fig. 6-7 our results for the evolution of the oxygen atom O for the three reduced electric fields as a

function of the time, shown for three selected positions: r = 6 mm, r = 12 mm and r = 18 mm. This radical also plays a role important in the conversion of nitrogen monoxide NO. It can be seen from Figs. 6-7 that the evolution, firstly depends on the inter-electrode space and secondly on the reduced electric field applied to the system. Indeed, heating is different for different chap selected.

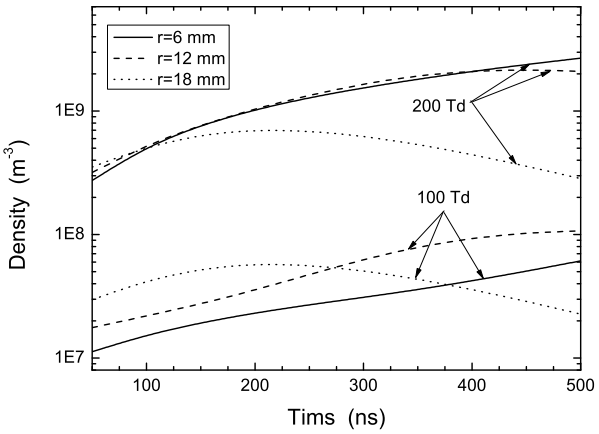

Figure 4. Evolution of the density of N for a negative point (with a 20 mm inter-electrode gap) discharge for two of the reduced electric field 100 Td and 200 Td, as a function of the time, shown for three selected positions: r = 6 mm, r = 12 mm and r = 18 mm.

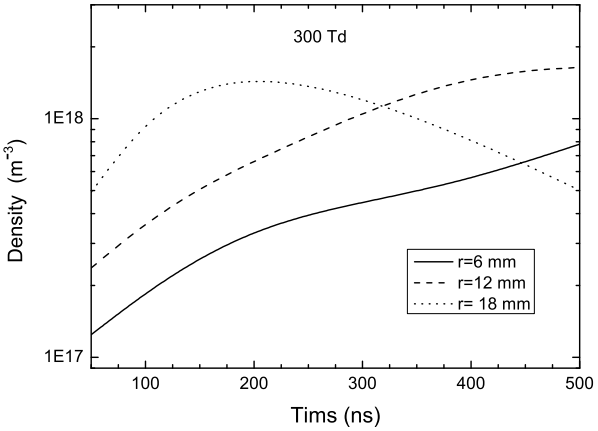

Figure 5. The same an in Fig. 4, but for other reduced electric field 300 Td.

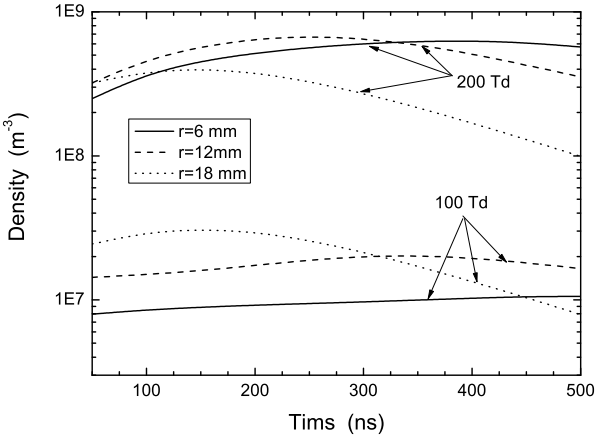

Figure 6. Evolution of the density of O for a negative point (with a 20 mm inter-electrode gap) discharge for two of the reduced electric field 100 Td and 200 Td, as a function of the time, shown for three selected positions: r = 6 mm, r = 12 mm and r = 18 mm.

From the results in Fig. 7 (i.e at 300 Td) it is clear that inclusion of the reduced electric field component can change considerably the density in the low-time range $t \simeq 50 - 200$ ns. At this range, for example, at r= 18 mm the evolution of density increases and reaches a maximum $\sim 5.52 \times 10^{17}$ m^{-3}, but it affects the reduced electric field of the density relatively moderately for $t \simeq 325$ ns. Now when r = 6 mm and 12 mm et $t \geq 330$ it increases rapidly the density, because of the heat flux which rise around the point region, the transfer of energy to neutral in our plasma is not spontaneous.

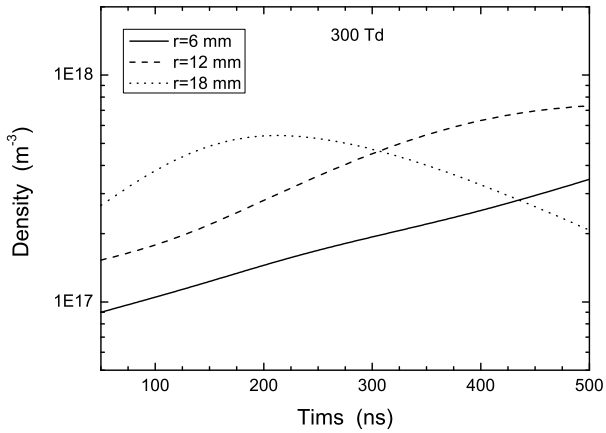

Figure 7. The same an in Fig. 6, but for other reduced electric field 300 Td.

IV. CONCLUSIONS

In this paper we have shown through a detailed analysis, the influence of energy transfer between the plasma (reduced electric field) and the neutral gas. This influence is observed on the NO and NO_2 species. The study is conducted for three values of the field reduced electric (100, 200 and 300 Td). Overall, the change in density caused by the diffusive movements of neutral particles, changes the spatial distribution of density.

The implemented equations are discretized by using a finite control volume with the approximation of a centred difference at the frontiers and solved by the F.C.T algorithm which allowed us to numerically simulate the spatio-temporal evolution of the density of two nitrogen oxides which are nitrogen monoxide NO and nitrogen dioxide NO_2 as well as the radicals N and O which are responsible for the creation of these two nitrogen oxides. The chosen gas mixture is a mixture of four species $N_2/O_2/H_2O/CO_2$ whose proportions are respectively 74 %, 10 %, 8 % and 8 %.

We can say that the ionized gas/neutral gas energy transfer, which we modeled by the reduced electric field, significantly influences the conversion of nitrogen oxides.

ACKNOWLEDGEMENTS

Dr A K FEROUANI gratefully acknowledges support from S.R.D.F.H.U, Algerian Ministry of Higher Education and Research (PRFU: B00L02UN130120190002).

Table 1. The main plasma reactions to generate the main radical to remove nitrogene oxides and their rate constants (in cm^3 $molecule^{-1}$ s^{-1}. $x[y]$ denotes $x \times 10^y$.

	Reaction	Rate Constants	Ref		Reaction	Rate Constants	Ref
R_1	$e^- + O_2 \rightarrow O + O + e^-$	15.0[-9]	[1]	R_{38}	$N + NO_2 \rightarrow N_2O + O$	0.15[-12]	[18]
R_2	$e^- + N_2 \rightarrow N + N + e^-$	2.00[-11]	[1]	R_{39}	$N + NO_2 \rightarrow 2NO$	0.15[-12]	[18]
R_3	$e^- + H_2O \rightarrow OH + H + e^-$	3.35[-10]	[1]	R_{40}	$N + N_2O \rightarrow N_2 + NO$	0.22[-1]	[18]
R_4	$e^- + CO_2 \rightarrow CO + O + e^-$	8.70[-11]	[1]	R_{41}	$N + O \rightarrow N + O$	0.07[-12]	[18]
R_5	$e^- + CO_2 \rightarrow CO + O^-$	3.60[-13]	[26]	R_{42}	$N + O_2 \rightarrow NO + O$	5.20[-12]	[26]
R_6	$N_2 + O_2 \rightarrow 2N + O_2$	0.11[-1]	[18]	R_{43}	$O + N_2 \rightarrow NO + N$	0.10[-5]	[18]
R_7	$N_2 + NO \rightarrow 2N + NO$	0.11[-1]	[18]	R_{44}	$O + O_2 + N_2 \rightarrow O_3 + N_2$	6.20[-34]	[26]
R_8	$N_2 + O \rightarrow 2N + O$	0.49[-1]	[18]	R_{45}	$O + 2O_2 \rightarrow O_3 + O_2$	0.30[-27]	[26]
R_9	$N_2 + N \rightarrow 3N$	0.49[-1]	[18]	R_{46}	$O + O_3 \rightarrow 2O_2$	0.80[-11]	[18]
R_{10}	$2N_2 \rightarrow 2N + N_2$	0.11[-1]	[18]	R_{47}	$O + N + O_2 \rightarrow NO + O_2$	$1.76[-31] \times T^{0.5}$	[27]
R_{11}	$O_2 + N_2 \rightarrow 2O + N_2$	0.33[-2]	[18]	R_{48}	$O + N + N_2 \rightarrow NO + N_2$	$1.76[-31] \times T^{0.5}$	[27]
R_{12}	$O_2 + NO \rightarrow 2O + NO$	0.33[-2]	[18]	R_{49}	$O + NO + O_2 \rightarrow NO_2 + O_2$	0.17[-27]	[18]
R_{13}	$O_2 + N \rightarrow 2O + N$	0.16[-1]	[18]	R_{50}	$O + NO + N_2 \rightarrow NO_2 + N_2$	0.17[-27]	[18]
R_{14}	$O_2 + O \rightarrow 3O$	0.16[-1]	[18]	R_{51}	$O + NO_2 \rightarrow NO + O_2$	0.52[-11]	[18]
R_{15}	$2O_2 \rightarrow 2O + O_2$	0.33[-2]	[18]	R_{52}	$O + NO_2 + O_2 \rightarrow NO_3 + O_2$	0.21[-26]	[18]
R_{16}	$N + O_2 \rightarrow NO + O$	8.90[-17]	[26]	R_{53}	$O + NO_2 + N_2 \rightarrow NO_3 + N_2$	0.21[-26]	[18]
R_{17}	$N + NO_2 \rightarrow N_2 + O + O$	0.91[-12]	[18]	R_{54}	$O + NO_3 \rightarrow O_2 + NO_2$	0.17[-10]	[26]
R_{18}	$N + NO_2 \rightarrow 2N_2$	0.23[-11]	[27]	R_{55}	$O + O + NO \rightarrow O_2 + NO$	0.19[-29]	[18]
R_{19}	$N + NO \rightarrow N_2 + O$	$1.05[-12] \times T^{0.5}$	[27]	R_{56}	$O + O + N \rightarrow O_2 + N$	0.95[-29]	[18]
R_{20}	$N + NO_2 \rightarrow N_2 + O_2$	0.70[-12]	[27]	R_{57}	$O + O + O \rightarrow O_2 + O$	0.95[-29]	[18]
R_{21}	$N + 2O \rightarrow NO + O$	0.66[-30]	[18]	R_{58}	$O + HNO_3 \rightarrow NO_3 + OH$	3.00[-15]	[26]
R_{22}	$N + O + NO \rightarrow NO + NO$	0.66[-30]	[18]	R_{59}	$2O + N_2 \rightarrow O_2 + N_2$	0.27[-30]	[26]
R_{23}	$N + NO_2 \rightarrow N_2 + O_2$	7.00[-13]	[27]	R_{60}	$2O + O_2 \rightarrow 2O_2$	0.27[-30]	[18]
R_{24}	$N + NO_2 \rightarrow N_2O + O$	0.24[-11]	[18]	R_{61}	$O + N_2 \rightarrow O + N_2$	0.18[-10]	[18]
R_{25}	$N + NO_2 \rightarrow 2NO$	0.60[-11]	[18]	R_{62}	$O + 2N_2 \rightarrow N_2O + N_2$	0.10[-34]	[18]
R_{26}	$N + CO_2 \rightarrow NO + CO$	$3.20[-13].\exp^{\frac{-1711}{T}}$	[18]	R_{63}	$O + N_2 + O_2 \rightarrow N_2O + O_2$	0.10[-34]	[18]
R_{27}	$2N + O_2 \rightarrow N_2 + O_2$	0.83[-33]	[18]	R_{64}	$O + O_2 \rightarrow O + O_2$	0.50[-11]	[18]
R_{28}	$2N + N_2 \rightarrow 2N_2$	0.83[-33]	[18]	R_{65}	$O + O_3 \rightarrow 2O + O_2$	0.12[-9]	[18]
R_{29}	$2N + NO \rightarrow N_2 + NO$	0.64[-25]	[18]	R_{66}	$O + O_3 \rightarrow 2O_2$	0.12[-9]	[18]
R_{30}	$2N + O \rightarrow N_2 + O$	0.27[-24]	[18]	R_{67}	$O + N_2O \rightarrow 2NO$	0.67[-10]	[18]
R_{31}	$3N \rightarrow N_2 + N$	0.27[-24]	[18]	R_{68}	$O + N_2O \rightarrow NO + O_2$	0.49[-10]	[18]
R_{32}	$2N + O \rightarrow NO + N$	0.66[-30]	[18]	R_{69}	$O + N_2O \rightarrow N_2 + O_2$	0.44[-10]	[18]
R_{33}	$OH + HNO_3 \rightarrow NO_3 + H_2O$	1.30[-13]	[26]	R_{70}	$O + NO_2 \rightarrow NO + O_2$	0.14[-9]	[18]
R_{34}	$OH + NO_2 \rightarrow HNO_3$	13.5[-11]	[18]	R_{71}	$O + NO \rightarrow N + O_2$	0.85[-10]	[18]
R_{35}	$N + N_2 \rightarrow N + N_2$	0.17[-13]	[18]	R_{72}	$NO + O \rightarrow O_2 + N$	0.13[-36]	[18]
R_{36}	$N + O_2 \rightarrow NO + O$	0.35[-12]	[18]	R_{73}	$O_3 + N \rightarrow NO + O_2$	0.10[-15]	[18]
R_{37}	$N + NO \rightarrow N_2 + O$	0.07[-10]	[18]	R_{74}	$O_3 + NO \rightarrow NO_2 + O_2$	0.18[-11]	[18]

V. REFERENCES

[1] K. Hatakeyama, S. Tanabe and Y. Hayashi et *al.*, J. Adv. Sci., **13**, 459 (2001).

[2] R. M. Balogh, I. Ionel and D. Stepan et *al.*, Termotehnica **2**, 32 (2011).

[3] J. S. Chang, Plasma Sources Sci. Technol. **17**, 045004 (2008)

[4] A. M. Pointu, A. Ricard and E. Odic et *al.*, Plasma Process. Polym. **5**, 559 (2008).

[5] M. Laroussi, A. Fridman and P. Favia et *al.*, Plasma Process. Polym. **7**, 193 (2010).

[6] A. K. Ferouani, M. Lemerini, L. Merad et *al.*, Plasma Sci. Technol. **17**, 469 (2015).

[7] J. Chen and J. H. Davidson, Plasma Chem. Plasma Process. **22**, 495 (2002).

[8] G. Fridman, G. Friedman, A., Shekhter et *al.*, Plasma Process. Polym. **5**, 503 (2008).

[9] M. Maulois, M. Ribière, and O. Eichwald et *al.*, Phys. Plasmas **23**, 043501 (2016).

[10] M. Bouzar, A. K. Ferouani and M. Lemerini et *al.*, High Temp. Mater. Process. **21**, 225 (2017).

[11] A. Mraihi, N. Merbahi and M. Yousfi et *al.*, Plasma Sources Sci. Technol. **20**, 065002 (2011).

[12] A. Abahazem, N. Merbahi, O. Ducasse et *al.*, IEEE Trans. Plasma Sci. **36**, 924 (2008).

[13] A. Abahazem, H. Guedah and N. Merbahi et *al.*, Mater. Today: Proceedings **2**, 4694 (2015).

[14] I. Orlandini and U. Riedel, Combust. Theory Model. **5**, 447 (2001).

[15] A. Haddouche amd M. Lemerini, Plasma Sci. Technol. **17**, 589 (2015).

[16] A. K. Ferouani, M. Lemerini and S. Belhour, Plasma Sci. Technol. **12**, 208 (2010).

[17] I. Orlandini and U. Riedel, J. Phys. D: Appl. Phys. **33**, 2467 (2000).

[18] O. Eichwald, N. A. Guntoro and M. Yousfi et *al.*, J. Phys. D: Appl. Phys. **35**, 439 (2002).

[19] A. Haddouche, " Etude électrique et physico chimique de la décharge couronne en vue de son application dans la réactivité des mélanges gazeux correspondants aux

effluents industriels". Tesis de doctorado, University Tlemcen-Algeria, 2015.
[20] J. P. Boris and D. L. Book, J. Comput. Phys. **11**, 38 (1973).
[21] J. P. Boris, F. F. Grinstein and E. S. Oran et *al.*, Fluid Dyn. Res. **10**, 199 (1992).
[22] D. Kuzmin, R. Löhner and S. Turek, Flux-corrected transport: principles, algorithms, and applications, (Springer Science, Business Media, 2012).
[23] R. Atkinson, D. L. Baulch and R. A. Cox et *al.*, J. Phys. Chem. Ref. Data **26**, 521 (1997).
[24] M. Yousfi, O.Eichwald and N. Merbahi et *al.*, Plasma Sources Sci. Technol. **21**, 045003 (2012).
[25] M. Bafoil, A. Jemmat and Y. Martinez et *al.*, PloS one **13**, 1 (2018).
[26] O. Eichwald, M. Yousfi, A. Hennad et *al.*, J. Appl. Phys. **82**, 4781 (1997).
[27] I. A. Kossyi, A. YuKostinsky, A. A. Matveyev et *al.*, Plasma Sources Sci. Technol. **1** 207 (1992).

DESIGN AND EVALUATION OF PIEZOELECTRIC SENSORS FOR THE MEASUREMENT OF BLOOD FLOW IN CORONARY IMPLANTS BY THE ULTRASONIC TRANSIT TIME METHOD

DISEÑO Y EVALUACIÓN DE SENSORES PIEZOELÉCTRICOS PARA LA MEDICIÓN DE FLUJO SANGUÍNEO EN IMPLANTES CORONARIOS POR EL MÉTODO DE TIEMPO DE TRÁNSITO ULTRASÓNICO

E. Carrillo[a†], A. Jiménez[a], R. López[a], J. J. Portelles[b], L. F. Desdín[c]

a) Instituto de Cibernética Matemática y Física (ICIMAF), CITMA, La Habana, Cuba; ernesto@icimaf.cu†
b) Facultad de Física, Universidad de la Habana, La Habana, Cuba.
c) Centro de Aplicaciones Tecnológicas y Desarrollo Nuclear, CITMA, La Habana, Cuba.
† corresponding author

Recibido 19/5/2020; Aceptado 00/00/2020

Nowadays, there is a small number of biomedical systems to verify the quality of coronary transplants. They are especially expensive and their closed architecture makes them impossible to reproduce. Based on the method known as Ultrasonic Transit Time Flow Measurement (TTFM), ultrasonic piezoelectric sensors useful to evaluate the quality of coronary implants during cardiovascular surgery were designed. They show repeatability in their parameters; produce a homogeneous acoustic field, an adequate acoustic intensity in their emission and allow a flow reading with an uncertainty below 5 ml/min. It is shown that the plastic known as Rexolite offers less acoustic attenuation and better mechanical coupling for the sensors compared to epoxy resin, attaining a better performance. These sensors operate together with an electronic module governed by a reconfigurable FPGA type platform. Finally, it is shown that time intervals in the order of tens of picoseconds can be detected by our sensor (i.e., flow rates smaller than 5 ml/min).

Internacionalmente existe un número escaso de sistemas biomédicos para verificar la calidad de los trasplantes coronarios, con elevados precios y una arquitectura muy cerrada, que imposibilita su reproducción. Basado en el método conocido como Tiempo de Transito Ultrasónico (TTFM), empleado para evaluar la calidad de los implantes coronarios durante la cirugía cardiovascular, se diseñaron y se desarrollaron sensores ultrasónicos piezoeléctricos TTFM que poseen una alta repetitividad en sus parámetros, producen un campo acústico homogéneo, una adecuada intensidad acústica en su emisión y poseen una incertidumbre de lectura inferior a 5 ml/min. Se concluyó que el material conocido como Rexolite brinda menor atenuación acústica y mejor acoplamiento mecánico respecto a la resina epóxica para el uso en sensores, lo que se traduce en una mejor prestación. Estos sensores operan conjuntamente con un módulo electrónico gobernado mediante una plataforma reconfigurable del tipo FPGA, permitiendo detectar intervalos de tiempo en el orden de las decenas de picosegundo (lo que equivale a flujos por debajo de 5 ml/min).

PACS: Medical uses of ultrasound (usos médicos del ultrasonido), 87.50.yt; piezoelectric devices (dispositivos piezoeléctricos), 85.50.-n; flow in cardiovascular systems (flujo en sistemas cardiovasculares), 47.63.Cb

I. INTRODUCTION

Smoking, obesity and a sedentary lifestyle are some of the factors that accelerate the occlusion processes in human coronary arteries, which constitutes one of the main causes of death worldwide [1]. When these occlusions become extreme, one of the most effective medical treatments to be applied is the implementation of coronary bypass implants, consisting in the placement of a grafted blood vessel parallel to the obstructed artery. The procedure substantially increases the life expectancy of individuals with high risk of heart attack.

One essential step in the coronary bypass surgery is to determine the value of the volumetric blood flow through the grafted vessel, which is an essential index to assess the quality of the implant: knowing it immediately indicates the effectiveness of the surgical procedure, and the eventual need to take correcting actions in order to avoid complications [2].

In spite of the good level of Cuban cardiovascular surgery, up to now surgeons have confirmed blood circulation by just applying tactile pressure on the grafted vessel segment. It constitutes a rough, unreliable clinical procedure that strongly depends on the surgeon's experience. Obviously, it does not allow estimating the volume of blood per unit time circulating through the vessel [3, 4].

Internationally, there is a small number of biomedical systems to verify the quality of coronary transplants, and their commercialization is monopolized by an U.S. company (MediStim). A typical system consists of a sensor and the measurement module. Each sensor can only be used around 10 times, and one surgery involves more than one of them. Eventually, the sensor can be sent to the company to be refurbished, which is an expensive process only affordable by developed countries.

Different techniques have been used In medical applications: electromagnetic flow meters [5], intraoperative arteriography

[6] and infrared ray angiography [7], constituting very invasive methods. The ultrasonic waves sensing method minimally affects the internal structure of the human body. Being a non-ionizing radiation, ultrasound is harmless to the internal structure of the body's cells. So, it has been intensively used in medicine, and experts agree that it will be used in the foreseeable future [8].

Ultrasound is used in two basic ways to measure blood flow: the Doppler technique and the Transit Time Flow Measurement Method (TTFM) [9]. The Doppler technique is used to detect obstructions and the assessment of the veins and arteries. The TTFM method allows quantifying the volumetric flow that circulates through a blood vessel in ml/min. The quality of coronary transplants is verified using both techniques.

In this article, which can be seen as a continuation of our previous work [10], the design and development of piezoelectric sensors, made of two different materials, is presented. Their design characteristics and measurement results are explained. The electrical signals produced by the sensors are conditioned and processed in an analog module, which allows measuring time intervals of tens of picoseconds, yielding a flow measurement uncertainty below 5 ml/min. Measurements of phase, resonance, anti-resonance, voltage and acoustic field are performed on the sensors in order to assess their performance within our system. The measurement moduli and the sensors constitute an inexpensive system, compared to similar equipment made by foreign firms, such as MediStim [11].

II. METHODS

II.1. Transit Time Flow Measurement (TTFM)

The ultrasonic Transit Time Method is based on the time the ultrasonic signal takes to propagate through a liquid (blood) travelling through a conduit (blood vessel), in favor or against the flow. The ultrasonic signal travelling against the flow, takes longer than the ultrasonic signal travelling in the same direction of the flow, assuming that the same route is followed in both cases.

The TTFM method is very accurate, even for the measurement of very small flows [11]. When an ultrasonic pulse is transmitted from a piezoelectric element (transmitter), it travels through the liquid medium and is received by another piezoelectric element (receiver). Then, the transmitter element becomes a receiver and the receiver element becomes a transmitter, repeating the cycle. Let us call td, the time ultrasound travels from one sensor to another, in favor of the flow, and ti the time it travels against the flow. The difference $\Delta t = (t_i – t_d)$ depends only on the volumetric flow rate and does not depend on the propagation speed of the ultrasound in the medium, as illustrated in Fig. 1 [10].

II.2. Integrated System

Fig. 2 shows the basic block diagram of the blood flow measurement system in coronary vessels, whose description and first results is the objective of this work. It is composed by the following parts [12]:

1. Ultrasonic bi-ceramic sensor.
2. Analog TTFM detection module.
3. Digital module for control and treatment.
4. Personal computer.

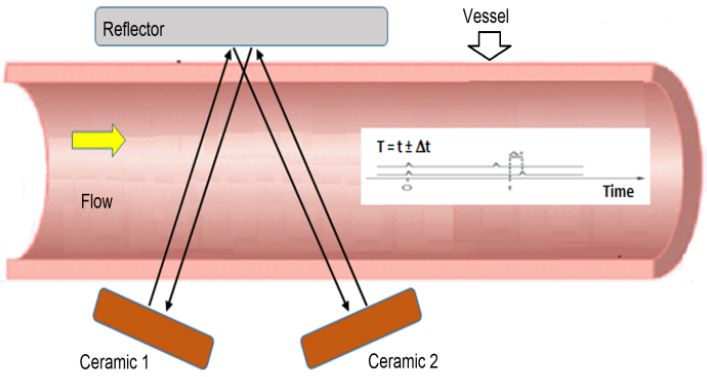

Figure 1. Scatter diagram of the variables voltage vs. flow in the phantom, Transit Time sensor measuring a blood vessel. (Adapted from [10]).

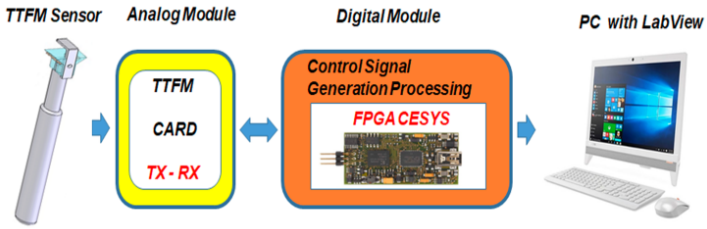

Figure 2. Block diagram of the TTFM system.

II.3. Analog module, digital module and A/D converter

The analog and digital moduli are presented in Fig. 3. They create the basic signals that provide the quantitative measurement of the volumetric blood flow. The process can be described in seven steps:

a. The transmitter (Tx) is excited by two 2 MHz phase-inverted 15-pulse train, with a 3.3 V logic level. At the output, a 10 V (peak to peak) signal is obtained at low output impedance (2 Ω).

b. The Tx exciter signal is channeled alternately to each ceramic element through two analog switches, (SW1 and SW2). The echo signals received in both directions are applied to the receiver input (Rx) [13–15].

c. Control signals 1 and 2 guarantee that while one piezoelectric ceramic emits an ultrasonic pulse, the other receives its reflected pulse, and vice versa.

d. The phase detector compares the received 2 MHz pulse train with a 2 MHz master digital signal, producing at its output a pulse train with the same phase as the received train, but with a variable mark-to-space ratio, depending on the magnitude of the flow.

e. The output of the phase detector is connected to a precision integrator, obtaining a voltage level proportional to the pulse duration [16]. This variable pulse train is sent to a precision integrator in the analog module, which converts phase (time) variations into voltage variations, with an uncertainty of 2 μV, which is applied to an A/D converter. The accuracy of the measured time values is determined by the high resolution, 24-bit A/D converter used in the system (20-bit reliable). In addition, each flow measurement is made every 1 ms, therefore, a large data averaging is achieved, warranting a very reliable final reading.

f. As a result, a serial 24-bit pulse train obtained from the A/D converter, is sent to a reconfigurable FPGA platform for further digital processing [17].

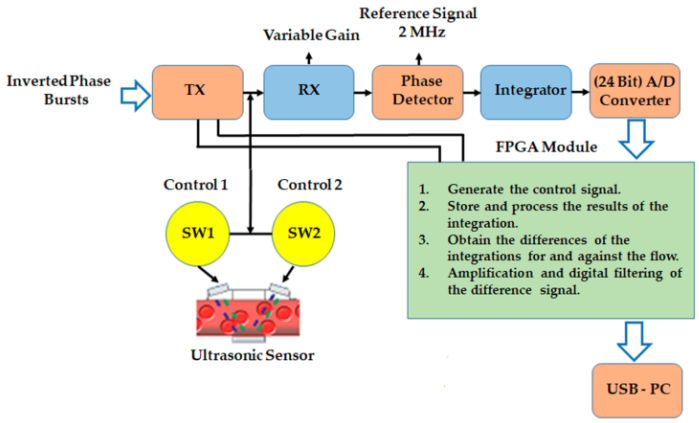

Figure 3. Block diagram of analog and digital moduli.

II.4. Ultrasonic TTFM sensor

The sensor is composed by two 2 MHz thickness mode rectangular piezoelectric ceramic elements, forming an angle. Both elements behave as transmitters and receivers alternately, i.e., if one element transmits, the other receives and vice versa. The measuring duct (vessel) is in the space between the ceramic elements and a metallic reflector. Then, the ultrasound crosses the duct four times per measurement. The ultrasonic sensor is composed of different parts, as shown in Fig. 4.

II.5. Design of TTFM sensors (determination of dimensions depending on the materials selection)

The dimensions of the sensors were calculated according to the used material, taking into account longitudinal waves, since the transverse waves in liquids are attenuated very quickly. Two alternative models are analyzed (model A and B). The distance between the coupling wedge and the reflector was selected as 3 mm, its weight and easy handling are considered too.

Another important aspect in the design is the ability to withstand the sterilization process (360 °C), which allows a larger reuse cycle that exceeds 10 measurements.

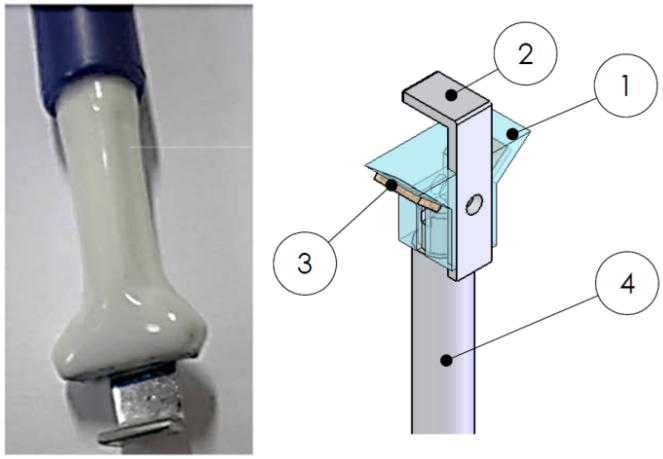

Figure 4. Structure of the TTFM sensor. Left panel: photograph of the real sensor. Right panel: sketch of the sensor; (1) wedge containing ceramic elements, (2) stainless steel reflector element, (3) two rectangular ceramic elements of 30 mm^2 area and (4) clamping rod.

Model A

In this model, a Rexolite wedge is proposed with an isosceles trapezoidal shape, where ceramics are glued on the two non-parallel sides of the wedge, to determine the direction of the emitted (received) ultrasonic beam from (to) the wedge. These beams impact in the center of the reflector element (P blue rectangle), which reflects them toward the wedge again (toward the "receiving" ceramic).

To achieve this, the refractions occurring inside the wedge are taken into account (see Fig. 5). To calculate the dimensions of the wedge, the following data was considered: h_1 (wedge height), h (distance from the wedge to the reflector), d (piezoelectric ceramic size), θ (wedge angle), V_a (longitudinal wave speed in water) and V_c (longitudinal wave speed in the wedge material).

Equations for design:

$$\text{Wavelength in ceramics (mm)} = \frac{\text{Wave speed in ceramic (km/s)}}{\text{Frequency (MHz)}}, \quad (1)$$

$$\text{Ceramics thikness} = \frac{1}{2}\text{Wavelength in ceramics}, \quad (2)$$

$$\text{Thikness (mm)} \times \text{Frequency (MHz)} = \frac{1}{2}\text{Wave speed (km/s)}. \quad (3)$$

Incidence angle of ultrasound in water (Fig. 5):

$$a = \arcsin\left(\frac{V_a}{V_c}\sin\theta\right), \quad (4)$$

$$L = 2(a + \frac{P}{2} + c), \quad (5)$$

$$a = h \tan\alpha \cos^1\theta, \tag{6}$$

$$P = \frac{d}{\cos\theta}, \tag{7}$$

$$c = \frac{e}{\cos\theta}, \tag{8}$$

$$e = d - \frac{h_1}{\sin\theta}. \tag{9}$$

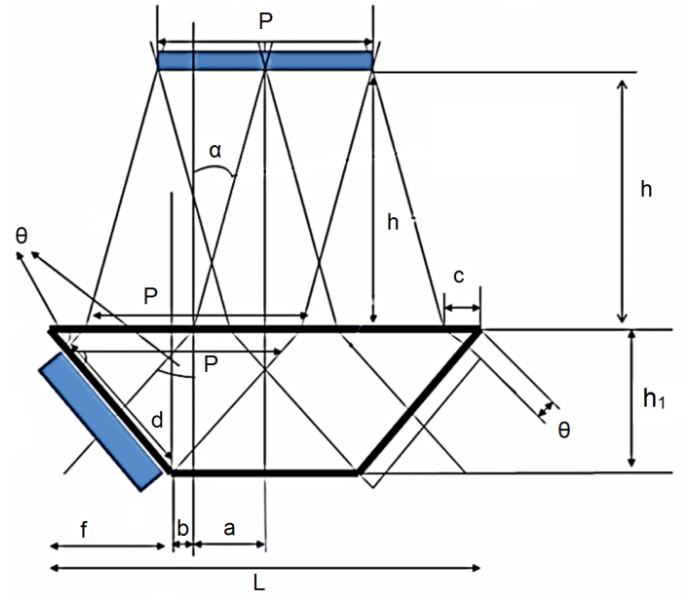

Figure 5. Scheme of the wedge's dimensions of TTFM sensors (Model A, Rexolite material). The reflector is represented as a blue rectangle on top, and only the left piezoelectric ceramic is shown, also represented as a blue rectangle.

Upper wedge length (Fig. 5):

$$L = 2h\tan\alpha + \frac{d}{2\cos\theta} + \frac{d - h_1/\sin\theta}{\cos\theta}, \tag{10}$$

$$b = \frac{L}{2} - a - f, \tag{11}$$

$$f = \frac{h_1}{\tan\theta}. \tag{12}$$

Lower wedge length (Fig. 5):

$$2(a+b) = L - \frac{2h_1}{\tan\theta}. \tag{13}$$

With equations (1 -13), all wedge dimensions are obtained (according to Fig. 5). The value of h corresponds to a diameter greater than or equal to the characteristic diameter of arteries (of the order of 2-3 cm, depending on blood pressure) [11]. The value of h_1 will be taken according to the width of the wedge's bottom (larger than 6 mm) so that the design of the handle is the same for all sensors. The value of d will be 4.9 mm, with a P size (width of the reflector) capable of reflecting adequately the ultrasonic beam.

Model B

This model has a wedge made with epoxy resin: the ceramics are glued to an acrylic support, and the remaining space is filled with epoxy resin, which forms the wedge (Fig. 6). The calculations for an epoxy resin wedge can be made using the equations below.

Height of the acrylic support (Fig. 6):

$$h_z = h_1 + g\cos\theta + k. \tag{14}$$

Outer length of the acrylic support (Fig. 6):

$$L_z = L + 2j = L + \frac{2g}{\sin\theta}. \tag{15}$$

End-to-end length of the Rexolite wedge (Fig. 6):

$$2i + 2(a+b) = 2g\sin\theta + L - \frac{2h_1}{\tan\theta}. \tag{16}$$

With equations (14 - 16), the geometric calculation can be made, obtaining the dimensions of the acrylic support to be implemented.

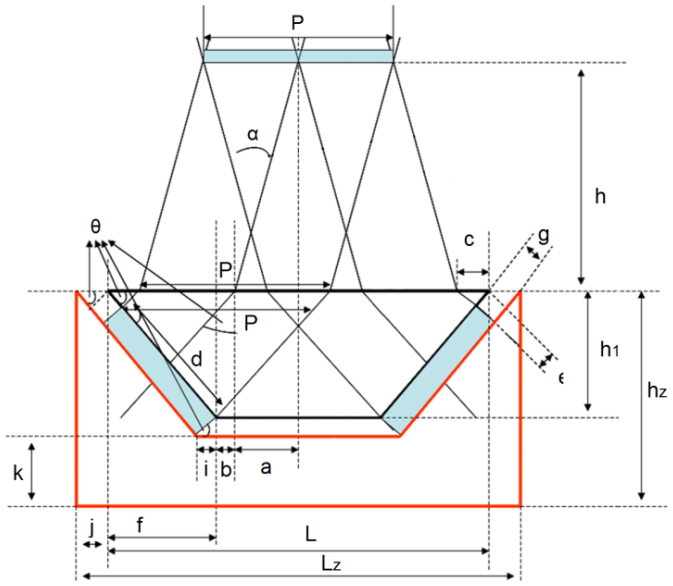

Figure 6. Scheme showing the dimensions of the TTFM sensors (Model B, epoxy resin material). The part indicated by red lines represents the acrylic support mentioned in the text.

Notice that g is the thickness of the piezoelectric ceramic element, and is related to the sensor's working frequency (see equations 1 and 2). h_z is the height of the acrylic support, L_z is the width of the acrylic support and j is the distance between the end of Rexolite wedge and the end of the acrylic support. The value of k is determined by the resistance selected in design, resulting in a value greater than 2 mm.

III. RESULTS FOR TTFM SENSORS (MODELS A AND B)

III.1. Results of TTFM sensors at 2 MHz working frequency

The design of sensors depends on an ultrasonic evaluation using the pulse-echo option, illustrated in Figs. 7 and 8. They show that the voltage amplitude for Rexolite is higher, in average, than that obtained for the epoxy resin (the difference

is as large as three-fold within the time interval from 90-100 μs). It represents a better performance in terms of material quality, with lower acoustic losses and higher sensitivity of the measurement system.

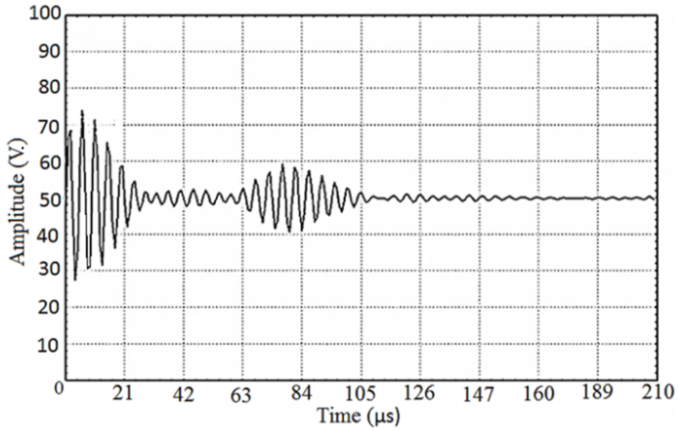

Figure 7. Average response of 3 mm, 2 MHz, epoxy resin TTFM sensors.

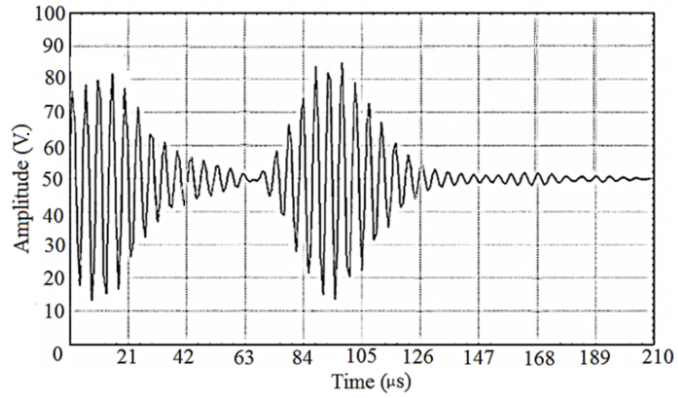

Figure 8. Average response of 3 mm, 2 MHz, Rexolite TTFM sensors.

It is worth noting that synchronization of images in Figs. 7 and 8 are different; because the materials under study have different acoustic properties.

III.2. Behavior of sensor's resonance frequency and phase

The TTFM sensors were designed to work at a frequency of 2 MHz, using two sensors for each model, as accounted in the color code of Figs. 9, 10 and 11. Using the Ultrascope Omicrom Lab. (Bode 100) equipment, the resonance frequency, the phase values and the impedance module (—Z—) of the sensors were measured [18].

For the same resonance frequency (2 MHz), the Rexolite sensors show the highest electromechanical quality, as observed in Fig. 9. They have a lower phase shift compared to those built with epoxy, showing lower electromechanical losses and larger amplitude. Taking into account the elastic properties of Rexolite material, a better acoustic impedance coupling (sensor vs. human tissue) can be achieved and as a consequence, the pulse-transmission signal is improved.

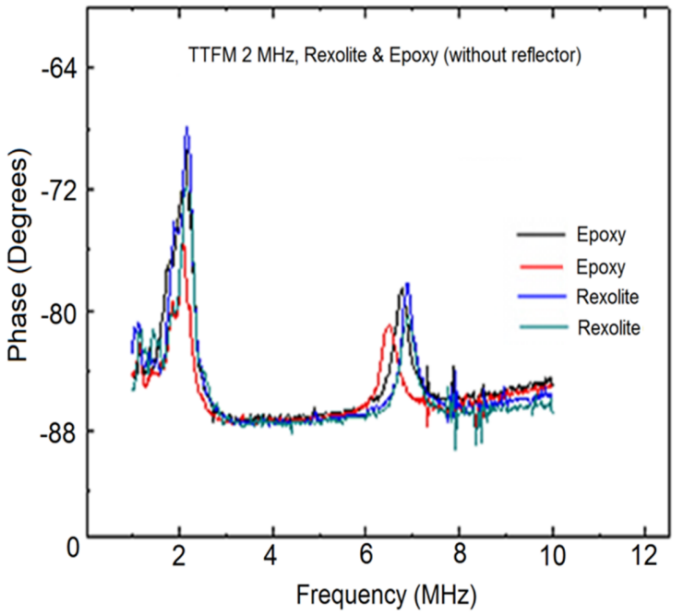

Figure 9. Phase behavior for 2 MHz TTFM sensors (models A and B).

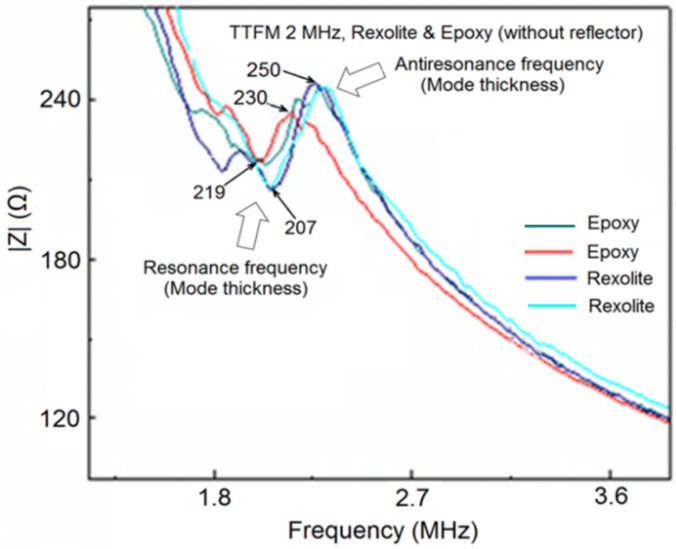

Figure 10. Impedance module behavior of 2 MHz TTFM sensors, (models A and B).

Rexolite has a lower value of serial impedance module at resonance frequency (207 Ω), higher value of parallel impedance module at antiresonance frequency (250 Ω) and lower electromechanical losses than Epoxy, see Fig. 10. Then, from now on, only results for Rexolite sensors will be presented.

III.3. Average response of sensors

The sensors made with Rexolite show higher voltage amplitude with respect to those made of epoxy. However, the transmission pulse response shows a similar behavior for all mounted sensors (model A and B), obtaining an average voltage variation of twice the maximum amplitude in both models.

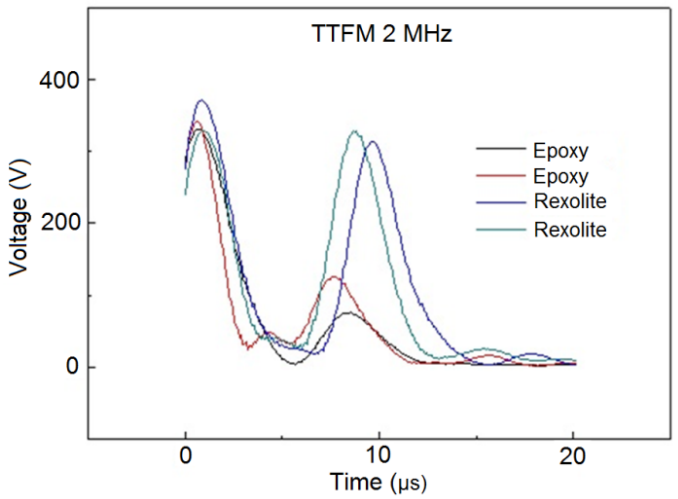

Figure 11. Pulse responses of the two materials used in the sensors (model A and B).

Thus, an acceptable repeatability for the application is obtained, see Fig. 11.

III.4. Results of the acoustic field measurement

The acoustic emissions of the 2 MHz TTFM sensors were evaluated and the radiation patterns were obtained using a calibrated hydrophone, in order to check construction procedure and repeatability. The cutting of the piezoelectric ceramics, the welding of the electrodes and the excitation data for this type of sensors, were taken into account. A 2 MHz 12-pulse train, an excitation voltage of 15 Vpp and a repetition frequency of 2 kHz, were chosen.

When both ceramics are excited at the same time, a maximum acoustic intensity is detected in a region centered around 4 mm in front of the sensor (within the A-B range), placing the hydrophone at the meeting point of both emissions (dot B), which is 1 mm away from the transducer, see Fig. 12.

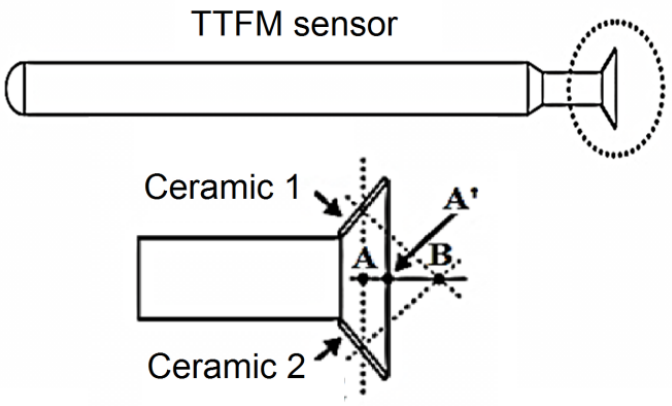

Figure 12. Range A-B of largest acoustic intensity of sensor emission (expected behavior).

The scanning of the space in front of the acoustic field generated by the sensors was done as illustrated in Fig. 13. A scan along the x-axis started at the upper left corner (seen by the hydrophone facing the transducer). When it finished at the right extreme, a new x-scan started at the next y-value. Notice that the XY plane contains the point B (Fig. 12). The inter-planar distance was of 0.1 mm.

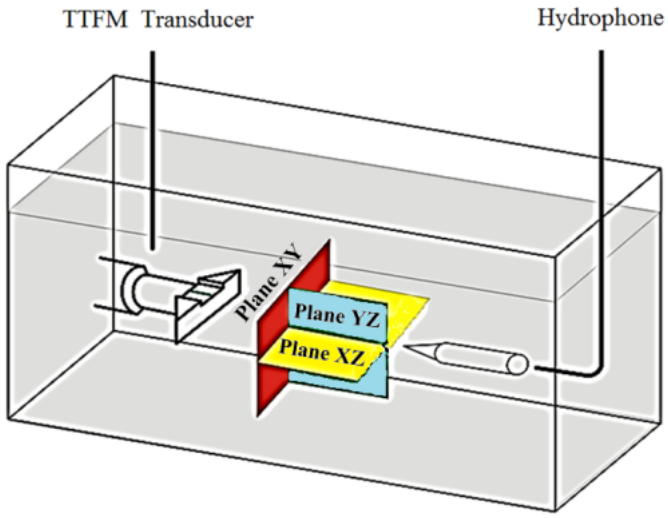

Figure 13. Configuration of the TTFM sensors and the hydrophone, showing the sweeping planes.

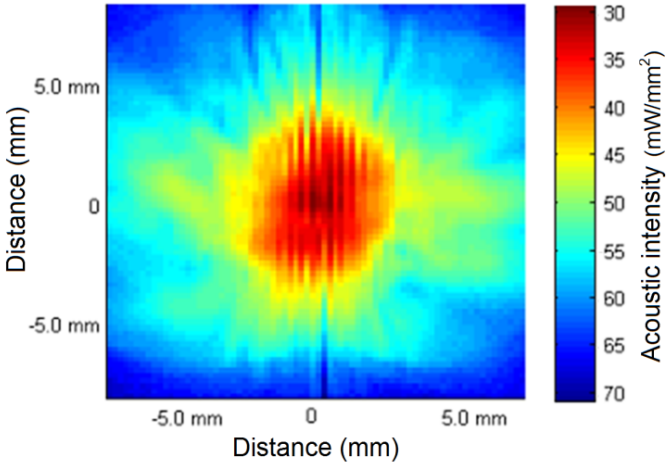

Figure 14. Acoustic intensity map on the X-Y plane for Rexolite ceramics (red plane in Fig. 13).

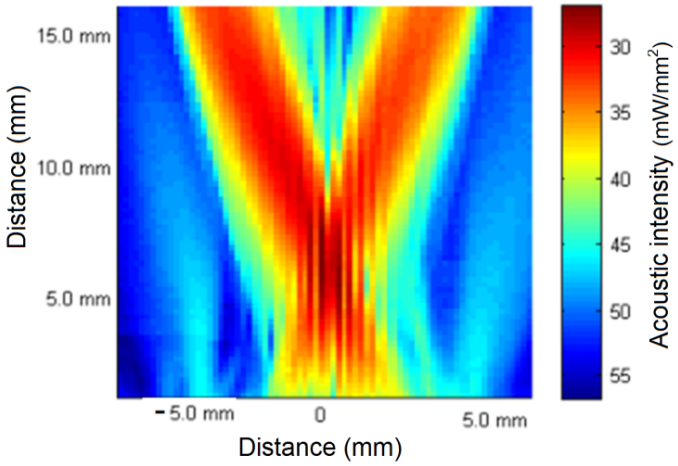

Figure 15. Acoustic intensity map on the XZ plane for Rexoline ceramics (yellow plane in Fig. 13).

From Fig.s 14 and 15, it can be concluded that 2 MHz TTFM sensors work correctly at a distance of 5.8 mm, they have a homogeneous near acoustic field that crosses through the artery to be measured. The crossed emissions of each ceramic are visible, which allows each of them to capture the incident signal coming from the reflector, emitted by both ceramics alternately. That is consistent with the physical principle of the ultrasonic transit time described earlier.

This behavior guarantees the construction and the repeatability in the building process of sensors, which includes equal cuts of the ceramic, equal mechanical supports and equal welding of the electrodes.

III.5. Flow measurement results using a pulsed flow phantom

The final validation of the results is mainly based on the flow measurements, through the use of a constant flow phantom that simulates blood circulation in an artery, see Fig. 16.

Through it, the operation of the sensor and the electronic module can be verified, which depends mainly on the used sensor. The phantom was filled with distilled water at room temperature (25 °C) [19].

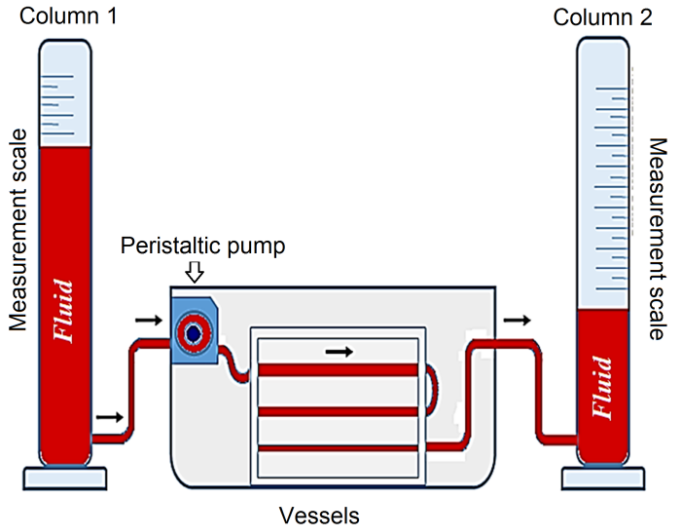

Figure 16. Schematic representation of the phantom able to produce a continuous flow (Peristaltic pump RS codes: 255-9605 and 330-834). The arrows indicate the direction of fluid motion.

Fig. 17 clearly indicates that the flow increases linearly as the voltage of the peristaltic pump increases. Therefore, a simple linear regression model was used to describe the relationship between the two variables. A summary of the results in the regression analysis and its corresponding model is shown in Table 1.

The high value of the Pearson correlation coefficient (R = 0.999) between the voltage and flow variables, means that there is a good correlation between them. On the other hand, the coefficient of determination indicates that 99 % of the flow variation depends mainly on the uncertainty of the applied voltage, interpreted as a good measure of the fitting quality. The standard error indicates that, on average, the dispersion of the observed values with respect to the values represented by the regression line is 1.022 ml/min.

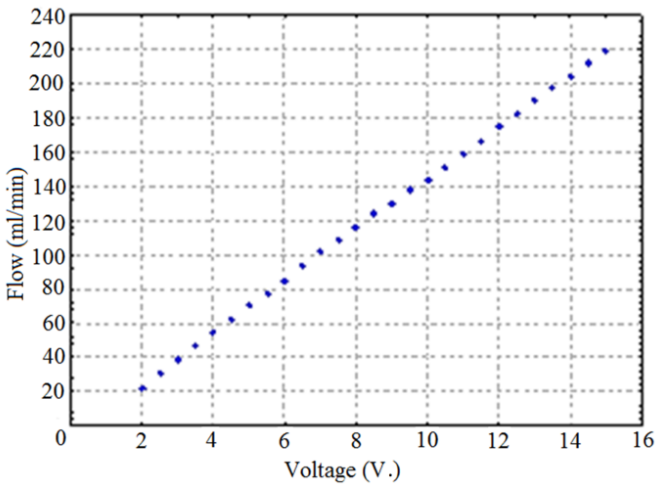

Figure 17. Scatter diagram of the variables voltage vs. flow in the phantom, considering all measurement made.

III.6. Flow measurement results using several sensors.

For the evaluation of the volumetric flow measurement system, three Rexolite 2 MHz ultrasonic sensors were used, named as: sensor 1, sensor 2 and sensor 3.

Table 1. Summary of regression analysis results (Fig. 17)

Model	Coefficients		t	p	Uncert. Coefficient 95 %	
	B	Stand. Error		Value	Lower Limit	Upper Limit
Intercept	-5.515	0.519	-10.634	0.000	-6.584	-4.447
Voltage (V)	15.018	0.055	270.734	0.000	14.904	15.132
R = 0.999, R^2 = 0.999, Standard Error of Estimation = 1.022 V.						

Voltage measurements were made according to the flow values used in the phantom calibration [20,21].

The voltage measured at the analog module output, for each sensor, as a function of flow values controlled by the pump, is directly proportional to the volumetric flow. This voltage was measured at the A/D's output, using a logic analyzer with a resolution of 20 mV, so two sets of measurements were obtained for each sensor.

To study the relationship between the variable flow (ml/min) and the variable voltage (V.), a data dispersion diagram was constructed, in which each sensor is identified by its name, see Fig. 18.

These sensors behave slightly differently, thus obtaining three data sets, measured under the same conditions. The behaviors obtained depend on the sensor construction process and the inherent differences in each ceramic.

The values of blood flow measurements, validated in the medical practice are between 20-80 ml/min [1]. Therefore, a 95 % linear regression model was performed for each sensor; considering that range of values, see Figs. 19, 20 and 21.

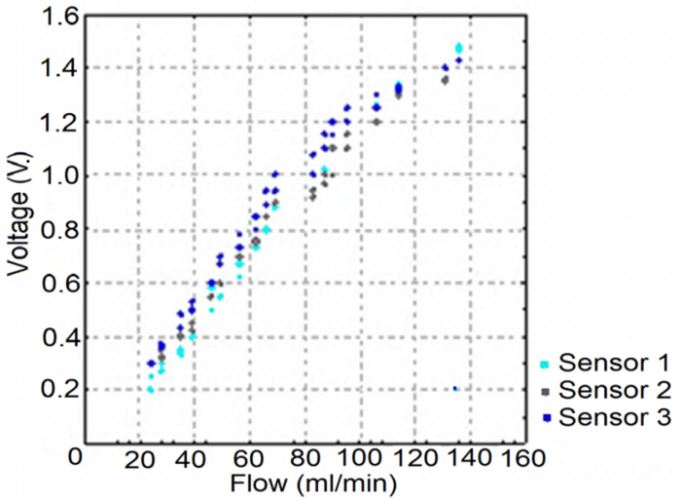

Figure 18. Data dispersion diagram of three Rexolite sensors, including all measurements.

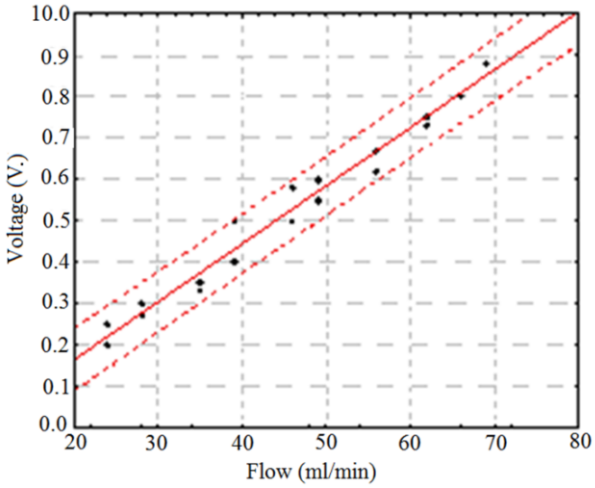

Figure 19. Rexolite sensor 1 regression diagram.

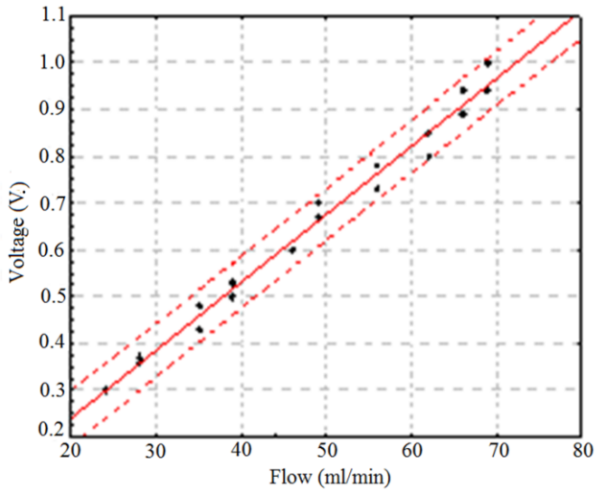

Figure 20. Rexolite sensor 2 regression diagram.

According to the results, a standard error of the predicted value of 2.4, 1.8 and 1.8 ml/min was obtained for the three sensors, respectively. The prediction error was calculated with a confidence of 95 % for each flow value, based on measured average voltage levels. So, the predicted error for future measurements are: 5.0, 3.7 and 3.7 ml/min, respectively. It consists of forecasts made in the medium term, with a time range between six months to three years, that is, errors occurring due to the continued use of the sensors [20].

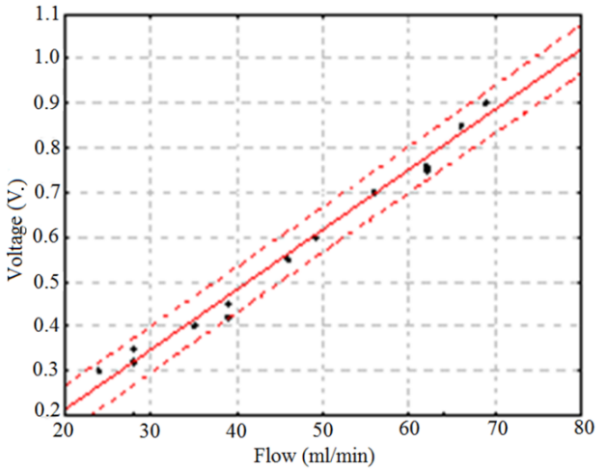

Figure 21. Rexolite sensor 3 regression diagram.

The minimum predicted values are lower than those reported by the commercial company MediStim, (5 ml/min) [11].

III.7. Implementation of LabView-based software (front panel designed for data presentation).

In order to visualize the blood flow signals and values, we designed an ad-hoc software (based on LabView). The front panel is shown in Fig. 22, where the blood flow signal can be visualized in real time, being updated constantly and stored during the signal acquisition, which is an advantage for the surgeon. It contains a Y axis scale showing the measured flow values expressed in ml/min. The time values associated with the measurements are indicated in the X axis. The REC key allows storing signal values during the desired period of time. In addition, some indicators are included: the flow average value (expressed in ml/min), the maximum and the minimum flow values, and the so-called Pulsatility Index (PI) [9]. Finally, the STOP key is included to stop the display of the signals and save the selected values.

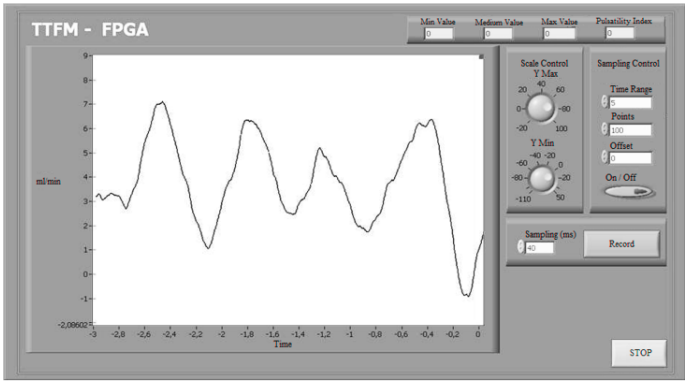

Figure 22. Front panel associated with the ad-hoc TTFM software.

IV. CONCLUSIONS

The basic aspects in the design of TTFM sensors are reviewed, considering the dimensions and the selection of materials

to be used. Two models were designed: model A (Rexolite wedge) and model B (epoxy resin wedge), which are the basic elements that allow flow measurements.

Both have high constructive repeatability, homogeneous acoustic field and allow a reading uncertainty lower than 5 ml/min. The Rexolite sensors provide larger acoustic intensity than the epoxy resin ones.

The resonance frequency and phase responses of the sensors were checked using the pulse transmission technique. Considering the dispersion of their values, the voltage difference of all sensors does not exceed twice the peak amplitude values, thus ensuring reading repeatability.

The flow measurement standard error was obtained for each of the three sensors with values of 2.39, 1.77 and 1.88 ml/min respectively, being smaller than those reported by similar sensors corresponding to the leader company (Medi-Stim), which is of 5 ml/min. The prediction error in the measurement, according to each sensor are: 5.02, 3.72 and 3.80 ml/min, respectively.

An analog module and a FPGA reconfigurable platform were implemented, capable of measuring time intervals of tens of picoseconds, allowing read errors of 5 ml/min.

The system as a whole was evaluated in a constant flow phantom.

ACKNOWLEDGMENTS

E. C.-B. thanks the "Abdus Salam" International Center for Theoretical Physics (Trieste, Italy) for a scholarship. The authors acknowledge the Department of Electrical Engineering, Bioelectronics Section, CINVESTAV (México D.F.) for support, and J. Prohías and A. Villar ("Hermanos Ameijeiras" hospital) for their valuable advice and help. We thank E. Altshuler for advise and suggestions.

V. REFERENCES

[1] M. Gwozdziewicz. Biomed. Papers **148**, 59 (2004).
[2] C. F. Barrera-Ramírez, J. Escaned. Arch. Cardiol. Méx, **75**, 335 (2005).
[3] J.A. Finegold, P. Asaria and D.P. Francis. Int. J. Cardiol. **168**, 934 (2013).
[4] J. Radcliffe. Soc. Thoracic Surgeons. **83**, 2251 (2007).
[5] R. Tabrizchi and N. Iida, Electromagnetic blood flow measurements. In J. Moore and G. Zouridakis (Eds.). Biomedical technology and devices handbook, (CRC Press LLC, New York, 2003).
[6] A. J. Room and D. Hoogerwerf, J. Vascular Surg. **16**, 239 (1992).
[7] K. Kogure and E. Choromokos. J. Appl. Physiol. **26**, 154 (1969).
[8] J. Seo and Y. -S. Kim. Biomed. Eng. Lett. 7, 57 (2017)
[9] D. P Taggart et al. J. Thoracic Cardiov. Surgery. **159**, 1283 (2020).
[10] A. Jiménez, E. Moreno, E. Carrillo and D. Torres, Rev. Cubana Fis. **28**, 4 (2011).
[11] Medi-Stim. "Adding a New Dimension to Intraoperative Guidance", Catálogo Informativo, (2017).
[12] A. Ramos, H. Calas, L. Diez, E. Moreno, J. Prohías, A. Villar, E. Carrillo, A. Jiménez, W.C.A. Pereira, M.A. Von Krüger. Physics Procedia. **89**, 42 (2016).
[13] Maxim, CMOS Analog Switches, MAX312/ MAX313/ MAX314. (2019) (www.maximintegrated.com/en/products/analog/analog-switches-multiplexers/MAX312.html).
[14] Maxim, 35MHz, Ultra-Low-Noise Op Amps, MAX 4106/MAX4107. (2019) (www.datasheets.maximintegrated.com/en/ds/MAX4106-MAX4107.pdf).
[15] Analog Devices, Low Noise, 90 MHz Variable-Gain Amplifiers, AD603. (2019) (www.analog.com/en/products/ad603.html).
[16] BURR-BROWN, Low Noise, Dual SWITCHED INTEGRATOR, ACF2101. (2019) (www.it.com/BURR-BROWN, Low Noise, Dual SWITCHED INTEGRATOR, ACF2101, pdf).
[17] EFM-02, Spartan-6LX FPGA module with USB 3.0. (2019) (www.cesys.com/en/our-products/fpga-boards/efm-02.html).
[18] OMICRONLAB, ULTRASCOPE, User's Manual. (2018) (www.omicronlab.com/documents.blackmagicdesign.com/UserManuals/BlackmagicUltraScopeManual.pdf).
[19] M.A. Kruger and F.A. Martins. Manual de Phantom de Flujo Sanguineo, Versión 1.0. (2007).
[20] D. F. Cardona, J. L. González. Inferencia estadística. Módulo de regresión lineal simple, 1ra Ed. (Universidad del Rosario, 2013).
[21] G. Cavada. Rev. Chil. Endocrinol. Diabetes. **6**, 127 (2013).

JABLONSKI DIAGRAM REVISITED

EL DIAGRAMA DE JABLONSKI REVISTADO

R. Šípoš, J. Šima

Dept. of Inorganic Chemistry, Institute of Inorganic Chemistry, Technology and Materials, Faculty of Chemical and Food Technology STU, Radlinského 9, 812 37 Bratislava;
† corresponding author

Recibido 3/5/2020; Aceptado 10/11/2020

This paper deals with new approaches towards the Jablonski diagram and the ξ state concepts from the viewpoint of the relationship between electronic deactivation and vibrational relaxation processes in electronically excited species. In both concepts, vibrational relaxation precedes the electronic deactivation processes of excited molecules. The experimental data accumulated up to the present using mainly time-resolved luminescence and transient absorption spectroscopy from the field of the photophysics of transition metal compounds and different organic molecules have clearly demonstrated that even spin-forbidden electronic deactivations are in many cases faster processes that vibrational relaxation. It means that the classical Jablonski diagram indicating that electronic deactivation processes occur after vibrational relaxation should be modified. In general, electronic deactivations occur from vibrationally higher states.

Este artículo trata sobre nuevas aproximaciones al diagrama de Jablonski y los conceptos del estado ξ desde el punto de vista de la relación entre la desactivación electrónica y los procesos de relajacion vibracional en especies electrónicamente excitadas. En ambos conceptos, la relajación vibracional precede a los procesos de desactivación electrónica de las moléculas excitadas. Los datos experimentales acumulados hasta el momento usando básicamente luminescencia resuelta en el tiempo y espectroscopía transiente de absorción del campo de la fotofísica de los compuestos de metales de transición y de diferentes moléculas orgánicas, han demostrado claramente que incluso las desactivaciones electrónicas de espín prohibido son, en muchos casos, más rápidas que la relajación vibracional. Ello significa que el diagrama de Jablonski clásico, que indica que los procesos de desactivación ocurren después de la relajación vibracional, pudieran modificarse. En general, las desactivaciones electrónicas ocurren desde estados vibracionales superiores.

PACS: Ultrafast processes (procesos ultra-rápidos), 82.53.-k; Born-Oppenheimer approximation (aproximacion de Born-Oppenheimer), 31.30-i; photon molecule interactions (interacciones fotón molécula), 33.80.-b

I. INTRODUCTION

When dealing with photodeactivation processes of electronically excited species it should be worth summarizing and reminding one aspect of the issue, namely the relationship of the rate constant of electronic deactivations (transitions lowering the electronic energy) and rotational-vibrational relaxation (lowering mainly vibrational energy within a given electronic state). In the history of photochemistry two solutions of the relationship have evolved, both obeying the Born-Oppenhaimer approximation.

The first approach applied originally in organic photochemistry was offered by Jablonski in his original paper devoted to anti-Stokes fluorescence of dyes [1]. It is usually expressed in the form of a diagram - called Jablonski diagram - which is a graphical depiction of the electronic states of a molecule and the transitions between those states. The vertical axis of the graph represents energy increasing from the bottom (ground state or S_0) to the top (singlet and triplet excited states or S_n and T_n). The transitions between the states (like excitation, internal conversion, fluorescence, intersystem crossing, etc.) are depicted as arrows (wavy arrows for nonradiative transitions, straight ones for radiative transitions). The Jablonski diagram (Fig. 1) is usually expressed for organic molecules and their singlet and triplet states, it can be, however, generally used for inorganic complexes too, e.g. for chromium(III) complexes and their quartet and doublet states.

Its current form can be found in many literature sources devoted to photochemistry and photophysics [2–5]. One of the characteristics of a typical Jablonski diagram is that any electronic deactivation occurs from the lowest vibrational level, i.e. vibrational relaxation precedes electronic deactivation. It is worth mentioning that Jablonski diagram in combination with Franck-Condon principles has been successfully applied in explanation the mirror shape of absorption and emission electronic spectra.

In the 1960s Adamson elaborated an analogous approach introducing the term "ξ-state" to characterize the state thermally equilibrated with its surroundings by the transfer of part of the vibrational energy of a populated excited state to surrounding molecules through collisions [6]. Adamson defined thexi (thermally equilibrated excited states) states as the chemically reacting species being in thermodynamic equilibrium with their surroundings and essentially high energy isomers of the ground state. By contrast, the species obtained by light absorption of wavelength around a ligand field band maximum are Franck-Condon states that have a nonthermodynamic distribution of vibrational excitations; such states are treated as pseudo pure electronic states in ligand field theory [7]. One of the experimental observations that contributed to the idea of the thexi state

was LF fluorescence, which is defined as the spin-allowed radiative deactivation occurring from a LF excited state of a coordination compound to its ground-state and involving the central atom centered orbitals [8]. Also, the Adamson's concept was based on the assumption that the thermal equilibration (i.e. vibrational relaxation) preceded the electronic deactivation processes of excited molecules. Adamson applied his concept mainly in the field of LF photochemistry of coordination compounds.

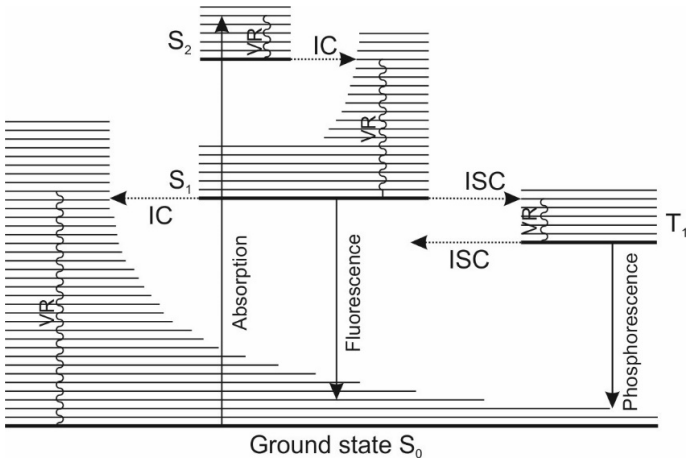

Figure 1. Jablonski diagram for organic molecules.

It should be pointed out that both - Jablonski's and Adamson's - concepts were formulated prior to introducing ultrafast flash-techniques (working in nano-, pico- and femtosecond time domain) into photochemistry and photophysics. The advent and introduction of the mentioned ultrafast techniques has documented that situation could be different, i.e. electronic deactivation is frequently a faster process that vibrational relaxation.

To support the idea, two kinds of experimental results are offered. The first one concerns photophysical deactivation processes, the other is based on photochemical deactivations.

Coordination compounds

The experimental data accumulated up to the present using mainly time-resolved luminescence and transient absorption spectroscopy from the field of the photophysics of transition metal compounds have clearly demonstrated that even spin-forbidden electronic deactivations are faster processes that vibrational relaxation. Data for iron(II) and iron(III) are gathered in several papers [9–11]. The issue of coupling of electronic deactivation and vibrational relaxation has been elaborated in detail and applied for both organic molecules and transition-metal complexes by Penfold and his coworkers [12]. They drew attention mainly to intersystem crossing processes. Instead of considering a simple ladder of states, as depicted in a Jablonski diagram, they propose to consider the more complicated spin-vibronic levels. Their main idea is that due to the strong mixing brought about by the simultaneous presence of nonadiabatic and spin-orbit coupling, the spin, electronic, and vibrational dynamics cannot be described independently [12, 13]. On the other hand, in cases of a significant difference between the rate of electronic deactivation and vibrational relaxation, these events can be considered, in accordance with Born-Oppenhaimer approximation, independent and represented as by a Jablonsky diagram. A new feature is that the vibrational relaxation is preceded by faster electronic deactivation, i.e. electronic deactivation processes occur from excited vibrational states.

In the photochemistry of coordination compounds, the energy order of electronic excited states decreases stepwise typically from the energy highest intraligand (frequently ring centered $\pi\pi^*$) states, via charge transfer (both ligand to metal and metal to ligand) states, and finishing in metal-centered states. One of such examples are iron(III) complexes with a Schiff base as a ligand. In Fig. 2 structure of such complex [Fe(salen)(CH_3OH)Br] together with excitation wavelengths into different excited states is illustrated. This and other similar complexes were photochemically investigated and quantum yield of Fe(II) formation was determined [14, 15]. From the results summarized in Table 1 we can see that iron(II) is formed at any of the applied excitation wavelengths. It indicates that there must be effective communication between the excited states involving the photoredox reactive LMCT state and that the LMCT state populated in different ways must have different content of vibrational energy. This can be depicted in the sequence of deactivation processes described by equation:

$$\text{IL(Ph)} \xrightarrow{\text{IC/ISC}} \text{IL(C=N)} \xrightarrow{\text{IC/ISC}} \text{LMCT} \xrightarrow{\text{IC/ISC}} \text{LF} \xrightarrow{\text{IC/ISC}} \text{GS} \qquad (1)$$

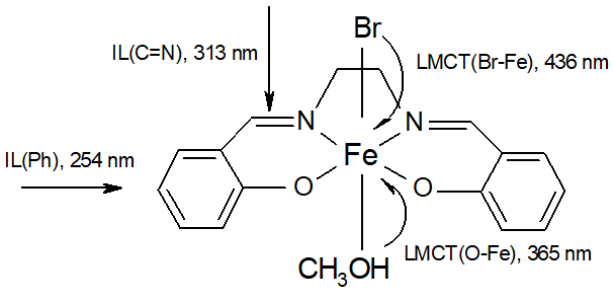

Figure 2. Schematic structure of the complex [Fe(salen)(CH3OH)Br] and excitation data.

Table 1. Excitation wavelength, $\lambda_{i\pi}$, populated excited state, quantum yield of iron(II) formation, $\Phi(Fe^{II})$, and order of mean vibrational energy of photoredox reactive LMCT state for the complex [Fe(salen)(CH_3OH)Br] irradiated in methanol at steady-state conditions.

$\lambda_{i\pi}$ nm	254	313	365	436
Populated excited state	IL(Ph)	IL(C=N)	LMCT (O→Fe)	LMCT (Br→Fe)
$\Phi(Fe^{II})$	0.0036	0.0031	0.00045	0.00020
Order of ν of reactive LMCT state(s)	ν >	ν >	ν >	ν

Another interesting result of this wavelength dependence is that the step-wise decreasing in electronic energy (1) is associated with a simultaneous increase in the vibrational energy content of the photoredox reactive LMCT state. This can happen when the vibrational relaxation is slower

than electronic deactivation and any deactivation process is accompanied by the accumulation of the vibrational energy.

Based on these results we can propose a modified Jablonski diagram for the deactivation processes in [Fe(salen)XY] (X, Y – monofunctional anionic and/or neutral ligands) systems as depicted in Fig. 3.

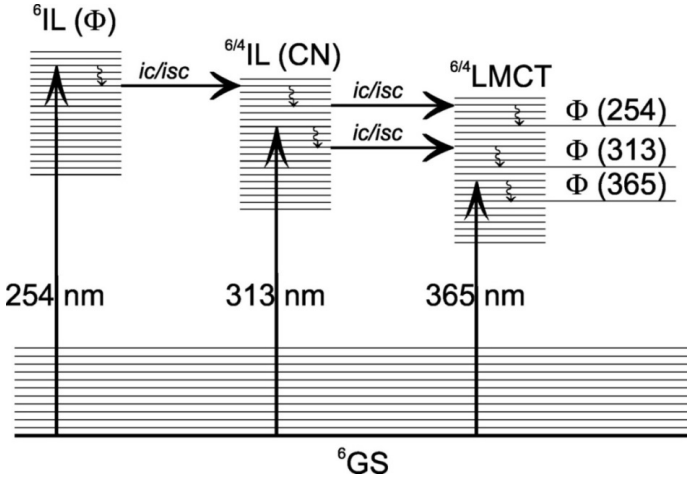

Figure 3. Modified Jablonski diagram for the deactivation processes in [Fe(salen)XY].

The femtosecond study of a similar Schiff base complex, [Fe(salpet)(CN)] (H_2salpet = N,N-bis(1-hydroxy-2-benzyliden) -1,6-di-amino-4-azahexan, Fig. 4) excited at 400 nm led to the values of 338 fs, attributed to electronic deactivation in the form of intersystem crossing, and 9.09 ps, assigned to vibrational cooling and/or simultaneously occurring other electronic deactivations [16].

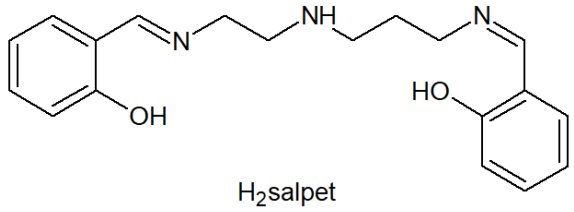

Figure 4. Structure of the ligand H_2salpet = N,N-bis(1-hydroxy-2-benzyliden) -1,6-di-amino-4-azahexan.

High-spin iron(III) salicylato complexes are another example of investigated systems. Complexes with 5-sulfosalicylic acid (SSA) and all isomers of fluorosalicylic (FSA) acids as ligands were investigated. In the case of SSA all three mono-, bis- and tris complexes were prepared in solution, whereas only monofluorosalicylato complexes were investigated. In all cases data treatment yielded two relaxation times as shown in Tables 2 and 3, the first one was ascribed to electron deactivation from hot excited state and the second one to vibrational cooling of the hot ground state [17,18].

Table 2. Lifetimes of excited states of Fe(III) complexes with fluorosalicylic acid isomers.

Complex	τ_1/ps	$\lambda_{max}(\tau_1)$/nm	τ_2/ps	$\lambda_{max}(\tau_1)$/nm
Fe-3FSA	0.8±0.1	670	2.6±0.3	580
Fe-4FSA	0.5±0.1	660	2.0±0.2	580
Fe-5FSA	0.6±0.1	695	2.1±0.2	610
Fe-6FSA	0.9±0.1	645	2.8±0.4	555

Rury and Sension investigated iron (III) tetraphenylporphyrin chloride in room temperature solutions in toluene and dichloromethane [19]. Depending on the excitation wavelength and solvent they were able to determine three relaxation times. First time of 0.4 - 0.6 ps was the relaxation from the lowest-lying porphyrin singlet manifold into a LMCT state followed by a MLCT from the iron to the porphyrin on a time scale of 1.8 - 2.3 ps that produced excited ^{4}T intermediate spin state of Fe^{III}TPPCl. The system relaxes back to the high spin $^6A_1$ ground state on a time scale of 13 - 18 ps. No vibrational cooling was observed.

Table 3. Lifetimes of excited states of Fe(III) complexes with sulfosalicylic acid.

Complex	τ_1/ps	tau_2/ps
FeSSA	0.26	1.8
$Fe(SSA)_2^{3-}$	0.1	1.4
$Fe(SSA)_2^{6-}$	0.17	1.5

In the field of ferrous complexes, different derivatives of pyridine as ligands were used. In the ultrafast study of $[Fe(bpy)_3]^{2+}$ global analysis of the transient absorption data revealed three relaxation times. The first 120 fs is the decay of the ^{3}MLCT, the second 960 fs was identified as the population time of the $^5T_2$ state, and the third 665 ps was attributed as its decay time to the ground state [20]. The group of McCusker investigated excited-state dynamics in a FeII polypyridyl complexes, $[Fe(tptn)]^{2+}$ and $[Fe(tren(py)_3)]^{2+}$, where tptn is tetrakis(2-pyridylmethyl)-1,3-propylenediamine and $tren(py)_3$ is tris(2-pyridylmethyl-iminoethyl)amine. In the first complex after excitation $^1A \rightarrow {}^1$MLCT a 700 fs transition into $^5T_2$ was observed following by 2 ps cooling of this state and 18 ns decay to the ground stay followed. The second study showed < 100 fs transition from ^{1}MLCT into a LF manifold of $^1T_2$, $^1T_1$, $^3T_2$ and $^3T_1$ from which in approximately 300 fs hot $^5T_2$ state was formed. Vibrational cooling of this state occurred in 8 ps followed by a transition into the ground state in 60 ns [10,21,22].

Well known is the tris(acetylacetonate) chromium(III) $Cr(acac)_3$ system. It has well documented photophysical properties, high symmetry, and low quantum yield for photosubstitution (<0.01). Following the $^4A_2 \rightarrow {}^4T_2$ excitation < 100 fs ISC into hot ^{2}E occurred, that was followed by 1.1 ps vibrational cooling and final 800 ps relaxation to the ground state [23–25]. The order of $k_{VR} > k_{IC} > k_{ISC}$ that is based on the analogy from organic systems is questioned, as it does not apply to metal complexes.

Organic and organometallic compounds

Different biomolecules such as DNA bases or dyes were investigated from the broad range of organic compounds. In a study focused on ultrafast measurements of deactivation for triphenylmethane dyes, malachite green (MG), brilliant green (BG), crystal violet (CV), and ethyl violet (EV) in different solvents the multiexponential decay of the excited state was found. The times of 4.8 and 5.8 ps for CV and EV in methanol were consistent with the picture of declining vibrationally hot and/or twisted ground state, the faster time 0.54 ps in MG was attributed to fluorescence decay in MG [26,27].

A deactivation mechanism was investigated in a sunscreen constituent - oxybenzone (OB) by transient electronic and vibrational absorption spectroscopy. The energy dissipation mechanism involves ultrafast 100 fs excited enol → keto tautomerization followed by 400 fs internal conversion relaxation processes. The cooling of the vibrationally hot ground state occurred in 5-8 ps coupled with keto → enol tautomerization or the minor pathway of vibrational cooling to keto-form and subsequent back isomerization occurred in > 1.3 ns [28].

A delayed fluorescence was observed in dithienylbenzothiadiazole (DTBT) and a carbazole substituted derivative CDTBT (Fig. 5) was used to study the dynamics in this system.

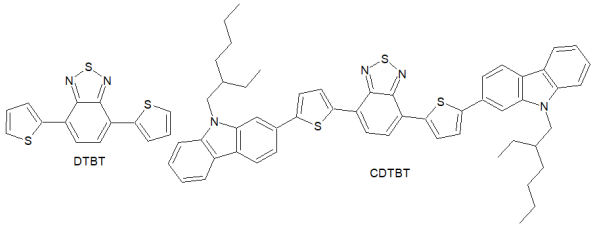

Figure 5. Structures of DTBT and CDTBT.

This study revealed a fast 300 fs IC from S_2 to hot S_1 state in DTBT followed by 33 ps cooling of this S_1 state. From this state, fluorescence occurred in 2 - 3 ns together with ISC/BISC into T_1 in 0.5 - 1 ns that was followed by 13 μs phosphorescence. In the heavier molecule of CDTBT 3.7 ps IC from S_2 into S_1 was observed and from this hot S_1 state 2.2 ns fluorescence occurred. No cooling of this hot S_1 state was observed [29].

Investigation of the photochromic reactions (transition between the open and the closed form) of a water-soluble indolylfulgimide led to four different times. The 0.06 ps and the 0.4 ps components of the C-form can be assigned to the relaxation of the excited molecule from the Franck-Condon region and solvent reorganization. The third lifetime component (1.8 ps) was attributed to the repopulation of the ground state, while the fourth one (~10 ps) was associated with the vibrational cooling of the ground state [30]. Koller and coworkers investigated different indolylfulgimide derivative and found 2.0 ps deactivation of the electronic excited state which was followed by 15 - 20 ps vibrational cooling [31,32].

Similar results were found in the studies of intramolecular vibrational relaxations. Carbonyl complexes of Re and Mn were investigated in tetrachloromethane and DMSO. The intramolecular vibrational energy redistribution (IVR) was faster in $[Re(CO)_5Br]$ than in Mn complex and IVR time constants are six times faster in a polar solvent (2.8-3.9 ps) than in nonpolar solvent (20-25 ps) [33]. Electronic deactivation together with vibrational energy relaxation were observed in nickel octaethylporphyrin complex. Here in this large molecule, the IVR occurred on subpicosecond scale following by intermolecular energy transfer that occurred in ~10 ps. However, there are two electronic deactivation processes. One is internal conversion (<350 fs) that forms an excited d-d state that deactivates in ~300 ps [34]. Investigation of IVR of cresyl violet in methanol showed a dephasing time constant 2.4 ps and authors hypothesize that the dominant process is IVR [35]. The vibrational energy relaxation of CH2I2 in different solvents was investigated by Charvat *et al.* [36]. They found that IVR occurs on 9-10 ps timescale while intermolecular vibrational energy transfer occurred in 60 - 120 ps and was solvent and excitation energy dependent.

In many other papers investigating electron transfer processes it is problematic to find information on vibrational relaxation times. Reverse intersystem crossing (RISC) was investigated in triazine derivatives froming exciplex used in OLEDs. Rate constatants for ISC were around $3 \cdot 10^7$ s^{-1} and for RISC$\approx$ 10^5 s^{-1} [37]. Aizawa *et al.* investigated RISC in organic donor-acceptor molecules. For 3-(2,7-dibromo-9,9-dimethylacridan-10-yl)xanthone and 3-(3,7-dibromo-phenoxazin-10-yl)xanthone they calculated and confirmed by measurements kRISC to be $8.7 \cdot 10^5$ s^{-1} and $2.6 \cdot 10^7$ s^{-1} [38]. Photoexcitation of formyluracil and formylcytosine showed $S_1 \rightarrow T_2$ transition 1950 fs to be rate determinig step, followed by hopping transitions between T_2 and T_1 states with time constants 4 and 17 fs. Formylcytosine first revealed rapid initial equilibrium in singlet manifold with time constants fs and 5 fs for $S_1 \rightarrow S_2$ and $S_2 \rightarrow S_1$, followed by rate determining step $S_1 \rightarrow T_2$ transition in 3559 fs. The subsequent IC $T_2 \rightarrow T_1$ occurred in 150 fs [39].

Calculations of Valiev *et al.* for different organic and organometallic compounds show different values of radiative and nonradiative rate constants. Values for certain molecules differed from experimental data due to inaccurate FC and adiabatic approximations [40]. Vennapusa *et al.* investigated receiver triplet state in carbonylpyrenes. They found out first occurs ultrafast IC from vibronically coupled higher S_n states to S_1 followed by ISC to T_4/T_5 receiver state followed byt IC into lower states. Lifetimes of receiver triplet states in substituted pyrenes were 24, resp. 15 fs [41].

II. CONCLUSIONS

Based on the above data the following conclusions can be formulated. The concept of thexi state and Jablonski diagram was introduced before the invention of ultrafast techniques. The concept was in accord with the Born-Oppenhaimer approximation. The data shows that the Jablonski diagram in its traditional form may not be fully valid, particularly in the case of coordination compounds. The original Jablonski diagram illustrates processes in organic molecules. However, in general even in such molecules the rate of electronic deactivations, spin-forbidden singlet-triplet intersystem crossing including, is higher than that of vibrational cooling. Processes occurring in open-shell transition metal complexes [42] were not involved and discussed. The relationship between vibrational relaxation and electronic deactivation processes was discussed in detail in the pioneering papers of McCusker *et al.* [21–24] who, based on experimental investigation, clearly documented that both IC and ISC processes in some Fe(II) complexes are much faster that vibrational relaxation. The selection rules that apply to organic compounds dealing with spin-forbidden processes

are not so strict for transition metal compounds. The result of this is that a rate constant of intersystem crossing is higher than that of internal conversion and electronic deactivation processes are faster compared to vibrational relaxation.

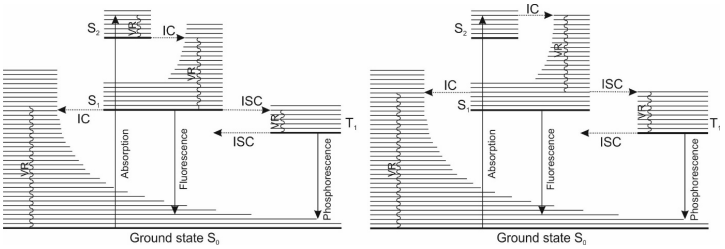

Figure 6. Original and modified Jablonski diagrams.

The better depiction of the Jablonski diagram for organic molecules, which can be used also for coordination compounds, that reflects current results is one shown in Fig. 6. There can be seen that only partial vibrational relaxation of excited states occurs and from this hot Franck-Condon states electron deactivation occurs.

ACKNOWLEDGMENTS

The authors gratefully acknowledge support of the VEGA and APVV agencies (1/0639/18, 1/0343/19 and APVV-17-0183).

III. REFERENCES

[1] A. Jablonski, Nature. **131**, 839 (1933).
[2] B. Wardle, Principles and Applications of Photochemistry, (Wiley, Chichester, United Kingdom, 2009).
[3] R. C. Evans, P. Douglas, H. D. Burrows, (Eds.). Applied Photochemistry, (Springer, Dordrecht, Germany, 2013).
[4] M. Klessinger, J. Michl, Excited States and Photochemistry of Organic Molecules, (VCH Publishers: New York, USA, 1995).
[5] M. Montalti, A. Credi, L. Prodi, M. T. Gandolfi, Handbook of Photochemistry, 3rd Ed. (CRC Press Inc, Boca Raton, USA, 2006).
[6] A. W. Adamson, Adv. Chem. **150**, 128 (1976).
[7] A. W. Adamson, Comments Inorganic Chem. **1**(1), 33 (1981).
[8] Y. Y. Chia, M. G. Tay, Dalton Transactions **43**, 13159 (2014).
[9] J. Šima, Acta Chim. Slov. **8**, 126 (2015).
[10] E. A. Juban, A. L. Smeigh, J. E. Monat, J. K. McCusker, Coord. Chem. Rev. **250**, 1783 (2006).
[11] M. Chergui, Acc. Chem. Res. **48**, 801 (2015).
[12] T. J. Penfold, E. Gindensperger, Ch. Daniel, Ch. M. Marian, Chem. Rev. **118**(15), 6975 (2018).
[13] C. Souza, M. Alías, A. Domingo, C. de Graaf, Chem. Eur. J. **25**, 1152 (2019).
[14] J. Šima, M. Izakovič, Croat. Chem. Acta. **78**(1), 29 (2005).
[15] J. Šima, Optimizing the Photoreactivity of Chemical Compounds - Necessity, Challenges and Obstacles in Coordination Chemistry Research Progress (T.W. Cartere and K.S. Verley, Eds.), (Nova Science Publishers, New York, USA, 2008), pp. 71-102.
[16] J. Šima, R. Šípoš, V. Szöcs, in Recent Developments in Coordination, Bioinorganic and Applied Inorganic Chemistry, edited by M. Melník, P. Segla, M. Tatarko (STU Press, Bratislava, Slovakia, 2013).
[17] I. P. Pozdnyakov, V. F. Plyusnin, N. Tkachenko, H. Lemmetyinen, Chem. Phys. Lett. **445**, 203 (2007).
[18] I. P. Pozdnyakov, A. A. Melnikov, R. Šípoš, S. V. Chekalin, J. Šima, Chem. Phys. Lett. **660**, 209 (2016).
[19] A. S. Rury, R. J. Sension, Chem. Phys. **422**, 220 (2013).
[20] W. Gawelda, A. Cannizzo, V.-T. Pham, F. van Mourik, C. Bressler, M. Chergui, J. Am. Chem. Soc. **129**(26), 8199 (2007).
[21] J. K. McCusker, K. N. Walda, R. C. Dunn, J. E. Simon, D. Magde, D. N. Hendricson, J. Am. Chem. Soc. **114**(17), 6919 (1992).
[22] J. E. Monat, J. K. McCusker, J. Am. Chem. Soc. **122**(17), 4092 (2000).
[23] E. Juban, J. McCusker, J. Am. Chem. Soc. **127**(18), 6857 (2005).
[24] J. N. Schrauben, K. L. Dillman, W. F. Beck, J. K. McCusker, Chem. Sci. **1**(3), 405 (2010).
[25] P. S. Wagenknecht, P. C. Ford, Coord. Chem. Rev. **255**(5-6), 591 (2011).
[26] Y. Nagasawa, Y. Ando, T. Okada, Chem. Phys. Lett. **312**, 161 (1999).
[27] Y. Nagasawa, Y. Ando, D. Kataoka, H. Matsuda, H. Miyasaka, T. Okada, J. Phys. Chem. A. **106**, 2024 (2002).
[28] L. A. Baker, M. D. Horbury, S. E. Greenough, P. M. Coulter, T. N. V. Karsili, G. M. Roberts, A. J. Orr-Ewing, M. N. R. Ashfold, V. G. Stavros, J. Phys. Chem. Lett. **6**(8), 1363 (2015).
[29] M. E. Mohanty, C. Madhu, V. L. Reddy, M. Paramasivan, P. R. Bangal, V. J. Rao, Phys. Chem. Chem. Phys. **19**, 9118 (2017).
[30] C. Slavov, C. Boumrifak, C. A. Hammer, P/ Trojanowski, X. Chen, W. J. Lees, J. Wachtveitl, M. Braun, Phys. Chem. Chem. Phys. **18**, 10289 (2016).
[31] F. O. Koller, W. J. Schreier, T. E. Schrader, A. Sieg, S. Malkmus, C. Schulz, S. Dietrich, K. Rück-Braun, W. Zinth, M. Braun, J. Phys. Chem. A. **110**, 12769 (2006).
[32] S. Malkmus, F.O. Koller, B. Heinz, W. J. Schreier, T. E. Schrader, W. Zinth, C. Schulz, S. Dietrich, K. Rück-Braun, M. Braun, Chem. Phys. Lett. **417**(1-3), 266 (2006).
[33] F. Yang, Q. X. Dong, M. Feng, J. Zhao, J. Wang, Phys. Chem. Chem. Phys. **20**, 3637 (2018).
[34] Y. Mizutani, Y. Uesugi, T. Kitagawa, J. Chem. Phys. **111**, 8950 (1999).
[35] S. Rafiq, G. D. Scholes, J. Phys. Chem. A. **120**(34), 6792 (2016).
[36] A. Charvat, J. Aâmann, B. Abel, J. Phys. Chem. A. **105**(21), 5071 (2001).
[37] T. B. Nguyen, H. Nakanotani, T. Hatakeyama, Ch. Adachi, Adv. Mater. **32** (9), 1906614 (2020).

[38] N. Aizawa, Y. Harabuchi, S. Maeda, P. Yong-Jin, Nat. Commun. **11**, 3909 (2020).
[39] A. Francés-Monerris, M. Lineros-Rosa, M. A. Miranda, V. Lhiaubet-Vallet, A. Monari, Chem. Commun. **56**, 4404 (2020).
[40] R. R. Valiev, V. N. Cherepanov, G. V. Baryshnikov, D. Sundholm, Phys. Chem. Chem. Phys. **20**, 6121 (2018).
[41] S. R. Vennapusa, R. S. Lekshmi, G. B. Kurup, Phys. Chem. Chem. Phys. **22**, 6145 (2020).
[42] K. Boguslawski, M. Reiher, Chemical bonding in open-shell transition-metal complexes. In: Frenking G, Shaik S (eds) The chemical bond: chemical bonding across the periodic table, (Wiley VCH Verlag GmbH & Co. KGaA, Weinheim, 2014)

ACCURACY AND PRECISION OF SMARTPHONES IN MEASUREMENTS OF ILLUMINANCE AND LIQUID TURBIDITY

EXACTITUD Y PRECISIÓN DE TELÉFONOS INTELIGENTES EN MEDICIONES DE ILUMINACIÓN Y TURBIDEZ LÍQUIDA

N. Tongjan[a], C. Sirisathitkul[b†]

a) Benjamarachutit School, Nakhon Si Thammarat, Thailand
b) Department of Physics, School of Science, Walailak University, Nakhon Si Thammarat, Thailand; schitnar@mail.wu.ac.th
† corresponding author

Recibido 16/5/2020; Aceptado 10/11/2020

Smartphones have demonstrated being attractive tools for illuminance and liquid turbidity measurements. The ambient light sensor and its corresponding mobile application can measure the reduction in illuminance with the distance away from a light source. The indirect measurement of turbidity is performed via the light passing through a solution. The illuminance linearly decreases with the increase in molar concentration of solution and a linear conversion equation to the turbidity can be obtained. By repeating the experiment, the uncertainty in direct measurements of illuminance is less than 1 %, ensuring an appropriate precision for educational and professional uses.

Los teléfonos inteligentes han demostrado ser herramientas atractivas para las mediciones de iluminación y turbidez. El sensor de luz ambiental y su aplicación para móvil son capaces de medir la reducción en la iluminación con la distancia desde la fuente de luz. La medición indirecta de la turbidez se hace mediante la luz a través de la solución. La iluminación decrece linealmente con el incremento en la concentración molar de una solución, de modo que se puede obtener una ecuación de conversión lineal a la turbidez. Repitiendo el experimento, la incertidumbre en mediciones de iluminación es menor que el 1 %, lo que asegura una precisión suficiente para usos educacionales y profesionales.

PACS: Education (educación), 01.40.-d; standards and calibration (estándares y calibración), 06.20.fb; photometers, radiometers, and colorimeters (fotómetros, radiómetros y colorímetros), 07.60.Dq

I. INTRODUCTION

In addition to their conventional uses in communication and multimedia access, smartphones have increasingly been under research and development as measurement tools in physics education. The challenge for the lecturers is to fully utilize high accuracy sensors included in smartphones. Oprea and Miron comprehensively explored and explained a variety of examples based on physical measurements made by smartphones [1]. The angle and acceleration sensors can be effectively utilized in the teaching of mechanics [1–4]. Quantitative experiments have been also set up for teaching magnetic field and waves [1,5,6].

For recent experiments in acoustics and optics, ambient sound has been analyzed by smartphones [7] and ambient light sensors have been used to verify the inverse-square law with the distance [8–10]. In addition, Diaz-Melián *et al.* also analysed the illuminance in diffraction and polarization experiments by using a smartphone [8]. The Malus' law has been demonstrated with smartphones by Monteiro *et al.* [11] as well as by Çolak and Erol [12]. Light absorption of materials has been studied according to the Beer–Lambert law [13,14]. Furthermore, oscillations can be detected by ambient light sensors [15].

Countryman suggested that students can be engaged in learning several aspects of physics and engineering from the installations and functions of these inbuilt sensors [16]. The mobile applications for the experiments mentioned above are widely available for free or commercial download. Moreover, some lessons can be arranged without downloading additional programs, as demonstrated by Lincoln [17].

Beyond science education purposes, there there are several reports on simple measurements in smart farming, healthcare, engineering and geology using smartphones. Colorimetry by a smartphone was used in the determination of fruit ripeness [18,19], cholophyl contents [20] and ancient pottery classifications [21]. Examples of healthcare applications include the measurements of blood pressure [22] and heart rate [23] by smartphones. Smartphone sensors are conveniently used by geologist in the field survey [24]. For engineering applications, the vibration of machines has been successfully monitored by the inbuilt accelerometer [25]. In additions, smartphones have been increasingly employed as data acquisition devices in other professional uses [24,25].

Of particular relevance to this report is the use of a smartphone as a light meter. The ambient light sensor, normally used for adjusting the brightness of the screen according to environmental lighting, is capable of measuring the illuminance. With a freely downloadable mobile application, the reading from a smartphone's light sensor can be calibrated with standard instruments in the unit of Lux. In addition to the obvious implementation in physics classes, the development is also beneficial for professional uses, including occupational health.

Interestingly, the potential use of smartphones in measuring the turbidity of liquids has also been explored. Determinations

of turbidity –a decrease in transparency of a liquid caused by the inclusion of suspended particles– are in demand for environmental monitoring and manufacturing processes. The traditional Secchi disk and Jackson candle turbidity meter relies on visual observations which are not easily standardized. Therefore, most commercial turbidity meters utilize the nephelometric 90° light scattering measurement and the unit of turbidity is defined in NTU (Nephelometric Turbidity Unit). The light from Mie scattering, depending on the liquid turbidity, is measured at right angle respect to the incident light. Based on this method, Hussain *et al.* devised a smartphone-based turbidity meter and tested it with formazin standard solutions [26].

In this report, the measurement of illumination associated to light passing through a liquid is demonstrated as a route to determine the turbidity. The configuration somewhat resembles the Jackson candle turbidity meter, but replaces the eye inspection with the smartphone opposing the light source.

II. EXPERIMENTAL SETUPS

Two different Android smartphones (Phone 1: Samsung Galaxy S7 and Phone 2: Vivo Y85) and two mobile applications (App 1: Lux Light Meter Free by Doggo Apps and App 2: Lux Light Meter Pro by Elena Polyanskaya) were firstly compared. Two incandescent bulbs were used as light sources. Defined by the Commission Internationale de l'Eclarage (CIE), such light sources correspond to the standard "illuminant A" with a relative power distribution of the Planck radiation around 2856 K [27]. This spectral range is effectively detected by the smartphone ambient light sensor [26]. In the first experiment, the illuminance was measured at varying distances (d) by aligning the ambient light sensor directly in front of a light bulb. Plots of illuminance from a 100 W light bulb as a function of $1/d^2$ was then calibrated with an Extech 407026 Light Meter. The turbidity was indirectly determined from the illuminance through the solution, prepared by dissolving sugar in water to obtain a molar concentration within the range 0.1-0.6. The solution of varying turbidity was poured into an acrylic box of dimensions 15×15×20 cm^3. The light bulb and the ambient light sensor were directly located on opposite sides of the container. By measuring the same solutions with an ECTN10IR Portable Turbidity Meter, the illuminance in Lux could be converted to the turbidity in NTU. All measurements were repeated three times for each data point.

III. RESULTS AND DISCUSSION

III.1. Smartphone as light meter

The measurements using three different combinations of smartphone devices and mobile applications were compared. All three plots in Fig. 1 similarly exhibit a linear trend of the inverse-square law in which the illuminance is inversely proportional to the distance squared (d^2) from the light bulb, approximated as a point source. The standard deviation from each measurement is minimal and the values of R^2 from three linear fits are comparable, ranging from 0.9924-0.9944. The difference in equations describing the straight three lines in Fig. 1 suggests that the changes in smartphone, and mobile application affect the illuminance reading and each combination needs a calibration with a standard instrument. Interestingly, the slope is significantly reduced by changing the smartphone, which reveals the characteristics of each ambient light sensor, but they are less sensitive to the mobile application used in this experiment.

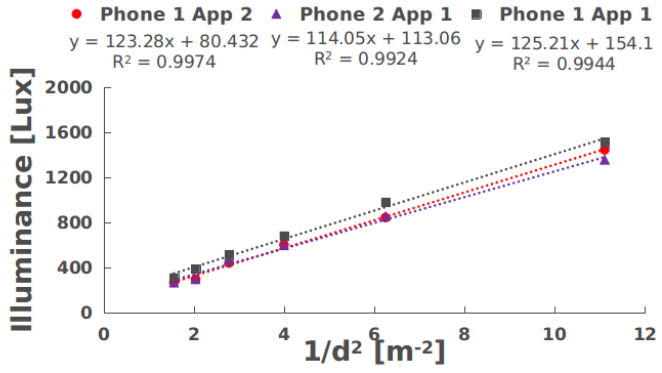

Figure 1. Variation of illuminance from with the distance (d) from the light source measured by using three different combinations of smartphone devices and mobile applications.

The illuminance reading by Phone 1 (Samsung Galaxy S7) and App 1 (Lux Light Meter Free by Doggo Apps) can be calibrated with the standard light meter as shown in Fig. 2. The straight line with $R^2 = 0.9996$ indicates very good agreement between the smartphone and the standard instrument. Error bars are not visible since the uncertainty from three repeated measurements are less than 1 %. The accuracy of the smartphone reading can be assessed by the slope of this calibration plot. The slope of 1.3289 from Fig. 2 means that the reading by the ambient light sensor and mobile application in smartphone is higher than the illuminance measured by the standard instrument. The difference is likely attributed to the infrared contribution from the light source. Because the illuminance is luminous flux per unit area incident on a surface perpendicular to it [27], the detection by the smartphone reading includes both visible light and infrared radiation from the incandescent light source. On the other hand, the Extech 407026 Light Meter is designed to eliminate this frequency range [28].

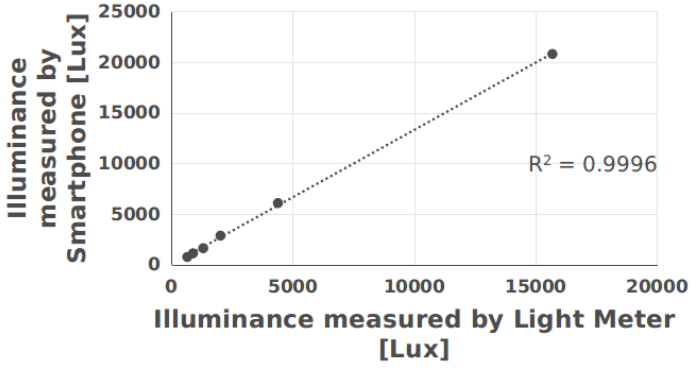

Figure 2. Linear relationship between illuminance measured by a smartphone and a light meter (Phone 1 and App1; see text).

III.2. Smartphone as turbidity meter

The results from the solutions of different concentrations, firstly measured by the turbidity meter, are shown in Fig. 3. The turbidity within the range of 4-20 NTU is directly proportional to the concentration of the solution from 0.1 to 0.6 Molar. Likewise, the illuminance of the light passing through the solution is also reduced with increasing molar concentration of the solution. This is consistent with the enhanced light absorption and scattering with increasing number of particles in solution.

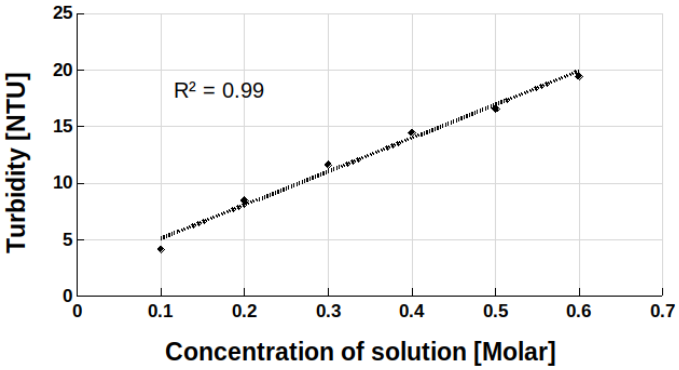

Figure 3. Variation of the turbidity measured by the turbidity meter as a function of the molar concentration of solutions.

By comparing the measurement by a smartphone with the turbidity meter reading, a straight line is obtained with $R^2 = 0.9958$ as shown in Fig. 4. Error bars indicate that the uncertainty in measurements by the smartphone is 1.77 %, higher than those made by the turbidity meter. This linear variation can be represented by a conversion equation;

$$\text{Turbidity} = -0.0092(\text{Illuminance}) + 35.462. \quad (1)$$

Certainly, the reproducibility of this measurement is highly influenced by the type of light source. Fluorescent lamps have a large variation of spectral distributions. Fluorescent light sources likely lower the sensitivity of this measurement set-up. Furthermore, the ambient light sensor may not be sufficiently sensitive to the light passing through very turbid water and the measurement of illumination by an opposing smartphone is therefore not effective in the case of waste water. With a different configuration, Hussain *et al.* demonstrated that the turbidity up to 400 NTU could be measured [26]. Their smartphone-based turbidity meter deployed an IR LED as a light source and measured the scattered infrared light at 90° using a proximity sensor.

The results in this section underline the versatility and precision of the ambient light sensors contained in smart phones. Besides the direct measurement of light, they can be used in the indirect measurement of other physical quantities by calibrating with standard instruments. As illustrated in the case of turbidity, the repeatability and linearity in an extended range are appropriate for educational and other professional applications.

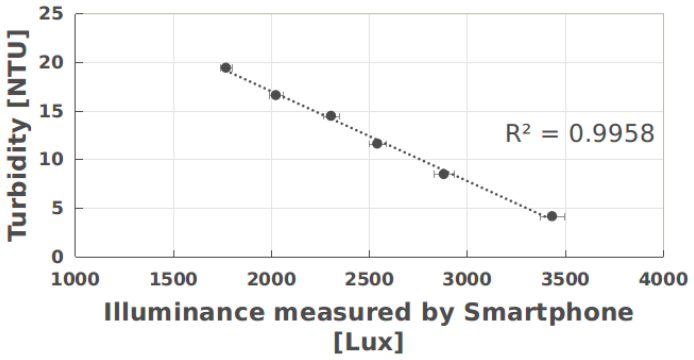

Figure 4. Linear relationship between the illuminance measured by the turbidity meter and the smartphone. (Phone 1 and App1; see text).

IV. CONCLUSION

The smartphone's ambient light sensors can measure light illuminance in a way comparable to a standard light meter. The study of three different combinations of smartphones and mobile applications confirms that the illuminance is inversely proportional to the distance squared from the light source. When increasing the concentration and the turbidity of the solution, the light sensor from the smartphone detects a linear reduction in the illuminance of the light passing through the solution. That makes smartphones useful for both educational and professional applications related to the quantification of turbidity.

ACKNOWLEDGEMENTS

The scholarship for the first author from Development and Promotion of Science and Technology Talents Project (DPST) is acknowledged.

V. REFERENCES

[1] M. Oprea and C. Miron, Rom. Rep. Phys. **66**,1236 (2014).
[2] J. Kuhn and P. Vogt, Phys. Teach. **50**, 182 (2012).
[3] T. Pierratos and H. M. Polatoglou, Phys. Educ. **53**, 015021 (2018).
[4] M. A. González, A. Gómez and M. A. González, Papers Phys. **10**, 100005 (2018).
[5] E. Arribas, I. Escobar, C. P. Suárez, A. Najera and A. Belendez, Eur. J. Phys. **36**, 065002 (2015).
[6] M. Thepnurat, P. Nikonphan, S. Mungkhalad, P. Saphet, K. Supawan and A. Tong-on, Phys. Educ. **55**, 035011 (2020).
[7] C. Florea, Phys. Teach. **57**, pp.214 (2019).
[8] V. L. Diaz-Melián, L. A. Rodriguez, F. Pedroso-Camejo, J. Mieres, Y. de Armas, A. J. Batista-Leyva and E. Altshuler, Rev. Cubana Fis. **36**, 4 (2019).
[9] I. Salinas, M. H. Gimenez, J. A. Monsoriu and J. C. Castro-Palacio, Phys. Teach. **56**, 562 (2018).
[10] J. A. Sans, J. Gea-Pinal, M H Gimenez, A R Esteve, J Solbes and J A Monsoriu, Eur. J. Phys. **38**, 025301 (2017).

[11] M. Monteiro, C. Stari, C. Cabeza and A. C. Martí, Phys. Teach. **55**, 264 (2017).
[12] İ. Ö. Çolak and M. Erol, J. Pend. Fis. Indonesia **16**, 9 (2020).
[13] P. Onorato, L. M. Gratton, M. Polesello, A. Salmoiraghi and S. Oss, Phys. Educ. **53**, 035033 (2018).
[14] K. Malisorn, S. Wicharn, S. Plaipichit, C. Pipatpanukul, N. Houngkamhang and C. Puttharugsa, Phys. Educ. **55**, 015012 (2020).
[15] J. A. Sans, F. J., Manjón, A. L. J. Pereira, J. A. Gómez-Tejedor and J. A. Monsoriu, Eur. J. Phys. **34**, 1349 (2013).
[16] C. L. Countryman, Phys. Teach. **52**, 557 (2014).
[17] J. Lincoln, Phys. Teach. **56**, 652 (2018).
[18] Z. Wang, A. Koirala, K. Walsh, N. Anderson and B. Verna, Sensors **18**, 3331 (2018).
[19] A. J. Das, A. Wahi, I. Kothari and R. Raskar, Sci. Rep. **6**, 32504 (2016).
[20] F. Vesali, M. Omid, H. Mobli and A. Kaleit, Photosynthetica **55**, 603 (2017).
[21] C. Sirisathitkul, K. Ekmataruekul, Y. Sirisathitkul and W. Noonsuk, Eur. J. Sci. Theol. **16**, 179 (2020).
[22] K. Matsumura, P. Rolfe, S. Toda and T. Yamakoshi, Sci. Rep. **8**, 7298 (2018).
[23] J.P. Lomaliza and H. Park, Multimedia Tools Appl. **76**, 21051 (2017).
[24] L. Novakova and T. L. Pavlis, J. Struct. Geol. **97**, 93 (2017).
[25] L. Vračar, M. Milovančevič and P. Karanikič, Facta Univ. Ser.: Mech. Eng. **13**, 143 (2015).
[26] I. Hussain, K. Ahamad and P. Nath, RSC Adv. **6**, 22374 (2016).
[27] A. J. Batista-Leyva, Rev. Cubana Fis. **36**, 66 (2019).
[28] https://www.electronicdesign.com/technologies/android/article/21801487/hardware-design-guide-to-smartphone-ambientlight-sensing

PROPIEDADES ELECTROQUÍMICAS DE POE-$LiClO_4$-LLTO, UN ESTUDIO PRELIMINAR

ELECTROCHEMICAL PROPERTIES OF POE-$LiClO_4$-LLTO, A PRELIMINARY STUDY

C. R. Milian-Pila†, E. Pérez-Cappe, Y. Mosqueda-Laffita

Instituto de Ciencia y Tecnología de Materiales de la Universidad de la Habana (IMRE-UH), Cuba; pila@imre.uh.cu
† autor para la correspondencia

Recibido 19/3/2020; Aceptado 13/11/2020

PACS: Lithium-ion battery (batería ion-Litio), 82.47.Aa; electrolyte (electrolitos) 82.45.Gj; polymer (polímeros), 82.45.Wx; composite materials (materiales compuestos), 77.84.Lf; electrical conductivity (conductividad electroquímica), 72.80.Ng

La mayoría de los electrolitos empleados en las baterías de ion-Li comerciales son líquidos. Sin embargo, su inestabilidad electroquímica y su naturaleza inflamable han conducido a plantear su sustitución por electrolitos sólidos poliméricos. Entre los polímeros más estudiados con este fin se encuentra el polioxietileno (POE) [1]. Este polímero por sí solo no es capaz de conducir Li, por lo que se mezcla con sales electrolíticas como el $LiClO_4$ las cuales al ser solvatadas son separadas en especies iónicas capaces de moverse en presencia de un campo eléctrico. Sin embargo, la conductividad iónica de este tipo de electrolito (10^{-7} S/cm) está muy por debajo del valor (10^{-3} S/cm) que exige la tecnología [1, 2]. Una de las estrategias empleadas para incrementar este valor de conductividad es la obtención de compósitos poliméricos usando nanopartículas cerámicas como aditivos, por ejemplo, el $Li_{0.33}La_{0.56}TiO_3$ (LLTO). Recientemente nuestro grupo confirmó [3] que al emplearse un 10 % en masa de nanopartículas de LLTO se logra una conductividad iónica del orden 10^{-3} S/cm a 65 °C en los electrolitos tipo POE-$LiClO_4$-LLTO, sin embargo el desempeño electroquímico de estos prometedores compósitos poliméricos no han sido abordados con anterioridad. A continuación se reporta un estudio electroquímico preliminar de los electrolitos tipo POE-$LiClO_4$-LLTO previamente preparados [3].

Los experimentos electroquímicos fueron realizados en celdas tipo Swagelok de 13 mm de diámetro, ensambladas en atmósfera de argón. El espesor de la membrana del electrolito fue de 510 μm Para los experimentos tanto en DC como en AC se empleó un Multi-Potentiostat/Galvanostat VMP3. Los registros de impedancia se realizaron entre 100 mHz y 1 MHz con una amplitud de 10 mV. Las ventanas electroquímicas de los electrolitos con distintas composiciones de LLTO (en lo adelante P-LLTO-x, donde x = 5, 10 y 15 % en masa de LLTO, respectivamente) se determinaron a 65 °C en celdas de configuración SS—P-LLTO-x—Li, donde SS es el electrodo de trabajo de acero inoxidable, Li es el electrodo de referencia de litio metálico y P-LLTO-x es el electrolito en estudio. En cada caso se varió linealmente el voltaje de la celda a 10 mV/s, desde el voltaje de reposo (V_o) hasta 5 V; mientras que con otra celda similar a partir de V_o se disminuyó el voltaje hasta 0 V.

En la Fig. 1 se observa que para voltajes menores a 2V (V_o), la densidad de corriente (J) registrada en las celdas ensambladas es despreciable para todos los electrolitos.

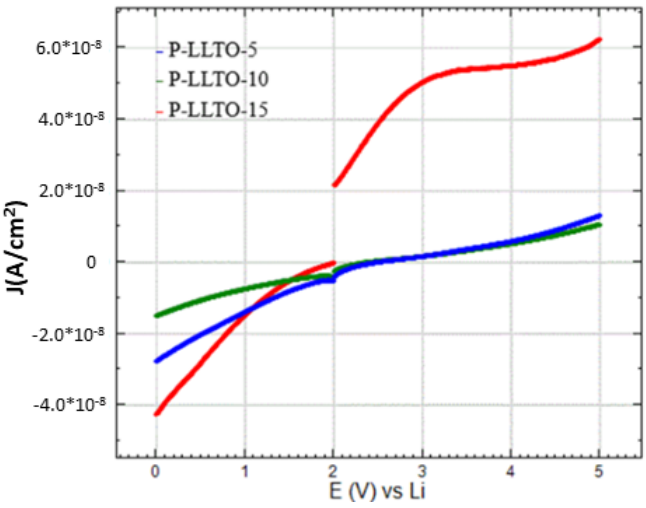

Figura 1. Medición de ventana electroquímica.

A voltajes superiores a V_o, las celdas ensambladas con los electrolitos P-LLTO-5 y P-LLTO-10 parecen ser estables. Sin embargo, la corriente de la celda que contiene el electrolito P-LLTO-15 aumenta bruscamente en el intervalo de 2-3 V, debido posiblemente a la descomposición electroquímica del electrolito en la superficie del Li. Este hecho es coherente con los resultados de un trabajo previo [3] donde se verifica que P-LLTO-15 es el compósito con mayor contenido de asociados iónicos, hecho que se ha relacionado en la literatura [4] con el incremento de reacciones electroquímica del anión ClO_4^- en la superficie del Li metálico, lo que es equivalente a inestabilidad electroquímica. Para P-LLTO-5 y P-LLTO-10, se observa un ligero cambio de pendiente a partir de los 4.5 V, lo que permite suponer que a partir de ese voltaje la estabilidad electroquímica comienza a disminuir. A partir de estos resultados afirmamos que la ventana electroquímica de P-LLTO-15 es 0-2 V; mientras que para los electrolitos P-LLTO-5 y P-LLTO-10 es de 0-4.5 V, valor que está entre

los más altos reportados para electrolitos poliméricos [5]. A partir de estos resultados y los valores de conductividad iónica previamente determinados [3] se seleccionó el compósito P-LLTO-10 para continuar el estudio electroquímico.

La estabilidad de la interfase del electrolito sólido P-LLTO-10 con el electrodo de Li metálico se verificó tras imponer 100 ciclos de carga/descarga a una celda simétrica tipo Li—P-LLTO-10—Li con una corriente de 10 μA durante 5 minutos en cada sentido. En la Fig. 2 se observa que durante los primeros 25 ciclos se alcanzan valores cercanos a 0.2 V de voltaje (E) para ambas polaridades. En los siguientes ciclos el valor de E se incrementa hasta estabilizarse en un valor alrededor de 0.3 V a partir del ciclo 50, lo cual es un claro indicio de la formación y posterior estabilización de una capa de pasivación (CP) en la interfase electrodo-electrolito que como se conoce [5–8] incrementa la resistencia de esta interfase.

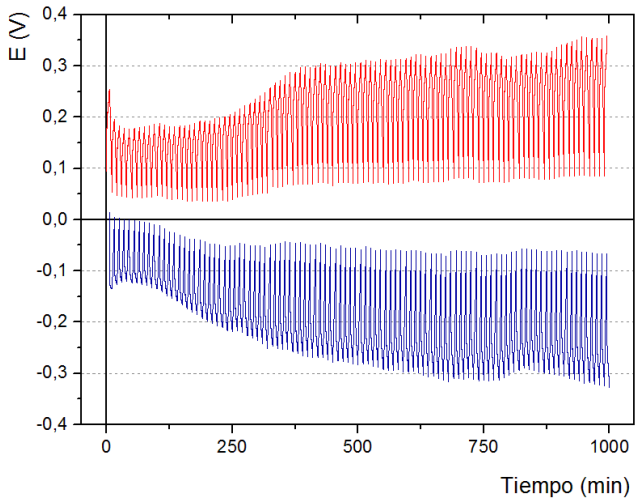

Figura 2. Ciclado de celda Li—POE-LLTO-10—Li a 65 °C para 100 ciclos carga/descarga.

Los estudios de impedancia en el plano complejo, antes y después del ciclado (Fig. 3), muestran a altas frecuencias un semicírculo, que se adjudica en la literatura a la conducción del Li^+ en el electrolito amorfo [5–8].

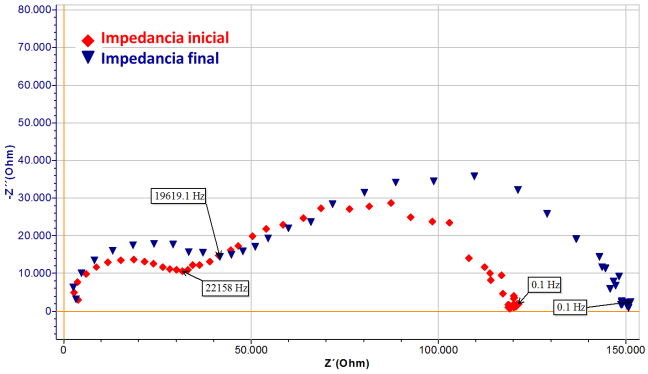

Figura 3. Espectros de Impedancia antes y después de los ciclados de celda Li—POE-LLTO-10—Li a 65 °C.

A bajas frecuencias se aprecia un segundo semicírculo, de un proceso más resistivo, que se asigna a reacciones de transferencia de carga en la interfase Li/POE-LLTO-10 [5–8].

Al terminar el ciclado las resistencias de ambos arcos aumentan, lo cual responde según la literatura [5–8] a la formación de la CP. El aumento de la resistencia del electrolito (primer arco) luego del ciclado sugiere que en la formación de la CP está involucrada la sal electrolítica [7, 8], lo que provoca una disminución de la concentración de portadores de cargas en el electrolito polimérico amorfo. El aumento de la resistencia del segundo arco se debe a que los procesos de transferencia de carga entre el electrolito y el electrodo de Li metálico, luego de varios ciclos carga/descarga, conducen a la formación de una capa nanométrica de un nuevo producto (la CP), que es permeable al Li^+, pero afecta la transferencia carga en la interfase [7,8].

Finalmente, se determinó el número de transferencia de Li^+ (T_{Li^+}) en P-LLTO-10 empleando el método de Bruce-Vincent [10] el cual combina la polarización del electrolito con un voltaje en DC (30 mV) con la técnica de espectroscopia de impedancia. Estos experimentos se realizaron, antes y después de aplicar el voltaje DC, como método para corregir los valores de corriente inicial de polarización Io y estática IS debido a la posibilidad de formación de una CP en la interfase del electrolito con el Li. La celda empleada con este fin fue tipo Li—P-LLTO-10—Li.

Para el cálculo se emplea la ecuación:

$$T_{Li^+} = \frac{I_S(\Delta V - I_0 R_{i0})}{I_0(\Delta V - I_S R_{iS})}, \quad (1)$$

Donde R_{i0} y R_{iS} representan la resistencia de la interfase antes y después de polarizar. Es válido aclarar que en las celdas ensambladas existen dos interfases electrolito-electrodo, R_{i0} y R_{iS}, por lo que el formalismo empleado [10] considera la contribución de ambas interfases a ese parámetro.

A partir de la curva de polarización, se determinó que los valores de I_0 y de I_S a 65 °C son $2.6 \cdot 10^{-4}$ mA y $8.1 \cdot 10^{-5}$ mA, respectivamente, Fig. 4.

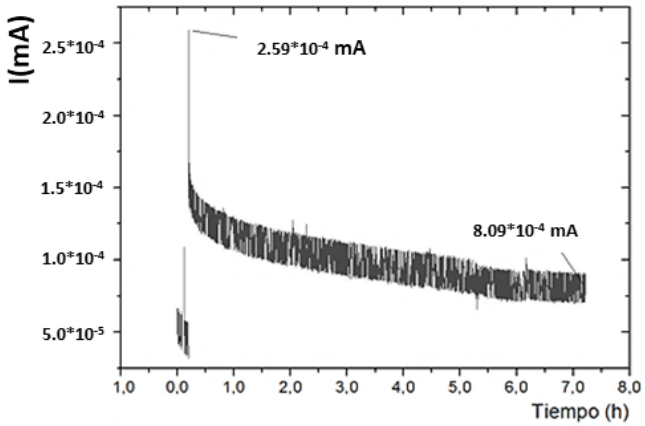

Figura 4. Curva de polarización de la determinación de T_{Li^+} para P-LLTO-10 a 65 °C.

De los registros de impedancia de la celda, antes y después de la polarización (no se muestran), ajustados con un circuito equivalente compuesto por dos bloques ZARC en serie, se determinaron R_{i0} y R_{iS} cuyos valores fueron 49.45 kΩ y 194.83 kΩ, respectivamente.

El T_{Li^+} calculado según la ecuación (1) es 0.52. Este valor es superior a lo reportado (0.3 y 0.4 [7,8]) en materiales similares basados en POE sin LLTO.

Concluimos que a partir de los valores de conductividad iónica, ventana electroquímica y T_{Li^+}, el P-LLTO-10 es un electrolito compósito polimérico con potencialidades para ser empleado en baterías basadas en Li. Sin embargo, al emplearse Li metálico como ánodo se constata la formación de una capa de pasivación que pudiera comprometer su empleo en este tipo de celdas por lo que se recomienda su estudio con otros electrodos anódicos comerciales, como los carbonosos.

Agradecemos al Proyecto P223LH001-073 del Programa Nacional de Ciencias Básicas de Cuba y al proyecto CONACyT-Mex.CB-2015/253342.

REFERENCIAS

[1] M. Marcinek, J. Syzdek y col., Solid State Ion. **276**, 107 (2015).

[2] Q. Zhang, K. Liu, F. Ding y X. Liu, J. Nano Res. **10**(12), 4139 (2017).

[3] C. R. Milian, E. L. Pérez, Y. Mosqueda y col., Solid State Sci. **88**, 41 (2019).

[4] M. Wood, C. Fang y col., Adv. Energy Mater. **8**, 1801427 (2018).

[5] X. Cheng, R. Zhang y col., Advanced Science **3**, 1500213 (2016).

[6] J. Ju, Y. Wang y col., ACS Appl. Mater. Interfaces **10**, 13588 (2018).

[7] L. Yue, M. Jun y col., Energy Storage Materials **5**, 139 (2016).

[8] J. B. Goodenough y Y. Kim, Chem. Matter. **22**(3), 587 (2010).

[9] M. Keller, A. Varzi y col., J. Power Sources. **392**, 206 (2018).

[10] P. G. Bruce, Solid state electrochemistry, 1ra Ed. (Cambridge University Press, London, 1997), pp. 95-162.

A GENERAL EXPRESSION FOR EQUIPARTITION OF ENERGY

UNA EXPRESIÓN GENERAL PARA LA EQUIPARTICIÓN DE LA ENERGÍA

P. Prasanth[a], K. M. Udayanandan[b†]

a) Department of Physics, Government Engineering College, Thrissur, Kerala, India.
b) Former HOD, Department of Physics, Nehru Arts and Science College, Kanhangad, Kerala, India; udayanandan@gmail.com†
† corresponding author

Recibido 13/4/2020; Aceptado 01/11/2020

PACS: Thermodynamics (termodinámica); 05.70.-a; statistical physics (física estadística), 05.40.-a; statistical mechanics (mecánica estadística), 05.20.Jj

I. INTRODUCTION

Equipartition theorem (EPT) is a very useful result obtained in thermodynamics. There were many physicists behind the development of this great concept. Rief [1], a famous author of the statistical physics book "Fundamentals of Statistical and Thermal Physics" wrote about the equipartition theorem as "If a system described by classical statistical mechanics is in equilibrium at the absolute temperature T, every independent quadratic term in its energy has a mean value equal to $\frac{1}{2}kT$." It was John James Waterston [2] who proposed the equipartition of energy first. Maxwell [3] and Boltzmann had also contributed to the theorem of equipartition. In order to find the energy distribution in black body radiation, Lord Rayleigh [4] used equipartition theorem. Those phenomena which were not in accordance with the EPT were later solved by the quantum theory [5,6]. Just like Rief many other authors considered systems with quadratic Hamiltonian, while non quadratic systems were not analyzed in their respective publications [1, 7–10]. Recently using Tolman's theorem [11] we [12] developed a general expression for the EPT which is applicable to non quadratic Hamiltonian also, which is given below.

$$< E >= \frac{DNkT}{l}, \tag{1}$$

where l is the power of energy function, N is the number of particles, k is the Boltzmann constant, T is the absolute temperature and D is the dimension. In the above mentioned paper we used only simple non quadratic Hamiltonian. But in this paper we develop a general expression for any type of Hamiltonian that can be expressed in polynomial form. Finally we applied the general equation to two nonlinear Hamiltonians which contain all possible combinations of position and momentum to find the internal energy.

II. FINDING AVERAGE ENERGY

In this paper our aim is not to redefine the EPT, but to find an expression for average energy for some Hamiltonian's in the polynomial form. We will do this only for one dimensional Hamiltonian, which can be extended to D dimension. Usually we apply the EPT for systems with Hamiltonian having one or several terms with each term of the form q^l where q is momentum or position variable and l is the power of that variable and we get the average energy using Tolman's theorem given by the equation

$$< q\frac{\partial H}{\partial q} >= kT. \tag{2}$$

But if we have a Hamiltonian containing terms like q_1q_2 (product of two variables) or $q_1^2q_2$, we cannot apply the above method to find the average energy. Hence, we find the average energy using Statistical Mechanics and then formulate a general expression. First we find the partition function and then we separate the partition function into temperature dependent and independent terms and then find the average energy.

III. GENERAL EXPRESSION FOR THE EQUIPARTITION OF ENERGY

If we have a Hamiltonian with n variables $q_1, q_2, q_3, ..., q_n$ with powers $l_1, l_2, l_3, ..., l_n$ like

$$H = \prod_i a_i {q_i}^{l_i},$$

where i is from 1 to n and a_i's are constants.

This will contribute

$$< E >= \frac{nkT}{\sum_{i=1}^{n} l_i},$$

towards the internal energy where $\sum_{i=1}^{n} l_i$ should not be zero.

Hamiltonian

$$H = a_1 q_1^{l_1} a_2 q_2^{l_2} a_3 q_3^{l_3} .....a_n q_n^{l_n} = \prod_i a_i {q_i}^{l_i}.$$

Single particle partition function

$$Q = C_1 \int_a^b dq_1 dq_2 dq_3 .....dq_n e^{-\frac{1}{kT}\left(\prod_i a_i {q_i}^{l_i}\right)},$$

where C_1 is a constant.

$$Q = C_1 \int_a^b dq_1 dq_2 dq_3 ..... dq_n e^{-\frac{\prod_i a_i}{k}\left(\frac{{q_1}^{l_1}{q_2}^{l_2}.....{q_n}^{l_n}}{T}\right)}.$$

Now we will separate the partition function into temperature dependent and independent terms by the change of variables. We know from the EPT for a single variable that for any arbitrary variable q^n, average energy is $\frac{DkT}{n}$. Thus the contribution from each q will depend on its power. If q_i's have the same power then they contributes equally to the energy. Then we will divide T equally to all the q_i's . If q_i's have different power then we have to find the ratio of the powers and then divide T in the that ratio. That is each ${q_i}^{l_i}$ will be divided by $T^{\frac{l_i}{\sum_i l_i}}$.

$$Q = C_1 \int_a^b dq_1 dq_2 .... dq_n e^{-\frac{\prod_i a_i}{k}\left(\frac{{q_1}^{l_1}}{T^{\frac{l_1}{\sum_i l_i}}}\frac{{q_2}^{l_2}}{T^{\frac{l_2}{\sum_i l_i}}}....\frac{{q_n}^{l_n}}{T^{\frac{l_n}{\sum_i l_i}}}\right)}.$$

Putting $\frac{q_1}{T^{\frac{1}{\sum_i l_i}}} = {q_1}'$, $\frac{q_2}{T^{\frac{1}{\sum_i l_i}}} = {q_2}'$,..., $\frac{q_n}{T^{\frac{1}{\sum_i l_i}}} = {q_n}'$ we get the partition function as

$$Q = CT^{\frac{n}{\sum_{i=1}^n l_i}},$$

where C is independent of temperature. Then the average energy

$$U = \frac{nkT}{\sum_{i=1}^n l_i}.$$

III.1. Note 1

If $\sum_{i=1}^n l_i = 0$ like $l_2 = -l_1$ or $l_3 = -(l_1 + l_2)$ we get zero in the denominator. Such cases cannot occur because, then their contribution to the energy will be zero and we cannot have a formula like this.

III.2. Note 2

We took the limits of the integral as a to b. In case of potentials with even exponents the limits are from $-\infty$ to ∞. Here if the l_i's are odd we take the modulus of q_i or we have to take the limit from 0 to infinity. Such issues usually occur in statistical mechanics. For example if we are taking the gravitation potential $V = mgz$, z is the height from the earth and we can take the limit only from 0 to ∞.

IV. EXAMPLES

We will work out one example using the same procedure as above. After confirming that our general formula will work we will apply for other Hamiltonian forms.

IV.1. Two different position variables with same power

1. Consider a potential of the form $V = Kxy$. Then let the Hamiltonian be

$$H = \frac{p_x^2}{2m} + \frac{p_y^2}{2m} + Kxy.$$

Here we already know the contribution from first two terms($\frac{kT}{2}$ each) which contains only one variable. We have to find out the contribution by the term Kxy towards average energy. For that we will find the average energy by the whole Hamiltonian and then subtract the contribution by the first two terms. Single particle partition function is

$$Q_1 = \int_{-\infty}^{\infty}\int_{-\infty}^{\infty} \frac{dp_x dp_y dx dy}{h^2} e^{-\frac{1}{kT}\left(\frac{p_x^2}{2m}+\frac{p_y^2}{2m}+Kxy\right)},$$

Putting $\frac{p_x}{T^{\frac{1}{2}}} = p_x'$, $\frac{p_y}{T^{\frac{1}{2}}} = p_y'$, $\frac{x}{T^{\frac{1}{2}}} = x'$, $\frac{y}{T^{\frac{1}{2}}} = y'$

$$Q_1 = \int_{-\infty}^{\infty}\int_{-\infty}^{\infty} \frac{T^{\frac{1}{2}}dp_x' T^{\frac{1}{2}}dp_y' T^{\frac{1}{2}}dx' T^{\frac{1}{2}}dy'}{h^2} e^{-\frac{1}{k}\left(\frac{p_x'^2}{2m}+\frac{p_y'^2}{2m}+Kx'y'\right)}.$$

We get $Q_1 = CT^2$ where C is independent of T.

$$U = kT^2\frac{\partial \ln CT^2}{\partial T} = 2kT.$$

We can see that potential energy $V = Kxy$ alone contributes kT towards internal energy, since the 2 dimensional kinetic energy contributes kT. Now we can find the same by using our general expression. We have

$$U = \frac{nkT}{\sum_{i=1}^n l_i} = \frac{2kT}{1+1} = kT.$$

2. Take another potential $V = Kx^2y^2 = K(xy)^2$
Here $n = 2$, $l_1 = 2$ and $l_2 = 2$.

$$U = \frac{nkT}{\sum_{i=1}^n l_i} = \frac{2kT}{2+2} = \frac{kT}{2}.$$

Similarly we can show that $V = K(xy)^3$ contributes $\frac{1}{3}kT$, $V = K(xy)^4$ contributes $\frac{1}{4}kT$ towards internal energy.

IV.2. Two position variables with same power with l negative

1. $V = \frac{K}{xy}$
Here $n = 2$, $l_1 = -1$ and $l_2 = -1$. So

$$U = \frac{nkT}{\sum_{i=1}^n l_i} = \frac{2kT}{-1+-1} = \frac{kT}{-1}.$$

2. $V = \frac{K}{x^2y^2} = \frac{K}{(xy)^2}$
Here $n = 2$, $l_1 = -2$ and $l_2 = -2$.

$$U = \frac{nkT}{\sum_{i=1}^n l_i} = \frac{2kT}{-2-2} = \frac{kT}{-2}.$$

Similarly we can show that $V = \frac{K}{(xy)^3}$ contributes $\frac{kT}{-3}$, and $V = \frac{K}{(xy)^4}$ contributes $\frac{kT}{-4}$ towards internal energy.

IV.3. *Two position variables with different powers*

1. For a potential $V = Kx\,y^2$

$n = 2$, $l_1 = 1$ and $l_2 = 2$.

$$U = \frac{nkT}{\sum_{i=1}^{n} l_i} = \frac{2kT}{1+2} = \frac{2kT}{3}.$$

So $V = Kxy^2$ contributes $\frac{2}{3}kT$ towards internal energy.

2. $V = Kxy^3$

Here $n = 2$, $l_1 = 1$ and $l_2 = 3$.

$$U = \frac{nkT}{\sum_{i=1}^{n} l_i} = \frac{2kT}{1+3} = \frac{kT}{2}.$$

IV.4. *Two position variables with different powers with l_1 and l_2 negative*

$V = \frac{K}{xy^2}$

Here $n = 2$, $l_1 = -1$ and $l_2 = -2$. By using our general expression

$$U = \frac{nkT}{\sum_{i=1}^{n} l_i} = \frac{2kT}{-1+-2} = \frac{-2kT}{3}.$$

IV.5. *Position and momentum variables with same and different powers*

1. $H = xp_x$

Here $n = 2$, $l_1 = 1$ and $l_2 = 1$.

$$U = \frac{nkT}{\sum_{i=1}^{n} l_i} = \frac{2kT}{1+1} = kT.$$

2. $H = x^2 p_x$

Here $n = 2$, $l_1 = 2$ and $l_2 = 1$.

$$U = \frac{nkT}{\sum_{i=1}^{n} l_i} = \frac{2kT}{2+1} = \frac{2kT}{3}.$$

3. $H = x^2 y^4 p_x {p_y}^2$

Here $n = 4$, $l_1 = 2$, $l_2 = 3$, $l_3 = 1$ and $l_4 = 2$. So

$$U = \frac{nkT}{\sum_{i=1}^{n} l_i} = \frac{4kT}{2+4+1+2} = \frac{4kT}{9}.$$

V. TWO NONLINEAR OSCILLATORS

V.1. *Henon Heiles oscillator*

In 1964 Michel Henon and Carl Heiles published an article titled "The applicability of the third integral of motion: Some numerical experiments" [13]. Their idea was to find a third integral of motion in a galactic dynamics. For that purpose they took a simplified two dimensional nonlinear axi-symmetric potential. They showed that this potential is equivalent to the problem of the motion a particle in a plane in an arbitrary potential. After several trials they took the following potential for study

$$V(x,y) = \frac{1}{2}x^2 + \frac{1}{2}y^2 - \frac{1}{3}y^3 + x^2 y.$$

The Hamiltonian of a Henon Heiles oscillator is

$$H = \frac{1}{2}p_x^2 + \frac{1}{2}p_y^2 + \frac{1}{2}x^2 + \frac{1}{2}y^2 - \frac{1}{3}y^3 + x^2 y.$$

In this Hamiltonian we have both x and y coordinates coming together. We had avoided constants with each component necessary for dimensional balance, which are not required for our purpose.

V.2. *Van der pol oscillator*

The Van der pol oscillator is an oscillator with non-linear damping obtained by Balthazar Van der pol, a Dutch electrical engineer who initiated modern experimental dynamics in the laboratory during the 1920's and 1930's. He first introduced this oscillator [14] in order to describe triode oscillations in electrical circuits. The Hamiltonian of Van der Pol oscillator [15] is

$$H = p_x p_y + xy - \mu(1 - x^2) y p_y.$$

In this Hamiltonian we have different combinations of position and momentum coordinates. Thus we had two different types of Hamiltonian which contain different combinations of position and momentum so that can apply the general equation for the EPT.

VI. APPLICATION OF THE GENERAL EQUATION

We will now apply our new expression to find the average energy of HHO and VPO oscillators. Based on the above Hamiltonian, the internal energy of a Henon Heiles oscillator is

$$U = \frac{kT}{2} + \frac{kT}{2} + \frac{kT}{2} + \frac{kT}{2} + \frac{kT}{3} + \frac{2}{3}kT = 3kT.$$

For a Vander pol oscillator we get

$$U = kT + kT + \frac{3}{4}kT + kT = \frac{15}{4}kT.$$

We had shown that it is very easy to find the internal energy of any complicated Hamiltonian using our expression. Otherwise using statistical mechanics to obtain internal energy would be very difficult [16].

VII. CONCLUSION

We developed a general expression for the equipartition theorem, which is applicable for all types of Hamiltonian appearing in the form of a polynomial. Using this general EPT we obtained the average energy of Henon Heiles and Van der Pol oscillators very easily.

ACKNOWLEDGEMENT

We wish to extend our thanks to the editor and the unknown referee for improvements in the manuscript.

REFERENCES

[1] F. Reif, Fundamentals of statistical and thermal physics, (Waveland Press, 2009).
[2] J.J. Waterston, Brit. Assoc. Rep. **2**, 6 (1851).
[3] J. C. Maxwell, Philos. Mag. **14**(88), 299 (1882)
[4] Lord Rayleigh, Philos. Mag. **49**(301), 539 (1900).
[5] S. G. Brush, Arch. Hist. Exact Sci. **4**(3), 145 (1967).
[6] A. Einstein, Ann. Phys **22**, 180 (1907).
[7] K. Huang, Introduction to statistical physics, (Chapman and Hall/CRC, 2009).
[8] S. Salinas, Introduction to statistical physics, (Springer Science and Business Media, 2001).
[9] R. Bowley and M. Sanchez, Introductory statistical mechanics, (Clarendon Press, Oxford, 1999).
[10] R. K. Pathria and P. D. Beale, Statistical Mechanics, (Butterworth, 2009).
[11] R.C. Tolman, The Principles of Statistical Mechanics, (Courier Corporation, 1979)
[12] P. Prasanth, P. Nishanth and K. M. Udayanandan, Physics Education(IAPT) **35**(4), (2019).
[13] M. Henon and C. Heiles, Astron J. **69**(1), (1964).
[14] B. Van der Pol, Philos. Mag. **2**(7), 978(1926).
[15] R. Chattopadhyay, T. Shah, and S. Chakraborty, Phys. Rev. E **97**, 062209 (2018).
[16] V. L. Berdichevsky and M. V. Alberti, Phys.Rev A **44**(2), 15 (1991).

BLACK HOLES AND THE 2020 NOBEL PRIZE IN PHYSICS

AGUJEROS NEGROS Y EL PREMIO NOBEL DE FÍSICA DE 2020

Y. Bonder[a†], B. A. Juárez-Aubry[a]

Instituto de Ciencias Nucleares, Universidad Nacional Autónoma de México, Apartado Postal 70-543, Ciudad de México, 04510, México; bonder@nucleares.unam.mx†
† corresponding author

Recibido 15/11/2020; Aceptado 30/11/2020

The 2020 Nobel Prize in Physics distinguished two research projects on black holes, which are one of the most striking predictions of General Relativity. The prize was divided in two parts. The first half was awarded to Roger Penrose in recognition of his singularity theorems that guarantee that black holes, which were mathematically found since an early stage of the study of General Relativity, are not mere highly-symmetric, curious gravitational configurations, but robust predictions of the theory. The second half was awarded to Andrea Ghez and Reinhard Genzel who led two independent groups that carried out sophisticated observations of the center of our galaxy, which suggest that therein is a supermassive black hole. In this note, the main ideas of the theory of General Relativity are briefly described, as well as the main features of black holes. The two works awarded in the aforementioned Nobel prize are described.

El Premio Nobel de Física 2020 distinguió dos proyectos de investigación sobre agujeros negros, que son una de las predicciones más sorprendentes de la Relatividad General. El premio se dividió en dos partes. La primera mitad fue otorgada a Roger Penrose y reconoce los teoremas de singularidad que garantizan que los agujeros negros, encontrados matemáticamente desde una etapa temprana del estudio de la Relatividad General, no son meras configuraciones gravitacionales curiosas con alta simetría, sino predicciones robustas de la teoría. La segunda mitad se otorgó a Andrea Ghez y a Reinhard Genzel quienes lideraron dos grupos independientes que realizaron complicadas observaciones del centro de nuestra galaxia, las cuales sugieren que ahí hay un agujero negro supermasivo. En esta nota se explican las ideas principales de la teoría de la Relatividad General, así como las características principales de los agujeros negros. Se describen las dos obras premiadas en el mencionado premio Nobel.

PACS: Black holes (agujeros negros), 04.70.Bw; singularity theory (teoría de las singularidades), 02.40.Xx; general relativity (relatividad general), 04.20.-q

I. INTRODUCTION

Gravity is currently best described by General Relativity (GR), a theory postulated by Albert Einstein in 1915. This theory successfully describes gravitational phenomena from mesoscopic to cosmological scales. Many experiments confirm GR predictions [1]: from the effects on Mercury's orbit and the bending of light rays, to the gravitational redshift that is nowadays detected in laboratories. More recently, an era began in which spacetime perturbations, known as gravitational waves, are regularly detected [2] and achieving high-precision cosmological measurements is no longer a dream [3]. This "golden age" for GR has been crowned with many awards, including four Nobel prizes within the last decade.

This note concerns the 2020 Nobel Prize in Physics [4], which recognises studies on one of the most striking GR predictions: the existence of black holes. Concretely, the above mentioned prize was awarded to Roger Penrose "for the discovery that black hole formation is a robust prediction of the general theory of relativity" and to Andrea Ghez and Reinhard Genzel "for the discovery of a supermassive compact object at the centre of our galaxy," for which a black hole is the leading candidate.

GR states that gravity is an effect of spacetime geometry. The basic idea is that spacetime's geometry is "deformed" by matter (and all sorts of energy, including gravity itself), which, in turn, affects the matter propagation[1]. The basic variable describing this geometry is a pseudo-Riemannian metric tensor, which is governed by the Einstein field equations –the equations of GR–: a set of ten nonlinear, second-order, coupled differential equations. Importantly, the metric tensor allows one to compute curve lengths between any two spacetime points, thus filling spacetime with special curves that extremize such lengths. These curves are called *geodesics*. For causally-related events, they represent the paths of light or of free point-like particles in the approximation where their effect on the spacetime curvature can be disregarded. The concept of geodesics plays a central role in the discoveries that have been awarded in the 2020 Nobel Prize, as well as in many other mathematical results and empirical observations.

While solving Einstein equations in full generality is extremely hard, only a few months after the publication of GR, the first exact solution was found by Karl Schwarzschild [6] while he was serving in the German army during World War I. This solution describes the exterior of a spherical and nonrotating source, like a static star. More formally, the Schwarzschild metric is a solution of Einstein equations in vacuum for a static and spherically symmetric configuration.

When the gravity source is extremely compact, the Schwarzschild solution has a series of mind-blowing features.

[1] For an accessible introduction to GR see, for example, Ref. [5].

If the source is confined to a radius smaller than the so-called Schwarzschild radius, $r_S = 2GM/c^2$, where G and c are Newton's gravitational constant and the speed of light in vacuum, respectively, and M can be identified with the source's mass, then, the spacetime region contained inside r_S is causally disconnected from the exterior. That is, nothing can travel from the interior to the exterior. Since not even light, which achieves the maximal speed in the universe, can escape to the exterior, these objects are called black holes [7].

What is more striking is that any spherical and nonrotaing object that is compressed below its Schwarzschild radius must undergo a complete gravitational collapse. In other words, for such a body, no interaction can stop gravity from completely compressing the object. The outcome of this process was calculated [8] and the result was the formation of a spacetime region where the geometry is infinitely deformed, hidden behind an *event horizon* from far-away observers. The event horizon defines the spacetime boundary separating the interior and exterior region of the black hole, and in this case sits precisely at the Schwarzschild radius. In fact, a black hole is *defined* in mathematical terms by the existence of an event horizon. In any case, infinite spacetime deformation is a situation that lies outside the mathematical framework of GR, and such a pathological region is known as a *singularity*.

Soon after, the generalisation of Schwarzschild's solution for electrically charged sources was found [9], and in 1963, Roy Kerr discovered an exact solution of Einstein equations for rotating bodies [10] (stationary and axially symmetric solution). In all these generalisations there is an event horizon and a singularity hidden behind it.

Today, we know that stars that have a mass above a certain threshold undergo the above described gravitational collapse when their nuclear fuel, which generates outward pressure, comes to an end. This is because the dominant interaction at that stage is gravity, which is attractive. Still, in the mid 20th century it was hard to believe that such a process could actually occur in nature. At that time, two important questions remained open: Are the singularities a feature of the simplifying assumptions used to find exact solutions or are they generic consequences of the gravitational collapse? And, do black holes actually exist or are they mere mathematical curiosities of GR? Answers to these questions were worth the 2020 Nobel Prize in Physics.

II. SINGULARITY THEOREMS

As we have mentioned, the 2020 Nobel Prize in Physics was divided in two parts. The half that was awarded to Roger Penrose corresponds to mathematical studies on the emergence of spacetime singularities. Concretely, for the development of the first so-called *singularity theorem* in 1965 [11]. Singularity theorems state that, under certain conditions, GR predicts the generation of a spacetime singularity. In particular, Ref. [11] shows that a singularity must develop inside a black hole.

The first task to study these theorems is to rigorously define singularities. Intuitively, a singularity is a spacetime region where the geometry has an infinite bending. However, this is not a good-enough definition in a theory where the dynamical variables describe the geometry itself. In addition, one needs to make sure that the variable describing the spacetime bending that blows up is coordinate independent as there are situations where problems in the coordinates give rise to infinities. The definition of a singularity that is used in these theorems reflects the fact that spacetime "suddenly endsïn a singularity. Therefore, one can "detect" a singularity if there are geodesics that cannot be extended any further.

The second step in proving the singularity theorems concerns a set of geodesics, technically referred to as a congruence. A key equation for singularity theorems is one developed by Amal Kumar Raychaudhuri to characterise the congruence evolution [12]. It is a consequence of Raychaidhuri's equation that if matter has nonnegative energy density –a reasonable physical assumption–, or more precisely, that certain *energy conditions* hold [13], then the congruences of causal geodesics tend to focus at some point within a finite geodesic parameter (e.g. within finite proper time for a test observer). Energy conditions imply geometrical conditions by the Einstein equations, and can thus be imposed even in spacetimes without matter.

The central concept introduced by Penrose to reach his conclusions is the following: consider now a two-dimensional, spacelike, closed set in spacetime. We can imagine such a set as a spherical surface or deformations thereof. There are two congruences of *lightlike geodesics* –the paths of light rays– orthogonal to this surface, defined by outgoing and ingoing sets of lightrays. Penrose defines such a two-dimensional set as a *trapped surface* if both its ingoing and outgoing lightlike congruences have a focusing behaviour towards the surface itself. Thus, congruences tend to locally meet in the future: they are trapped! The key insight is that such trapped surfaces exist generically in the interior region of black hole spacetimes, whether they are static and spherically symmetric or not.

The Nobel-winning result that Penrose showed is that if a spacetime satisfies the Einstein equations and is globally hyperbolic (i.e., has well-posed dynamics) with a noncompact Cauchy surface, and a suitable energy condition holds, then the existence of a trapped surface implies the existence of a singularity – the spacetime cannot be *null geodesically complete* in the sense that there is at least one null ray that "ends", thus defining a singularity.

The proof is by contradiction and, remarkably for its time, applies techniques of *differential topology* to GR. It relies on defining the set of all points to the future of the Cauchy surface (technically in its future time development) that can be joined to the trapped surface by a future-leading smooth timelike curve. The boundary of this set is a compact lightlike surface, since lightrays meeting the trapped surface form a caustic in the future at finite geodesic parameter due to the energy condition. The contradiction is now achieved by assuming sufficiently "long"null curves on the lightlike surface (which is acceptable if one has null geodesic completeness) and constructing a homeomorphism between this compact lightlike surface and the noncompact Cauchy

surface of spacetime. Note that there are no assumptions regarding spacetime symmetries in this proof, and for the matter fields it is only assumed that they are physically realistic in the sense of the energy conditions.

The above mentioned result was the first singularity theorem to be proven, but not the last! Soon after, Roger Penrose and Stephen Hawking were able to generalise this result [14]. In particular, they were able to prove singularity theorems that do not require the assumption that spacetime must be globally hyperbolic and, importantly, used similar techniques to show that, under certain assumptions, the singularity at the beginning of the universe, i.e., the Big Bang, is an unavoidable consequence of GR.

III. ASTROPHYSICAL EVIDENCE OF SUPERMASSIVE BLACK HOLES

According to the results discussed in the previous section, it is clear that the mathematical structure of GR predicts the existence of singularities, which are generally believed to lie inside a black hole. Yet, at the time it was unclear if there were black holes lurking out there in the universe. There are now several empirical indications of the existence of black holes; one of them was awarded with the other half of the 2020 Nobel Prize in Physics. Other experiments that have collected evidence supporting the existence of black holes include the detection of gravitational waves that are compatible with what is expected from binary black hole collisions [2], and the "picture" of the object at the centre of the Messier 87 galaxy by the array called Event Horizon Telescope [15].

The black holes evidence that merited Andrea Ghez and Reinhard Genzel the 2020 Nobel Prize was obtained by observing the centre of our galaxy. While each one of the Nobel Laureates lead an independent experiment [16,17], both of these are similar and their basic principle is as follows: if one can trace the path of stars located close to the centre of the galaxy to the point that one can reconstruct their orbits, then, using Kepler's third law, it is possible to infer the mass of the central object. In addition, one can set an upper limit on the radius of the central object, since it must be smaller than the perihelion of the star's orbit. Interestingly, for the object at the centre of our galaxy, the mass is estimated to be several million times the mass of the Sun –the orbiting stars can be seen as test particles following geodesics–, but its size is such that it is smaller than the corresponding Schwarzschild radius. In addition, this central object does not seem to emit light. Therefore, the best suiting candidate to lie at the centre of our galaxy is a black hole.

It should be mentioned that these astronomical observations are daring, as there is dust in our light path to the centre of our galaxy, which absorbes visual light, and a high resolution is required. Therefore, the observations are done in the infrared and using sophisticated adaptive optics techniques to correct for atmospheric disturbances. The group of Andrea Ghez [16] uses a 10 m telescope at the W.M. Keck Observatory, which is located in Hawaii, while Reinhard Genzel's group [17] utilises the Very Large Telescope located in the Atacama desert, in the northern part of Chile.

Note that the object in the centre of our galaxy has a mass that is many orders of magnitude larger than the mass of a black hole that can be generated by the gravitational collapse of a star. Hence, this type of black holes are called *supermassive black holes*. Remarkably, to date there is no compelling explanation of the mechanisms that produces these black holes [18].

IV. CONCLUDING REMARKS

Black holes are one of the most intriguing predictions of GR and we now have mathematical and empirical evidence that these objects do exist in our universe. Crucially, the role of black holes in future scientific developments seems bright: on the one hand, understanding how supermassive black holes arise is one of the most important questions in astrophysics. On the other hand, singularities can be regarded as a breakdown of the theory at hand, GR, suggesting that there should be a new theory of gravity that resolves the singularities. It is believed that this new theory should also be compatible with the quantum description of the matter fields, and thus, it goes by the name of *quantum gravity*.

In the quest for quantum gravity, black holes must play a central role. In fact, as Hawking postulated [19], if quantum phenomena and gravity are considered together, black holes are not as dark as we think. They surprisingly emit radiation at the so-called *Hawking temperature* and should, in principle, eventually evaporate. In any case, the yet-unknown quantum gravity theory will, very likely, revolutionise Physics, and black holes could be key players in the construction of such a theory. While the 2020 Nobel Prize was awarded to scientific projects that solved very important questions, they also raised new questions that should improve our understanding of concepts like space, time, and gravity.

ACKNOWLEDGEMENTS

Y. Bonder acknowledges support from the grant UNAM-DGAPA-PAPIIT IG100120. B. A. Juárez-Aubry is supported by a CONACYT postdoctoral fellowship.

REFERENCES

[1] C.M. Will, Living Rev. Relativ. **17**, 4 (2014).
[2] B.P. Abbott et al. (LIGO Scientific Collaboration and Virgo Collaboration), Phys. Rev. Lett. **116**, 061102 (2016).
[3] Y. Akrami, R. Kallosh, A. Linde, and V. Vardanyan, Fortschr. Phys. **67**, 1800075 (2019).
[4] The Nobel Prize in Physics 2020 (www.nobelprize.org/prizes/physics/2020/summary).
[5] R.M. Wald, "Space, Time, and Gravity: The theory of the big bang and black holes," second edition (The University of Chicago Press, 1992).
[6] K. Schwarzschild in "The Collected Papers of Albert Einstein" **8a**, 169 (1915).
[7] R. Ruffini and J.A. Wheeler, Physics Today **24**, 30 (1971).
[8] J.R. Oppenheimer and G.M. Volkoff, Phys. Rev. **55**, 374 (1939).
[9] G. Nordström, Verhandl. Koninkl. Ned. Akad. Wetenschap. **26**, 1201 (1918).

[10] R.P. Kerr, Phys. Rev. Lett. **11**, 237 (1963).
[11] R. Penrose, Phys. Rev. Lett. **14**, 57 (1965).
[12] A.K. Raychaudhuri, Phys. Rev. **98**, 1123 (1955).
[13] R.M. Wald, "General Relativity," (The University of Chicago Press, 1984), section 9.2.
[14] S.W. Hawking and R. Penrose, Proc. R. Soc. Lond. A **548** 314529 (1970).
[15] K. Akiyama et al. (The Event Horizon Telescope Collaboration), Astrophys. J. Lett. **875** (1): L1 (2019).
[16] A. Ghez et al., Astrophys. J. Lett. **509**, 678 (1998).
[17] R. Schödel et al., Nature **419** 694 (2002).
[18] A. Kulier et al., Astrophys. J. **799** 178 (2015).
[19] S. W. Hawking, Commun. Math. Phys. **43**, 199 (1975).

WHAT ARE ELEMENTARY PARTICLES? FROM DARK ENERGY TO QUANTUM FIELD EXCITATIONS

¿QUÉ SON LAS PARTÍCULAS ELEMENTALES? DE LA MATERIA OSCURA A LAS EXCITACIONES DE CAMPOS CUÁNTICOS

W. Bietenholz

Instituto de Ciencias Nucleares, Universidad Nacional Autónoma de México, A.P. 70-543, C.P. 04510 Ciudad de México, Mexico; wolbi@nucleares.unam.mx.
† corresponding author

Recibido 12/4/2020; Aceptado 10/11/2020

We describe the very nature of the elementary particles, which our (visible) Universe consists of. We underline that they are not point-like, and we depict their ways of interacting. We also address puzzles that occur even in the absence of particles, in the vacuum.

Describimos la naturaleza misma de las partículas elementales, las cuales componen nuestro Universo (visible). Subrayamos que no son puntuales, y representamos sus formas de interactuar. Abordamos también acertijos que ocurren incluso en ausencia de partículas, en el vacío.

PACS: Theory of fields and particles (teoría de campos y partículas), 11.40.-q; supersymmetry (supersimetría) 11.30.Pb; cosmological constant (constante cosmológica), 98.80.Es; dark energy (energía oscura) 95.36.+x.

This article is meant to be qualitative and very simple; slightly technical remarks are added as footnotes and as an appendix.

I. BASIC BUILDING BLOCKS OF MATTER

If we break up any kind of matter into smaller and smaller pieces, we ultimately reach a point of basic building blocks, which are not divisible anymore: Democritus would have called them "atoms", but for us these are the *elementary particles*. So far 25 types of elementary particles have been experimentally confirmed; the entire visible Universe consists of them.[1] They are incorporated in the Standard Model of Particle Physics, see *e.g.* Ref. [1]; prominent examples are the *electron* and the *photon* (the particle of light). As if this wasn't enough, the literature of theoretical physics is replete with speculations about additional types of elementary particles.

Figure 1. We can easily decompose a Lego house into its building blocks. If we keep on decomposing matter down to its most fundamental building blocks, we end up with elementary particles.

We do not go through the list of all these known elementary particles (let alone the hypothetical ones); their table can easily be found in many places. Instead we want to address a question, which is seldomly discussed in popular science: *what kind of objects are elementary particles?* Amazingly, even in the physics literature this issue is treated as an orphan: there are numerous textbooks devoted to particle physics, which hardly clarify what these objects actually are.[2]

The common intuitive picture, which is based on our perception of macroscopic objects, views them as "tiny balls". We are going to point out that this picture is erroneous, and that they are not "point-like objects" either. The latter (mysterious) claim is wide-spread, but that doesn't make it correct.

II. QUANTUM FIELD THEORY

The mathematical formalism that successfully describes elementary particles is called *Quantum Field Theory*. In the course of the 20th century it has replaced Quantum Mechanics.[3]

In order to symbolically interpret the term *field theory*, we could view the entire Universe as the "meadow-land", endowed with some kind of "grass blades" everywhere. The latter take an abstract mathematical form: certain variables are permanently attached to each point in space. A "field" is one type of such variables. Each variable, at a given point, can change its value as a function of time, we could say that

[1] This includes quarks and gluons, although they cannot be directly detected, as well as leptons, electroweak gauge bosons and the Higgs particle. We refer to the *visible* part of the Universe in order to exclude Dark Matter and Dark Energy; the latter will be addressed in Appendix A. Gravitation belongs to our daily experience, but the particle, which is held responsible for it — the graviton — has not been observed.

[2] The text is written in terms of "particles", and the formulae in terms of "fields", but the question of how these terms are related is by no means as clear as it is supposed to be.

[3] In contrast to Quantum Mechanics and classical physics, Quantum Field Theory successfully incorporates the concepts of both quantum physics and Special Relativity. (A complete unification of quantum physics with General Relativity has not been achieved.)

it "vibrates" or "oscillates". In the following we are going to refer to an "oscillator", a term which can be reasonably well justified, see *e.g.* Ref. [2].

Figure 2. A field in the usual sense. In physical field theories, the meadow-land is converted into space, and the grass blades into abstract mathematical variables, which we denote as "oscillators".

It is always risky to invoke a simplified picture for illustration purpose, but we do so nevertheless. There is a rough analogy with sound in the air: let us assume the absence of wind in some volume, so the molecules of the air have (essentially) static equilibrium positions, but their vibrations around them represent sound. This bears some similarity with field theory, which we can further strengthen by referring to sound in a crystalline solid, where ions oscillate around their grid sites, with displacements analogous to a field variable. We repeat, however, that actual field variables are abstract mathematical quantities.

So let us denote a field variable at one point as an *oscillator*. It can be in its *ground state*, where its energy E_0 is minimal (in quantum physics we have $E_0 > 0$),[4] or in an *excited state* with a higher energy $E > E_0$. As we mentioned before, the state of any of these oscillators (which fill the entire space) is time-dependent.

III. VACUUM AND PARTICLES

At this point, we only consider one field, *i.e.* one type of oscillator.

Let is assume all the oscillators in some volume to be in their ground state. We denote this as the *vacuum*, which means that the field takes its state of minimal energy in this volume.[5] We would say "nothing is there", although the oscillators are actually there, but none of them vibrates with any excitation energy $E > E_0$. It is tempting to interpret the ground state energy throughout the Universe as *Dark Energy*; this leads, however, to a dreadful puzzle, which we address in Appendix A.

Figure 3. A set of classical oscillators; quantum oscillators are hard to depict.

Now let us insert a single particle into this volume, say a particle at rest (with respect to the volume). This requires a massive particle, like the electron, and we denote its mass as $m > 0$.[6]

What does this mean for the field under consideration? It will be excited, such that its total energy inside this volume takes its minimal value above the vacuum energy. In quantum physics, this minimal excitation corresponds to a finite energy gap ΔE; the energy cannot be increased continuously above the vacuum energy. We also know that this energy gap, *i.e.* the particle's rest energy, is related to the particle mass by a famous formula, $\Delta E = mc^2$ (where c is the speed of light in vacuum).

If these oscillators were all independent, the obvious way to arrange for a minimal excitation would be to excite just one of them to the first energy level and leave all the rest in their ground state. However, this is not how it works: the oscillators are *coupled* to the their nearby neighbours, hence exciting one of them inevitably affects its vicinity (cf. footnote 6).[7]

Instead we obtain a smooth excitation energy profile, which we assume to have a maximum in its centre. It turns out that it decays exponentially with the distance from this centre, where (in the free case) the range of the decay is proportional to the inverse particle mass, range $\propto 1/m$. This range coincides with the Compton wavelength [3].

For a massless particle, like the photon, this decay is slower: here it only follows some negative power of the distance from the particle centre, but not an exponential decay [3]. In either case, with $m = 0$ or $m > 0$, we see that particles do have

[4] We are referring to the simple case of bosonic fields, like the photon field or the Higgs field. There is another class of particles called *fermions*, which include the electron, and which emerge from fields with $E_0 < 0$, see Appendix A.

[5] For simplicity we refer to a free "neutral scalar field", where the field is real valued. Other fields involve different types of variables, and when the fields are self-coupled or coupled to other fields, *i.e.* not free, then even the vacuum often takes a complicated structure.

[6] Mathematically this is achieved by applying a so-called creation operator to the vacuum state. It may have a fixed momentum, but it is not restricted to one spatial point.

[7] In mathematical terms, there are field derivatives contributing to the energy, hence a discontinuous spike — or even just a very sharp peak — is not suitable for an excitation with minimal energy.

an *extent*, they are *not* point-like objects.[8] Such profiles are symbolically illustrated in Figure 4.

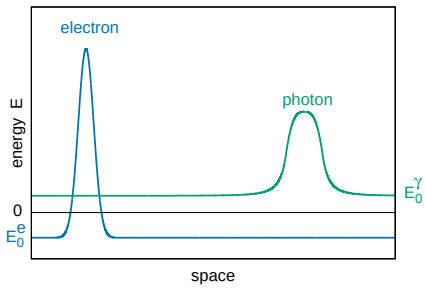

Figure 4. A symbolic illustration of the energy profiles of an electron and a photon, as examples for a massive and a massless elementary particle (E_0^e and E_0^γ are the corresponding ground state energies).

In the framework of this qualitative note, we stay with the observation that an elementary particles is not a point particle, only marginally touching upon the somewhat distracting question what its size amounts to. We could, for instance, define the size of a free electron with the exponential profile decay that we just mentioned, or we could refer to the so-called *form factor*, which is observed in electron scattering experiments. Mathematically, the electron form factor is the spatial Fourier transform of its electric charge distribution.[9]

Finally one might be tempted to refer to the resolution of a particle detector, for instance to the size of a pixel in a raster image. However, no matter how small the pixels are, a single photon will always be detected in only one of them, so we cannot determine a photon size in this way. This does not imply that the photon has zero extent: its profile "collapses" into just one pixel at the moment of the detection.[10]

IV. PARTICLES IN MOTION

We have seen that elementary particles can be understood as small regions, or zones, where a (quantum) field is excited. These zones, *i.e.* the particles, can *move* (say, relatively to each other). A descriptive picture is that the excited oscillators lose energy, and eventually drop down to the ground state, transferring their energy to nearby other oscillators, and so on. In this way, the particle centre moves, and with it all the excitation zone.

This picture is reminiscent of an ordinary (though Lorentz invariant) wave,[11] but one issue must be stressed: if the terms "particle" and "wave" are understood from a classical (not quantum) perspective, *i.e.* as concepts, which match our macroscopic perception, then neither of these two terms describes a quantum particle appropriately. For the lack of quantum terminology in colloquial language, we are using those terms, which have led to never-ending confusion.

V. MULTIPLE FIELDS AND PARTICLE INTERACTIONS

We now go beyond the consideration of just one particle type. From Section 1 we know that there are at least 25 different fields, *i.e.* at least 25 types of "oscillators" being present at each point of the Universe, at any time. Some of these fields are self-coupled or *coupled to each other*, this is specified in the Standard Model. Each field has its zones of excitations, corresponding to a huge number particles in the Universe,[12] which may all be in motion.

If such excitation zones of coupled fields *overlap*, particles can directly *interact* and we talk about *particle collision*. The rule that instantaneous interactions do not happen over a distance is known as *locality*. When a collision takes place, energy can be transferred from one field to another. This dynamics can also affect fields, that have not been excited before in this zone, so additional types of particles can be generated.[13]

Obviously the creation of a heavy particle requires a lot of energy. Therefore some laboratories, like CERN, accelerate massive particles almost to the speed of light and arrange for collisions at extremely high energy, in order to investigate whether this creates heavy particles, which have not yet been observed — possibly one of the hypothetical particles that theoretical physicists speculate about. The famous Higgs particle, which had been predicted since 1964 [10], was finally observed in this manner at CERN in 2011/12 [11,12] (a popular science description is given in Ref. [13]).

Once a rather heavy particle is generated, it tends to decay very rapidly (unless there is a conservation law preventing this). Then it transfers its energy to other fields, thus creating several lighter particles, which corresponds to a process of energy diffusion.[14] For instance the Higgs particle, with a mass of 125 GeV/c^2 — the second-most heavy elementary particle that we know[15] — has a lifetime is only about 10^{-22} sec.

VI. THE INTERWOVEN UNIVERSE

Another manifestation of particle interactions are attractive or repulsive *forces*.[16] In contrast to Newton's formulation of

[8] This is correctly emphasised *e.g.* in Refs. [4,5].

[9] Ref. [6] explains how to compute this radius in Quantum Electrodynamics.

[10] We don't know how exactly this happens, but it does happen. It is analogous to the notorious "collapse of a wave function" in Quantum Mechanics.

[11] Frank Wilczek occasionally denotes a quantised field excitation as a *"wavicle"* [7], which makes sense, but the established term is "particle".

[12] Even the "empty" cosmic space is packed with about 411 photons and 366 neutrinos per cm^3, see *e.g.* Ref. [8]. These are the most abundant types of particles.

[13] Capturing the dynamics of particle creation and annihilation is an essential achievement of Quantum Field Theory, in contrast to traditional Quantum Mechanics. This property is intimately related to the statement in footnote 3, see *e.g.* Ref. [9].

[14] For further reading about particle scattering and decay, we recommend Ref. [14].

[15] 1 GeV = 10^9 eV (electronvolt) is a unit of energy, 1 eV $\simeq 1.6 \cdot 10^{-19}$ J. For comparison, the electron and the proton have a masses of 0.000511 GeV/c^2 and 0.938 GeV/c^2, respectively.

[16] The question of how forces really emerge in Quantum Field Theory is another subject, which is not well covered in the literature, despite its importance. A sound pedagogical explanation is given in Ref. [15].

gravity, such forces do not act instantaneously at a distance — field theory is consistent with the principle of locality, as we pointed out before. For instance, the Coulomb force between two electrons is indirect: each electron affects at its location the photon field (they are coupled by the electric charge of the electron). When the electrons move closer, the energy of the coupled field system is enhanced, which implies a repulsive force[17] (in jargon, this is due to the "exchange of virtual photons").

We know that the electromagnetic force can also be attractive, for instance between the electron and its anti-particle, the positron, which carries positive electric charge.[18] Other types of intermediate fields (so-called "gluon fields") give rise to the *"strong interaction"*, and in particular to strong attraction, which (in suitable circumstances) outweighs electromagnetic repulsion. Due to such forces, some elementary particles form *bound states*, which are composite particles. The best known examples are the proton and the neutron, which build the atomic nuclei. Together with the electrons we obtain atoms, which can be further clustered to molecules. Following this sequence of composition, we reconstruct the larger structures of matter, which we have decomposed in the very beginning of this article.

However, from a fundamental perspective, such composite objects, and the entire visible Universe, ultimately consist of the elementary particles that we have described before. This is the particle physicist's view of the world: the interactions among these particles imply a very complicated, interwoven dynamics, following probabilistic rules, which we investigate.

At last, returning to the simplistic analogy with sound, we could — figuratively speaking — call this interwoven dynamics the "cosmic symphony", or "cosmic salsa concert", whatever you prefer.[19]

A. THE MYSTERY OF DARK ENERGY

The consideration in the second paragraph in Section 3 suggests the presence of a non-zero energy density ρ_{E_0} throughout the Universe. Actually ρ_{E_0} even seems to diverge: for a given field there is not just one oscillator at each space-point, but there is an oscillator for each possible frequency.

For the free, neutral, massless scalar field, one oscillator contributes the ground state energy $E_0 = \frac{1}{2}\hbar\omega$, where $\omega = \sqrt{\omega_1^2 + \omega_2^2 + \omega_3^2}$, ω_i being the angular frequencies in different directions (in 3 spatial dimensions), and $\hbar$ is Planck's constant. If we compute ρ_{E_0} for the photon field by integrating $\int d^3\omega\, \hbar\omega$, we obviously run into a divergence (a factor 2 accounts for the two photon polarisation states).

It seems natural to introduce an *ultraviolet cutoff*, say at the Planck scale $E_{\text{Planck}} = \sqrt{\hbar c^5/G} \simeq 1.2 \cdot 10^{28}\,\text{eV}$, where G is Newton's gravitational constant. This restricts the integral to $4\pi \int_0^{E_{\text{Planck}}} d\omega\, \hbar\omega^3$. Taking into account the Fourier normalisation factor $1/(2\pi)^3$, we obtain — due to the ground state energy of the free photon field — the energy density

$$\rho_{E_0} \approx \frac{E_{\text{Planck}}^4}{8\pi^2(\hbar c)^3}\,.$$

In usual studies of quantum physics, such an additive constant in the energy is irrelevant, since we are only concerned with energy *differences*.[20] If we add a constant term to the potential of some system, then this does neither affect the (field) equations of motion, nor the expectation values in Quantum Field Theory. However, this changes when we include *gravity:* note that a constant energy density ρ cannot be added to the potential in the simple space-time integrated form $\propto \int dt\, d^3x\, \rho$ — that term is not covariant. Instead the space-time metric must be involved, which is therefore affected by the quantity ρ (in General Relativity even the metric is dynamical).

As a consequence, such a constant leads to a prominent physical effect, namely (if it is sufficiently large) the *accelerated expansion of the Universe.* The driving energy density is denoted as *Dark Energy*, which can be interpreted (up to a constant factor) as Einstein's *Cosmological Constant*.[21] It corresponds to a negative pressure, which is occasionally denoted as "gravitational repulsion".

So at the *qualitative* level, it seems that we have found a neat explanation for this accelerated expansion, which was discovered at the very end of the 20th century [22, 23]. The 2011 Physics Nobel Prize was awarded for this observation.

However, our enthusiasm comes to an abrupt end when we proceed to the *quantitative* level: the observation of Refs. [22, 23], which is based on the distance and redshift of a set of type Ia supernovea, corresponds to a vacuum energy density

[17] As a simple classical picture: if static electrons are next to each other, an electric field $\vec{E}(\vec{x})$ emerges, which is almost doubled compared to a single electron. Thus the field energy $\propto \int d^3x\, \vec{E}(\vec{x})^2$ decreases when the electrons move apart.

[18] When they are close, they form a small, electrically neutral compound, which hardly affects the photon field, hence their proximity is energetically favoured.

[19] Symbolically, this seems to bear some similarity with the concept of the "harmony of spheres and numbers" or "musica universalis", a philosophical concept which was supposedly advocated by the Pythagoreans over 2500 years ago [16]. Unlike them, however, we do not focus on the motion of celestial bodies, and we discard mystical interpretations.

[20] Considering well-defined differences of physical quantities, while putting aside, or isolating, a divergent additive constant, is the basic idea of *renormalisation*.

[21] Albert Einstein introduced such a constant in his formulation of General Relativity, in order to construct a static Universe [17]. Once Edwin Hubble and others convinced him that the Universe is rapidly expanding, and it turned out that his static solution would be unstable, he dismissed this constant and accepted the expanding solutions to his theory by Alexander Friedmann and Georges Lemaître [18–20] (see Ref. [21] for a historic account). Then, for almost seven decades, the Cosmological Constant was assumed to vanish, which implies a decelerated expansion. Einstein's original value was positive, just at the (unstable) transition between a decelerated and an accelerated expansion. Today a somewhat larger Cosmological Constant is appreciated as the most obvious explanation for the observed accelerated expansion. If we understand General Relativity as a low-energy effective theory, then the presence of this constant is natural.

of about $\rho_{\rm obs} \approx (0.002\,{\rm eV})^4/(\hbar c)^3$. Now we are stunned by a tremendous discrepancy from the theoretical estimate ρ_{E_0},

$$\frac{\rho_{E_0}}{\rho_{\rm obs}} \approx 10^{121} \,.$$

This is perhaps the worst discrepancy between a theoretical prediction and an observed value in the history of science.

$E_{\rm Planck}$ is the most natural energy cutoff, but a conceivable alternative might be $E_{\rm GUT} \simeq 10^{25}\,{\rm eV}$, the energy where the three gauge couplings of the Standard Model are predicted to converge to the same strength. That reduces the above discrepancy to $\rho_{E_0,{\rm GUT}}/\rho_{\rm obs} \approx 10^{109}$, which is no salvation. If we really wanted to maintain the previous derivation, we had to lower the energy cutoff to $\approx 0.006\,{\rm eV}$ instead of $E_{\rm Planck}$, but such a ridiculously low cutoff does not make any sense whatsoever: even the rest energy of an electron is almost 10^8 times higher.[22]

To make it even worse, there is in addition the *coincidence problem:* by default, the Cosmological Constant, and therefore the Dark Energy density, is assumed to be really *constant* during the evolution of the Universe, whereas the matter density decreases due to its expansion; it has decreased by many orders of magnitude since the time of the Early Universe, see Figure 5. At that time matter density[23] dominated over vacuum energy, and in the far future it will be the other way around. It so happens that just in our time the matter density — which is dominated to about 85 % by Dark Matter (which does not interact with the photon field) — is of the same magnitude as the Dark Energy density (they only differ by about a factor of 3). Is it by accident that we just have the privilege to witness this transition, or does this "coincidence" require an explanation?[24] (Some people try to argue with the "anthropic principle", which seems like an act of desperation.)

So far we have considered the example of a *bosonic* field, in particular the photon. As we anticipated in footnote 4, there are other types of particles called *fermions* (the electron is an example), where such a huge vacuum energy density emerges with a *negative* sign, so one might hope for a large amount of cancellation.

If we were living in a perfectly *supersymmetric* world, the bosons and fermions would appear in pairs with the same mass, and indeed the vacuum energy would exactly cancel. However, even if supersymmetry exists, it has be to be *broken*, in the low-energy regime where we are living: for instance the bosonic partner of the electron, the "selectron", must be much heavier than the electron — if it exists at all — otherwise it would have been observed. The extent of supersymmetry breaking, which is required to avoid contradictions with observations, would allow for a strong reduction of the ratio $\rho_{E_0}/\rho_{\rm obs}$. It still has to be huge, though, estimates suggest at least $\approx 10^{60}$ [31] (even before knowing the LHC results), so supersymmetry does not overcome this problem either. Also the string community tried to solve the Cosmic Constant problem, without arriving at any key clue [31,32].

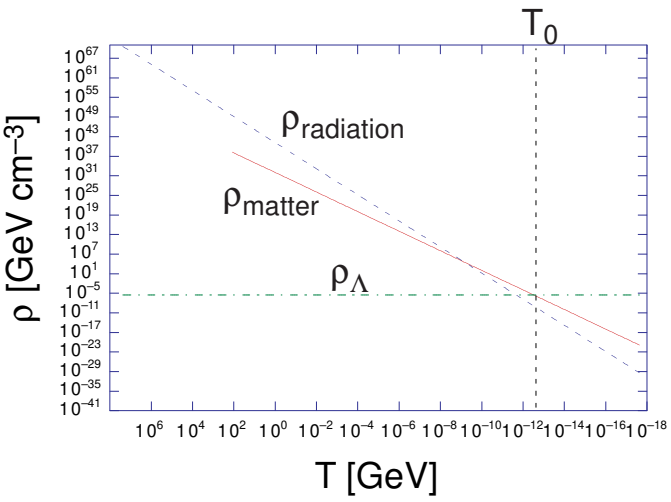

Figure 5. Illustration of the coincidence problem, adapted from Ref. [30]. That work (and many others) distinguishes "radiation" (fast moving, *i.e.* relativistic particles, mostly photons and neutrinos) from "matter": in the former (latter), most energy is kinetic (contained in the rest mass). In these terms, the first $\approx 47\,000$ years after the Big Bang were radiation-dominated, followed by the matter-dominated era, which lasted until $\approx 9.8 \cdot 10^9$ years after the Big Bang. Today, the age of the Universe is $\approx 13.8 \cdot 10^9$ years, the cosmic microwave background has the temperature $T_0 \simeq 2.7$ K (indicated in the figure), and our era is dominated by Dark Energy (ρ_Λ), to about 70 %. (For the Hubble constant, Ref. [30] inserted $H_0 = 65$ km/(s Mpc).)

It is outrageous that we do not have any convincing solution to this stunning puzzle, so this appendix finishes without a happy ending. For reviews of this outstanding issue we refer to Refs. [24,31].

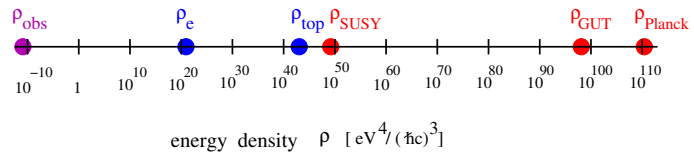

Figure 6. The energy density as observed in the Universe, $\rho_{\rm obs}$, and as obtained from the vacuum energy in Quantum Field Theory, if we insert a cutoff at the rest energy of the electron, ρ_e, or of top-quark (with a mass of 173 GeV/c^2 the heaviest known elementary particle), $\rho_{\rm top}$. These cutoffs are not motivated, they are included just for comparison. Scenarios that could be considered as somehow motivated are referring to broken supersymmetry ($\rho_{\rm SUSY}$ corresponds to the lower bound for its breaking), a cutoff at the Grand Unification scale, $\rho_{\rm GUT}$, or at Planck scale, $\rho_{\rm Planck}$. In all these cases, the theoretical energy density exceeds $\rho_{\rm obs}$ by *many* orders of magnitude.

ACKNOWLEDGEMENT

I am indebted to Uwe-Jens Wiese for sharing his insight into the concept of "wavicles". I thank Tamer Boz,

[22] At this point, the question arises whether also the field theoretic vacuum energy has been observed, since the Casimir force is now confirmed experimentally [25,26]. Then this discrepancy would be even more puzzling. However, this conclusion is not compelling, since the Casimir effect can also be derived without referring to the vacuum energy of the photon field [27–29].

[23] Here we include radiation, unlike the terminology of Ref. [30], but it doesn't matter for the statements in this paragraph.

[24] Meanwhile a number of cosmologists speculate that the Cosmological "Constant" might have changed in the course of the evolution of the Universe [24] (this is reminiscent of the coupling "constants" in Quantum Field Theory, which actually depend on the energy scale; in jargon, they are "running").

Jaime Nieto-Castellanos and Lilian Prado for reading the manuscript, as well as the authors of Ref. [30] and the American Physical Society for the permission to reproduce Figure 5. This work was supported by UNAM-DGAPA-PAPIIT, grant number IG100219.

REFERENCES

[1] M. D. Schwartz, Quantum Field Theory and the Standard Model, (Cambridge University Press, 2014).
[2] M. E. Peskin and D. V. Schroeder, An Introduction to Quantum Field Theory, (Westview Press, 1995) (Chapter 2).
[3] W. Bietenholz and U.-J. Wiese, Quantum Field Theory and the Standard Model of Particle Physics: From Fundamental Concepts to Dynamical Mechanisms, to appear in Cambridge University Press (Chapter 4).
[4] G. Scharf, Finite Quantum Electrodynamics: The Causal Approach, (Springer, 1995) Chapter 3.
[5] O. Steinmann, Perturbative Quantum Electrodynamics and Axiomatic Field Theory, (Springer, 2000), Chapter 1.
[6] S. Weinberg, The Quantum Theory of Fields, volume I, (Cambridge University Press, 1995), Chapter 11.
[7] F. Wilczek, Cent. Eur. J. Phys. **10**, 1021 (2012).
[8] A. Aguilar-Arevalo and W. Bietenholz, Rev. Cubana Fís. **32**, 127 (2015) .
[9] O. Nachtmann, Elementary Particle Physics, (Springer, 1990), Chapter 4.
[10] P. Higgs, Phys. Rev. Lett. **13**, 508 (1964).
[11] CMS Collaboration, Phys. Lett. **B716**, 30 (2012).
[12] ATLAS Collaboration, Phys. Lett. **B716**, 1 (2012).
[13] W. Bietenholz, Rev. Cubana Fís. **30**, 109 (2013).
[14] M. Maggiore, A Modern Introduction to Quantum Field Theory, (Oxford University Press, 2005), Chapter 6.
[15] A. Zee, Quantum Field Theory in a Nutshell, (Princeton University Press, 2010), Chapter 1.
[16] B. L. Van der Waerden, Die Astronomie der Pythagoreer, (North-Holland Publishing Company, 1951).
[17] A. Einstein, Sitzungsberichte der Königlich Preußischen Akademie der Wissenschaften, Berlin (1917) 142. In a letter to his friend Paul Ehrenfest (who worked in Leiden, Netherlands), dated February 4, 1917, Einstein wrote: "Ich habe auch wieder etwas verbrochen in der Gravitationstheorie, was mich ein wenig in Gefahr setzt, in einem Tollhaus interniert zu werden. Hoffentlich habt Ihr keins in Leiden, dass ich Euch ungefährdet wieder besuchen kann." (I have again committed a crime in the theory of gravitation, which endangers me a bit of being interned to a madhouse. I hope you don't have any in Leiden, so I can visit you again without danger.
[18] A. Friedmann, Z. Phys. **10**, 377 (1922).
[19] Über die Möglichkeit einer Welt mit konstanter negativer Krümmung des Raumes, Z. Phys. **21**, 326 (1924).
[20] G. Lemaître, Annales de la Société Scientifique de Bruxelles **A47**, 49 (1927).
[21] H. Nussbaumer and L. Bieri, Discovering the Expanding Universe, (Cambridge University Press, 2009).
[22] A. Riess *et al.*, Astron. J. **116**, 1009 (1998).
[23] S. Perlmutter *et al.*, Astrophys. J. **517**, 565 (1999).
[24] J. Solà, J. Phys. Conf. Ser. **453**, 012015 (2013).
[25] S. K. Lamoreaux, Phys. Rev. Lett. **78**, 5 (1997).
[26] U. Mohideen and A. Roy, Phys. Rev. Lett. **81**, 4549 (1998).
[27] J. Schwinger, Lett. Math. Phys. **1**, 43 (1975).
[28] J. Schwinger, J. DeRaad and K. A. Milton, Ann. Phys. (N.Y.) **115**, 1 (1978).
[29] R. L. Jaffe, Phys. Rev. D **72**, 021301 (2005).
[30] N. Arkani-Hamed, L. J. Hall, C. F. Kolda and H. Murayama, Phys. Rev. Lett. **85**, 4434 (2000).
[31] S.M. Carroll, Living Rev. Rel. **4**(1), 1 (2001).
[32] E. Witten, Lecture at DM2000, arXiv:hep-ph/0002297.

LA MUJER CUBANA EN LA CIENCIA Y EN LA FÍSICA: PRESENCIA, ROL Y DESAFÍOS

CUBAN WOMEN IN SCIENCE, AND IN PHYSICS: PRESENCE, RÔLE AND CHALLENGES

A. Peláiz-Barranco

Facultad de Física, Universidad de La Habana, San Lázaro y L, Vedado, La Habana 10400, Cuba; pelaiz@fisica.uh.cu
† autor para la correspondencia

Recibido 15/7/2020; Aceptado 15/8/2020

La discriminación de género es un fenómeno omnipresente en el mundo, y si bien en las últimas décadas se han observado importantes avances alcanzados por las mujeres en la educación, la aplicación de las legislaciones sobre igualdad, cambios en los roles familiares y el desafío de las tradicionales normas de género, no se ha avanzado en todas las regiones de igual manera. En la ciencia, la diferencia de género ha ido disminuyendo, pero esto no significa que las mujeres tengan hoy igualdad de oportunidades para lograr un rendimiento académico y posiciones de liderazgo igual al de los hombres, particularmente en ciencia y tecnología. Cuba no está ajena a esta situación, y aunque sus avances son relevantes, queda mucho por recorrer en este tema. Este trabajo presenta un análisis de la presencia de la mujer cubana en la ciencia, y particularmente en la física, ciencia donde la presencia masculina ha sido predominante históricamente.

Gender discrimination is an universal phenomenon, and although in recent decades important advances have been observed in women's education, the application of equality legislation, changes in family roles and the challenge of traditional gender norms, the progress has not been the same in all regions. In science, gender difference has been decreasing, but this does not mean that women have opportunities to achieve academic performance and leadership positions equal to that of men, particularly in science and technology. Cuba is not free from the problem, and although its progress is remarkable, there is still a long way to go in this area. The present paper analyzes the presence of Cuban women in science, and particularly in physics, where male presence has been traditionally dominant.

PACS: History of science (historia de la ciencia), 01.65.+g; social systems, social organizations (sistemas sociales, organizaciones sociales), 89.65.Ef

I. MUJERES EN LA CIENCIA. CONTEXTO MUNDIAL

La discriminación de género ha sido reconocida desde hace mucho tiempo como un fenómeno omnipresente en el mundo. En las últimas décadas hemos sido testigos del avance de las mujeres en la educación, la aplicación de las legislaciones sobre igualdad, cambios en los roles familiares, y el desafío de las tradicionales normas de género. Sin embargo, no ha avanzado en todos los continentes de igual manera.

En la ciencia, el avance hacia la igualdad de género no puede darse por sentado. Si bien la diferencia de género en carreras científicas está disminuyendo, con mujeres y hombres con trayectorias profesionales y familiares más parejas, eso no significa que las mujeres tengan igualdad de oportunidades para lograr un rendimiento académico igual al de los hombres. La ausencia de mujeres en posiciones de liderazgo tiende a ser más aguda en ciencia y tecnología que en otros campos.

De acuerdo a cifras del instituto estadístico de la UNESCO al cierre de 2017, las científicas mujeres representan el 28 % en todo el mundo [1]. Si bien el número de mujeres que se inscriben en la universidad para estudiar carreras de ciencias e ingenierías muestra crecimiento, no sucede así con los cargos más altos desde investigador hasta líderes de proyectos.

En América Latina y el Caribe la participación de las mujeres en la investigación es alrededor del 45 % del total de investigadores, superior a la cifra de Europa Occidental y América del Norte (32 %) o de Asia Oriental y el Pacífico (23 %). Sin embargo, esta cifra varía mucho entre los países de la región, desde un 55 % en Bolivia y Venezuela, hasta menos del 30 % en Chile, Honduras y México.

Se avanza en el tema de la discriminación, pero las mujeres aún no pueden desarrollarse por completo en una carrera científica en igualdad de condiciones respecto a los hombres. En la ciencia y la ingeniería son profesiones que muestran menos avances hacia la igualdad de género que otras profesiones altamente calificadas, como los abogados y médicos.

La discriminación de género en la educación es la base inicial de la discriminación de género en la ciencia. El grado de integración en el sistema educativo y el grado de igualdad de género en la sociedad son factores relevantes. La familia juega también un papel fundamental en las bajas tasas mundiales de mujeres que desarrollan una carrera científica. Las tensiones familia-carrera son considerables en todas las etapas de la carrera científica, desde la obtención de un título universitario hasta el seguimiento del largo trayecto de formación profesional (maestrías, doctorados y postdoctorados), período que muchas veces coincide con los años fértiles de las mujeres y las expectativas sociales sobre el momento de establecer una familia.

La UNESCO ha reportado que existe un equilibrio cercano de género entre investigadores a nivel de postgrado [1]. En 2013 las mujeres representaron entre el 44 % y el 54 % de

los graduados en postgraduación según un estudio realizado en un amplio número de países, excepto en Japón, donde se alcanzó solo un 33 %. Sin embargo, también es ampliamente reconocido que más allá del nivel de postgrado, las mujeres dejan el camino académico en diferentes etapas y por diversas razones. Muchas mujeres jóvenes terminan creyendo que la ciencia es incompatible con la vida familiar.

Por su parte, en las instituciones científicas los procedimientos de contratación y selección sobre la base de transparencia y criterios de rendimiento independientes del género son vistos como un desafío a las habituales prácticas académicas de protección y parcialidad. Además, la existencia de procedimientos tradicionales de evaluación cuantitativa tiende a favorecer el conformismo intelectual, exacerbar la competencia a nivel individual y afectar el progreso hacia la igualdad de género, especialmente en un contexto de incremento de la competencia para la financiación de la investigación y la intensificación del trabajo.

Para el logro de la igualdad de género en la ciencia no solo es necesario apoyar a las mujeres; se necesita superar los sesgos de género en la producción del conocimiento, pues estos solo limitan la creatividad científica, la excelencia y el beneficio para la sociedad. En el área de las humanidades y ciencias sociales se ha avanzado mucho en los últimos treinta años y se está avanzando cada vez más en la medicina, pero se mantiene un avance más lento en ingeniería y tecnología.

PUBLICACIONES CIENTIFICAS Y PATENTES

En general, las revistas científicas invitan a más hombres que mujeres para evaluar los artículos que les llegan para su publicación. Por otro lado, las mujeres rechazan con más frecuencia ser evaluadoras alegando falta de tiempo, mucho trabajo o no ser expertas en el tema que trata el artículo. En las revistas del grupo "Frontier", que abarca medicina, ciencia, ingeniería y ciencias sociales, el porcentaje de mujeres evaluadoras solo alcanzó el 30 % en el 2015 [2].

De la misma forma, los hombres superan a las mujeres como primeros autores de las publicaciones [2]. Un estudio realizado en el 2015, abarcando más de cinco millones de publicaciones en medicina, ciencia, ingeniería y ciencias sociales, ha revelado que los hombres producen una mayor cantidad de artículos (70 %) y tienen más primeras autorías (66 %) que las mujeres [3].

Con relación a las citas, solo el 13 % de los autores altamente citados en 2014 eran mujeres, desde un 3.7 % en ingeniería hasta un 31 % en las ciencias sociales [3]. Por su parte, se ha encontrado que el porcentaje de auto-citas de hombres supera en un 70 % al de las mujeres (Fig. 1) y cuando se analizan los hombres que nunca se citan a sí mismos, las mujeres ganan a los hombres en un 10 %. De esta forma los hombres consiguen una mayor visibilidad que las mujeres [4].

Finalmente, las solicitudes de patentes por mujeres científicas, como autoras principales, aumentaron del 10 % en el período del 1996 al 2000, hasta un 14 % en el período del 2011 al 2015. Igualmente creció la cantidad de solicitudes que incluyeron al menos una mujer entre los autores, del 19 % en 1996-2000 al 28 % en 2011-2015 [5].

Figura 1. Porcentaje de auto-citas por género [4].

ACADEMIAS Y SOCIEDADES CIENTÍFICAS

Las membresías en 2015, según cifras de la Red Interamericana de Academias de Ciencia (IANAS, IAP/ASSAF), en tres de las principales academias de ciencia mundiales o regionales (Academia Mundial de Arte y Ciencia, WAAS; Academia Mundial de Ciencias, TWAS; y Academia de Ciencias del Mundo Islámico, IAS), muestra que por cada miembro femenino hay entre cinco y diez masculinos. En particular, en la TWAS las mujeres solamente representan el 10 % del total de miembros, con un porcentaje variado por regiones (Fig. 2) [6].

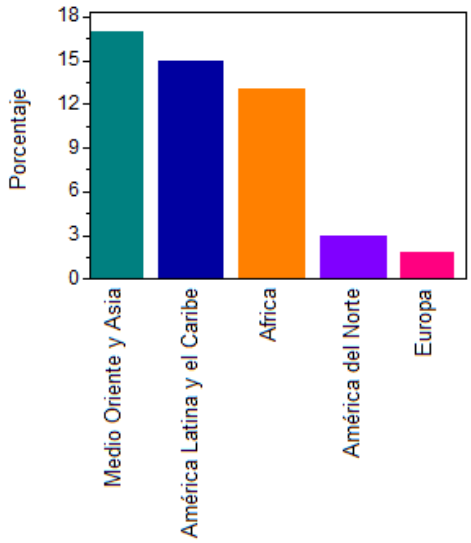

Figura 2. Membresía femenina en la TWAS (en porcentaje del total de miembros) para diferentes regiones, 2015 [6].

Con relación a la membresía femenina en academias nacionales de ciencias, no existe mucha diferencia entre América Latina y el Caribe y otras regiones [6]. Las cifras varían entre un 10 y un 40 % entre los diferentes países, destacándose Cuba y Panamá con cifras incluso superiores a Países de Europa y América del Norte. Sin embargo, las cifras de participación de la mujer en las direcciones de las academias nacionales son, en general, inferiores con relación a los países europeos y de América del Norte. El Reino Unido, los Países Bajos y Suecia muestran cifras superiores al 40 %, mientras que en Canadá y Estados Unidos se tiene un 38 y

un 47 %, respectivamente. En América Latina y el Caribe se destacan en este aspecto países como Panamá, Cuba, México y Honduras (con cifras ≤ 30 %).

PREMIOS Y RECONOCIMIENTOS

Desde que Marie Curie ganara el Premio Nobel de Física en 1903, han sido muy pocas las mujeres científicas que han sido premiadas con tan alto reconocimiento científico, representando solo un 3 % del total de galardonados en Física, Química y Medicina durante toda la historia. Por su parte, los Premios TWAS han sido entregados a 147 hombres (84 %) y solo 27 mujeres (16 %) desde 1985 hasta 2018.

MUJERES EN LA FISICA

La Física, como el resto de las áreas de la ciencia y la tecnología, no está exenta de la discriminación de género. El campo de la física es mayoritariamente descrito como de dominio masculino y las mujeres están poco representadas en el pregrado y aún menos en el posgrado, el postdoctorado y la posición profesional.

Las profesoras y profesionales de la física tienden a tener una menor visibilidad en sus campos que sus colegas masculinos: participan menos que los hombres en conferencias académicas y tienen menos probabilidades de aparecer como autores en posiciones de liderazgo en las publicaciones científicas.

Según un estudio de la Sociedad Americana de Física, las mujeres están poco representadas en todas las áreas de la física. A nivel de pregrado, en 1966 menos de un 5 % del total de títulos de licenciatura de física fueron logrados por mujeres; en 2002 solo un 23 % y en 2012 menos de un 20 % [7]. En el postgrado también las cifras con muy bajas, en programas de doctorado solo representan el 20 % y un 18 % en posiciones de postdoctorado [7]. En el período de 1980 a 2015, las mujeres que obtuvieron su doctorado en física solo representaron entre un 5 y un 20 % del total [8].

En general, el interés de las mujeres por la física es mejor que otras disciplinas de ciencia y tecnología, ingeniería y matemática, de un 0.2 % en física hasta un 16 % en ciencias biológicas en el período de 1971 a 2013 [7]. Por su parte, el interés por desarrollarse en áreas de la investigación científica es mayor en mujeres físicas que en el resto de las disciplinas de ciencia y tecnología, ingeniería y matemática. Otras elecciones que destacan incluyen la ingeniería, la medicina, la enseñanza universitaria (Fig. 3) [7].

II. LA MUJER CUBANA EN LA CIENCIA. LAS FÍSICAS CUBANAS

Como ya hemos comentado anteriormente, la ciencia y la tecnología no están ajenas al orden patriarcal que ha existido en la sociedad por siglos, centrada más en el hombre que en la mujer, y Cuba no está exenta de dificultades en este sentido, aun cuando ha mostrado avances importantes en las últimas décadas.

La ciencia y la tecnología en Cuba desarrollaron cambios trascendentales a partir de 1959 y de forma particular la participación de la mujer en la ciencia ha sido un producto genuino de nuestra Revolución. Estos cambios crearon las premisas fundamentales para la constitución de un nuevo modo de vida de la mujer, comenzaron a cambiar las formas tradicionales de división del trabajo entre los sexos, y la mujer se convirtió en un ente productivo en la sociedad, incluyendo la producción de conocimientos. La mujer cubana ha salido del exclusivo ámbito doméstico y se ha incorporado al trabajo, reconociéndose su capacidad creadora, sus potencialidades y su igualdad tanto jurídica como socialmente. En 1959 las mujeres representaban el 55 % de la población analfabeta cubana. En 2015, las mujeres cubanas constituían el 48 % de los científicos del país y el 66.8 % de la fuerza de mayor calificación técnica y profesional [9]. En proporción de Doctores en Ciencias, Cuba es el segundo país de América Latina y el Caribe, y el doce a nivel mundial; es el tercero en la producción de patentes y el quinto en volumen e importancia de publicaciones cienfíficas [10]. Hasta 2016 en el país se habían otorgado 15266 grados científicos y en los últimos 10 años el número de investigadores ha aumentado el 24 %, llegando a 6839 en 2016, de los cuales el 53 % son mujeres. Todo esto ha sido en gran medida por la voluntad política que ha permitido establecer la igualdad y equidad entre mujeres y hombres. El elemento de inclusión está ímplicito en la política cubana.

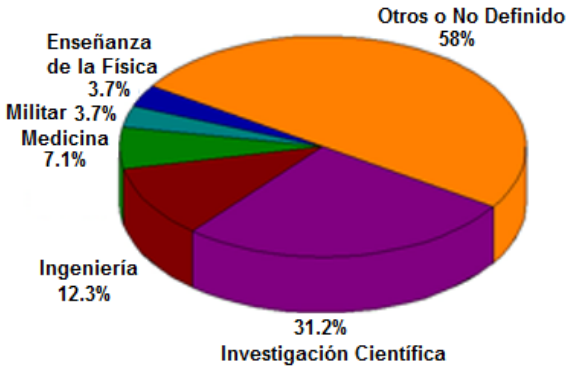

Figura 3. Áreas destacadas de interés para las mujeres físicas en su desarrollo profesional [7].

Sin embargo, en la práctica la manifestación concreta de las acciones es diferente. Para cambiar ideas y costumbres tradicionales no basta sólo con erigir políticas, ya que las modificaciones y cambios en las concepciones tardan más para madurar. Es por ello que aún subsisten rezagos y criterios propios de formas caducas de pensar, por lo que se debe seguir trabajando para avanzar y revertir totalmente cualquier rasgo de discriminación de género.

LA EDUCACION SUPERIOR

La inserción de la mujer en la esfera educacional ha abierto una gran brecha en la cultura patriarcal de la sociedad cubana, que con el paso del tiempo ha crecido, a medida que las acciones de las mujeres se han planteado metas superiores y reivindicativas en este ámbito.

La historia educacional de Cuba es un ejemplo cuando se intenta explicar la participación de la mujer no solo como estudiante sino también como educadora, investigadora y dirigente en las instituciones educacionales y científicas.

En las universidades cubanas ingresaron en el curso 2017-2018 un total de 61762 estudiantes de nuevo ingreso (primer año), de los cuales 38811 (63 %) fueron mujeres [11]. En particular, en ciencias naturales y matemática (incluida la física y la física nuclear) ingresaron 1166, de los cuales 674 (58 %) fueron mujeres. En la Licenciatura en Física y Física Nuclear ingresaron un total de 100 estudiantes, incluyendo 34 mujeres (34 %). Por su parte, la matrícula total en carreras de ciencias naturales y matemática (incluida la física y la física nuclear) en el curso 2017-2018 fue de 4365 estudiantes, de ellos 2494 mujeres (57 %) [11]. En la Licenciatura en Física y Física Nuclear se tuvo un total de 290 estudiantes, incluyendo 72 mujeres (25 %). La Tabla 1 muestra la distribución de estas matrículas en las tres universidades del país donde se estudian.

Tabla 1. Matrícula de nuevo ingreso (primer año) y matrícula total de las carreras de física en el curso 2017-2018 [11].

	Nuevo Ingreso		Matrícula Total	
	Total	Mujeres	Total	Mujeres
Universidad de La Habana	83	27 (32 %)	216	54 (25 %)
Universidad Central de las Villas	6	0 (0 %)	27	2 (7 %)
Universidad de Oriente	11	6 (64 %)	47	16 (34 %)

Con relación a la graduación del curso 2016-2017, en ciencias naturales y matemática (incluida la física y la física nuclear) se graduaron 625 estudiantes, incluyendo 374 (60 %) mujeres. En las carreras de física se graduaron 32 estudiantes y de ellos 7 (22 %) mujeres. La Tabla 2 muestra la distribución de graduados según las universidades del país. Las graduadas de las carreras de física representaron solo el 1 % del total de graduadas en ciencias naturales y matemática.

Tabla 2. Graduados en las carreras de física en el curso 2016-2017 [11].

	Total	Mujeres
Universidad de La Habana	18	2 (11 %)
Universidad Central de las Villas	12	4 (33 %)
Universidad de Oriente	2	1 (50 %)

La Fig. 4 muestra las cifras de graduados en la Licenciatura en Física en la Universidad de La Habana desde 1980 al 2018, en períodos de cinco años. Puede apreciarse que históricamente las graduaciones de mujeres físicas oscilan entre el 10 y 25 %.

En postgrado también la representación femenina en física se evidencia, tanto en la maestría en ciencias físicas, como en el doctorado en ciencias físicas. La Fig. 5 muestra las cifras de graduados por género. Puede apreciarse que las graduaciones postgraduadas de mujeres físicas oscilan entre el 15 y 20 %.

El personal docente en las universidades también se destaca por la presencia femenina. La Fig. 6 muestra la distribución de hombres y mujeres en el curso 2017-2018, siendo la representación de la mujer superior al hombre [11].

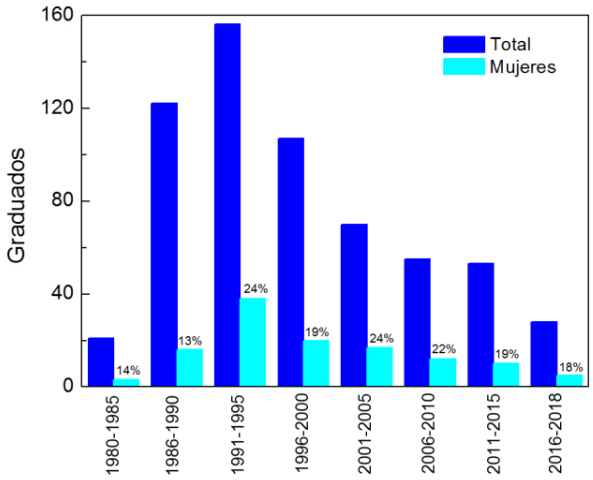

Figura 4. Graduados en la Licenciatura en Física en la Universidad de La Habana desde 1980 al 2018, en períodos de cinco años.

La distribución por categorías docentes del personal a tiempo completo también muestra una buena presencia de la mujer en la educación superior cubana (Fig. 7) [11].

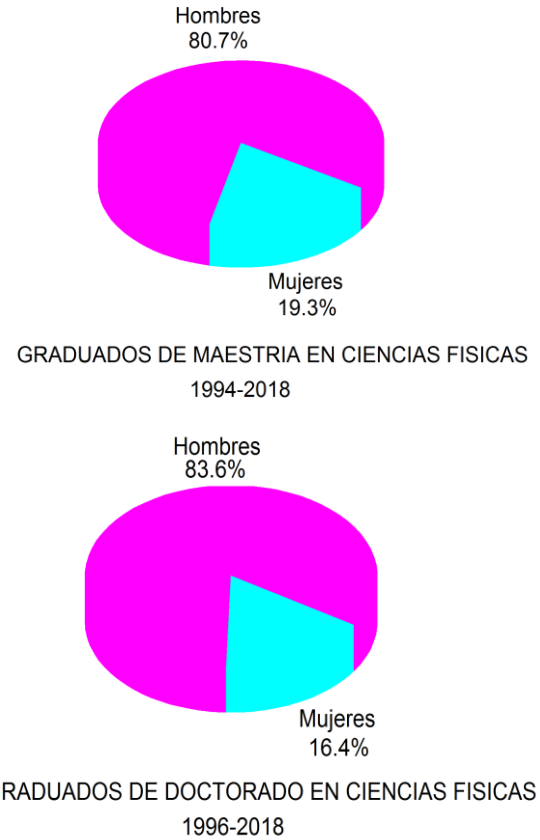

Figura 5. Distribución por género de los graduados de Maestría en Ciencias Físicas y Doctorado en Ciencias Físicas.

Igualmente, los grados científicos muestran una importante representación femenina. Del personal docente a tiempo completo: 4922 son doctores en ciencias y de ellos 2410 son mujeres (49 %), y 30260 son masters en ciencias y de ellos 18232 son mujeres (60 %). Estas cifras muestran como en la educación

superior cubana, la cantidad de mujeres que continúan su superación científica es importante [11].

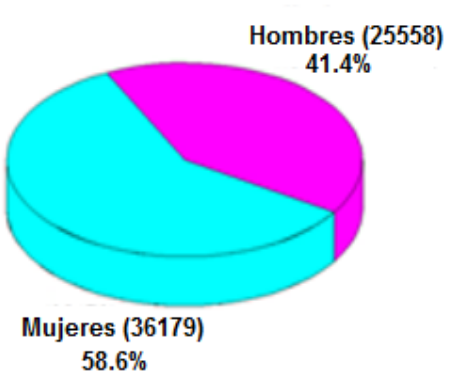

Figura 6. Distribución por género del personal docente en la educación superior cubana en el curso 2017-2018 [11]. Las cifras incluyen el personal a tiempo completo, el personal a tiempo parcial y el personal docente en adiestramiento.

Si finalmente analizamos estas cifras en el personal docente de la Facultad de Física de la Universidad de La Habana, tenemos que de un total de 75 profesores (personal a tiempo completo, personal a tiempo parcial y personal docente en adiestramiento), 17 son mujeres (23 %); de un total de 41 doctores y 19 masters, se tienen 8 (20 %) y 5 (26 %) mujeres en tales categorías, respectivamente.

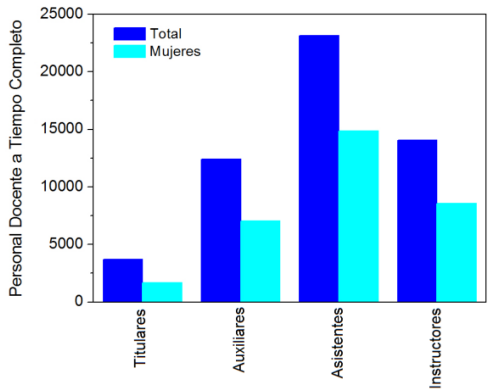

Figura 7. Distribución del personal docente a tiempo completo, por categoría y género, en la educación superior cubana en el curso 2017-2018 [11].

ACADEMIA DE CIENCIAS DE CUBA Y SOCIEDAD CUBANA DE FISICA

La Academia de Ciencias de Cuba, en el último período concluido en el 2017, contó con un 28 % de mujeres del total de miembros. En el nuevo período iniciado en 2018, la comisión de ciencias naturales y exactas cuenta con un total de 78 miembros, entre académicos titulares, académicos de mérito, miembros de honor y asociados jóvenes. De ellos, 19 son mujeres para un 24 %, indicativo del notable papel desempeñado por las mujeres en Cuba.

La Sociedad Cubana de Física ha sido dirigida en varias ocasiones por mujeres, y su presidencia actual es femenina. También hay presencia femenina en su comité ejecutivo actual. De igual forma la edición de la Revista Cubana de Física fue dirigida, un largo período, por una mujer.

En cuanto a su membresía, la Sociedad Cubana de Física cuenta en el 2018 con 377 miembros, de los cuales 102 son mujeres (27 %).

Por otra parte, las mujeres físicas han tenido presencia en el Comité Regional para América Latina y el Caribe, y el Consejo Internacional para la Ciencia (ICSU). Una física cubana fue miembro del Consejo Ejecutivo de la Organización del Tercer Mundo para la Mujer en la Ciencia (TWOWS) en el período 1999-2006.

La vicepresidencia de la Federación Latinoamericana de Física (FEIASOFI) la ocupa una física cubana, al igual que una de las consejerías del Centro Latinoamericano de Física (CLAF).

PREMIOS Y RECONOCIMIENTOS

La Academia de Ciencias de Cuba cuenta con premios anuales en sus diferentes secciones científicas, y en ellos la representación de la mujer es destacada. Dentro de las ciencias naturales y exactas, en el período 2013-2016 se otorgaron un total de 82 premios y de ellos 30 tenían a una mujer como primera autora (para un 36 %).

Cuba cuenta, además, con la distinción "Carlos J. Finlay", la máxima otorgada por el Estado cubano a profesionales con contribuciones importantes a la ciencia y la tecnología en el país. Hasta la fecha la han recibido aproximadamente un 33 % de mujeres.

El premio internacional "Sofia Kovalevskaya", otorgado por la fundación del mismo nombre para estimular a la mujer científica de las naciones en desarrollo, y que comenzó a entregarse en Cuba en 2003, ha galardonado hasta la fecha a 24 científicas cubanas, de las cuales 6 han sido físicas.

En el medio internacional, científicas cubanas también han sido galardonadas: tres recibieron el premio de la TWOWS en 2010 y 2011, dos recibieron el premio de la Academia de Ciencias del Caribe (CAS-TWAS) en 2012 y 2014, y una recibió el premio regional de la TWAS (TWAS-ROLAC) en 2011. De estos seis premios, cuatro correspondieron a físicas.

DESAFIOS DE LAS FISICAS CUBANAS

Hoy en Cuba no puede decirse que exista una exclusión explícita de la mujer en las universidades y centros de investigación, ni tampoco que existan criterios abiertos alegando inferioridad intelectual de la mujer respecto al hombre, pero no puede obviarse que existen todavía determinados mecanismos implícitos que de manera sutil contribuyen a la discriminación de la mujer.

En la opinión de esta autora, aún queda mucho por recorrer en este tema y la mujer debe ser la protagonista en ello, demostrando su igualdad de capacidades científicas, en particular en aquellas ciencias donde la presencia masculina ha sido predominante históricamente, como lo es en la física.

La ciencia y la tecnología demandan de hombres y mujeres que contribuyan a enriquecer el patrimonio mundial de

conocimientos, y esto depende de su creatividad científica y excelencia, no de las políticas de género.

AGRADECIMIENTOS

La autora desea agradecer al Profesor Julio Vidal Larramendi (Facultad de Física, Universidad de La Habana, Cuba) por su contribución con materiales que permitieron desarrollar la sección sobre la mujer cubana en la educación superior.

REFERENCIAS

[1] UNESCO Institute for Statistics, http://data.uis.unesco.org
[2] J. Lerback, B. Hanson, Nature **541**, 455 (2017).
[3] L. Bornmann, J. Bauer, R. Haunschild, Journal of the Association for Information Science and Technology **66**(12), 2715 (2015).
[4] M.M. King, C.T. Bergstrom, S.J. Correll, J. Jacquet, J.D. West, Socius: Sociological Research for a Dynamic World **3**, 1 (2017).
[5] Gender in the global research landscape (Elsevier Science Publishers B. V., The Netherlands, 2017).
[6] V. López-Bassols, M. Grazzi, C. Guillard y M. Salazar, Las brechas de género en ciencia, tecnología e innovación en América Latina y el Caribe, Banco Interamericano de Desarrollo, 2018.
[7] L.J. Sax, K.J. Lehman, R.S. Barthelemy, G. Lim, Phys. Rev. Spec. Top.-Phys. Educ. R. **12**, 020108 (2016).
[8] R. Ivie, Statistical Research Center, American Institute of Physics, 2018.
[9] R. Castro Ruz, Conferencia de líderes globales sobre igualdad de género y empoderamiento de las mujeres: un compromiso de acción, Nueva York, Septiembre, 2015.
[10] E. Rosa Pérez, Ministra del CITMA, Día de la Ciencia, Cuba, 2017.
[11] Prontuario de la Educación Superior, Cuba, Curso 2017-2018.

EVOLUCIÓN, PRESENTE Y FUTURO DE LA ENSEÑANZA DE LA FÍSICA PARA INGENIEROS EN CUBA

EVOLUTION, PRESENT AND FUTURE OF TEACHING OF PHYSICS FOR ENGINEERS IN CUBA

A.D. Rodríguez-Llerena[a†], H. Astigueta-Quintana[a], J. J. Llovera-González[a]

Departamento de Física, Instituto de Ciencias Básicas, Universidad Tecnológica de la Habana "José Antonio Echeverría", Cujae; deysi@automatica.cujae.edu.cu
† autor para la correspondencia

Recibido 20/8/2020; Aceptado 20/9/2020

La enseñanza de la física en la formación básica de ingenieros en Cuba ha transitado por diferentes etapas desde los años 1960's hasta la actualidad. Cada etapa ha estado marcada por cambios en los planes de estudio de la disciplina, que se han modificado notablemente tanto en los contenidos como en el número de horas lectivas dedicadas a su impartición. En este artículo se presenta un breve resumen de estos cambios, el estado actual de estos programas y se alerta acerca de los retos que hoy se deben asumir para garantizar una sólida formación básica de los futuros ingenieros sobre los fundamentos físicos de las presentes y futuras tecnologías.

Physics teaching in the basic formation of engineers in Cuba has evolved through different stages since the 1960's until the present. Each stage has been marked by changes in the plans of study, which have been modified substantially both in terms of contents and of teaching hours. This paper presents a brief summary of these changes, the current state of the Physics programs, and warns about the challenges to be faced nowadays in order to guarantee a solid basic formation of the future engineers in connection with the physical foundations of present and future technologies.

PACS: General physics (física general), 01.55.+b; course design and evaluation (diseño y evaluación de cursos), 01.40.Di; engineering (ingeniería), 89.20.Kk; careers in physics and science (carreras en física y en ciencia), 01.85.+f

I. INTRODUCCIÓN

Como bien se conoce, la Física constituye un pilar fundamental en la formación de los ingenieros por lo que, de manera general, en la mayor parte de las universidades del mundo se insiste en prestar atención especial a una sólida formación en Física como ciencia básica en los planes y programas de estudio de las diferentes carreras de ingeniería, pretéritos y actuales.

Analicemos cómo ha variado la enseñanza de la Física para ingenieros en Cuba en los últimos 60 años a través de sus diferentes planes de estudio, tanto en contenidos como en presupuesto de tiempo destinado a su enseñanza, a fin de revelar los retos que hoy enfrenta la formación en Física de los futuros ingenieros cubanos.

II. LA FÍSICA EN LOS PLANES DE ESTUDIO DE INGENIERÍA EN CUBA (1960-2020)

Desde la primera etapa de la Reforma Universitaria en el año 1960 hasta la fecha se han puesto en práctica varios planes de estudio para las carreras de ingeniería en Cuba. Los mismos se han ido ajustando a las condiciones socioeconómicas por las que ha transitado la Educación Superior Cubana hasta llegar al actual Plan E, que se encuentra en estos momentos en ejecución en su segunda edición.

Aunque la Reforma Universitaria de 1962 significó un hito en la introducción de los estudios de ciencias básicas y la investigación en las ingenierías, en ese momento no se logró unificar los fundamentos de la enseñanza de la Física para todas las carreras de ingeniería que se estudiaban en el país, manteniéndose en las diferentes especialidades diversos programas de estudio de Física diseñados básicamente por los profesores que la impartían, de acuerdo con su experiencia previa. Analicemos sucintamente los cambios más significativos que se han producido en los diferentes planes de estudio hasta hoy.

Tomemos como referente de partida el plan de la carrera de ingeniero electricista establecido con la primera etapa de la Reforma Universitaria en 1960 [1, 2]. En este plan, la Física se impartía durante 4 semestres de 15 semanas cada uno, siendo los contenidos correspondientes respectivamente a Mecánica (90 h/c), Termodinámica (90 h/c), Electricidad y Magnetismo (105 h/c) y Óptica (90 h/c) para un total de 375 h/c de Física General. De estas, 150 h/c eran explícitamente dedicadas a prácticas de laboratorio [2].

Con el plan "**A**" establecido en el curso 76-77, se actualizaron los contenidos comenzando a impartirse la Teoría de la Relatividad y la Física Moderna. Anteriormente la Física que se impartía solo abarcaba los contenidos hasta la Óptica Ondulatoria. Se inició en este plan un proceso de preparación didáctica de los docentes en las universidades y se promovió la formación de habilidades prácticas y experimentales en los estudiantes a través de clases prácticas y prácticas de laboratorio [3].

En el plan "**B**" (1982) se continuó el proceso de actualización de los contenidos, incluyéndose en el programa la Física de los Semiconductores, completando y actualizando la concepción

del Cuadro Físico del Mundo y se trató de lograr una mejor articulación con la Matemática. Se estableció entonces un programa de la disciplina Física General único para todas las carreras a fin de unificar contenidos esenciales comunes [4].

El plan "**C**" y el C perfeccionado (**C'**) (1991), tuvieron como objetivo acercar la disciplina al perfil del profesional, manteniendo los llamados "núcleos básicos". Se disminuyó el número de horas dedicadas a conferencias y se aumentaron las horas de clases prácticas y laboratorios, encaminadas a lograr que los estudiantes tuvieran una participación más activa en su aprendizaje y fortaleciéndose el trabajo científico estudiantil [5].

Se diseñaron programas específicos para las diferentes ingenierías, lo que condujo a que en algunas especialidades dejaran de impartirse algunos núcleos básicos de la disciplina y se estrechara el perfil del ingeniero en formación.

El plan "**D**" (2003) retomó la concepción de una Física General única para todas las carreras, pero permitiendo entre un 10 % y un 20 % de horas para el acercamiento de la disciplina al perfil profesional de la especialidad sin afectar los núcleos básicos. Se lograba así un justo equilibrio entre la formación básica y su vínculo con la especialidad en cada caso. Durante este periodo, se introdujo con mucha fuerza el uso de las TIC en la enseñanza y se mantuvo una proporción de hasta solo un tercio de las horas lectivas dedicadas a conferencias [6].

A partir del año 2016, se analizó por la dirección del país la necesidad de reducir las carreras universitarias a 4 años, orientándose a las diferentes comisiones de carrera elaborar un Plan "**E**" (2016) en el cual también se redujeron horas lectivas y algunos contenidos básicos de los anteriores programas de Física General en las diferentes carreras.

Tabla 1. Presupuestos de horas clase (h/c) dedicadas a la enseñanza de la Física General en carreras de ingeniería en Cuba y sus decrementos sucesivos (Δh/c) entre 1960 y 2020.

Plan	Pre Ref. Univ. 1960	A	B	C y C′	D	E
Curso de inicio de plan	60-61	76-77	82-83	91-92	03-04	16-17
h/c	375	320	300	240	216	208 160*
Δh/c	-	-55	-20	-60	-24	-8 -56*
Δh/c acumulado entre 1960 y 2020: -167 (-215)*						
* Carreras que eliminaron la Física Moderna (Física III) del plan de estudio.						

La Tabla 1 resume las cantidades de horas clase (h/c) dedicadas a la Física para carreras de ingeniería en los sucesivos planes de estudio implementados en Cuba desde el año 1960 hasta la actualidad.

Como se puede apreciar en dicha tabla, durante el período de los últimos 60 años transcurridos la cantidad de horas lectivas dedicadas a la formación en Física General de los estudiantes de ingeniería ha ido en franco decremento.

III. SACRIFICIOS PREOCUPANTES

El número de horas dedicadas a la Física General en los planes de estudio ha disminuido en 167 horas (44,5 %) en algunas carreras y hasta en 215 horas (57,3 %) en otras, y aunque se ha declarado como indicación no restar tiempo al tratamiento de los núcleos básicos de la disciplina, varias carreras optaron por eliminar la Física III, privando al programa del contenido de la Física Moderna totalmente, en tanto en todas las asignaturas de Física el desarrollo de habilidades por parte de los estudiantes en presencia de su profesor ha tenido una afectación considerable.

Es así como en el último de los planes (plan **E**) por primera vez se sacrifica la uniformidad en los contenidos esenciales de enseñanza de la Física en algunas carreras respecto a otras incluyendo diferencias sustanciales en cuanto a horas entre estas dedicadas a la Física, debido a que siete de las once carreras de ingeniería que se estudian en Cuba e incluyen la disciplina Física, decidieron limitar el estudio de la Física General solamente a dos asignaturas, eliminando del plan de estudio la Física III (Física Cuántica, Física Atómica y Física Nuclear).

Esta decisión priva a los estudiantes de estas carreras, desde su formación básica, del conocimiento de la mayor parte de los fundamentos sobre los que descansan los adelantos de la ciencia y la tecnología moderna basados en la física aplicada, reduciendo la enseñanza de la Física al desarrollo que esta tuvo solo hasta finales del siglo XIX [7] lo que está afectando en más de 120 años la actualidad de la formación básica del ingeniero en lo que a la Física se refiere en dichas carreras[1].

Esta última reducción en horas dedicadas a la Física en los planes de estudio se ha basado en una concepción del proceso de enseñanza en la cual el estudiante debe autogestionar su aprendizaje a partir de un incremento de sus horas de estudio individual en detrimento de las horas presenciales, logrando un aprendizaje comprometido con sus resultados más activo y autónomo, como declara el Reglamento Docente Metodológico vigente cuando establece que: "... se debe garantizar un balance adecuado del tiempo que los estudiantes dedican a las actividades presenciales y a las no presenciales, como vía para fomentar su aprendizaje autónomo bajo la orientación y control de los profesores" [8]. Sin embargo, en la actualidad es difícil de lograr este objetivo.

A finales de la última década del siglo XX, como consecuencia de la crisis de profesores que se produjo en la enseñanza precedente acompañada de la eliminación de la prueba de Física de los exámenes de ingreso a la Educación Superior, los estudiantes que lograban matricular en las carreras de ciencias técnicas comenzaron a mostrar insuficientes conocimientos básicos de Física y Matemática, lo que incidió negativamente

[1] En estas carreras se eliminó totalmente la impartición de los contenidos de la Física Moderna, reduciendo la disciplina a solo dos asignaturas de 80 h/c cada una; una dedicada a la Mecánica newtoniana, la Física Molecular y la Termodinámica y la otra al Electromagnetismo y la Óptica Ondulatoria lo que implica un retroceso involutivo con respecto incluso al plan A; no solo en tiempo de horas lectivas sino también, y sobre todo, en contenidos fundamentales de la Física de los siglos XX y XXI que hoy no son tratados en el curso.

en el rendimiento académico de dichos alumnos en estas asignaturas [9]. Esta situación se mantiene en la actualidad.

La mayor parte de los estudiantes continúan careciendo de la suficiente base en Física y Matemática al arribar a la universidad desde la enseñanza precedente, nivel en el cual inclusive, no se logra formar hábitos de estudio independiente en la mayor parte de los jóvenes.

Por otra parte, el plan "**E**" ha reducido drásticamente el tiempo dedicado a prácticas de laboratorio desde 90 h/c hasta apenas 26 h/c, contrariamente a lo que se venía logrando con los planes anteriores. Ello se ha instrumentado limitando la cantidad de prácticas de laboratorio posibles a realizar, actividad reconocida por la didáctica como la clase por excelencia para la enseñanza de las ciencias y, particularmente, en la formación de los ingenieros [10].

Es interesante recordar que desde la Reforma Universitaria de 1962 se planteaba: "...*las escuelas de ciencias (física, química, matemática) tendrán que proveer también los profesores que en poco tiempo se encarguen de prepararnos ese nuevo tipo de graduados de la enseñanza secundaria y darle al aspirante a estudios universitarios el nivel adecuado, para enfrentarse con disciplinas que ahora le resultan poco menos que torturantes, por su apartamiento de ellas antes de llegar a las aulas superiores*..." [11].

Este planteamiento ha vuelto a tener total vigencia, por lo que consideramos que tomar conciencia de esta situación es de vital importancia para lograr garantizar una formación básica sustentable de los futuros ingenieros y revertir los bajos rendimientos académicos en Fisca en las carreras de ingeniería.

IV. EL "TRONCO COMÚN" ¿UN PARADIGMA NECESARIO?

Otra situación que compromete la calidad en la formación de los ingenieros es el llamado 'tronco común" de Física General para todas las especialidades que se ha establecido en algunas universidades, implicando un retroceso en lo que se había avanzado en didáctica de la Física Universitaria para carreras de ingeniería desde el Plan "**C**" hasta la actualidad en cuanto a vincular cada vez más la Física a la especialidad.

Esta concepción consiste en disponer que todas las especialidades reciban un programa de Física idéntico concretado a "esencialidades", sin considerar las características específicas de cada carrera en cuanto a articular la Física con las demás asignaturas básicas específicas a las que sirve de base. Este proceder ha provocado un distanciamiento entre la Física General y el perfil profesional del futuro ingeniero lo que, según se asevera en [12]: "impactará negativamente en la motivación para estudiar la asignatura; conllevará a un distanciamiento de la Física y las Ciencias Técnicas, provocará un debilitamiento entre la teoría y la práctica y no favorecerá el aprendizaje significativo".

Como bien se ha afirmado en un artículo recientemente publicado en esta revista [13] "Es imprescindible rescatar la enseñanza de la Física, como ciencia básica, amena, moderna y con rigor, en todos los niveles de enseñanza". Enfatizando, entre otras direcciones, en la enseñanza de la Física en las carreras universitarias de ciencias básicas e ingenierías.

V. CONCLUSIONES

Entre los retos que enfrenta la Educación Superior Cubana en cuanto a la formación en Física de los ingenieros hoy están:

a) Revisar los presupuestos de tiempo que se han asignado a la enseñanza-aprendizaje de la Física General para estudiantes de ingenierías, rescatando urgentemente la actualidad del contenido en algunos de estos planes en que se ha eliminado la Física Moderna.

b) Propiciar cada vez más el estrecho vínculo de la Física con las especialidades, a fin de lograr en el estudiante la motivación necesaria por el estudio de esta ciencia como base de su carrera, propiciando un aprendizaje sostenible (aprender a aprender), que contribuya a su futuro modo de actuación.

c) Contribuir a elevar el nivel de desarrollo de las habilidades prácticas, en particular las experimentales, que se deben lograr en los estudiantes de ingeniería para desempeñarse con independencia cognoscitiva en cualquier contexto de aprendizaje futuro sobre la base de una sólida y actualizada formación en Física como fundamento imprescindible de las actuales y futuras tecnologías.

Docentes y directivos con ingenio y voluntad podemos ser capaces de enfrentar con éxito estos retos. ¿Estamos todos dispuestos a aceptar el desafío?

AGRADECIMIENTOS

Los autores desean agradecer al profesor, Ing. José B. Altshuler-Gutwert, (Dr. C) por la rica información ofrecida, en comunicación personal, relativa al proceso de conformación de los planes de estudio en las carreras de ingeniería en Cuba que sirvieron de base a la Reforma Universitaria de 1962, en particular en la carrera de ingeniero electricista; planes de los cuales fue uno de sus principales gestores.

REFERENCIAS

[1] Facultad de Ingeniería: Ingeniería eléctrica: Nuevo plan de estudios. Universidad de La Habana, 15 pp. multicopiadas (1960)

[2] L. Altshuler "Para una Historia de las Ciencias Física y Técnicas en Cuba" (Ed. Científico-Técnica, Bogotá, Colombia, 2006) p.p. 103.

[3] H. Falcón-Tanda "Una concepción de profesionalización desde la disciplina Física General en Ciencias Técnicas". Tesis doctoral, Cujae, Cuba, (2003).

[4] A. Hernández-Calzada, "Sistema de actividades para propiciar la evaluación formativa en la enseñanza de la física". Tesis doctoral, Palma de Mallorca, (2013).

[5] J. A. Alejo-Díaz "Una Propuesta Didáctica para la Enseñanza en contexto para la disciplina Física General en carreras de ingeniería", Tesis doctoral, Cujae, Cuba, (2006).

[6] Ministerio de Educación Superior de Cuba (MES) Plan de Estudio "D", (2003).
[7] F. J. Ynduran-Muñoz, Rev. Real. Acad. Cienc. Exac. Fis. Nat. Esp. **99**, 97 (2005).
[8] Ministerio de Educación Superior Resolución No. 2/2018 (GOC-2018-460-O25).
[9] E. Moltó, E. Altshuler, Rev. Cubana Fís. **30**, 58 (2013).
[10] Cruz y Espinosa, Revista Virtual Universidad Católica del Norte, [ISSN: 0124-5821] 35 feb-mayo (2012) (http://www.redalyc.org/articuloa?id19422436).
[11] C.R. Rodríguez-Rodríguez, Economía y Desarrollo **148**, 273 (2012).
[12] J. A. Alejo-Díaz, J. B. Cruz-Arencibia, J. J. Llovera-González, Rev. Cubana Fís. **35**, E52. (2018).
[13] C. Cabal, Rev. Cubana Fís. **36**, 87 (2019).

RUSSIAN-CUBAN OBSERVATORY: OPTICAL OBSERVATION STATION

OBSERVATORIO RUSO-CUBANO: ESTACIÓN DE OBSERVACIÓN ÓPTICA

A. Alonso Diaz[a†], M.R. Rodriguez Uratsuka[a], O. Pons Rodriguez[a], Z. Barcenas Fonseca[a], R. Zaldivar Estrada[a], N. Paula Acosta[a], M.A. Ibrahimov[b], D.V. Bisikalo[b], M.E. Sachkov[b], A.M. Fateeva[b], I.S. Savanov[b], M.A. Nalivkin[b], S.A. Naroenkov[b], A.S. Shugarov[b]

a) Institute of Geophysics and Astronomy, Havana, Cuba; alonso@iga.cu
b) Institute of Astronomy, Russian Academy of Sciences, Moscow, Russia
† corresponding author

Recibido 20/8/2020; Aceptado 20/9/2020

The prolongation of a project to create an optical observation station in the frame of the Russian-Cuban Observatory (RCO) is described. The paper reports some important elements regarding the creation of the RCO optical station layout in Havana. The equipment and some scientific observation projects planned to be done using the layout are discussed. The main instrument of the optical station layout is a wide-field 20 cm robotic telescope. The observational project program includes both fundamental and applied tasks. It is argued that the layout itself could be used as an independent observatory because of its ability to solve universal observational tasks and to serve as a real segment of a global optical telescope network.

El artículo describe la continuación de un proyecto para crear una estación de observación óptica en el marco del Observatorio Ruso-Cubano (RCO). El documento informa algunos aspectos principales relacionados con la creación del diseño de la estación óptica RCO en La Habana. Se discuten los equipos y algunos proyectos de observación científica que se planean realizar utilizando el diseño. El instrumento principal del diseño de la estación óptica es un telescopio robótico de 20 cm de campo amplio. El programa de observación incluye tareas tanto fundamentales como aplicadas. Se argumenta que el diseño en sí mismo podría usarse como un observatorio independiente debido a su capacidad para resolver tareas de observación universales y servir como un segmento real de una red global de telescopios ópticos.

PACS: Telescopes (telescopios), 95.55.-n; optical instruments iInstrumentos ópticos), 07.60.-j; astronomical observations (observaciones astronómicas), 95.85.-e

I. INTRODUCTION

The creation of distributed global optical telescope networks is one of the most important issues of modern observational astrophysics. The main advantage of global networks is an opportunity to realize nearly uninterrupted sky observations 24 hours/365 days a year. Another advantage is a global network possibility to implement universal research tasks. Universality implies ability to monitor nearEarth, near-Solar and deep space to cover an entire variety of available natural and technogenic origin space objects. In order to achieve universality, two types of telescopes have to be included into the network - scan wide-field and astrophysical narrow-field telescopes. Telescopes of such global and universal network should have the following typical characteristics: i) apertures of 0.2-0.5 m and fields of view of the order of several angular degrees for scan telescopes, and ii) apertures of 1m or more and fields of view of the order of fractions of an angular degree for astrophysical telescopes.

This paper describes a prolongation of the Russian-Cuban team collaboration on a project to create a separate segment of the above described network in the Cuban territory. Our first paper dealt with general issues of segment creation and its usage [1]. This paper deals with the creation of the optical station layout within the future segment. The layout equipment and some research projects planned to be done using it are discussed in the paper.

II. RCO AND ITS OPTICAL STATION

Since 2017, Cuba and Russia have been collaborating to create the Russian-Cuban Observatory (RCO). RCO is built on Cuban territory, and believed to be a separate segment of a global optical network created within the frame of world-wide international cooperation. The process of RCO building is divided into two stages. In the first stage, a layout of the RCO will be created. In the second stage, a fully functional observatory will be created. The layout is built in Havana, while the operating observatory will be built in the site of Valle de Picadura, located 80 km east of Havana.

Both the RCO itself and its layout consist of two main stations: a co-location GNSS station and an optical observation station. International partners, equipment and tasks concerning a layout of the GNSS station in Havana are described in [2]. This paper describes the partners, equipment and tasks concerning the layout of the optical observation station in Havana.

The optical station layout is created in cooperation between the Institute of Geophysics and Astronomy, Havana, Republic of Cuba (IGA) and the Institute of Astronomy of the Russian Academy of Sciences, Moscow, Russia (INASAN). Some

advantages of having the RCO optical station in Cuba and thus, of using a large Cuba-Russia arc were discussed and theoretically analyzed in [1].

III. EQUIPMENT OF THE OPTICAL STATION LAYOUT

IGA donated a part of its territory and a separate building to mount the RCO layout. A satellite image of the territory in IGA and a photography of the building are given in [2] (see Figs. 4 and 5 there). Also in [2] (see Fig. 6 there), a scheme of the GNSS station and optical station main observation facilities location is given. These facilities are located on the roof of the building. Inside the building, the electrical, computer and network equipment are accommodated. The latter is fully grounded and a lightning protection system provided by an IGA's specialized team. An automated weather station with its own lightning-conductor is located 20 m from the building.

A more detailed scheme of the layout observation facilities location on the roof of the building is shown in Fig. 1. On a concrete pillar at the left front corner of the roof, a receiving equipment of the GNSS station layout is located (cf. with Fig. 7 in [2]). On a circular parapet also located on the roof, an automated dome for the optical station is deployed. Inside the dome, a 20 cm robotic telescope is installed. The telescope is lifted to roof level using a 4.2 meter concrete column. A drawing of the column inside the building along with the circular parapet, the dome, and 20 cm robotic telescope is shown in Fig. 2.

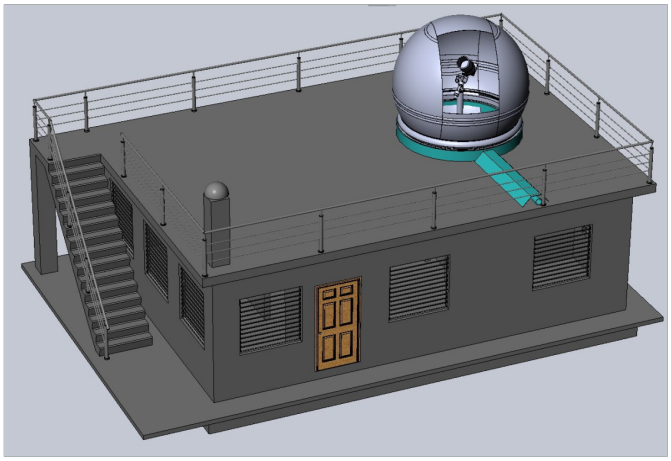

Figure 1. Scheme of the RCO layout at IGA (Havana). See text for explanations.

The equipment of the RCO optical station layout includes:

a) automated dome,

b) wide-field telescope with large field of view,

c) telescope mount,

d) image registration unit with CCD camera and focusing device,

e) computer, network and meteorological equipment.

To robotize the observations, the following specific equipment were chosen for the station:

- 3-meter ScopeDome 3M automated dome;
- 20-cm Officina Stellare Veloce RH20 wide-field telescope with 5 angular degrees field of view, automated focusing unit, a set of optical photometric filters, Atlas FLI automated filter wheel for 7 positions, and FLI PL16803 4K CCD camera;
- high-precision 10Micron GM1000 HPS equatorial mount with 25 kg load capacity and absolute position sensors.

The 20 cm Officina Stellare Veloce RH20 widefield telescope provides collection and conversion of optical information. 10Micron GM1000 HPS mount with absolute encoders, providing pointing to an object using its specified coordinates and tracking the object. The image registration unit includes CCD camera, focusing device and filter wheel. All equipment is controlled and operated by a server computer using USB interface.

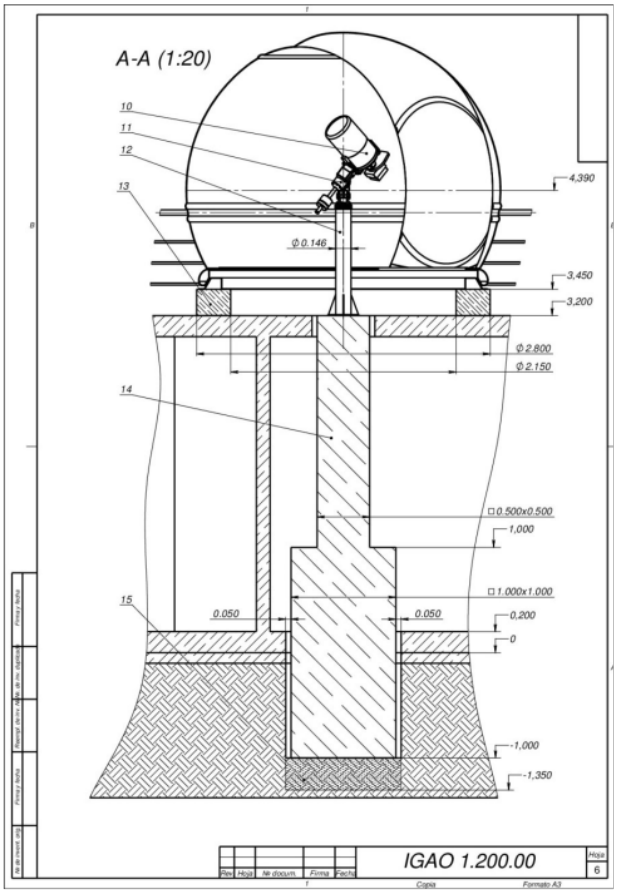

Figure 2. Drawing of installation of the RCO optical station layout main observational equipment: 20 cm telescope lifted using the 4.2 m concrete column and its dome on the roof of the building.

The time service unit operates using GPS and GLONASS time signals. It provides timing for all acquired frames and obtained coordinate information. The dome control unit is responsible for the telescope protection by closing the dome following a signal from meteorological unit. The power supply unit includes an uninterrupted power supply

device, a 8-port SNMP power management device, IP and GPRS interfaces, and lightning protection systems. The data exchange between all the units of the optical station layout is provided by the data exchange unit. It includes a router with Ethernet and fiber-optic interfaces, USB extenders, and lightning protection devices. Full operation of optical station layout equipment is provided by standard programs and device drivers, which are used within the specially created software package.

IV. SCIENTIFIC PROJECTS FOR THE OPTICAL STATION LAYOUT

The 20 cm wide-field robotic telescope is the main observational instrument of the optical station layout at IGA (Havana). In the future, a wide-field 1-m telescope is planned to be installed in the RCO full operating optical station in Valle de Picadura. These two telescopes are thought to be used for both fundamental and applied observational tasks. Eventually, both optical stations in Havana and Valle de Picadura will create a united Cuban segment of a global optical telescope network. This segment is thought to be able to perform the following universal tasks:

a) Monitoring near-Earth and near-Solar space to solve applied tasks: planetary Earth defense and monitoring of natural and technogenic origin objects which posed space threats (potentially hazardous objects and space debris);

b) Monitoring deep space to solve fundamental tasks: ground-based optical follow-up observations to support already launched and awaiting launch scientific space missions and multitask observations of various types of optical transients (Gamma-Ray Bursts, observational effects of gravitational-wave events in optics, etc).

So far, the Cuban segment of a global network is under construction. So, all taskes described above are supposed to be carried out using 20-cm robotic telescope of the RCO optical station layout. Obviously, the observations of some specific objects have to be done taking into consideration the technical limitations of a 20-cm telescope.

It is important to note that observation projects using the 20 cm telescope are planned to be carried out in collaboration with telescopes of INASAN Zvenigorod Observatory [3] and INASAN Collective Using Center [4, 5]. This center includes a 1 m Zeiss-1000 telescope of INASAN Simeiz Observatory [6] and a 2 m Zeiss-2000 telescope of INASAN Terskol Observatory. Such collaboration will be crucial to check the efficiency of the RCO itself and its layout as a segment of a global optical telescope network.

V. CONCLUSIONS

The creation of the Russian-Cuban Observatory (RCO) in the Republic of Cuba is in progress. The RCO is being created in 2 stages: first, a layout of the observatory is built in Havana, then the operating observatory will be built in Valle de Picadura. Here, we have described the equipment and some scientific observation projects planned to be implemented using the RCO optical station layout in Havana. The main instrument of the optical station layout is a wide-field 20 cm robotic telescope. The entire observational project program includes the both fundamental and applied tasks. For these reasons, the layout itself could be used as an independent observatory, because of its ability to solve universal observational tasks and to serve as a real segment of a global optical telescope network.

ACKNOWLEDGMENTS

The Russian team acknowledges financial support by the Ministry of Science and Higher Education of the Russian Federation (Project No. RFMEFI61319X0093, Agreement No. 075- 15-2019-1716 of November 20, 2019). The Cuban team acknowledges material, technical, and financial support by the Ministry of Science, Technologies and Environment of the Republic of Cuba.

REFERENCES

[1] D.V. Bisikalo, I.S. Savanov, S.A. Naroenkov, M.A. Nalivkin, A.S. Shugarov, *et al.*, Astron. Rep. **62**, 367 (2018).

[2] D. Marshalov, O. Pons Rodriguez, Yu. Bondarenko, V. Suvorkin, I. Bezrukov, S. Serzhanov, Rev. Cubana Fis. **37**, 73 (2020).

[3] INASAN Zvenigorod Observatory: http://www.inasan.ru/en/divisions/zvenigorod/

[4] INASAN Collective Using Center: http://www.inasan.ru/divisions/terskol/ckp/ (in Russian).

[5] INASAN Collective Using Center: http://www.inasan.ru/scientific_activities/projects/ckp_project/ (in Russian).

[6] I.V. Nikolenko, S.V. Kryuchkov, S.I. Barabanov, I.M. Volkov, Institute of Astronomy RAS Scientific Proceedings **4**, 85 (2019).

JOSÉ ANTONIO VUELVE AL EDIFICIO DE FÍSICA

Busto de José Antonio Echeverría justo tras ser develado en los jardines del edificio de Física el 16 de julio de 2020.

Tras 14 años de renovación del inmueble, el líder estudiantil José Antonio Echeverría vuelve al actual edificio de Física –antigua sede de Ingeniería y Arquitectura. En efecto, un busto en bronce del antiguo estudiante de Arquitectura fue emplazado en uno de los jardines del frente del edificio, el día 16 de julio de 2020. Echevarría había sido abatido a balazos por la policía de Batista el 13 de marzo de 1957, apenas a una cuadra del lugar de emplazamiento del busto, tras haber tomado la estación de Radio Reloj, anunciando al pueblo de Cuba el asalto al Palacio Presidencial, y la presunta muerte del tirano Fulgencio Batista. Tras develarse el busto ante la presencia de docenas de estudiantes, profesores y dirigentes, se realizó una memorable apología del líder estudiantil por parte del profesor Eduardo Torres Cuevas.

Una vez finalizada la ceremonia, muchos de los participantes pasaron a la entrada principal del edificio de Física, para presenciar la inauguración formal de su planta baja, que ocurre tras 14 largos años de trabajos de reparación y remodelación no exentos de luces y de sombras. La ceremonia incluyó cortar una cinta que atravesaba el portón de entrada, de lado a lado. La decana de la Facultad de Física, Dra. Aimé Peláiz-Barranco, pronunció unas sentidas palabras en las que realizó un recuento de los enormes esfuerzos que los que estudiantes y profesores de la Facultad de Física han debido realizar en este casi decenio y medio de espera; agradeció a todas las instancias que hicieron posibles el proceso de reparación, y terminó apuntando "Este edificio no es solo piedra; es historia. Es cada generación que ha estudiado y trabajado en él, por lo que hoy celebramos más que una remodelación concluida, una obra que se continúa, un futuro que se potencia. Hoy miramos con alegría este nuevo éxito, que compartimos con toda la comunidad universitaria. Les damos a todos la bienvenida la Casa de la Física Cubana".

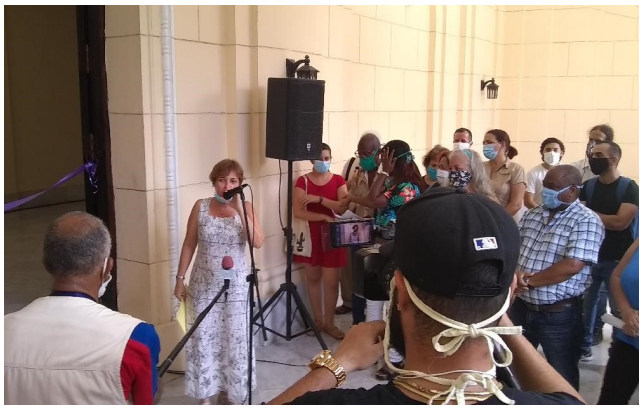

La decana de Física, durante las palabras de inauguración del edificio de Física reparado.

Acto seguido, los visitantes pasaron a los locales de la planta baja que, como en tiempos mejores, albergará los laboratorios de investigación, además del anfiteatro "Manuel F. Gran". Aunque dichos locales no están terminados al 100%, y aún se acomete la reparación de techos en pisos superiores debido a la mala calidad de la reparación inicial, lo cierto es que el edificio de Física vuelve a estar lleno de vida, y pronto dará cobijo nuevamente a la investigación en Física experimental.

E. Altshuler

ASUME NUEVO DIRECTOR DEL CLAF

Como parte de las actividades de la cuadragésima reunión del Consejo Directivo del Centro Latinoamericano de Física (CLAF), se realizó la elección de un nuevo director de dicha organización, resultando el chileno Luis Huerta. La actividad, que tuvo lugar los días 15 y 16 de noviembre de 2019 con la presencia de representantes de Argentina, Bolivia, Brasil, Chile, Costa Rica, Cuba, México, Perú, Uruguay y Venezuela, comenzó con el informe de la Dirección del año 2019, presentado por Carlos Trallero-Giner, el físico cubano que presidió la organización desde 2012. Para mayor información sobre la trayectoria del Dr. Trallero-Giner y su papel como director del CLAF, véase el artículo correspondiente en la sección "Momentos de la Física en Cuba" de nuestro número anterior .

E. Altshuler

LUIS CIMINO-QUIÑONES

(27 de agosto de 1932-15 de septiembre de 2020)

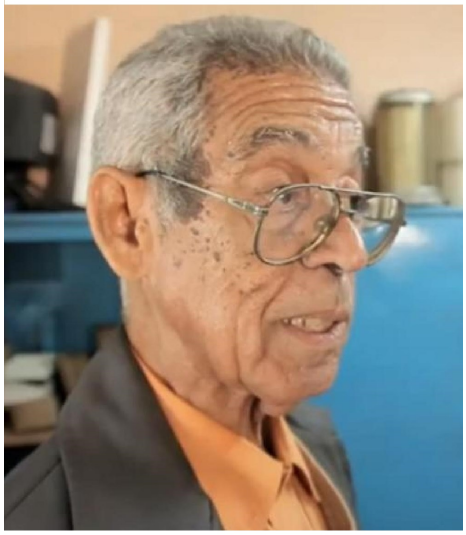

Luis Cimino-Quiñones (Foto: cortesía del InsTEC).

Luis Cimino es uno de los actores iniciales de las investigaciones científicas de la entonces Escuela de Física de la Universidad de La Habana (hoy Facultad de Física), en los primero años 1960's. Los talleres de mecánica, vidrio y electrónica –en cuya creación Cimino constituyó pieza clave– fueron decisivos en el impulso que recibieron las investigaciones científicas a finales de los 1960's y principio de los 1970's en dicha Escuela, cuyos efectos repercuten hasta aún hoy día en numerosas generaciones de físicos y físicas cubanos.

En paralelo con su intensa labor en los mencionados talleres, Cimino estudió licenciatura en Física, carrera de la que se graduó en julio de 1976. Durante los años 1960's y 1970's, realizó innumerables contribuciones a la instrumentación para las investigaciones en Física. Curiosamente, entre ellas se encuentra el diseño y construcción de un transductor para espectroscopía Mössbauer, utilizado por uno de los abajo firmantes (E.A.) para realizar su Tesis de Diploma de 1986: una más entre los abundantes frutos cuya semilla Cimino sembró, sin adjudicarse mérito alguno por ello. Durante su época como profesor en la Escuela de Física, Luis Cimino desarrolló un marcado interés por la Física Nuclear, al punto de sugerir insistentemente la necesidad del desarrollo de la energía nuclear en Cuba, cuando dichas materias se impartían, de forma incipiente, en la Escuela de Física. De hecho, desde 1976 hasta 1981, fue profesor de Física Nuclear y Electrónica en la Facultad de Física de la Universidad de La Habana. En 1981, con la creación de la Facultad de Ciencias y Tecnología Nucleares, Luis Cimino pasó a laborar en su departamento de Física Nuclear, donde defendió la Maestría en Física Nuclear en 1996. A lo largo de casi cuatro décadas, desarrolló en ese centro –hoy conocido como Instituto Superior de Tecnología y Ciencias Aplicadas (InSTEC)– una amplísima labor docente, organizativa e investigativa. Dentro de su extensa hoja de servicios, ha impartido cursos de Electrónica, Instrumentación nuclear, Microprocesadores, Aceleradores de partículas, Reactores nucleares, Física de neutrones, Satélites artificiales, y otros. Ha sido Presidente de la Cátedra Docente de Metrología, Jefe de la Cátedra de Estudios Aeroespaciales, y Presidente del tribunal especial para las categorías docentes de Adjuntos. Su mano ha estado virtualmente presente en todos los proyectos experimentales de relevancia abordados por el actual InSTEC. Fue contraparte cubana con el OIEA y el PNUD para el Desarrollo de Infraestructura Docente de Nivel Superior, trabajó en el Diseño y el Montaje de una planta para la producción de nitrógeno líquido (por un valor de $120,000 dólares como proyecto otorgado por el OIEA), trabajó en el Diseño y Montaje del Laboratorio del Conjunto Subcrítico en 1987. Desde 1999 venía desarrollando el Proyecto "Laboratorio Regional del Microtrón MT 25", que incluye la asimilación, puesta en operación y modernización de este acelerador de electrones.

Resulta claro que existían razones sobradas para que se le otorgara a Luis Cimino la condición de Miembro de Mérito de la Sociedad Cubana de Física en 2005. Su contribución a la Física cubana –especialmente en su rama experimental– es verdaderamente monumental.

E. Altshuler, E. Vigil
Facultad de Física,
Universidad de La Habana

L. A. Pérez-Alarcón
InSTEC,
Univesidad de La Habana

Revista Cubana de Física
ISSN 0253-9268
Online ISSN 2224-7939

Revista Cubana de Física
ISSN 0253-9268
Online ISSN 2224-7939

Revista Cubana de Física
ISSN 0253-9268
Online ISSN 2224-7939